$La_{0.5}Sr_{0.5}Fe_{1-y}M_yO_{3-\delta}$ (M = Ti, Ta) Perovskite Oxides for Oxygen Separation Membranes

THÈSE Nº 4137 (2008)

PRÉSENTÉE LE

À LA FACULTE SCIENCES ET TECHNIQUES DE L'INGÉNIEUR

LABORATOIRE DE CÉRAMIQUE

PROGRAMME DOCTORAL EN SCIENCE ET GÉNIE DES MATÉRIAUX

ÉCOLE POLYTECHNIQUE FÉDÉRALE DE LAUSANNE

POUR L'OBTENTION DU GRADE DE DOCTEUR ÈS SCIENCES

PAR

Defne Bayraktar

M.Sc. in Ceramic Engineering, New York State College of Ceramics, Alfred University, Etats-Unis
et de nationalité turque

accepté sur proposition du jury :

Prof. A. Mortensen, président du jury
Prof. N. Setter, Dr P. Holtappels, directeurs de thèse
Dr E. Pfaff, rapporteur
Prof. J. Ribeiro Frade, rapporteur
Dr J. Van Herle, rapporteur

EPFL
ÉCOLE POLYTECHNIQUE
FÉDÉRALE DE LAUSANNE

Suisse
2008

Defne Bayraktar THÈSE Nº 4137 (2008)

Abstract

Mixed ionic electronic conducting perovskite materials have been receiving considerable attention for the application of oxygen separation membranes. These membranes have potential to be integrated in industrial processes that require pure oxygen and to provide advantages considering economical and environmental aspects. The used perovskite materials can accommodate a high concentration of disordered oxygen vacancies and provide high oxygen permeation flux in the presence of an oxygen partial pressure gradient. However, the materials with high oxygen flux are observed to have low chemical and mechanical stability, originating from oxygen vacancy formation and reduction of the B-site transition metal ion. Based on the fact that the stability of the materials at reducing pO_2 is dependent on the redox stability of the B-site cation, a partial substitution of the B-site transition metal with a more stable cation is considered in this thesis to improve the stability of the base perovskite oxide.

The approach used for the identification of the suitable material based on the host composition $La_{0.5}Sr_{0.5}FeO_{3-\delta}$ (LSF) was to first explore the B-site substituting elements in terms of their effect on the thermal expansion and the isothermal expansion measured during the atmosphere change from air to argon. The elements Al, Cr, Zr, Ga, Ti, Sn, Ta, In, V, and Mg were used for 10 or 20% substitution of Fe. The isothermal expansion of the host material was decreased by substitution, which was attributed to decreased amount of oxygen vacancy formation as it was evidenced later by TGA of chosen compositions. As a result, the compositions substituted with higher valence ions (particularly, 20% Ti^{4+}, LSFTi2, and 10% Ta^{5+}, LSFTa1) were identified as the least expanding materials in isothermal conditions. The effect of substitution was further characterized extensively including structural, mechanical, and oxygen transport properties.

The oxygen vacancy ($V_O^{\bullet\bullet}$) concentration changes induced by substitution of Fe were reflected in unit cell sizes of heat-treated samples under argon atmosphere. The increase in the unit cell size was attributed to the isothermal expansion due to B-site reduction and lowered to half in case of substituted LSFTi2 and LSFTa1 compared to the host material LSF. Similar trends were observed for interrelated properties such as the coefficient of thermal expansion, isothermal expansion, and the actual amount of oxygen vacancies formed under argon at 900°C, all of which were higher for LSF.

The mechanical properties of LSF, LSFTi2, and LSFTa1 were characterized at room temperature. The Young's modulus and the bending strength of the materials were in the same range (141-147 GPa and ~120 MPa, respectively) while the fracture toughness of the LSF sample was improved by Ti and especially Ta substitution. The fractography of the samples provided evidence that the several LSF samples showed extended cracks possibly

related to residual stresses forming during cooling, due to non-equilibrated oxygen stoichiometry across the sample.

The potential step measurements showed that the chemical diffusion and the surface exchange coefficients measured during oxidation of the samples were higher than the ones measured during reduction of the samples. The tendency was reversed at lowered pO_2 along with the decrease of both coefficients. The influence of B-site substitution on both coefficients was not substantial.

The oxygen permeation flux of LSF, LSFTi2, and LSFTa1 was measured under air/argon gradient on planar membranes. The permeation rates of the membranes with thicknesses close to1 mm were considered to be limited by surface exchange kinetics at temperatures above 875°C. The permeation rate of LSF was decreased (from 0.2 $\mu molcm^{-2}s^{-1}$) to its third by Ti and Ta additions. The permeation rate of Ti and Ta-substituted samples showed a drop around 875°C, keeping a similar activation energy at lower and higher temperature regions. Oxygen vacancy ordering in the perovskite structure was given as a possible explanation, which provided explanation for the slow equilibrium in the lower temperature region.

Tubular membranes of LSF and LSFTi2 (0.47 mm and 0.36 mm thick, respectively) and a planar LSFTa1 membrane were characterized using an air/(Ar-CH$_4$) gradient. The measurements conducted using pure Ar on the lean-side provided the possibility to compare the thickness dependence of the permeation. In agreement with the previous observations, the permeation of the materials at and above 900°C was independent of the thickness, therefore, surface exchange limited. Stability under reducing atmospheres was increased by substitution. The LSF membrane failed shortly after the introduction of CH$_4$ to the system, while LSFTi2 survived 5% CH$_4$ and its oxygen permeation was improved substantially by a factor of 14.

LSFTa1 membrane was measured with pure CH$_4$ and the permeation was increased by a factor of 9, reaching 0.7 $\mu molcm^{-2}s^{-1}$ at 900°C. The membrane operated stably over 2000h with pure CH$_4$, 1000h. A slow degradation of 3.7% per 1000h was observed at 1000°C, most probably due to cation migration.

The compositions identified as a result of B-site substitution screening were effective in improving the stability of the materials without extensive loss of the oxygen permeation rate. Ta-substituted material was shown to be promising with its long-term stability as a partial oxidation membrane.

Résumé

Les membranes séparatrices d'oxygène sont très attractives pour la production d'oxygène pur à l'échelle industrielle. Leur utilisation constitue un enjeu économique et environnemental très important. De nouveaux matériaux comme les matériaux à structure pérovskite conducteurs mixtes (ioniques (ions oxygène) et électroniques) sont développés pour cette application. Ces pérovskites ont la propriété d'accommoder une grande concentration de lacunes d'oxygène de manière désordonnée. Ainsi, elles permettent un important flux de perméation d'oxygène quand un gradient de pression partielle d'oxygène est appliqué. Cependant, leur stabilité chimique et mécanique est médiocre. Cette instabilité est due à la formation de lacunes d'oxygène en raison de la réduction du métal de transition en site B. Sachant que la stabilité en atmosphère pO_2 réductrice pour ces matériaux dépend de la stabilité redox des cations en site B, une substitution partielle du métal de transition en site B par un cation plus stable devrait améliorer la stabilité de la pérovskite de base. Le but de ce travail de thèse est la caractérisation des pérovskites substituées et la comparaison de leurs propriétés à celles de la structure de base.

Différents substituants du site B pour la structure de base $La_{0.5}Sr_{0.5}FeO_{3-\delta}$ (LSF) ont été considérés dans cette étude. Fe est substitué par Al, Cr, Zr, Ga, Ti, Sn, Ta, In, V et Mg à la hauteur de 10 à 20%. Les effets de la substitution sur le coefficient d'expansion thermique et d'expansion isothermique sont mesurés lors du changement d'atmosphère d'air à argon. L'expansion isothermique du matériau hôte diminue lorsqu'il est substitué. L'analyse thermo-gravimétrique montre que cette diminution peut être attribuée à la diminution de la formation de lacunes d'oxygène. Ainsi, les pérovskites substituées par des ions de valence élevée (en particulier avec 20% de Ti^{4+}, LSFTi2, et 10% de Ta^{5+}, LSFTa1) sont peu susceptibles de s'expandre en conditions isothermiques.

Les variations de concentration en lacune d'oxygène ($V_O^{\bullet\bullet}$) liées à la substitution de Fe se reflètent dans la taille des mailles des échantillons traités sous argon. L'augmentation de la taille de la maille est attribuée à l'expansion isotherme due à la réduction du site B. Elle est réduite de moitié dans le cas de LSFTi2 et LSFTa1 substitués en comparaison de celle observée pour le matériau hôte LSF. Des dépendances similaires sont observées pour les coefficients d'expansion thermique, d'expansion isothermique et la quantité effective de lacunes d'oxygène formées sous argon à 900°C, ces valeurs étant plus grandes dans le cas de LSF.

Les propriétés mécaniques de LSF, LSFTi2 et LSFTa1 ont été caractérisées à température ambiante. Le module de Young et la résistance en flexion des matériaux sont du même ordre de grandeur (141-147 GPa et ~120 MPa, respectivement) pour tous les échantillons, alors que la ténacité de LSF est améliorée par la substitution de Ti et encore plus

de Ta. La fractographie des échantillons indique qu'ils présentent des fissures profondes provenant peut-être des contraintes résiduelles apparaissant au refroidissement et dues à la stoechiométrie en oxygène non équilibrée à travers l'échantillon.

Les mesures par pas-de-potentiel montrent que la diffusion chimique et les coefficients d'échange de surface mesurés durant l'oxydation des échantillons étaient plus importants que la réduction des échantillons. La tendance est inverse pour les faibles pO_2. L'influence de la substitution sur les deux coefficients n'est pas substantielle.

Le flux de perméation de l'oxygène de LSF, LSFTi2 et LSFTa1 a été mesuré sous un gradient air/argon pour des membranes planes. Les taux de perméation des membranes ayant des épaisseurs proches de 1 mm sont considérés comme étant limités par la cinétique d'échange de surface pour des températures supérieures à 875°C. Le taux de pénétration de LSF (0.2 $\mu molcm^{-2}s^{-1}$) est diminué d'un tiers par addition de Ti et Ta. Le taux de perméation des échantillons substitués par Ti et Ta chute à environ 875°C, gardant une activation d'énergie similaire à basse et haute température. La mise en ordre des lacunes d'oxygène dans la structure pérovskite est présentée comme une explication possible permettant d'expliquer le lent équilibre aux basses températures.

Des membranes tubulaires de LSF et LSFTi2 (0.47 mm et 0.36 mm d'épaisseur, respectivement) et une membrane planaire de LSFTa1 ont été caractérisées sous gradient air/(Ar-CH_4). Les mesures sous air/Ar ont permis d'établir une corrélation entre l'épaisseur de la membrane et le taux de perméation. En accord avec les résultats précédents, la perméation des matériaux à 900°C, ainsi que pour les températures supérieures, est indépendante de l'épaisseur ; en conséquence, l'échange de surface est limité. La stabilité sous atmosphère réductrice est augmentée par la substitution. La membrane de LSF s'est brisée juste après l'introduction de CH_4 dans le système, alors que LSFTi2 a résisté à 5% de CH_4 et sa perméation d'oxygène est améliorée substantiellement d'un facteur 14.

La membrane de LSFTa1 a été mesurée sous CH_4 pur et la perméation est augmentée par un facteur 9 atteignant 0.7 $\mu molcm^{-2}s^{-1}$ à 900°C. La membrane a opéré de manière stable pendant 2000 heures sous pur CH_4. Une dégradation lente de 3.7% par 1000 heures est observée à 1000°C probablement due à la migration des cations.

Les substitutions du site B étudiées ont permis d'améliorer la stabilité du matériau hôte LSF sans perte importante du taux de perméation en oxygène. En particulier, les matériaux de structure pérovskite substituée par Ta sont prometteurs pour l'utilisation en tant que membranes d'oxydation partielle car ils offrent une longue stabilité thermique.

Table of contents

List of Symbols and Abbreviations

a, a'   : unit cell parameter (Å)

a   : notch depth (mm)

A   : pre-exponential constant

A   : cross-section area (cm^2)

c   : crack length (cm)

c, c'   : unit cell parameter (Å)

c_i : concentration of component i (mol/cm^3)

d   : crystal plane spacing (Å)

d_{or}, d_{ir} : distance between the outer and inner rollers in bending tests (mm)

$\tilde{D}$: chemical diffusion coefficient (cm^2/s)

D^* : tracer diffusion coefficient (cm^2/s)

D_K : component diffusion coefficient (cm^2/s)

e   : electric charge, 1.60217×10^{-19} (C)

E   : electrical potential (V)

E_a : activation energy (kJ/mol)

Ey   : Young's modulus (GPa)

f   : Haven ratio

f   : fundamental frequency of flexural vibration (kHz)

F   : Faraday's constant, 96485 (C/mol)

F_{max} : the peak force at fracture (N)

G   : shear modulus (GPa)

I   : electrical current (A)

j : permeation flux (mol/cm^2/s)

k   : Boltzmann constant, 1.3806×10^{-23} (m^2kg/s^2K)

k_S : surface exchange coefficient (cm/s)

k_0, k_L : surface exchange coefficients at surfaces of the membrane (cm/s)

K : equilibrium constant

K_{Ic} : fracture toughness (MPa·$m^{1/2}$)

l : distance between the voltage leads (cm)

l   : length of the sample (mm)

L   : thickness of the membrane, length of the sample (cm)

L_c : critical thickness (mm)

L_2, L_3 : absorption edges

L_{ij} : general transport coefficients

m	: mass of the sample (g)
n	: number of charged particles per unit volume
p	: porosity fraction
$p\mathrm{O}_2$	: partial pressure of oxygen (atm)
r_i	: ionic radius of component I (Å)
R	: ideal gas constant, 8.314 (J/K.mol)
R	: resistance (Ohm)
t	: tolerance factor
t	: thickness of the sample (mm)
t_i	: transference number of component i
T	: absolute temperature (K)
Q	: total charge (C)
V	: volume (cm^3)
V_m	: molar volume (cm^3/mol)
w	: width of the sample (mm)
x_i	: fraction of component i
z	: number of charges

α, α'	: interaxial angle
β, β'	: interaxial angle
δ	: oxygen non-stoichiometry
ε_C	: chemical strain
ε	: strain
η	: electrochemical potential (V)
Λ	: constant, $k_\mathrm{T}\mathrm{L}/\tilde{D}$
ϕ	: electronic potential (V)
γ, γ'	: interaxial angle
γ	: shear strain
γ	: thermodynamic surface energy
λ	: wavelength of X-rays (Å)
λ_n	: roots of the equation $\lambda \tan(\lambda) = \Lambda$
μ	: chemical potential (J/mol)
ν	: Poisson's ratio
θ	: angle between the incident ray and the scattering planes
ρ	: density (g/cm^3)
σ	: stress (N)

σ_i : partial conductivity of component i (S/cm)

σ_f : fracture strength (MPa)

τ : shear stress (N/m^2)

τ_d, τ_g : time constant associated with diffusion and oxygen pump response

BSE   : back-scattered electron

CTE   : coefficient of thermal expansion

EDX   : energy dispersive X-ray

JCPDS : Joint Committee on Powder Diffraction Standards

LSF   : $La_{0.5}Sr_{0.5}FeO_{3-\delta}$

LSFMy : $La_{0.5}Sr_{0.5}Fe_{1-0.y}M_{0.y}O_{3-\delta}$

LS/HS   : low spin/high spin

MIEC   : mixed ionic electronic conductor

PE   : polyethylene

POX   : partial oxidation

QENS   : quasielastic neutron scattering

SE   : secondary electron

SEM   : scanning electron microscope

SIMS   : secondary ion mass spectroscopy

SSA   : specific surface area

TGA   : thermo gravimetric analysis

XAS   : X-ray absorption spectroscopy

XRD   : X-ray diffraction

YSZ   : yttria stabilized zirconia

Chapter 1

General Introduction

Oxygen in its pure form is one of the most widely used chemicals in areas such as medical applications and combustion processes. Therefore, a production process that is low-cost compared to readily available techniques would enhance the availability of pure oxygen. There is increasing amount of efforts for the development of efficient oxygen separation processes from gas mixtures like air. A new perspective has emerged in the last few decades considering the use of dense ceramic membranes for the application of oxygen separation. Especially the use of mixed ionic electronic conducting ceramic materials for oxygen separation offers a possibility for a clean, cost-effective, and flexible technique.

This chapter provides an introduction to the main topics concerning the oxygen separation using dense ceramic membranes and their application to partial oxidation of hydrocarbons.

1.1. O$_2$ production

There is a large number of different methods for obtaining oxygen.[1] Earlier commercial techniques used were either catalytic decomposition of solid potassium chlorate or the catalytic decomposition of hydrogen peroxide. After the improvements made in vacuum and gas compression techniques, cryogenic distillation became possible. Liquid air is a mixture of liquid nitrogen and oxygen, which have boiling points of –196°C and –183°C, respectively. Therefore, nitrogen boils off before oxygen during heating, which is the basis of oxygen production through cryogenic air distillation. Another commonly used technique is pressure swing adsorption. It is based on the preferential absorption of nitrogen on adsorbents such as zeolites or a carbon molecular sieve, which leaves an oxygen enriched gas phase.[1] This process is not continuous and may need to be repeated to obtain high-purity oxygen, which raises the cost of the process sharply.

It has been demonstrated that dense ceramic oxygen separation membranes can offer advantages over the techniques in use today. Especially, 100% selectivity of dense ceramic membranes for oxygen ions makes the process very attractive. There have been already extensive research on applications for these membranes mainly on electrically-driven membranes for medical O$_2$ production, pressure-driven membranes to be integrated with combustion or gasification processes, and chemical potential driven partial oxidation (POX) for syngas production from natural gas.[2-6] The latter is the focus of interest for the materials investigated in this thesis. However, before going into details of partial oxidation applications of the membranes, a short overview is given below on the general concept of dense ceramic membranes.

1.2. Dense ceramic membranes for oxygen separation

A membrane, by definition, is a barrier that preferentially allows one species to permeate through it. The rate of the permeation depends on the pressure, concentration, and temperature of the permeating species on both sides of the membrane in addition to the permeability of the membrane. In case of dense ceramic membranes, the permeation of any molecular gas is hindered by the high density of the membranes and the oxygen permeation occurs by selective transport of oxygen anions via oxygen vacancies in the crystal structure by a hopping mechanism. This process is thermally activated and only possible when the oxygen ions have sufficient thermal energy to overcome the energy barrier to jump from one crystallographic site to the other one. The necessary temperature for activation of oxygen ionic hopping is dependent on the type and composition of the material. For mixed ionic electronic conducting perovskites, it is generally in the range of 700 – 1000°C.

The other important condition is that there should be a driving force for the process either chemically or electronically. The oxygen ionic transport in a material has to be balanced by electronic transfer in the opposite direction to maintain the charge neutrality in the material. Considering the operation concepts, there are three main types of membranes.[7] The first one is the mixed ionic electronic conducting (MIEC) membrane, for which the ionic and electronic transport occur simultaneously in the same material under the driving force of a oxygen chemical potential across the membrane. The second type is the so-called oxygen pump, where the membrane material is ionically conductive (electrolyte) and an externally applied potential is the driving force for the oxygen permeation. The potential is applied via porous electrodes on both sides of the membrane. The third type is a dual-phase membrane that operates similar to MIEC membranes; however, these membranes are composed of two phases, one of which is an ionic conductor while the other is an electrical conductor. The drawback of the last two concepts is that the oxygen can be incorporated into or released from the membrane at the triple phase boundaries, lowering the active surface for oxygen exchange. This situation is eliminated in case of MIEC membranes.

1.3. Oxygen separation membranes for partial oxidation of methane to syngas

Synthesis gas ($2H_2 + CO$), or syngas in short form, is the most important intermediate in the conversion chain for upgrading natural gas to liquid products such as methanol, formaldehyde, or ethylene so that they can be more easily stored, decreasing the cost of transport.[8-10] Syngas can be produced either by steam reforming[11], which is the conventional route, or partial oxidation[12]. The latter is advantageous considering the process conditions (low operation pressure, shorter time, no need for external energy, exothermic) and produces stoichiometric syngas, eliminating the need for further modifications. Using air as the oxygen supply would be cheap; however, almost 80% of air is composed of N_2. The advantages of using O_2 instead of air include the high product selectivity, eliminating N_2 contamination, and also NO_x environmental pollutants.[8] O_2 production by itself has the highest portion in the total gas to liquid conversion cost. Therefore, the capital cost can be reduced significantly with a reduction on the oxygen supply cost of the process. A membrane reactor at which O_2 is separated and simultaneously fed into the methane stream (combined oxygen separation and catalytic reaction) has been suggested to improve the design.[13, 14]

A schematic of the oxygen membrane reactor integrated in partial oxidation of methane is shown in Fig. 1.1.
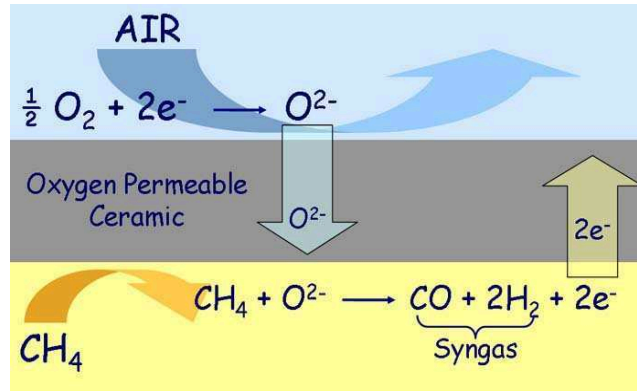
Fig. 1.1. Schematic of oxygen separation process from air, integrated with syngas production.

The net transport of oxygen through the membrane includes several processes. On the oxygen exposed-side, after the dissociation and ionization of oxygen by uptaking electrons from the membrane surface, the oxygen diffuses to the structure by occupying an oxygen vacancy. While on the oxygen-lean (low $p\text{O}_2$) side of the membrane, oxygen ion releases its electrons to recombine to oxygen or react further with the methane in a reforming reaction. The half-reactions at air- and gas-side of the membrane depicted in Fig. 1.1 are given in Eqs. 1.1 and 1.2 using Kröger-Vink notation[15] as follows:

$$\frac{1}{2}O_2 + V_O^{\bullet\bullet} \rightarrow O_O^X + 2h^{\bullet} \tag{1.1}$$

$$CH_4 + O_O^X + 2h^{\bullet} \rightarrow 2H_2 + CO + V_O^{\bullet\bullet} \tag{1.2}$$

$$CH_4 + \frac{1}{2}O_2 \rightarrow 2H_2 + CO \tag{1.3}$$

where $V_O^{\bullet\bullet}$ is the oxygen vacancy, $h^{\bullet}$ is the electron hole, O_O^x is lattice oxygen, and the sum $2H_2 + CO$ is syngas and the sum of these two reactions leads to the overall reaction given in Eq. 1.3.

An economic analysis for syngas production comparing the O_2 membrane reactor technology with a traditional reforming route showed that the suggested new technology could be competitive when O_2 fluxes through dense ceramic membranes of 10 ml/min.cm^2 can be obtained at a membrane cost of 1600\$/m^2.[16] The cost figure appears attainable. However, in case of flux, either the required values are not reachable or the high values are not stable over a long time.

Several classes of ceramics have been investigated to use as oxygen separation membranes. These are mainly fluorite- and perovskite-based materials.[7] Especially, the

mixed ionic electronic conducting (MIEC) perovskites or related materials receive considerable attention due to their superior oxygen flux.[17-19] However, materials with high oxygen flux show problems in both chemical and dimensional stability under operating conditions. Therefore, the major challenges waiting to be addressed include the stability of the membranes under operation conditions, and the long term reliability.[2, 16] In this thesis, the interest is focused on improving the stability of mixed ionic-electronic conducting perovskite oxides for application in dense oxygen separation membranes. The next chapter aims to give an introduction on these materials including their structure, permeation, and stability.

Chapter 2

Theoretical Background, State of the Art, and Motivation

This chapter provides theoretical background on the structure of the considered materials, perovskites and mixed ionic electronic conducting perovskites in particular. The defect chemistry of $La_{1-x}Sr_xFeO_{3-\delta}$ materials is introduced. In addition, the theory of oxygen transport in MIEC materials is explained followed by stability issues in these materials, focusing on the redox stability and isothermal expansion. Finally, the choice of materials is explained and the scope of the thesis is given.

2.1. Mixed ionic-electronic conducting perovskites

2.1.1. Perovskite structure

The ideal perovskite structure, shown in Fig. 2.1, has the formula ABO_3. The structure consists of cubic arrays of corner-sharing BO_6 octahedra, where B is a transition metal cation, which has six-fold coordination with oxygen ions, as represented in the right schematic in Fig. 2.1. The interstitial site between the octahedra is occupied by the A cation, which has twelve-fold coordination to oxygen ions and can be an alkali, an alkaline earth, or a rare earth ion.[7]

○ A   ● B   ◎ O
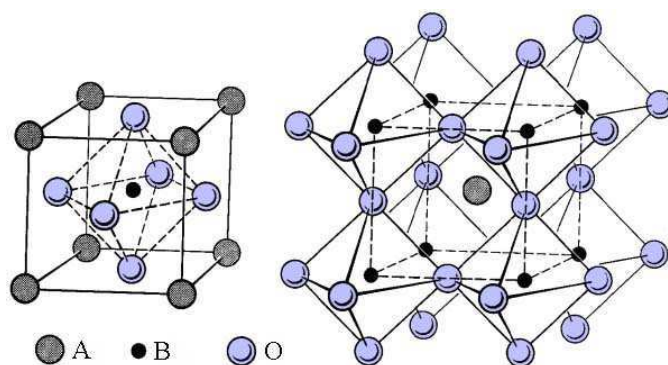
Fig. 2.1. Ideal cubic perovskite structure, ABO_3, showing the BO_6 octahedra, taken from Ref.[20]

The perovskite structure may be defined also as cubic closed packed layers of AO_3 with B cations in the interlayer octahedral sites, as represented in the left schematic in Fig. 2.1. The ideal perovskite has cubic structure. The tolerance limits of the structure were defined by Goldschmidt[21], which will be explained later in Chapter 3. Most materials show deviations from ideality causing tilting and distortion of the cubic structure, shifting the symmetry of the perovskite to rhombohedral, orthorhombic, or tetragonal structure.

The perovskite lattice generally exists even with large deviations from stoichiometry, which provides stability to the material and allows for tailoring the materials properties to a large extent. The desired properties of the perovskite materials are obtained by substitution on A- and B-site of the structure. The substituted perovskite material can be denoted as $AA'BB'O_{3-\delta}$ where A is a lanthanide, A' is an alkaline earth (Ca, Sr, Ba), B and B' are transition metals. In case of mixed ionic electronic conducting (MIEC) perovskites, mobile oxygen vacancies, which are responsible for the oxygen ionic conductivity and thus oxygen permeability, are introduced by so-called acceptor doping with the lower valence cations on

A'- or B'-site, which is charge balanced by formation of oxygen vacancies and/or oxidation of B-site cation.[22]

The electronic conduction occurs via B-O-B bond chains[23] (which will be explained more detailed in Chapter 5) and therefore the electronic conductivity of the material depends on the nature of the B-site cation. The oxygen transport in the material occurs via oxygen vacancies. Therefore, the oxygen vacancies need to be disordered and mobile, i.e. favorable for oxygen hopping. However, it has been reported that an increased amount of defects in the material may cause defect interactions, lowering the number of mobile oxygen vacancies.[7] Another possible consequence of high defect concentration is the ordering of oxygen vacancies, again limiting the oxygen vacancy movement.[24]

With increasing oxygen vacancy concentration, the ABO_3 perovskite structure can change to a brownmillerite structure with formula $A_2B_2O_5$, i.e. every one sixth oxygen ion is removed from the initial perovskite structure. The resulting unit cell is a super structure of the perovskite with orthorhombic symmetry. The brownmillerite structure is shown in Fig. 2.2 (b) together with the ideal perovskite structure (a). The oxygen vacancies are ordered in [110] direction forming alternating octahedral (BO_6) and tetrahedral (BO_4) layers as shown in Fig. 2.2 (b).
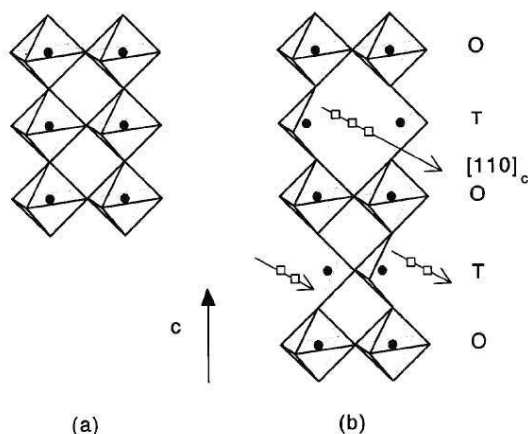
Fig. 2.2. a) Ideal perovskite structure, b) brownmillerite structure with ordered oxygen vacancies in the [110] direction, taken from Ref.[7]

The transition from the disordered perovskite to the ordered brownmillerite structure occurs below a so-called transition temperature, which depends on the material. In $Sr_2Fe_2O_5$ materials, it was found that the tetragonally coordinated Fe existed even at temperatures higher than order-disorder transition temperature, suggesting formation of micro domains with ordered structure, which were not visible to XRD.[25]

2.1.2. Acceptor-doped perovskite materials

An approach to increase the vacancy concentration is the acceptor doping by partial substitution of the A-cation with lower valent ones. The interest in acceptor-doped perovskite materials has been increasing since Teraoka et al.[22, 26, 27] published their studies on oxygen permeation of lanthanide cobaltite based materials. The effects of lanthanide and transition metal cations on the oxygen permeation of $La_{1-x}A_xCo_{1-y}B_yO_{3-\delta}$ were studied. The oxygen permeation was found to increase with increased A-site substitution amount. It was also reported to increase in the orders La < Pr < Nd < Sm < Gd for lanthanide cation, Na < Sr < Ca < Ba for A-site substitution, and Mn < Cr < Fe < Co < Ni < Cu for the B-site transition metal substitution. These trends basically follow the thermodynamic stability of the perovskite in the opposite direction. The thermodynamic stability of the perovskites will be discussed further later in this chapter. The perovskites with Mn and Cr on the B-site are good electronic conductors but do not possess high ionic conductivity; therefore, are not considered to be used as oxygen separation membranes but for solid oxide fuel cells.[28, 29]

Among the above-mentioned materials, the most promising and commonly studied ones are cobaltites and ferrites with La on the A-site. They are predominant electronic conductors, still their ionic conductivities are generally 1-2 orders of magnitude higher than those of other oxygen-ionic conductors such as yttria-stabilized zirconia.[26]

The materials with Co on the B-site have high oxygen permeation and it increases further with increasing amount of acceptor doping on A-site. $SrCo_{0.8}Fe_{0.2}O_{3-\delta}$ material is found to have a very high oxygen permeation rate, however, accompanied by low stability.[30] Another widely studied material is $Ba_{0.5}Sr_{0.5}Co_{0.8}Fe_{0.2}O_{3-\delta}$, which is one of the high-permeation possessing membrane materials. It was reported that the partial substitution of Sr by Ba increases the stability of the material.[31, 32]

Owing to their increased stability, $La_{1-x}Sr_xFe_{1-y}Co_yO_{3-\delta}$ materials have received extensive interest. Commonly, the amount of Co in the material is reduced to obtain increased stability. This point will be further discussed after introducing the defect chemistry of these materials.

2.2. Defect Model of La$_{1-}$xSrxFeO3

The defect chemistry of $La_{1-x}Sr_xFeO_{3-\delta}$ has been studied by Mizusaki et al.[33, 34] and can well explain the electrical properties of these materials. The next section of this chapter is devoted to the defect model of these materials.

Taking LaFeO$_3$ as the host, substitution of Sr^{2+} on the La^{3+} A-site can be represented as follows:

$$SrFeO_3 \xrightarrow{\quad LaFeO_3 \quad} Sr'_{La} + Fe^{\bullet}_{Fe} + 3O^X_O \qquad (2.1)$$
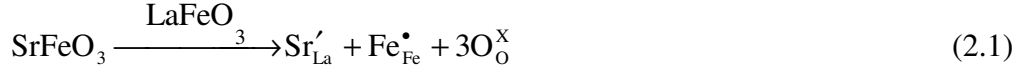
In this case, the acceptor doping by Sr is compensated by oxidation of Fe^{3+} to Fe^{4+}. The reaction between oxygen and defects can further be expressed (using Kröger-Vink notation[15]) as:

$$\frac{1}{2}O_2 + V^{\bullet\bullet}_O + 2Fe^X_{Fe} = O^X_O + 2Fe^{\bullet}_{Fe} \qquad (2.2)$$

$$2Fe^X_{Fe} = Fe'_{Fe} + Fe^{\bullet}_{Fe} \qquad (2.3)$$

where V$_O^{\bullet\bullet}$, Sr$_{La}$', Fe$_{Fe}$', and Fe$_{Fe}^{\bullet}$ are the major defects in La$_{1-x}$Sr$_x$FeO$_{3-\delta}$.[33, 35] The equilibrium constants for equations 2.2 and 2.3,

$$K_{ox} = \frac{\left[O^X_O\right]\left[Fe^{\bullet}_{Fe}\right]^2}{pO_2^{1/2}\left[V^{\bullet\bullet}_O\right]\left[Fe^X_{Fe}\right]^2} \qquad (2.4)$$

$$K_i = \frac{\left[Fe'_{Fe}\right]\left[Fe^{\bullet}_{Fe}\right]}{\left[Fe^X_{Fe}\right]^2} \qquad (2.5)$$

If [V$_O^{\bullet\bullet}$] = δ and therefore [O$_O^X$] = 3-δ, and [Sr$_{La}$'] = x. The site conversation and the charge neutrality equations can be written as,

$$\left[Fe'_{Fe}\right] + \left[Fe^{\bullet}_{Fe}\right] + \left[Fe^X_{Fe}\right] = 1 \qquad (2.6)$$

$$x + \left[Fe'_{Fe}\right] = 2\delta + \left[Fe^{\bullet}_{Fe}\right] \qquad (2.7)$$

These equations can be used together with experimentally measured data to construct a defect concentration diagram as shown in Fig. 2.3.[33] In this figure, the concentration of oxygen (3-δ) is shown as a function of partial pressure of oxygen pO$_2$ in log scale.
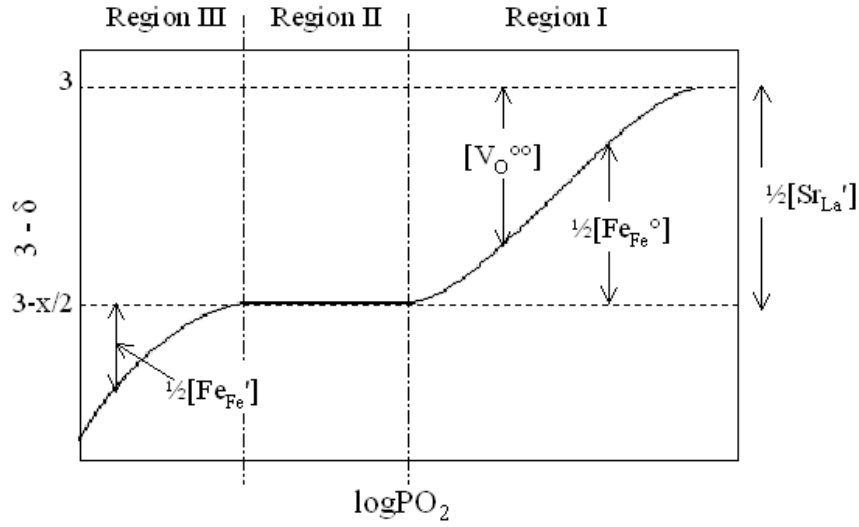
Fig. 2.3. The schematic of the defect concentrations $[Sr_{La}']$, $[V_O^{\bullet\bullet}]$, $[Fe_{Fe}']$, and $[Fe_{Fe}^{\bullet}]$ as a function of $\log pO_2$, redrawn from Ref.[33]

There are three regions in Fig. 2.3, first of which is the higher pO_2 region where $[V_O^{\bullet\bullet}]$ and $[Fe_{Fe}^{\bullet}]$ are the main defects and $[Fe_{Fe}'] \approx 0$. In the second region, $[Fe_{Fe}^{\bullet}]$ becomes sufficiently low and there is a plateau where equation 2.7 becomes $x \approx 2\delta$; therefore, the position of the plateau depends on the amount of Sr-substitution. Finally, in the last region with low pO_2, Fe is reduced further to form $[Fe_{Fe}']$ until the point that the material starts to decompose.

The defect concentrations shown in Fig. 2.3 can be used to model the electronic conductivity behavior of the material as will be shown in Chapter 5.

2.3. Theory of oxygen transport in mixed conducting perovskites

2.3.1. Bulk Transport

In oxygen transport, Wagner's theory is most widely used, in which the transport equations are formulated for irreversible thermodynamics.[36] The basic assumptions made for the theory are as follows. The oxygen transport through the bulk determines the oxygen flux, which is one-dimensional. Considering the perovskite structure under investigation, the mobile species are electronic holes and oxygen ions, for which the transport is assumed to occur via oxygen vacancies in the form of oxygen ions, rather than molecules. The charge compensation occurs by simultaneous flux of electrons without the use of external circuitry.[7, 37]

Here we consider the interaction of oxygen in gas form with the oxide vacancies that can be obtained for example by doping aliovalent cations. The reaction is represented as:

$$\frac{1}{2}O_2 + V_O^{\bullet\bullet} + 2e' = O_O^X \tag{2.8}$$

The general equations for one-dimensional transport of the components, i and k (oxygen ions/vacancies and electrons/electron holes in our case) in an isotropic sample at constant temperature and pressure without internal stress are:

$$j_i = L_{ii}\frac{d\eta_i}{dx} + L_{ik}\frac{d\eta_k}{dx} \tag{2.9.a}$$

$$j_k = L_{ki}\frac{d\eta_k}{dx} + L_{kk}\frac{d\eta_k}{dx} \tag{2.9.b}$$

where j is the flux of component i or k, L_{ii}, L_{ik}, L_{ki}, and L_{kk} are the general transport coefficients, also called Onsager coefficients, where $L_{ik} = L_{ki}$, and $d\eta$ is the electrochemical potential.

Since in our case, the movement of oxygen vacancy is coupled with transport of electron hole, the rate j_k for transport of electrons is equal to the rate of transport of oxygen ions. Hence, whenever the electronic conduction prevails, the result is independent of cross-coefficients.[37] Therefore, the single particle flux of charge carriers, neglecting the cross-terms becomes:

$$j_i = L_{ii}\nabla\eta_i = -\frac{\sigma_i}{z_i^2 F^2}\nabla\eta_i \tag{2.10}$$

where σ_i is the conductivity, z_i the charge number of component i, F the Faraday constant (F = 96485 C/mole), and $\nabla\eta_i$ the gradient of the electrochemical potential. $\nabla\eta_i$ consists of a gradient in chemical potential $\nabla\mu_i$ for each charge carrier i, and a gradient in electrical potential $\nabla\phi$.

$$\nabla\eta_i = \nabla\mu_i + z_i F\nabla\phi \tag{2.11}$$

The relation between the fluxes of ionic and electronic defects ($j_{V_O^{\bullet\bullet}}$, $j_{e'}$, and $j_{h^\bullet}$, are fluxes of oxygen vacancy, electrons, and electron holes, respectively) at steady-state can be written as follows:

$$2j_{V_O^{\bullet\bullet}} = j_{e'} - j_{h^\bullet} \tag{2.12}$$

Assuming that there is local equilibrium that is not disturbed by transport of oxygen, the following equilibrium equations of potential gradients of individual charge species can be written.[38, 39]

$$\frac{1}{2}\nabla\mu_{O_2} + \nabla\mu_{V_O^{\bullet\bullet}} + 2\nabla\mu_{e'} = 0 \text{ and} \tag{2.13}$$

$$\nabla\mu_{e'} + \nabla\mu_{h^\bullet} = 0 \tag{2.14}$$

Eqs. 2.10 to 2.14 can be combined to derive a relationship for oxygen flux, j_{O_2}, using $j_{O_2} = -1/2 \ j_{V_O^{\bullet\bullet}}$, $(\sigma_{e'} + \sigma_{h^\bullet}) = \sigma_{el}$, and $\sigma_{V_O^{\bullet\bullet}} = \sigma_{ion}$, where σ_{el}, and σ_{ion} are partial electronic and ionic conductivities. The resulting general equation is shown below:

$$j_{O_2} = -\frac{1}{16F^2}\frac{\sigma_{el}\sigma_{ion}}{\sigma_{el} + \sigma_{ion}}\nabla\mu_{O_2} \tag{2.15}$$

The partial conductivities can be related to each other and to total conductivity, σ_{total}, by transference numbers, t_{el} and t_{ion}, for electronic and ionic conductivities, respectively.

$$t_{el} t_{ion} \sigma_{total} = t_{ion} \sigma_{el} = t_{el} \sigma_{ion} \tag{2.16}$$

The Wagner's equation for bulk diffusion can be obtained by integrating Eq. 2.15 across the thickness of the membrane, L, and inserting $\nabla\mu_{O2} = \partial RT \ln pO_2 / \partial x$:[40]

$$j_{O_2} = -\frac{RT}{16F^2L}\int_{\ln p'O_2}^{\ln p''O_2}\frac{\sigma_{el}\sigma_{ion}}{\sigma_{el} + \sigma_{ion}}d\ln pO_2 \tag{2.17}$$

$$j_{O_2} = \frac{RT}{16F^2L}\frac{\sigma_{el}\sigma_{ion}}{\sigma_{el} + \sigma_{ion}}\left(\ln p_1 - \ln p_2\right) \tag{2.18}$$

where p_1 and p_2 are the partial pressures of oxygen (pO_2) on the air and the fuel side, respectively.

2.3.2. Chemical Diffusion Coefficient

In processes involving stoichiometric changes in the solid, electrical neutrality should be satisfied by simultaneous migration of ions, electrons or defects and the flux of each are related to each other. The diffusion coefficient in such a process is called the chemical diffusion coefficient, $\tilde{D}$. In 1855, Fick stated the empirical equation for diffusion flux, j_x in a concentration gradient, $\partial c/\partial x$, as $j_x = -D\, \partial c/\partial x$, which is known as Fick's first law. Fick's first law applied for the transport of oxygen atoms, where the gradient in neutral oxygen, $\partial c_O/\partial x$, the driving force for the diffusion, is shown below:

$$j_O = -\tilde{D}\frac{\partial c_O}{\partial x} \tag{2.19}$$

where $\tilde{D}$ is the chemical diffusion coefficient. On the grounds of electrical neutrality, the oxygen gradient can be related to the vacancy gradient with $\partial c_O/\partial x = -\partial c_V/\partial x$. Therefore, the same equation can be written for the diffusion of oxygen vacancies when diffusion is dominated by vacancies. Combining equations 2.15 and 2.19 noting that $j_{O_2} = \frac{1}{2}\, j_O$, provides:

$$\tilde{D} = \frac{1}{8F^2}\frac{\sigma_{el}\sigma_{ion}}{\sigma_{el}+\sigma_{ion}}\frac{\partial \mu_{O_2}}{\partial c_O} \tag{2.20}$$

The value of $\partial \mu_{O2}/\partial c_O$ can be obtained directly by measuring the oxygen stoichiometry as a function of oxygen partial pressure through the relation:

$$\frac{\partial \mu_{O_2}}{\partial c_O} = RTV_m \frac{\partial \ln pO_2}{\partial \delta} \tag{2.21}$$

where R is the ideal gas constant, T the absolute temperature, V_m the molar volume of the oxide, and δ the oxygen nonstoichiometry.

When the material has predominantly electrical conductivity, Eq. 2.20 can be simplified to:

$$\tilde{D} = \frac{D^*}{fRT}\frac{1}{2}\frac{\partial \mu_{O_2}}{\partial \ln c_O} \tag{2.22}$$

where D^* is the tracer diffusion coefficient, f the Haven ratio, which is a proportionality constant between D^* and D_K, the component diffusion coefficient, with $D^* = fD_K$. The component diffusion coefficient is related to the partial ionic conductivity by:[39]

$$D_K = \frac{\sigma_{ion}RT}{c_O z_i^2 F^2} \qquad (2.23)$$

Haven ratio depends on the geometrical arrangement of particles in the lattice together with the diffusion mechanism. The tracer diffusion coefficient is related to the random walk of a chemical component and f is generally close to unity so it is equal to the component diffusion coefficient. On the other hand, the chemical diffusion coefficient is related to the transport of neutral mass under a chemical potential gradient.[41]

2.3.3. Ionic conductivity in terms of permeation and chemical diffusion coefficient

Values of the oxygen ionic conductivity (σ_i) can be calculated from the data of both current relaxation and permeation measurements assuming that the oxygen permeation rate is governed by bulk diffusion. For a predominantly electronic conductor ($\sigma_e \gg \sigma_i$), the ionic conductivity is related to the chemical diffusion coefficient through[42]

$$\sigma_i = -\frac{8F^2}{RTV_m}\frac{d\delta}{d\ln pO_2}\tilde{D} \cong \frac{\Delta Q}{V\Delta E}\tilde{D} \qquad (2.24)$$

where F is the Faraday's constant, R is the ideal gas constant, V_m is the molecular volume of the sample, V is its volume, and $d\delta/d\ln pO_2$ is the slope of the oxygen nonstoichiometry vs. pO_2 data. In the right hand side of Eq. 2.24, the latter has been evaluated from the amount of charge ΔQ extracted from (or incorporated in) the sample during a potential step ΔE, i.e. the integral of the current over the measurement time.[42]

Similarly, if one assumes that the oxygen transport through a dense membrane is limited by the bulk diffusion, an average ionic conductivity (σ_i) can be calculated from the permeation flux (j_{O_2}) shown in Eq. 2.18:[43]

$$\sigma_i = -\frac{16F^2L}{RT\Delta\ln pO_2}j_{O_2} \qquad (2.25)$$

where L is the thickness of the membrane and $\Delta \ln p O_2$ is the difference of the natural logarithms of the partial pressures of oxygen on the air and the reaction sides of the membrane.

2.4. Oxygen permeation

As explained previously, the oxygen permeation through a membrane is basically controlled by two parameters, diffusion in the bulk and the interfacial oxygen exchange on the air and the lean side of the membrane. A common way to show the effect of these two processes is presented in Fig.2.4. The chemical potential of oxygen, μo_2, is shown across the membrane from the oxygen rich side ($p O'$) towards the lean side ($p O''$).
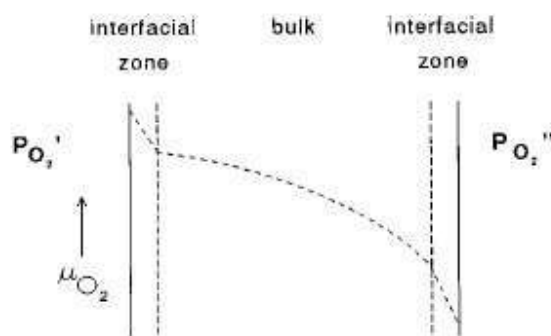
Fig. 2.4. Schematic of chemical potential across the membrane dropping from oxygen rich side ($p O'$) towards the oxygen lean side ($p O''$), taken from Ref.[7]

In Fig. 2.4, the interfacial zones are shown so to indicate the surface exchange kinetics at both sides. Even for membranes with bulk transport being the rate-limiting step, the chemical potential of oxygen is supposed to drop at the interfacial zones. However, the largest drop is supposed to occur across the least permeable zone. The bulk zone is also called as the Wagner-zone where the bulk diffusion occurs.[7]

A common practice to increase the oxygen flux independent of the composition is to decrease the thickness of the membrane to create a higher chemical potential gradient across the membrane. This of course is possible when the bulk diffusion governs the transport properties. With the attempts of obtaining higher oxygen flux, it became important to be able to produce thin membranes. Thin membranes (<200μm) may lack necessary mechanical stability; therefore, it is common to produce supported membranes. The porous support is made either from a material similar to the membrane or totally different materials such as MgO. The thin-film membranes produced by pulsed layer deposition (PLD) was used by van der Haar[44] and the membrane was found to possess an order of magnitude higher oxygen permeation compared to a 0.44 mm thick planar membrane.

An important feature of using mixed-conducting oxides for partial oxidation reactions is that the oxygen flux may influence the relative presence of different oxygen species on the catalytic surface and this results in selectivity for the reaction.

2.5. Stability of MIEC perovskites

As pointed out earlier, in addition to the requirement that the membrane material should have high oxygen flux, it should also be sufficiently stable for long-term operation. Therefore, the material should sustain the stability at the operation temperature and the highly reducing and oxidizing conditions that it is exposed to. The main sources of stress on the membranes are differential thermal expansion coefficients of different components, temperature gradients, oxygen activity gradients, and external mechanical loading. The magnitude of the stress depends on the materials properties, the operating conditions and the geometry of the design. Among all, the chemical strain resulting from oxygen activity gradient seems to be the most crucial.

At reducing atmospheres and high temperatures, oxygen vacancies are formed in the membrane material accompanied by the reduction of B-site cation to a larger ion, which results in expansion of the structure, also called isothermal expansion (or chemical expansion). The bulk of the problem is created due to the varying oxygen activity, in other words varying oxygen non-stoichiometry, across the membrane. In oxygen separation membranes used for partial oxidation, one side of the membrane is exposed to air and the other to reducing conditions. This causes higher lattice expansion on the lean side and membranes have tensile stresses on the surface exposed to low pO_2, which increases the crack probability pointing from the reaction side to the air side.[45] Additionally, depending on the material, decomposition of the material down to metallic state at further reducing atmospheres or reaction with impurities causes chemical instability.[45] In short, the stability of the perovskite is inversely proportional to the non-stoichiometry of the material, which follows the trend of relative redox stability of the transition metal cations on the B-site. Therefore, as a general trend, the oxygen flux and the stability of the perovskites materials show opposite tendencies, as they are both dependent on the oxygen vacancy formation. As mentioned previously, $SrFe_{0.2}Co_{0.8}O_3$ is one of the highest ionic conductive materials[27]; however, it shows very high isothermal expansion and starts to decompose at relatively high pO_2.

Several authors have studied the oxygen non-stoichiometry and the thermodynamic stability of perovskite materials in different ways.[35, 46-48] A figure on relative weight change related oxygen loss as a function of pO_2 is given in Fig. 2.5. [47]
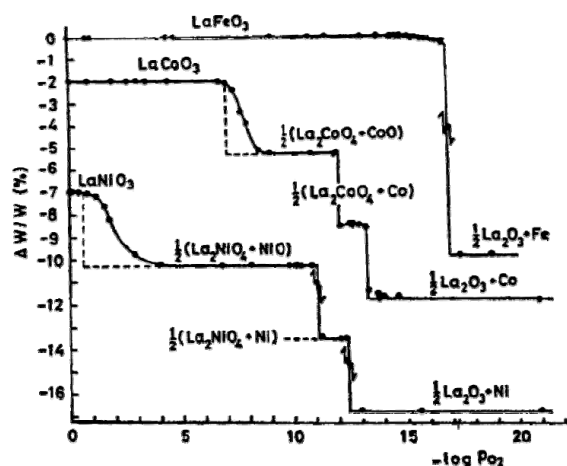
Fig. 2.5. Weight loss of various perovskite-type oxides at 1000°C, taken from Ref. [47]

The relative weight loss of $LaFeO_3$, $LaCoO_3$, and $LaNiO_3$ materials were measured by TGA at 1 bar and 1000°C. The results showed that $LaFeO_3$ was stable down to $pO_2 = 10^{-16.95}$ bar, while $LaCoO_3$ was stable down to $pO_2 = 10^{-7}$ bar. The stability range for nickel containing perovskite was much less. Another plot showing the non-stoichiometry of Sr-substituted perovskite materials is shown in Fig. 2.6.
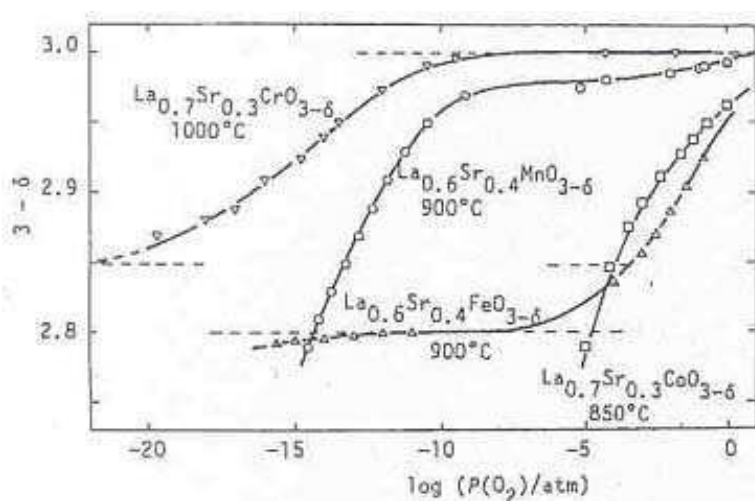
Fig. 2.6. Oxygen non-stoichiometry (3-δ) of various Sr-substituted perovskite-type oxides at 1000°C as a function of pO_2 (atm), taken from Ref.[35]

In this figure, the stability of different B-site cation can be seen. It is possible to observe the plateau of $La_{0.6}Sr_{0.4}FeO_{3-\delta}$, where $\delta = x/2$ as explained in section 2.2. The improved stability of Cr-based material is seen in the figure. It was found by Tejuca et al.[48] that the stability of the perovskite oxide increases with increasing size of the A ion. However, it decreases by partial substitution of the A ion by aliovalent cations. It can be concluded from these results that the isothermal expansion is increased with A-site substitution of the

19

perovskite and with a B-site cation that has lower relative redox stability, both increasing the oxygen non-stoichiometry.

The correlation of oxygen ion transport and the coefficient of thermal expansion (CTE) of several perovskite materials were shown by Ullmann et al.[49] showing a linear dependency between the logarithm of ionic conductivity and the CTE. This feature is presented in Fig. 2.7.
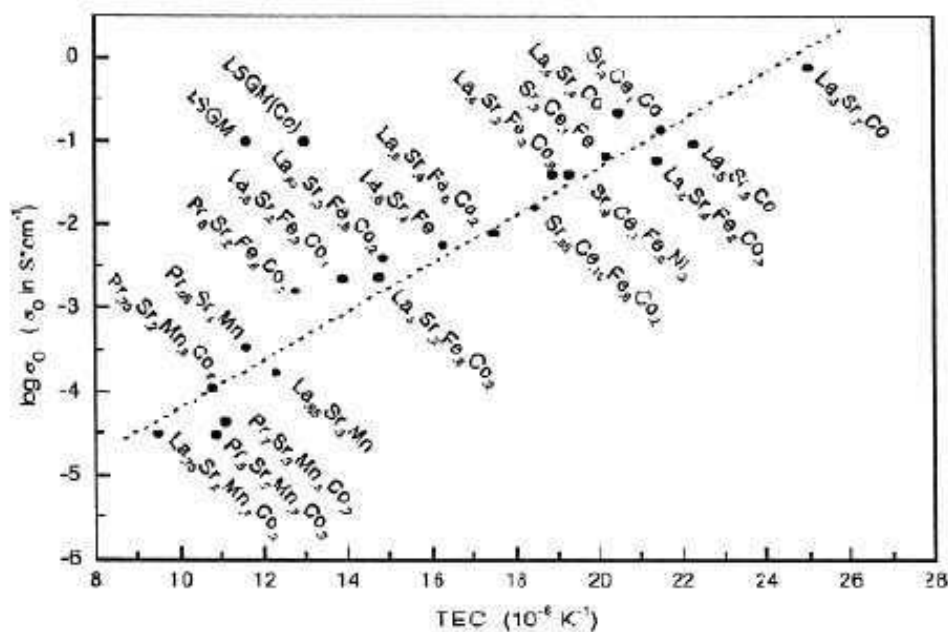
Fig. 2.7. Correlation of ionic conductivity (σ_0) and thermal expansion coefficient, taken from Ref.[49]

In Fig. 2.7, it is observed that the high thermal expansion coefficients are accompanied by high ionic conductivities. This suggests the dependence of both properties to the oxygen vacancy concentration.

The thermal expansion coefficient is related to the nature of the bonding of atoms in the material. The interatomic potential for a pair of atoms consists of an attractive term and a repulsive term. The summation of these terms results in a minimum in the potential, which is the equilibrium atomic spacing. This depends on the nature of the bonding between the atoms. The strong directional bonding in covalent bonds results in a deep potential well in interatomic potentials and a sharper curvature at the potential minimum. Therefore, more energy is needed to separate the atoms and this leads to higher melting points and elastic constants and lower thermal expansion coefficients. In the case of acceptor-doped perovskite materials, the thermal expansion is known to be accompanied by chemical expansion at higher temperatures, resulting in values more than 20×10^{-6} K^{-1}.

The common strategy to decrease the chemical expansion is to substitute the B-site transition metal with a "more stable" ion (e.g. Cr instead of Fe or Co) or "stable" ion (e.g. Ga, Al). [50-52] This decreases the amount of B ions reduced with lowered oxygen activity but also decreases the oxygen vacancy formation, therefore the ionic conductivity. In fact, these additions are reported to cause a decrease in ionic conductivity with exception of Ga [53] in oxidizing conditions.

Most of the work in literature considering the dimensional stability has been performed on $LaCrO_3$-based perovskites.[50, 54-56] Hilpert[55] mentions 0.23% of chemical expansion ($\Delta L/L_0$) at $pO_2 \approx 10^{-18}$ bar as the extreme case for $La_{0.8}Sr_{0.2}CrO_{3-\delta}$ while values factor of three lower were measured for materials doped with Mg and Al on B-site. Assuming that chemical strain, $\varepsilon_C = \Delta L/L_0$, (where L_0 is the reference length and ΔL is the length change at the same temperature) is proportional to the oxygen vacancy concentration (δ); the parameter ε_C/δ is taken as an indicator for isothermal expansion per vacancy formation.[50] This value is used in literature[50, 57] to compare the chemical expansion of different materials. It was concluded in Hilpert's work[55] that as a result of the correlation between the oxygen non-stoichiometry and the isothermal expansion, it can be deduced that isothermal expansion can be related to the change of the average B-site cation radius of the perovskites obtained from the defect structure.

The chemical strain values of $LaCrO_{3-\delta}$ materials are very low compared to $(La,Sr)FeO_{3-\delta}$-based materials that may show the same amount of isothermal expansion at pO_2 values higher than 10^{-2} bar (rather than 10^{-18}) at the same temperature.[57] Small amount of work on chemical expansion of $(La,Sr)FeO_{3-\delta}$-based materials[57] shows that substitution of B-site of $La_{0.3}Sr_{0.7}FeO_{3-\delta}$ with 40% Ga considerably decreases the lattice expansion (from around 0.4 to 0.2 at $\log pO_2 = -4$), although it is still high for application purposes. On the same material, Al-substitution was studied[58] and it was found less favorable compared to Ga-addition considering the oxygen ionic transport. Although Al and Ga have the same oxidation states, their ionic radii differ and this seems to play a role in the oxygen transport. Therefore, it is important to identify a suitable substitution cation for the specific base-material and this subject forms the first part of this thesis as will be explained in more detail below.

In the search of a suitable material for oxygen separation membrane to be used for partial oxidation of methane, the following properties are considered the most important: high oxygen permeability, sufficient structural and chemical stability. As explained previously in this chapter, a compromise is needed for these two properties and Fe on the B-site seems to be the best choice considering that the stability is decreased for Co-based materials, as it was shown in Figs. 2.5 and 2.6. The oxygen vacancies are introduced to the material by A'-doping, which is more influential than B'-doping.[27] Considering the aliovalent alkaline earth ions on the A-site, the flux decreases with Ba > Sr > Ca in terms of flux; therefore, Sr was preferred on the A-site as a compromise among these three cations.

$La_{1-x}Sr_xFeO_{3-\delta}$ perovskites show promising transport properties that were studied extensively by others, and their defect chemistry is well understood as a function of Sr-content, oxygen partial pressure and temperature.[33, 35] The effect of Sr^{2+} addition on transport properties of $La_{1-x}Sr_xFeO_3$ materials was studied by Patrakeev et al.[59] and it was shown that the x = 0.5 was optimum as Sr-content and further substitution lead to worse ionic conductivities because of possible vacancy ordering resulting in layered structures, which means they become inefficient for oxygen transport. Therefore, $La_{0.5}Sr_{0.5}FeO_{3-\delta}$ perovskite material is an interesting material for oxygen separation membranes for partial oxidation and is the center of focus in this thesis.

2.6. Motivation and scope of the thesis

In this study, the general aim is to improve the mechanical and chemical stability of $La_{0.5}Sr_{0.5}FeO_{3-\delta}$ perovskite oxygen separation membranes that are used for the partial oxidation of methane. It is expected that the expansion behavior can be tailored by substitution of the multi-valent B-site cation (Fe in this case) with a more stable cation (V, Cr, etc.) or stable cation (Al, Ga, etc.). Considering the nature of the electrical and ionic conductivity of these materials, these substitutions are expected to result also in degraded transport properties. However, the effect of B-site modification on stability and permeation is still not fully understood and it is the aim of this study to provide a more in-depth understanding to it.

In order to achieve this goal, suitable B-site substitution elements need to be identified. A selection of suitable B-site substitute for iron has not been commonly reported in the literature; therefore, Chapter 3 of this thesis is devoted to the screening of B-site substitution elements. The properties such as phase-purity, densification, and thermal and isothermal expansion are used for the identification. Prior to experimental results, the theoretical approach used in identification of good ionic conductors is explained to provide a comparison ground. Basically four kinds of substitutions will be used for modification. Those are stable cations with 2+, 3+, 4+, 5+ valence state and multi-valent cations of which the most stable valences are variable with pO_2. In this way the effect of modification with different conditions can be studied. At the end of this chapter, the most promising substitutions are chosen for further characterization.

As explained throughout this chapter, oxygen transport and stability tend to show opposite tendencies. Therefore, both of these properties are studied extensively to identify the simultaneous effects. In Chapter 4, the structural and chemical properties of short-listed compositions are studied. The effect of substitution on the structure and oxygen non-stoichiometry relating to isothermal expansion is studied. The electronic structures of

materials at room temperature are compared using X-ray absorption spectroscopy. In Chapter 5, the total conductivity of the materials is studied. The conductivities at reduced pO$_2$ are characterized. Mechanical properties of the membrane materials are addressed in Chapter 6. In this way, the direct effect of substitution is studied on the mechanical stability of the materials.

In the following three chapters (7-9), oxygen transport related properties are characterized by permeation and potential-step measurements. The correlation between B-site substitution and permeation, chemical diffusion and surface exchange coefficients are studied. Finally, the performances of the membranes are measured as partial oxidation reactors, which provided direct information on the oxygen permeation flux and stability of the membranes. The summary and conclusions of the thesis are given in Chapter 10.

Chapter 3

Synthesis and Characterization of B-site Substituted $La_{0.5}Sr_{0.5}FeO_{3-\delta}$ Perovskites

In this section, the production of B-site substituted $La_{0.5}Sr_{0.5}FeO_{3-\delta}$ (LSF) materials is explained. Their phase-purity (XRD) and microstructures (density, SEM) are investigated. An important property is the expansion of the materials in air and Ar measured by dilatometry experiments. From these results and the electrical conductivities, promising compositions are selected for further detailed investigations.

3.1. Introduction

In the general introduction and the motivation of the thesis, the stability issues were addressed. The reason behind the materials choice was explained and the base material, $La_{0.5}Sr_{0.5}FeO_{3-\delta}$ was introduced. As explained before, the redox stability of the perovskite materials can be improved by partial substitution of the Fe-ions with cations that have higher redox stability. As a result, the non-stoichiometry of the material at atmospheres with low oxygen activity is altered and the structural stability of the material is improved.

The first step in this thesis is to identify a suitable B-site substitute for $La_{0.5}Sr_{0.5}FeO_{3-\delta}$ material. Therefore, it is the aim of this chapter to provide the understanding for the material selection criteria applied to the B-site substitution screening. In this context, first of all the theories to obtain a stable perovskite material as well as good oxygen ionic conductivity are explained and then checked for the possible substituting materials. Afterwards, the production and characterization of the substituted materials are described, the selection criteria are applied step by step including the confirmation of the phase purity, sintering behavior (if the required density is achievable), and the thermal and expansion behavior as a criterion for improved stability.

3.2. Theory

3.2.1. Effective ionic radii of the B-site of complex perovskites

The general formula for the considered B-site substituted complex ABO_3 perovskites is $La_{0.5}Sr_{0.5}(Fe^{3+}/Fe^{4+})_{1-y}B^{n+}_yO_{3-\delta}$, where B: Mg, Al, Ga, In, Sn, Zr, Cr, Ti, Ta, and V. The ionic radii used in calculations are taken from Shannon.[60] The B-site substitutions, their oxidation states, ionic radii are shown in Table 3.1 together with the abbreviations that are going to be used throughout this thesis. The host composition, $La_{0.5}Sr_{0.5}FeO_{3-\delta}$, is abbreviated as LSF and the substituting elements are included with the amount, 1 for 10% and 2 for 20% on the B-site. Therefore, for example, $La_{0.5}Sr_{0.5}Fe_{0.9}Ti_{0.1}O_{3-\delta}$ is abbreviated as LSFTi1.

The ionic radii depend on the coordination number and oxidation state of the element. All the values shown correspond to 6-fold coordination. Some of these elements (Fe, Cr, Ta, and V) can exist in different oxidation states for the same coordination value. In this case, all possible ionic radii are written with the corresponding oxidation states. The oxidation states that are most probable for these elements in perovskite structures are used for the calculations and shown in bold characters in Table 3.1. In case of Fe, it is possible that the iron ion can exist in high-spin or low-spin when its oxidation state is 3+ and the electronic configuration is $3d^5$. Fe^{3+} was found to remain in the high-spin $3d^5$ configuration by Abbate et al.[61] in LSF

composition as a result of x-ray absorption data and in $LaFeO_3$ by Russo et al.[62] as a result of Mössbauer spectroscopy. Therefore, the high-spin ionic radius of 0.645 Å is used for Fe^{3+} for the calculations of the effective ionic radii. The ionic radii of A-site ions with 12-coordination, La^{3+} and Sr^{2+}, and O^{2-} are given at the end of the Table 3.1. The high and low spin radii of the related cations are shown in parentheses as (LS/HS). All the ionic radii are given in Angstrom (Å).

Table 3.1. The B-site substitutions, oxidation states, ionic radii, and abbreviations used through out the thesis for $La_{0.5}Sr_{0.5}Fe_{1-y}B_yO_{3-\delta}$.

B-Sub.	Ox. State	Ionic Radius	y = 0.1	y = 0.2
Fe	2+/**3+**/4+	(0.61/0.78)/(**0.55/0.645**)/0.582	LSF	
Mg	2+	0.72	LSFMg1	
Al	3+	0.535	LSFAl1	LSFAl2
Ga	3+	0.62	LSFGa1	LSFGa2
In	3+	0.8	LSFIn1	LSFIn2
Sn	4+	0.69	LSFSn1	LSFSn2
Zr	4+	0.72	LSFZr1	LSFZr2
Cr	2+/**3+**/4+	(0.73/0.8)/**0.62**/0.55	LSFCr1	LSFCr2
Ti	3+/**4+**	0.67/**0.605**	LSFTi1	LSFTi2
Ta	3+/4+/**5+**	0.72/0.68/**0.64**	LSFTa1	LSFTa2
V	2+/3+/4+/**5+**	0.79/0.64/0.58/**0.54**	LSFV1	
La	3+	1.36		
Sr	2+	1.44		
O	2–	1.40		

The overall effective ionic radii of the B-sites for $La_{0.5}Sr_{0.5}(Fe^{3+}/Fe^{4+})_{1-y}B^{n+}_yO_{3-\delta}$ materials are calculated based on the atomic percentages of the Fe^{4+}, Fe^{3+}, and B^{n+} considering the charge neutrality. An important point to note is that the compositions are assumed to be stoichiometric at room temperature for the following calculations. Although it may not be necessarily true, the non-stoichiometry of these materials is low at room temperature (3-δ is reported as 2.97 for $La_{0.5}Sr_{0.5}FeO_{3-\delta}$ at room temperature[63]) and the calculated values will provide a basis for the general trend. The overall charge of the A-site is +2.5, therefore the amounts of B-site ions are calculated so that the overall charge of B-site is +3.5 to maintain charge neutrality. Provided that the fraction (y) and the oxidation state (n) of the substituting B ion is known, the fractions of 3+ and 4+ iron ions (x_{Fe3+} and x_{Fe4+}, respectively) are calculated as follows:

$$x_{Fe^{3+}} = 0.5 + y(n-4) \tag{3.1a}$$

$$x_{Fe^{4+}} = 0.5 + y(3-n) \tag{3.1b}$$

The effective radius of the B-site is calculated by:

$$r_B = x_{Fe^{3+}} \times r_{Fe^{3+}} + x_{Fe^{4+}} \times r_{Fe^{4+}} + x_{B^{n+}} \times r_{B^{n+}} \tag{3.1c}$$

These calculated ionic radii are used throughout this thesis for further calculations of tolerance factors, unit cell volumes, and when a property is represented as a function of the ionic radii.

3.2.2. Tolerance factor and cell volume

Goldschmidt defined a so-called tolerance factor (also called Goldschmidt factor), t, based on geometrical considerations to provide information on tolerable limits to form perovskite structure.[21] It is defined as:

$$t = \frac{r_O + r_A}{\sqrt{2}(r_O + r_B)} \tag{3.2}$$

where r_O, r_A, and r_B are the ionic radii of O, A, and B in ABO_3 structure, respectively. This equation can be used to estimate the distortion of the structure compared to the ideal cubic structure when t = 1. The perovskite lattice occurs only within the range $0.75 < t \leq 1$. When the structure deviates from cubic, it can get other crystal symmetries such as orthorhombic, rhombohedral, or monoclinic.

Fukunaga et al. suggested an empirical formula for the calculation of averaged interatomic distance or cubic root of cell volume in perovskites based on the tolerance factor. More than 200 perovskite volumes were calculated with good accuracy. The cell volumes were than used to estimate ionic radii and it was suggested to predict the molar volume of perovskite by a given combination of elements.[64] The formula for cubic root of volume for 12-coordinated A-cation is found as:

$$V^{1/3} = 2.37 r_B + 2.47 - 2(s-1) \tag{3.3}$$

where r_B is the ionic radius of B-cation and s is the inverse of the tolerance factor.

Kilner and Brook[65] came up with a rather simple concept of a critical radius for oxygen ion conductivity in their attempt to model the ionic conductivity and relate migration

and association enthalpies to the effects of the structure, host cation type, and dopant size. They defined a critical radius, r_{crit}, in a saddle point configuration for anion migration as shown in Fig. 3.1. The O^{2-} ion must pass the saddle point formed by two A ions and a B ion. Therefore the associated energy barrier for migration decreases with increasing B-cation size and decreasing A- cation. The geometric equation for r_{crit} equation derived from this configuration is as follows:

$$r_{crit} = \frac{r_A^2 + \frac{3}{4}a_O^2 - \sqrt{2}a_O \times r_B + r_B^2}{2r_A + \sqrt{2}a_O - 2r_B} \tag{3.4}$$

where r_A, and r_B, radii of A-site and B-site cations. a_0 is the lattice parameter either experimentally measured or calculated with equation 3.3.
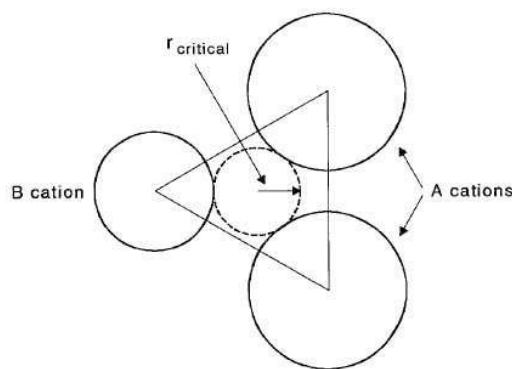
Fig. 3.1. Saddle point configuration showing the critical radius, r_{crit}, for anion migration, taken from Ref.[7]

The tolerance factor and critical radius are calculated here in an attempt to see an influence with B-site substitution of LSF composition. The graph showing these two values as a function of the effective B-site radius, rB_{eff}, is given in Fig. 3.2. rB_{eff}, tolerance factor, t, and the critical radius, r_{crit}, are calculated from equations 3.1, 3.2, and 3.4 as explained previously. In this figure, the abbreviations of the compositions, except LSF, are shortened to the last part of the normal abbreviations used and shown as the substitution name and amount.
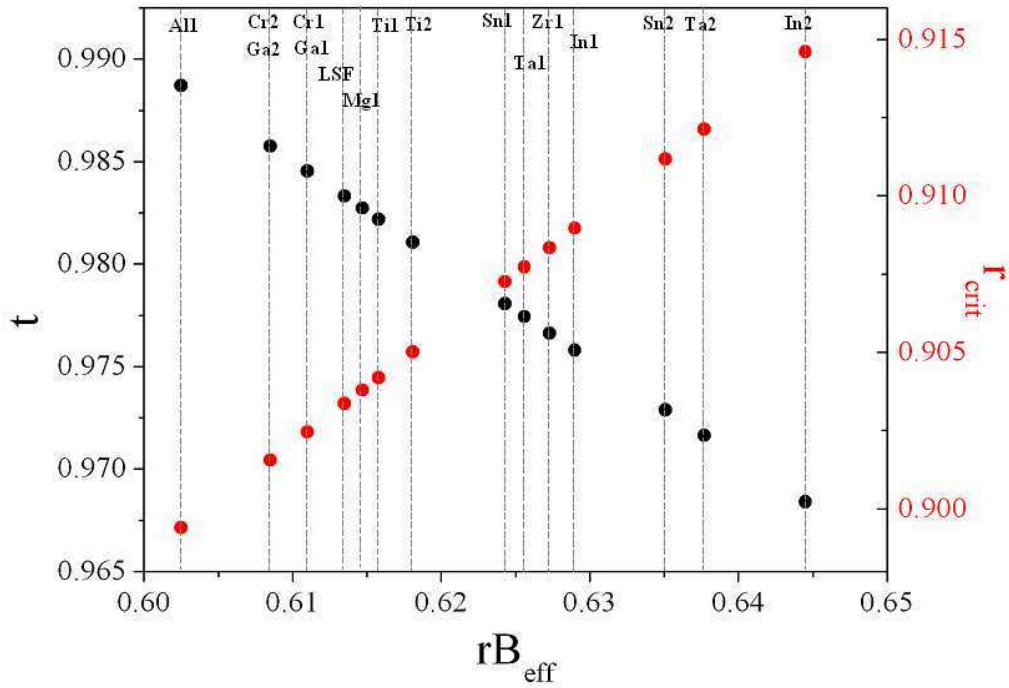
Fig. 3.2. Tolerance factor, t, calculated from Eq. 3.2, critical radius, calculated from Eq. 3.4 of B-site substituted LSF materials as a function of effective B-site radius.

The first aspect to point out in Fig. 3.2 is the dependence of the effective B-site radii on the size and the oxidation state of the substituting cation. In LSF, without substitution, the amount of Fe^{3+} and Fe^{4+} is identical, given the materials is assumed to be stoichiometric for comparison purpose. Most of the B-site substitutions have smaller ionic radii than Fe^{3+} (Table 3.1); therefore, the effective B-site radius becomes smaller. In^{3+} is an exception to the situation with its considerably larger radius (0.8 Å). The only 2+ ion in substitution list, Mg, has also large ionic radius; however, due to the charge neutrality, the amount of Fe3+ is decreased. Therefore, the overall effect of Mg on the rB_{eff} is negligible. The rB_{eff} is increased with all higher oxidation state substitutions with their larger radii compared to Fe^{4+}, whose radius is 0.582 Å.

The oxygen transport is favorable when the crystallographic sites are energetically equivalent. Therefore, the ideal structure for oxygen transport is cubic. LSF is known to be rhombohedral at room temperature slightly deviating from cubic structure,[66, 67] as the tolerance factor is slightly less than 1 and close to 0.98. The tolerance factor, t, decreases with increasing rB_{eff} implying an even further deviation from the ideal cubic structure. However, the difference is not large even for the end case of 20% In-substitution (0.99 to 0.97). Considering the suggested range of stable perovskites that is between 0.75 and 1 these materials are closer to the higher end, which is the ideal cubic case. There is a linear relation between rB_{eff} and the critical radius, r_{crit}. Although this suggests that the diffusion of O^{2-} maybe improved for the compositions staying on the right of LSF in Fig. 3.2, the change in

r_{crit} is very small and the other effects such as association enthalpy suggested by Kilner et al. can play a more important role for defining the migration of oxygen ions.[65] It was deduced in the same work that the migration enthalpy for O^{2-} found from r_{crit} could be dependent more on the structure since the cation dependency was small. In addition, the enthalpy of association that restricts the migration was found to be strongly dependent upon the cation size with a probable minimum when the radii of the dopant and the host are similar.

As pointed by Bouwmeester et al.[7], another important variable for the overall ionic conductivity is the concentration of the mobile oxygen ions.

In this section, the theoretical aspects of B-site substitution were investigated in terms of tolerance factor and critical radius for oxygen transport. The calculated effective ionic radius of the B-site changes up to 5% (depending on the substituting cation and its amount), which is predicted to be accompanied by a change in the unit cell volume.

3.3. Experimental

3.3.1. Materials synthesis and preparation

The compositions of $La_{0.5}Sr_{0.5}Fe_{1-x}B_xO_{3-\delta}$ (x=0, 0.1, 0.2 and B: Al, Cr, Zr, Ga, Ti, Sn, Ta, In, V, and Mg) were prepared by solid state reaction of the reagents $La(OH)_3$, $SrCO_3$, Fe_2O_3, Al_2O_3, Cr_2O_3, ZrO_2, GaO, TiO_2, SnO_2, Ta_2O_5, In_2O_3, V_2O_5, and MgO. Stoichiometric amounts of reagents were mixed by ball-milling in isopropyl alcohol for 24 hours and dried while stirring. Powders were calcined at 1250°C for 4 hours or at 1350°C for 4 hours if secondary phases were detected by XRD.

All compositions were pressed into small pellets for the identification of sintering temperature. A range of sintering temperatures and durations were studied to optimize the sintering conditions to achieve dense samples (generally >95% of theoretical density). Dilatometry was used for the compositions for which the sintering temperature could not be optimized otherwise. The samples, which showed second phase after calcination, were checked again by XRD for phase-purity. Uniaxial pressing was used (70MPa) to produce bars (~3×4×45mm) from these compositions, which were considered to be of high phase-purity. Pressed bars were sintered in air in the temperature range of 1430-1530°C for 4-20 hours.

The density of the samples were measured by Archimedes method and crosschecked by scanning electron microscopy (SEM) (Vega Plus 5136 MM © Tescan). The fractured surfaces of the samples were used for investigation without sputtering as the materials were electronically conducting enough for the measurement. The surface of investigation was sputtered by Au-Pt when charging was observed in the case of insulating materials (LSFTa2).

3.3.2. X-ray diffraction

When X-rays, which have wavelengths comparable to the interatomic distances, hit an ordered structure, the separately reflected waves will stay in phase if the difference in the path length of each wave is equal to an integer multiple of the wavelength (constructive interference). Therefore, Bragg's law states:

$$2d\sin\theta = \lambda \tag{3.5}$$

where d denotes the crystal plane spacing, θ is the angle between the diffracted beam and the original beam, and λ is the wavelength of the X-rays.

The phase-purity of the calcined powders in this work was examined by XRD analysis on an X'pert PRO PW3040 (PANalytic) using CuKα radiation (λ = 1.54060 Å). Phase identification was done using X'pert HighScore Plus software program.

3.3.3. Dilatometry measurements

The expansion behavior of the samples as a function of temperature in air and Ar atmospheres was studied by a dilatometer (802 S, Baehr Thermoanalyse GmbH, Germany), equipped with an inductive length change measurement head. The principal is to measure the current change produced by the movement of an iron core at the end of spring-loaded quartz tubes, one of which holds a reference material and the other holds the measured sample. The sample is placed in a one end closed quartz tube to control the atmosphere, which is placed in a furnace.

Rectangular dilatometry bars were prepared by polishing both ends of the sintered bars with a final length of 35 mm. A sapphire bar with the same length was used as the reference. The samples were measured in air with a heating rate of 5 K/min up to 900°C and kept at this temperature until the equilibrium expansion was reached. Afterwards, the atmosphere was changed to Ar to determine the isothermal expansion at these conditions.

3.4. Physical and chemical properties of B-site substituted La$_{0.5}$Sr$_{0.5}$FeO$_{3-\delta}$ materials

3.4.1. XRD analysis of B-site substituted La$_{0.5}$Sr$_{0.5}$FeO$_{3-\delta}$ materials

The XRD plots of the samples prepared by solid-state reaction route are presented in two groups according to the B-site substitution amount. The compositions with 10% Al, Cr, Ga, Mg, V1, Ti, Sn, Ta, Zr, and In are shown in Fig. 3.4 and the ones with 20% Al, Cr, Ga, Ti, Sn, Ta, Zr, and In are shown in Fig. 3.5. The figures show the XRD of the powders with best purity obtained after calcination for four hours at 1250 – 1350°C. Higher temperatures were not used as they resulted in hard agglomerates. The results are shown in the order of increasing effective B-site radius of the composition from the bottom towards top of the plot. In addition, the abbreviations are shortened to the element name. In order to make comparison easier, the peak positions of the reference pattern[66] of La$_{0.5}$Sr$_{0.5}$FeO$_3$ are shown on the bottom of the both plots in Fig. 3.4 and Fig. 3.5.
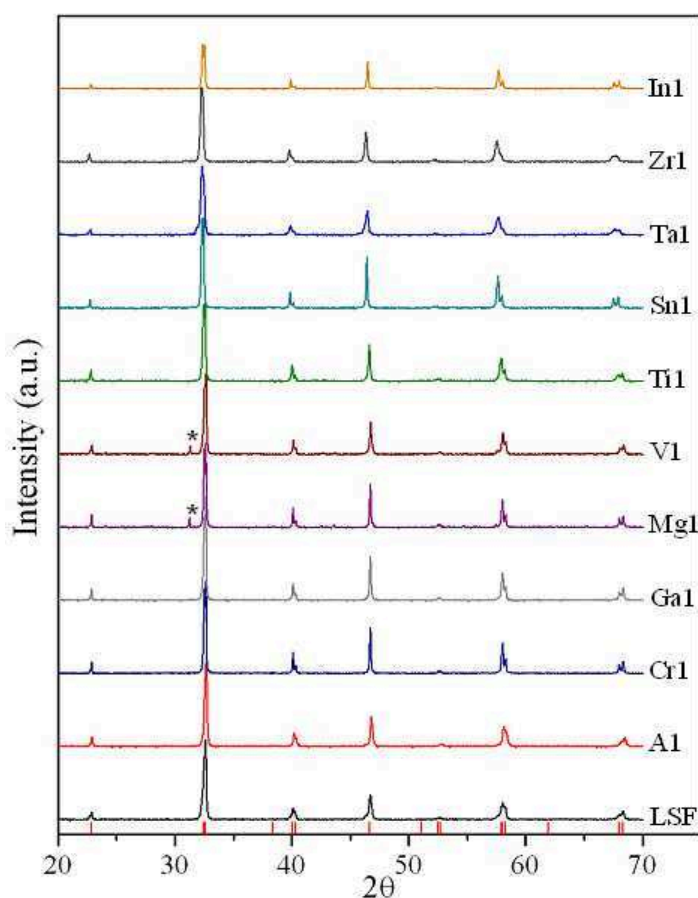
Fig. 3.4. XRD patterns of LSF with 10% B, La$_{0.5}$Sr$_{0.5}$Fe$_{0.9}$B$_{0.1}$O$_{3-\delta}$ where B: Fe, Al, Ga, In, Sn, Zr, Cr, Ti, Ta, Nb.
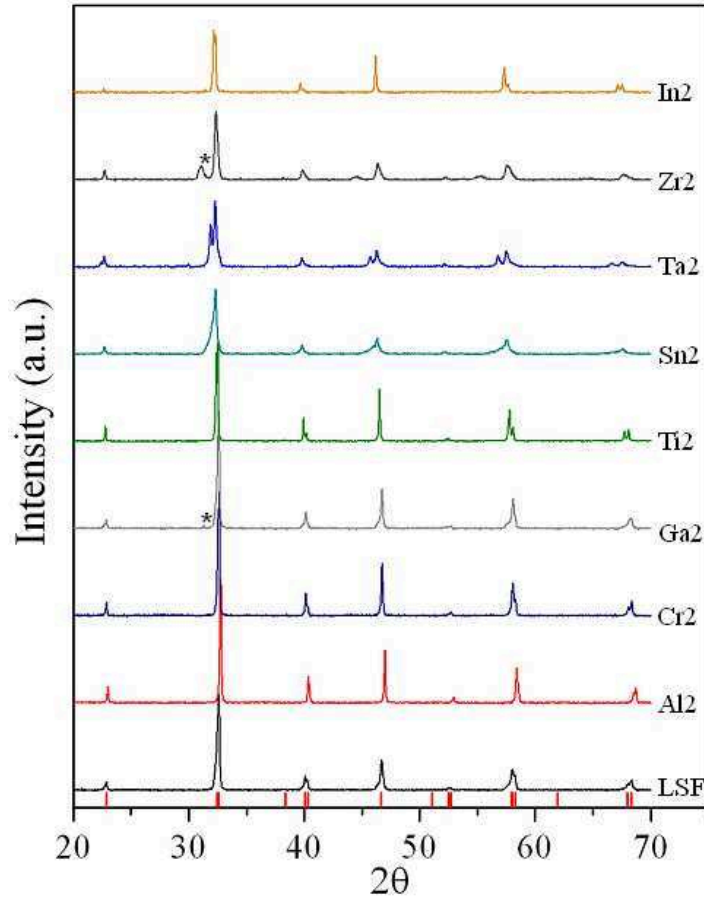
Fig. 3.5. XRD patterns of LSF with 20% B, $La_{0.5}Sr_{0.5}Fe_{0.8}B_{0.2}O_{3-\delta}$ where B: Fe, Al, Ga, In, Sn, Zr, Cr, Ti, and Ta.

$La_{0.5}Sr_{0.5}FeO_{3-\delta}$ material is reported as rhombohedral (R-3c) in the literature with a = 5.5111 Å, c = 13.4158 Å and V = 352.87 Å^3 (JCPDS No: 01-082-1962).[66] Comparing the XRD pattern of LSF with the reference pattern shown as sticks on the bottom of Figures 3.4 and 3.5, it is observed that they have similar patterns.

XRD analysis showed that small amounts of a Ruddlesden-Popper phase ($A_{n+1}B_nO_{3n+1}$, n = 0, 1, 2,…) were present in almost all of the compositions, which are not always visible in the figures shown (3.4 and 3.5). In such a case, when the second-phase amount is less than 1-2 percent, the material was considered to be phase-pure. The compositions with considerable amount of second-phase are easily visible. The presence of a second phase can be seen on the left of the main peaks denoted with asterisk (*). This phase seen in the XRD patterns is similar to $LaSrO_4$, which has a tetragonal structure (JCPDS No: 00-029-1305) with a = 3.8750 Å and c = 12.7180 Å.

It can be deduced from the XRD plots that most of the compositions with 10% substitution have high purity while secondary phases become more pronounced when the substitution amount is increased to 20%. In case of LSFMg1, LSFV1, and LSFZr2, the

amount of second phase is very high as shown in Fig. 3.4 and Fig. 3.5, while a peak can be seen on LSFGa2 material, although it is not as high in this case. There is no separable second-phase peak in case of LSFSn2, however, the unusual large bases of the normal peaks raise doubts about purity of this material.

As a result of the phase-purity studies by XRD, the compositions LSFMg1, LSFV1, LSFZr2, LSFGa2, and LSFSn2 were eliminated from the candidate list for further characterizations.

The main Bragg peak with the highest intensity in LSF materials is close to $2\theta = 32°$, which is a double peak due to the rhombohedral distortion of the structure. According to the diffraction law for ordered structures explained in section 3.3.2, the diffraction angle is supposed to decrease with increasing interatomic spacing. Therefore, the effect of substituting ions is studied to see if the doping elements are incorporated into the perovskite structure. The changes in the main double peak with the addition of substitutions are shown in Fig. 3.6. Two peak values for each dopant are shown with circles for the higher angle peak and the triangles for the lower ones. Blue and red symbols are used for compositions with 10% and 20% doping, respectively.
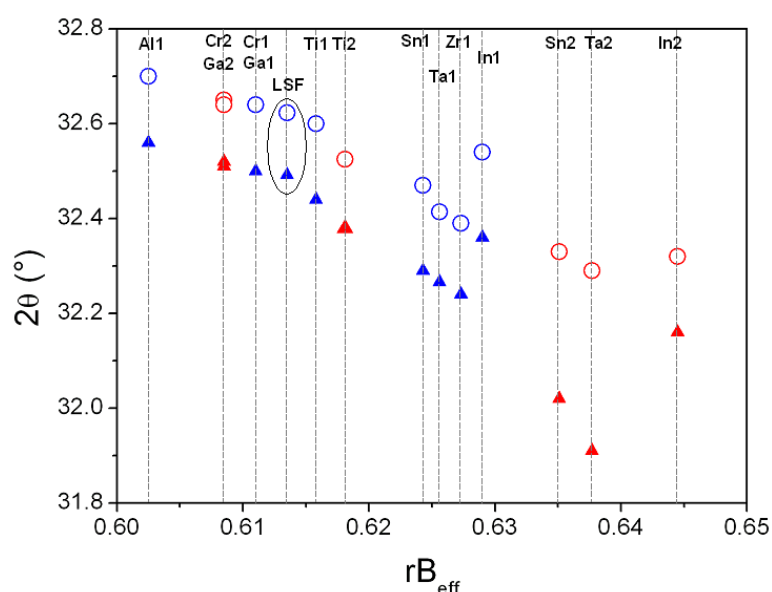
Fig. 3.6. Values of the highest intensity double peak as a function of the calculated effective ionic radii of the B-site of $La_{0.5}Sr_{0.5}(Fe^{3+},Fe^{4+})_{1-y}B_yO_{3-\delta}$. Blue and red symbols indicate compositions with 10% and 20% substitutions, respectively.

A more or less linear relation between the peak position and the B-site radius is seen in Fig. 3.6, which is in agreement with the theory. The base material LSF is circled in the figure. The peaks shift to larger angles with addition of smaller cations, and to smaller angles with larger substitutions. The same trend can be observed also from Figures 3.4 and 3.5. Only

In-substituted compositions lie out of the line, although follow the trend. This may be a result of the fact that either the In ion is relatively large compared to the host ion and can not incorporate to the structure or due to the volatile nature of Indium ion.[68] Due to the fact that the XRD spectrums of LSFIn1 or LSFIn2 show no sign of another phase other than the main perovskite phase, the possibility of In loss with high calcination temperatures becomes more likely.

Another point worth mentioning in Fig. 3.6 is the difference between the two peak values. It becomes considerably larger for LSFSn2 and doubles for LSFTa2. This suggests an increased distortion in the material, which is not surprising considering that the Ta is a larger ion. This also supports the argument about the In ion being volatile since LSFIn2 shows no further distortion although it has the highest effective B-site radius.

3.4.2. The Microstructure and the density of B-site substituted $La_{0.5}Sr_{0.5}FeO_{3-\delta}$

The compositions with high phase purity were used to produce bars for dilatometry. In order to obtain dense sample to achieve gas-tight samples, several sintering temperatures and durations were used. At this stage, densities of the materials were checked by SEM. Note that LSFIn2 was not further studied due to the questions raised about the incorporation of In to the structure.

It was possible to achieve dense samples for most of the substitutions. In case of Al-substituted samples, sintering either did not provide necessarily dense samples or caused over-sintering. SEM micrographs of the surfaces and the fracture surfaces of LSFAl1 samples sintered at two different temperatures are shown Fig. 3.7. In Fig. 3.7. (a) and (b) show the surface and the fracture surface of the LSFAl1 sample sintered at 1430°C for four hours. Fig. 3.7 (c) shows the surface of the same sample sintered at 1480°C for 4 hours with (d) showing a closer look to the grain boundaries, and (e) shows the fracture surface of LSFAl1 sample sintered at 1430°C for 12 hours. Finally, the surface of a fractured LSFAl2 sample is given in Fig. 3.7 (f).
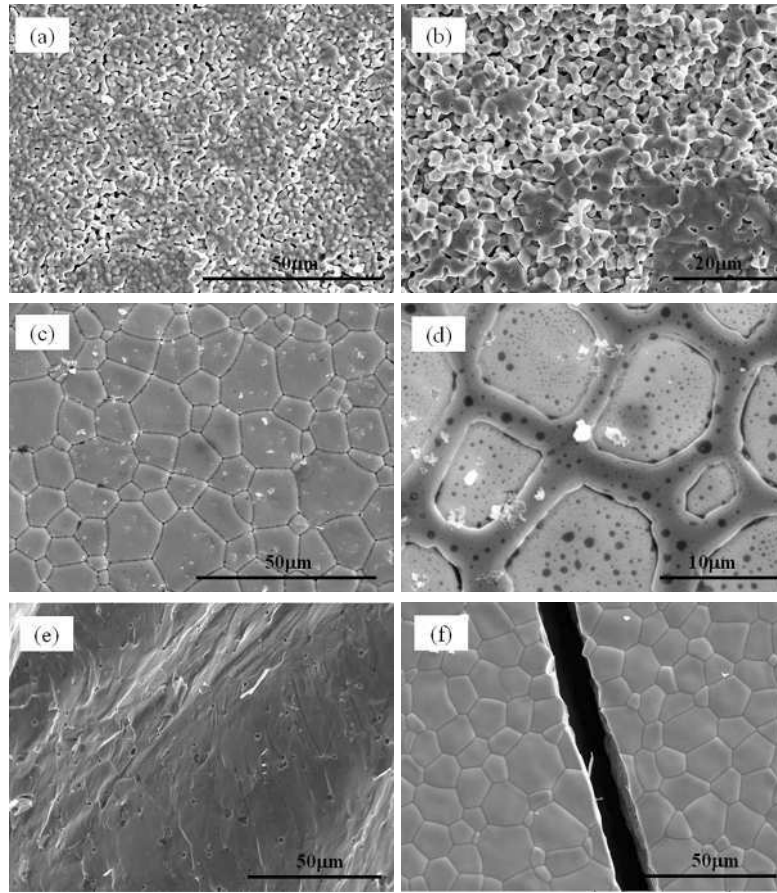
Fig. 3.7. SEM micrographs of LSFAl1 (a-d) and LSFAl2 materials. (a) and (b) the surface and the fracture surface of LSFA1 sintered at 1430 for 4 hours, (c) the same material sintered at 1480 for 4 hours, (d) higher magnification of the surface showed in (c), (e) the fracture surface of LSFAl1 sintered at 1430°C for 12 hours (f) the surface of LSFAl1.

The initial temperature used to sinter LSFAl1 composition was 1430°C, which was found optimum for LSF base material. The composition seemed porous after sintering (Fig. 3.7 (a) and (b)). Increasing the sintering temperature to 1480°C caused over sintering of the material as seen in Fig.3.7 (c) and (d). Although the material seemed dense, second phase formation was observed with glassy looking grain boundaries. However, increasing the sintering duration at 1430°C to 12 hours provided dense samples with no visible second-phase formation as shown in Fig. 3.7 (e). This material shows total intragranular fracture and very brittle nature. A micrograph of the surface of LSFAl1 broken into two pieces is shown in Fig. 3.7 (f) showing this behavior clearly.

SEM micrographs of fracture surfaces of other substituted elements are shown in Fig. 3.8. These include LSF, LSFGa1, LSFTa1, LSFCr1, LSFZr1, LSFIn1, LSFTi2, and LSFTa2.
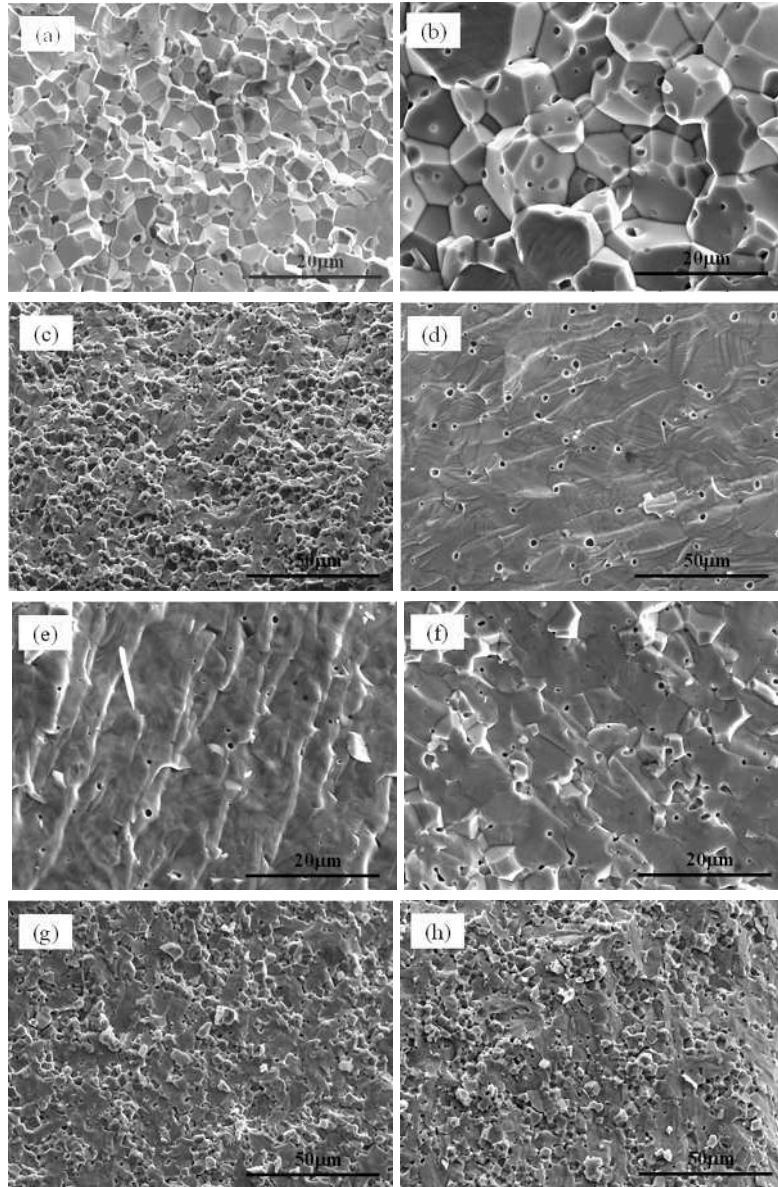
Fig. 3.8. SEM micrographs of fracture surfaces of (a) LSF, (b) LSFGa1, (c) LSFTa1, (d) LSFCr1, (e) LSFZr1, (f) LSFIn1, (g) LSFTi2, and (h) LSFTa2.

The crystalline ceramic materials generally fracture transgranularly (through grains) by cleavage over particular crystallographic planes. They tend to fracture intergranularly (along the grain boundaries) at high temperatures as a result of grain-boundary shearing causing cracks in the grain boundaries.[69]

In general, all the compositions showed some degree of transgranular fracture behavior except LSFGa1 (Fig. 3.8 (b)), for which the fracture is intergranular. It is observed that the LSFGa1 material has large grain size reaching 20 μm. For LSF, LSFTi2, and LSFTa2 it is a mixture of both. On the other hand, the compositions, LSFCr1, LSFZr1, and LSFIn1 fractured mostly transgranularly. The intergranular fracture observed in some of the materials suggest the possibility of weaker grain boundaries, which may be caused by inclusions in the

grain boundaries or microcracks associated with stress induced during cooling from high-temperatures. It may be important to be cautious during cooling of the samples.

All samples were dense enough to be considered gas tight with the sintering conditions used further in this thesis to obtain dense samples, which are given in Table 3.2. These compositions were pressed into bars for dilatometry and conductivity measurements. The densities of the pressed bars were measured by Archimedes method and the results are shown in Table 3.2.

Table 3.2. The sintering conditions, temperature (T/°C) and duration (d/hours), for the B-site substituted materials and the Archimedes densities of the sintered bars.

Composition	y =0.1		y = 0.2	
	Sintering T / d (°C / hours)	ρ (g/cm^3)	Sintering T / d (°C / hours)	ρ (g/cm^3)
LSF	1430 / 4	5.980	-	-
LSFAl	1430 / 12	6.025	-	-
LSFGa	1480 / 12	6.004	-	-
LSFIn	1430 / 4	5.825	-	-
LSFSn	1430 / 20	6.097	-	-
LSFZr	1430 / 20	5.930	-	-
LSFCr	1430 / 20	5.936	-	-
LSFTi	1480 / 4	5.959	1530 / 4	5.820
LSFTa	1430 / 20	6.235	1430 / 20	6.372

Note that the aim of the sintering studies was not to obtain the optimum microstructure but dense samples that would assure gas tightness. Although, it is not exactly correct to compare the densities due to the lack of information on the exact porosity amount, densities obtained for pressed bars are in similar range; with Ta-doped samples having the highest density. This is an expected result considering the high molecular weight of Ta-ion.

The sintered bars of LSFAl1 were found to be extremely brittle. This may be speculated to be because of the glass formation on the grain boundaries by diffusion of small Al ions with high temperature and resulting in weak grain boundaries. The increased density of LSFAl1 compared to LSF also supports this theory. It is possible that the first temperature used to sinter this composition (1430) was already too high, although the material was porous. A similar situation was observed by Trunec et al.[70] for $La_{0.7}Ca_{0.3}Fe_{0.85}Co_{0.15}O_{3-\delta}$ perovskite materials. The materials, sintered at higher temperatures than necessary were

porous and this was attributed to pressure arising from oxygen release at high temperatures. The samples expanded by a mechanism of grain boundary sliding.[71]

As a result of the sintering studies, it was possible to produce dense bars for further tests for the compositions shown in Table 3.2, except for the LSFAl1, which was eliminated from candidates due to its brittleness.

3.5. Thermal and isothermal expansions

The thermal expansion of the sintered bars was measured up to 900°C in air by heating with a rate of 5 K/min followed by the change of the atmosphere from air to Ar for the isothermal expansion behavior of the materials. A typical measurement is shown in Fig. 3.9, which was conducted for LSF. The relative expansion of the material compared to its initial length, $\Delta l/l_0$, is shown as a function of time. The corresponding temperature program is shown on the left hand side of the plot.
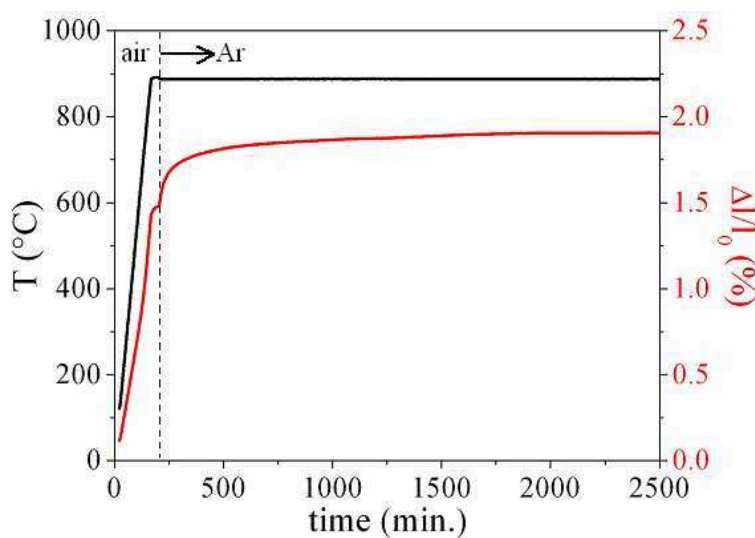
Fig. 3.9. An example of the dilatometry experiment conducted on LSF material in air and Ar at 900°C. The atmosphere is changed from air to Ar after the expansion reaches equilibrium.

The thermal expansion part of the plot in Fig. 3.9 corresponds to around the first 200 minutes of the experiment. There was still slight expansion in air after the temperature reached the 900°C; therefore, Ar was introduced to the system after the equilibrium was reached. The non-linear thermal expansion behavior of the material is obvious in Fig. 3.9, which will be discussed further in the next chapter. In this chapter, only the equilibrium expansion values in air and Ar are taken into account.

The expansion values of all B-site substituted materials are plotted in Fig. 3.10 showing the thermal expansion at 900°C in air and in Ar in percentages where l_0 is the initial

length at RT in air. Fig. 3.10 (b) shows the isothermal expansion at the same temperature as a result of the change of atmosphere from air to Ar. In this case, l_0 is taken as the equilibrium length at 900°C in air.
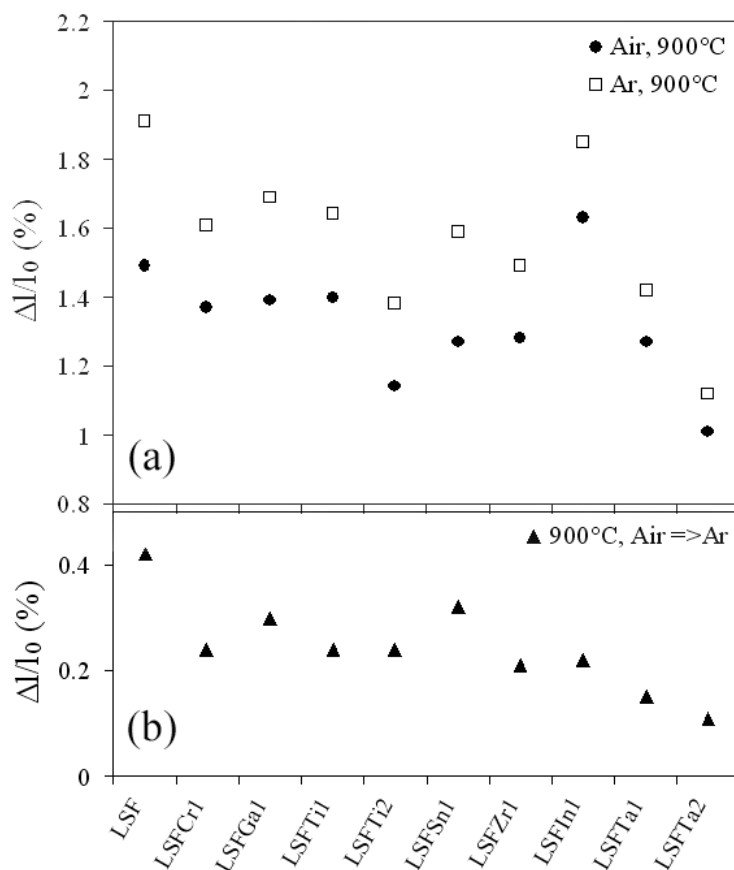
Figure 3.10. a) Total expansion in air and Ar and b) isothermal expansion of B-site substituted LSF materials at 900°C.

As is seen in the Fig. 3.10, the thermal and isothermal expansion is suppressed in case of each substitution compared to LSF, except for the LSFIn1. Replacing the multi-valence Fe-ion reduces the concentration of the Fe^{4+} cation, which (at high temperatures and reducing atmospheres) is accompanied with oxygen vacancy formation. It is expected that the effect would be more pronounced if the substituting ion has higher valence state (e.g. 4+ or 5+), which forces Fe ions to the 3+ state and therefore reduces the B-site reduction. This is in agreement with the results obtained. The isothermal expansion (Fig. 3 (b)) is reduced to half of its value compared to LSF in case of several additives (Cr, Ti, Zr, In), while it is considerably lower for LSFTa samples as Ta has a 5+ valence. LSFIn1 sample showed comparable isothermal expansion to other 3+ or 4+ additions; however, the total expansion

was measured as high as the base material itself. This may be related to the conclusion drawn in section 3.4.1 that the In may not be incorporated into the structure. This would result in a perovskite material with B-site deficiency, which could show higher thermal expansion.

As a result of the thermal and isothermal expansion experiments, LSFTi2 and the samples with Ta, LSFTa1 and LSFTa2 were identified to be the most promising material considering the expansion behavior since they show the lowest total and isothermal expansions under Ar. The isothermal expansion of LSFTi2 is similar to some other compositions; however, it was distinguished among the others due to its lower total expansion.

3.6. Summary and conclusions

In this chapter, a general B-site substitution screening of $La_{0.5}Sr_{0.5}FeO_{3-\delta}$ was shown to identify a suitable doping material. The B-site substituted $La_{0.5}Sr_{0.5}Fe_{1-y}B_yO_{3-\delta}$ compositions were produced by solid-state reaction route. The chosen elements for possible B-site doping were B is Mg, Al, Ga, In, Sn, Zr, Cr, Ti, Ta, and V. The phase purity of the materials was checked by X-ray diffraction analysis and the ones with 10% Mg, 10% V, 20% Zr, 20 % Ga, and 20% Sn were ruled out of the candidates due to the presence of second-phases in the structures. The positions of the main Bragg angle of the perovskite structures were found to be in good agreement with the effective ionic radius of the B-site of the materials. An overall increase of the B-site radius shifted the main diffraction peak to lower angles, which means larger unit cell volumes.

As a result of the sintering studies, the materials with Al-doping were found to be porous after sintering at 1430°C for 4 hours and extremely brittle when sintered for longer times although the high-density was achieved. This was attributed to possible glass formation on the grain boundaries. Therefore, this material was ruled out of candidates. The other materials were pressed into bars and sintered for further characterization.

Thermal and isothermal expansions of the sintered bars were measured by dilatometry experiments. Thermal expansion was measured in air up to 900°C and then the atmosphere was changed to Ar at the same temperature to measure the isothermal expansion of the materials. This expansion was related to the increase in the unit cell as a result of simultaneous oxygen loss and reduction of Fe^{4+} to Fe^{3+}. As a result of these studies, the compositions with Ta were found to suppress the expansion most effectively. Due to the possibility of severe reduction of conductivity in LSFTa2, this sample was ruled out. Therefore, the compositions $La_{0.5}Sr_{0.5}Fe_{0.8}Ti_{0.2}O_{3-\delta}$ and $La_{0.5}Sr_{0.5}Fe_{0.9}Ta_{0.1}O_{3-\delta}$ were chosen as the most promising candidates for oxygen separation membranes to be used in partial oxidation purposes.

In this chapter, the B-site substitution screening was conducted on the basis of few key parameters considering the formability of the structure and the sample, and the isothermal expansion as a stability indicator. It is now important to characterize these candidates further to conclude on their possible use as oxygen separation membranes. Therefore, in the following chapters of this thesis, in detail characterization of the compositions identified as the promising candidates are reported.

Chapter 4

Structural and Chemical Properties of La$_{0.5}$Sr$_{0.5}$Fe$_{1-y}$(Ti/Ta)$_y$O$_{3-\delta}$

In this chapter, structural and chemical properties of the selected LSF(Ti/Ta) compositions are discussed in detail. Long-term XRD scans were used to study the structure of the as produced and heat-treated materials in reducing conditions, such as Ar or Ar/H$_2$ mixtures. Synchrotron radiation was used to investigate the high-temperature structural changes of LSF, which provided the basis for comparison of the changes in the unit cell parameter with the dilatometry experiments. X-ray absorption spectroscopy (XAS) was performed on calcined and heat-treated powders to study the electronic structure of the materials at room temperature. Finally, thermo gravimetric analysis (TGA) of the selected compositions shown later in this chapter provides information on the oxygen non-stoichiometry in Ar-atmosphere.

4.1. Introduction

In the previous chapter, systematic ionic radius changes (due to substitution and valence changes) in $La_{0.5}Sr_{0.5}FeO_{3-\delta}$ upon substitution of Fe were discussed on a theoretical basis and using assumptions. Several compositions with different B-site doping were produced, and their expansion behavior was studied in air and Ar in a broad manner in an attempt to identify a promising candidate with improved stability compared to the host composition. Their crystal structures were not refined but broadly compared to the reference materials. However, a full understanding of the functionality of a material lies in the understanding of its structure. That is why this chapter is devoted to the understanding of the structure of the selected B-site substituted materials, $La_{0.5}Sr_{0.5}FeO_{3-\delta}$ $La_{0.5}Sr_{0.5}Fe_{0.8}Ti_{0.2}O_{3-\delta}$, and $La_{0.5}Sr_{0.5}Fe_{0.9}Ta_{0.1}O_{3-\delta}$.

There has been a tremendous effort to visualize the materials on an atomic scale in the last two centuries. The most of the progress became possible with the discovery of x-rays by W.C. Röntgen[72] in 1895. Afterwards, several structure-sensitive techniques have been established for use in the scientific world. The first synchrotron accelerator was built in 1946 and announced in 1947 by General Electric, which also gave the name to this kind of radiation.[73] In 1970s, X-ray absorption became an important tool to study the electronic and structural properties on the atomic level. In this chapter, these two techniques were used to study the temperature dependence of the crystal structure of LSF and the changes in the electronic structure of $La_{0.5}Sr_{0.5}FeO_{3-\delta}$ are shown based on x-ray absorption spectroscopy results. Conventional X-ray diffraction and thermo gravimetric analysis are reported complementarily to study the room temperature structures and oxygen non-stoichiometry of the materials.

4.2. Theory

4.2.1. Electronic structure of $La_{1-x}Sr_xFeO_{3-\delta}$

By definition, a transition metal is an element whose atom has an incomplete d sub-shell. This is one of the most important features of transition metals distinguishing them from other metal ions. These d electrons are involved in bonding and give rise to many interesting properties of these elements. The transition elements can have variable oxidation states, which can all be energetically favorable at certain conditions. In general, higher states are usual when bonded to electronegative elements such as oxygen. In the free atom, there are five d orbitals all having the same energy. When the transition metal ion forms a complex with ligands, the spherical symmetry of the ion is lowered and this causes the energetic

degeneration of the atomic *d* levels. This occurs by a split in the *d* orbital energy levels (also called crystal field splitting), the magnitude of which (ΔE) defines how the electrons are distributed between the *d* orbitals. A schematic of the 5 possible *d* orbitals are shown in Fig. 4.1.
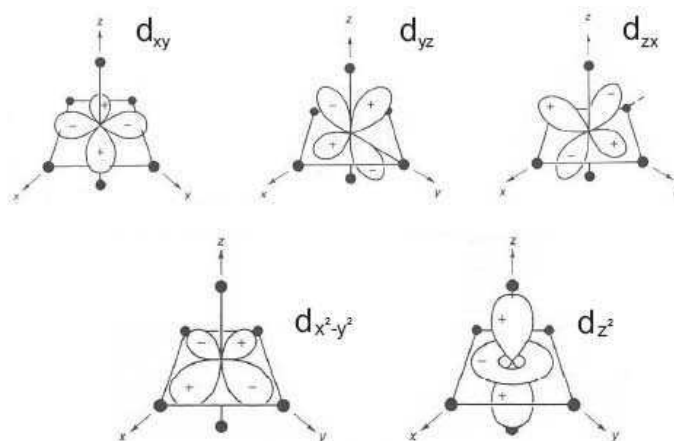
Fig. 4.1. Schematic of the 5 possible d orbitals of a transition metal ion, taken from Ref.[74]

Each orbital can accommodate 2 electrons, adding up to 10 electrons for a totally occupied *d* shell. The orbitals d_{xy}, d_{yz}, and d_{xz} (also called t_{2g} orbitals) are degenerated and are responsible for molecular bonding in tetragonal symmetry, on the other hand d_{z2} and d_{x2-y2} (also called e_g orbitals) are responsible for bonding in octahedral symmetry. The electrons of the *d*-shell are filled according to Hund's Rule, which indicates that, each orbital in the same band, either t_{2g} or e_g, will be filled with an electron with a parallel spin orientation before the opposite spin occupies an orbital. However, when the splitting (Δ) of the *d*-orbitals is large, it is not favorable to fill the high-energy orbitals and therefore, the low-energy orbitals are filled first. Such complexes are called "low-spin" while in case of the opposite situation they are called "high-spin". A simple schematic of an octahedral splitting is shown in Fig. 4.2 (a). In the same figure, (b) shows an illustration of the Fe 3*d* levels in LaFeO$_3$.
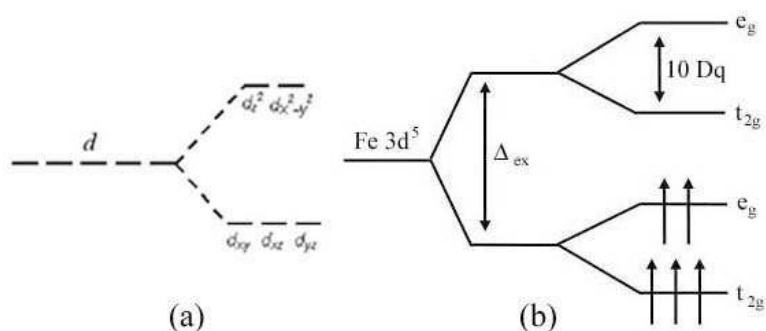
Fig. 4.2. Schematic showing a) octahedral splitting, b) energy levels of Fe 3*d* in LaFeO$_3$ taken from Ref.[61]

The schematic in Fig. 4.2 (b) is taken from a work by Abbate[61] et al. on valence properties of $La_{1-x}Sr_xFeO_3$. The formal valence state of Fe in $LaFeO_3$ is +3, which corresponds to the electronic structure of $3d^5$. In the Fig. 4.2, Fe $3d^5$ energy level first splits by Δ_{ex} due to exchange interactions into spin-up and spin-down states. Each state is further split because of the octahedral crystal field (also called ligand-field splitting and denoted as $10Dq$) as shown in Fig. 4.2 (a). Fe $3d$ electrons are reported to be in high-spin configuration because the $10Dq$ is lower than the exchange interaction splitting (Δ_{ex}).

X-ray absorption spectroscopy (XAS)

When X-rays hit a sample, they interact with the electrons bound in an atom. As a result, they will be either scattered or absorbed exciting the electrons. When the energy of the incident photons is sufficient to cause an excitation of a core electron of the absorbing atom, the absorption increases and creates an absorption edge. The energies of these edges correspond to the binding energies of electrons in different shells of the absorbing element, specific to the nature of the element and in addition, site and symmetry sensitive. Therefore, it provides information on the local structure and on the local electronic states of the material.[75, 76]

4.2.2. X-ray absorption data on $La_{1-x}Sr_xFeO_{3-\delta}$

In x-ray absorption spectra, the peak positions and shapes are extremely sensitive to the $3d$ states and the crystal-field interactions. Therefore, they can be used to study the occupancy of these states. An example x-ray spectra of $LaFeO_3$ and $SrFeO_x$ showing the energy levels corresponding to the Fe $2p$ absorption is shown in Fig. 4.3.
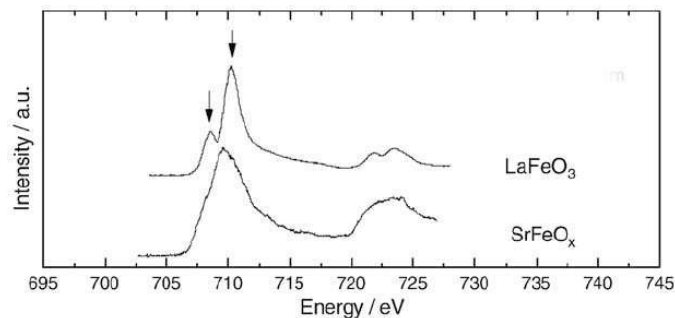
Fig. 4.3. Fe$2p$ x-ray absorption spectra of $LaFeO_3$ and $SrFeO_x$, taken from the work of Mineshige et al.[77]

There are two absorption regions in the plot in Fig. 4.3. The one around 708-713 eV belongs to the $2p_{3/2}$ (L_3) edge while the one around 720-725 eV belongs to the $2p_{1/2}$ (L_2) edge. According to these spectra, the valence of Fe in $LaFeO_3$ is reported to be 3 and it is 3.4 in $SrFeO_x$.[77] Therefore Fe in the latter compound is a mixture of 3+ and 4+ and there is certain amount of oxygen nonstoichiometry for the charge neutrality. In the same work, $La_{0.6}Sr_{0.4}Fe_{0.8}Co_{0.2}O_{3-\delta}$ was found to resemble $SrFeO_x$ under high pO_2 (0.2 atm) and $LaFeO_3$ under lower pO_2 (10^{-8}).[77] The peak area ratio of the two peaks at 708 eV and 710 eV was used to provide semi-quantitative results for valence state of the other samples using $LaFeO_3$ and $SrFeO_x$ as reference points together with spectra of Co.

The Fe $2p$ and O $1s$ x-ray absorption spectra of $La_{1-x}Sr_xFeO_{3-\delta}$ with varying Sr-content taken from Abbate's work[61] are shown in Fig. 4.4. The left plot shows the Fe $2p$ absorption spectra for x = 0, 0.1, 0.3, 0.5, 0.7, and 1.0 and the right plot shows the corresponding O $1s$.
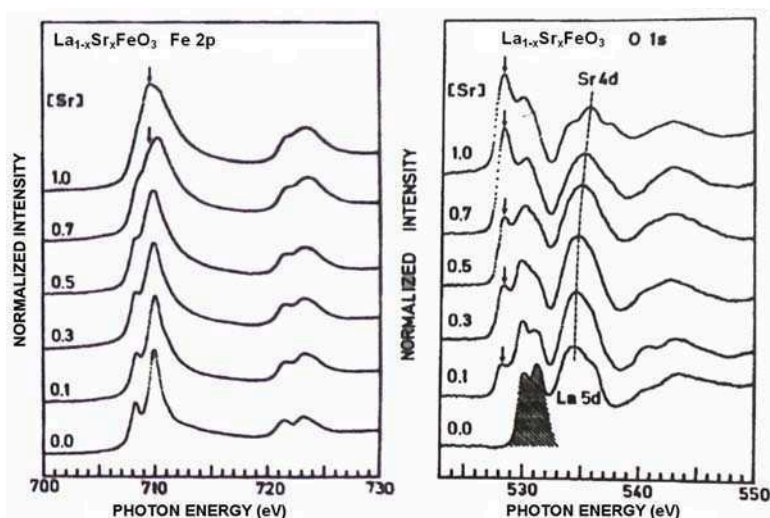
Fig. 4.4. Fe $2p$ (left) and O $1s$ (right) x-ray absorption spectra of $La_{1-x}Sr_xFeO_{3-\delta}$ for x = 0.0-1.0 taken from Ref.[61]

Abbate et al[61] reported $LaFeO_3$ to have high-spin $3d^5$ configuration. The results were in good agreement with the theoretically simulated ones assuming a high-spin state with a $10Dq$ (crystal field parameter) of 1.8 eV. It was found in the same work that the shape of the Fe $2p$ peaks remains essentially unchanged when the Fe^{3+} was replaced by Sr^{2+} up to 50%. Therefore, it was suggested that the charge neutrality was preserved by holes induced that go to the states of the oxygen character. They concluded that the ground state of $La_{1-x}Sr_xFeO_3$ for x ≈ 0.5 was mostly $3d^5$ $\underline{L}$, where $\underline{L}$ denotes a ligand hole and not $3d^4$. In the O $1s$ spectra, the absorption occurs due to the transitions to the unoccupied states with O $2p$ character hybridized with metal states according to Abbate et al[61]. The O $1s$ spectrum of $LaFeO_3$ shown on the bottom of the plot in Fig. 4.4 (right) is shaded to point out the doublet, which is attributed to bands of minority (spin-down) Fe $3d$ states split by the octahedral crystal field

into t_{2g} and e_g orbitals. Therefore, the energy difference between the split peaks gives the value for 10Dq, which is found to be 1.2 eV in case of LaFeO$_3$ according to the spectrum shown. The peak around 535 eV is attributed to La 5d character, which changes its shape and shifts towards higher energies, meaning a change from La 5d to Sr 4d. A prepeak around 528 eV starts to appear with addition of Sr ions and dominates for high Sr compositions and it is attributed to transitions to new states, which contain O 2p character by the authors[61]. In addition, the doublet seen in LaFeO$_3$ changes its shape and becomes a shoulder to the prepeak.

4.3. Experimental

The powders of LSF, LSFTi2, and LSFTa1 used for characterization were synthesized as explained in section 3.3.1. Prior to the XRD measurements, they were heat treated at 1000°C for 1 hour and cooled to room temperature slowly (1 K/min) to provide necessary time for oxygen uptake for equilibrium in the material. In case of samples treated in reducing atmospheres, such as Ar, they were cooled with a faster rate (10 K/min) in the same atmosphere to avoid oxygen uptake.

4.3.1. XRD and synchrotron radiation

Two different kinds of X-ray sources were used for diffraction experiments. The phase-purity of the calcined powders was examined by conventional X-ray source on an X'pert PRO PW3040 (PANalytic) using CuKα radiation (λ = 1.54060 Å). High-temperature diffraction experiments were conducted at the HASYLAB[78] using synchrotron radiation.

Synchrotron radiation is an electromagnetic radiation generated by acceleration of charged particles through electromagnetic fields. The energy of the electromagnetic radiation depends on the velocity of the individual particles emitting the radiation. On the contrary to the defined wavelengths a conventional X-ray source can provide, a range of high-energy X-ray radiation is obtained when the charged particles are accelerated close to the speed of light with synchrotron radiation. In addition to the high brightness and intensity obtained, the synchrotron radiation provides high brilliance and small angular divergence of the beam (high collimation) providing higher resolution data that can be collected in shorter times. Therefore, the technique provides far better possibilities for special measurements where the timing and/or accuracy are very important, e.g. cell-parameter changes at high-temperatures.

The measurements at HASYLAB (Hamburg, Germany) were carried out at the B2 beamline[79, 80], which is a multi-purpose bending magnet apparatus used for high-resolution investigations of polycrystalline materials. A picture of the experimental station at the B2

beamline is shown in Fig. 4.5. Currently, an accessible wavelength range of 0.35-2.4 Å is possible with direct beam setting. Further specifications can be found else where.[79] In this study, a wavelength of 0.50023 Å and a heating rate of 5K/min for high-temperature measurements were used. Before each measurement, sample was allowed 10 min. to equilibrate. The refinement of the cell parameters is carried out as will be explained in the next chapter.

Fig. 4.5. Experimental station at the beamline B2 for high-resolution investigation of polycrystalline materials at HASYLAB (taken from the web site of the lab[79]).

Structure refinement

The structure refinement was done in two steps: first of all the peak positions were obtained individually, and then the unit cell parameters were refined. The program CMPR[81] was used to fit the peaks one by one. In this program peaks are fitted with a Pseudo-Voigt function, where Gaussian and Lorenztian peak shapes are mixed. A data set is selected including a single peak (or multipeaks when they are inseparable) and a representing range of background. The position of the peaks are first entered manually and then optimized by the least-squares algorithm. The peak position, the peak area, the background, the peak width, and the mixing term of the Pseudo-Voigt were adjusted during the fitting procedure. The resulting fittings were reliable and residuals were small due to the high signal/noise ratio obtained in the measurements.

The resulting 2θ values were used to refine the unit cell parameters using the UnitCell[82] program. UnitCell uses a non-linear least squares method, which doesn't require initial estimates for cell parameters and allows refinement on the observed data.

4.3.2. Thermogravimetric analysis (TGA)

The oxygen losses of the samples were determined by thermo gravimetric analysis (TGA) (Netzsch STA 409, Netzsch-Geraetebau GmbH, Germany) in air and Ar. Alumina crucibles were used as sample holder and the reference holder. Around 50 mg of powder was used for each measurement. The system was allowed for equilibrium prior to measurement before and after placing the powder in to the crucible. 5 K/min heating rate was used. The difference in weight was related to the change in non-stoichiometry (δ) of the compositions. The schematic of the Netzsch used for the measurements is shown in Fig. 4.6.
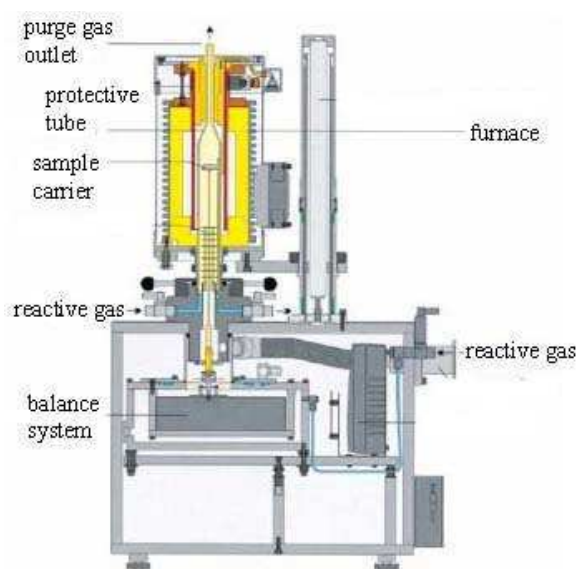
Fig. 4.6. The schematic of the Netzsch 409 TGA measurement unit taken from the Ref.[83]

4.3.3. X-ray Absorption spectroscopy (XAS)

X-ray absorption spectra were recorded at the beamline 1.1 at the Daresbury Synchrotron,[84] United Kingdom. The beamline 1.1 at the Daresbury SRS is a soft x-ray UHV spectroscopy beamline and it provides monochromatic photons over the energy range of 175-1200 eV. Further particulars can be viewed at the web page of the laboratory, dedicated to this beamline.[85] The samples were kept as coarse granules and ground to fine powder prior to the experiments, to assure the oxygen content was kept at equilibrium. The powders were dispersed over sticky carbon tape and then transferred into the vacuum chamber (p ~$5*10^{-10}$ Torr (~$1.3*10^{-3}$ atm)). The spectra were recorded with the surface sensitive total electron yield with an energy resolution of $\Delta E/E$ ~1/5000, around 0.5 eV. The signals belonging to carbon tape was used for the energy calibration, which has a characteristic peak at 532 eV.

4.4. Structural refinement of $La_{0.5}Sr_{0.5}Fe_{1-y}(Ti/Ta)_yO_{3-\delta}$ by X-ray diffraction

4.4.1. Crystal structure of $La_{0.5}Sr_{0.5}FeO_{3-\delta}$ studied by synchrotron radiation

The diffraction patterns measured with the synchrotron radiation source recorded at room temperature (25°C) and the maximum measurement temperature (900°C) are shown in Fig. 4.7. The black and red lines denote the patterns at 25°C and 900°C, respectively. The range of the measurements was $2\theta = 5\text{-}50°$. The data shown are as measured and includes the background information.
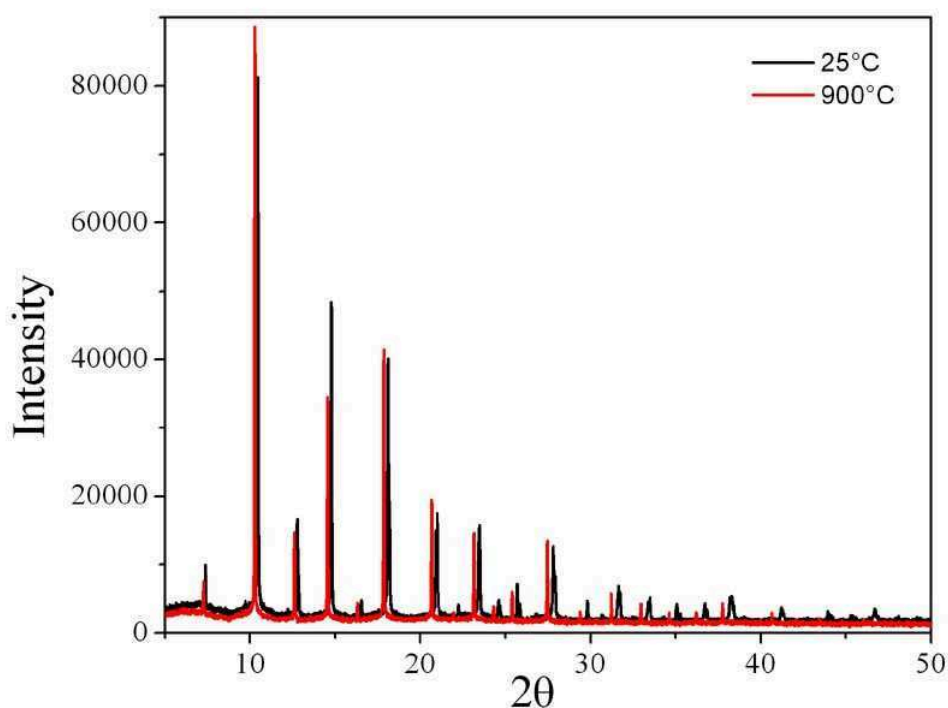
Fig. 4.7. XRD diffraction patterns of LSF recorded at at 25°C and 900°C using synchrotron radiation with wavelength of 0.50023 Å.

The material is rhombohedral at room temperature and cubic at 900°C. The changes in the diffraction pattern with increased temperature are clear. It was observed that with increasing temperature the peaks shifted to smaller angles, which indicates an increase in the unit cell dimensions. The splitting of the peaks show the rhombohedral distortion of the unit cell at low temperatures, which is visually clearer at higher angle peaks. Therefore, a magnified part of the XRD patterns shown in Fig. 4.7 between the 2θ-values 20° and 25° is

shown in Fig. 4.8. The black and red lines denote the patterns at 25°C and 900°C, respectively.
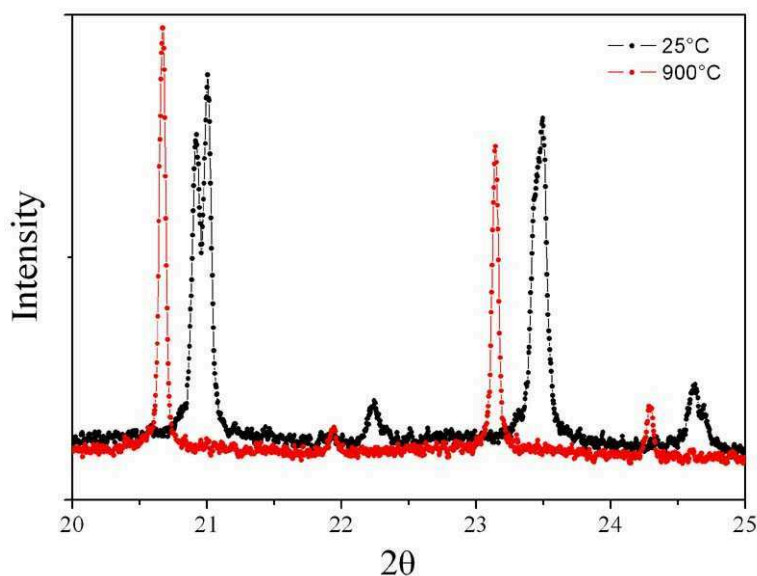
Fig. 4.8. Diffraction patterns of LSF between 2θ of 20 and 25° showing the rhombohedral splitting of the peaks at room temperature and the single cubic peaks at 900°C.

All of the peaks of the room temperature diffractograms could be indexed as rhombohedral perovskite phase except for the small peak observed at 2θ of 9.70° (Fig. 4.7). This is a phase similar to $LaSrO_4$ as mentioned in the section 3.4.1. It was not visible in the XRD patterns shown before because of the low resolution of the XRD measurements. Assuming that this peak is the highest intensity peak of the tetragonal phase, the comparison of its intensity to the intensity of the main peak of rhombohedral phase gives a percentage of 1.2 %. Therefore, the material is considered to have high-phase purity.

The 2θ values obtained as a result of the peak-fitting program, CMPR, are shown in Table 4.1. The rhombohedral and cubic values correspond to the diffractions patterns recorded at 25 and 900°C, respectively. These 19 rhombohedral and 14 cubic reflection indices were used for crystal structure refinement as long as the peak fitting could be done reliably.

Table 4.1. The lists of reflection indices (h k l) used for calculation for rhombohedral and cubic phases

	Rhombohedral		Cubic	
	h k l	2-theta	h k l	2-theta
1	0 1 2	7.374	1 0 0	7.276
2	1 1 0	10.413	1 1 0	10.299
3	1 0 4	10.455	1 1 1	12.622
4	2 0 2	12.774	2 1 0	16.318
5	0 0 6	12.844	2 1 1	17.886
6	0 2 4	14.782	2 2 0	20.681
7	1 2 2	16.504	3 1 0	23.154
8	1 1 6	16.565	3 1 1	24.303
9	0 1 8	18.189	2 2 2	25.399
10	2 2 0	20.919	3 2 1	27.473
11	2 0 8	21.005	3 3 0	31.239
12	1 3 4	23.436	4 2 0	32.976
13	1 2 8	23.497	3 3 2	34.638
14	4 0 4	25.711	5 1 0	37.761
15	0 0 12	25.858		
16	0 4 8	29.818		
17	2 4 4	33.373		
18	2 2 12	33.489		
19	1 0 16	35.262		

Unit cell parameters were calculated as explained in the section 4.3.1 using the 2-theta values given in Table 4.1. As a result of the synchrotron radiation experiments conducted in this study, LSF was found to have a hexagonal structure with a = 5.51046 Å, c = 13.41531 Å, and the volume, V = 352.87 Å^3. The crystal structure was indexed as cubic at 900°C with a = 3.94104 Å.

In the literature, the host material $La_{0.5}Sr_{0.5}FeO_{3-\delta}$ is reported to be rhombohedral as well with the space group R-3c at room temperature.[66, 67] The unit cell parameters a, c, and the volume, V, are reported in hexagonal symmetry as 5.5111 Å, 13.4158 Å, and 352.87 Å^3, respectively, which are in very similar range as found in this study. The cubic structure of LSF at 900°C was reported to be 3.9425 Å by Fossdal et al[67]. These values are very close to each other with less than 0.05 % difference.

In order to make the comparison easier between low-temperature hexagonal and high temperature cubic structures, the hexagonal unit cell parameters are converted to rhombohedral symmetry. Hexagonal structure has the primitive cell with a = b ≠ c, α = β =

90°, and $\gamma = 120°$ while rhombohedral structure is defined with $a = b = c$, and $\alpha = \beta = \gamma \neq$ 90°. A schematic is shown in Fig. 4.9 showing the relation of rhombohedral structure with hexagonal symmetry. The prime sign (') is used to indicate the calculated rhombohedral (a', α') values further on in this section of the thesis.
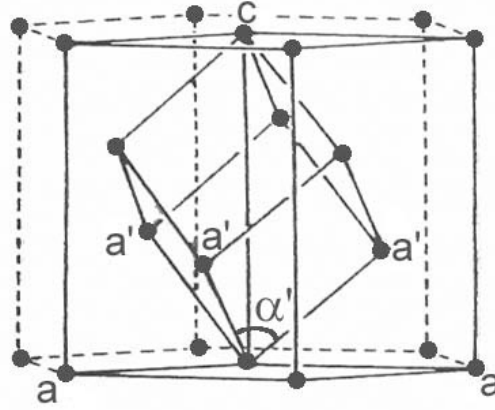
Fig. 4.9. A rhombohedral lattice referred to hexagonal axes.

It can be observed in Fig. 4.9 that the hexagonal unit cell is 3 times of the rhombohedral unit cell. The calculations for rhombohedral conversion were applied to half of the hexagonal unit cell, i.e. half the c value. The equations used to convert hexagonal unit cell parameters (a and c) to rhombohedral representatives (a' and α') are shown below[86]:

$$a = a'\sqrt{2}\sqrt{(1-\cos\alpha')} = 2a'\sin\left(\frac{\alpha'}{2}\right) \tag{4.1}$$

$$c = a'\sqrt{3}\sqrt{(1+2\cos\alpha')} \tag{4.2}$$

$$a' = \frac{1}{3}\sqrt{(3a^2 + c^2)} \tag{4.3}$$

$$\sin\left(\frac{\alpha'}{2}\right) = \frac{3}{2\sqrt{\left(3+\dfrac{c^2}{a^2}\right)}} \tag{4.4}$$

The hexagonal unit cell parameters of LSF at RT (a = 5.51046 Å, c = 13.41531 Å) become a' = 3.88844, α' = 90.24° when converted to rhombohedral. The angle α' of 90.24° is very close to 90°; therefore the distortion of the material is very slight. If the smaller unit cell shown in Fig. 4.9 is considered as a cubic cell, the rhombohedral distortion in LSF occurs via the depression of the diagonal of the cube in the z-direction of the hexagonal structure, resulting in an angle α larger than 90°. The data was analyzed starting from RT with

hexagonal and from 900°C with cubic structures towards the middle temperatures until it was no longer possible to index the structure. It was found difficult after 400°C to refine the structure as hexagonal while it was possible to refine the data as cubic below 400°C, however, the rhombohedral splitting of the peaks were obvious below 400°C. Therefore, the refinement was done with hexagonal structure up to 400°C and cubic afterwards.

The unit cell parameters for cubic (a) and for rhombohedral (a') structures of LSF are shown in Fig. 4.10 as a function of temperature. The circles (T = 25 - 400°C) show the calculated a' and the triangles (T = 400 – 900°C) show the cubic parameter, a. In addition, black symbols are for the data taken during heating the sample up to 900°C and the red symbols are for the measurements taken during cooling down the sample. The black lines show the linear fits to the data and the dashed line is the continuation of the fit. The error bars are shown for all points in Fig. 4.10; however, they stay in the range of the symbols and therefore, are not very clear.
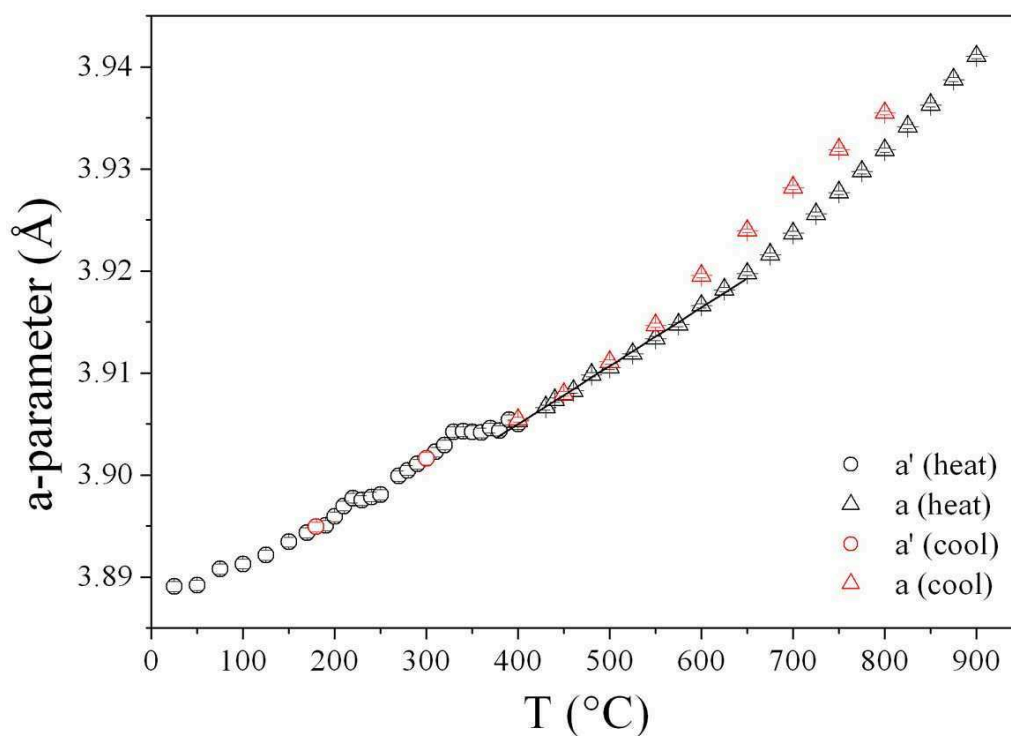
Fig. 4.10. The unit cell parameter, a for cubic (triangles) and a' for rhombohedral (circles) structures as a function of temperature, the black symbols show the data taken during heating and red symbols during cooling.

According to the results taken during heating (black symbols), the unit cell expands almost linearly up to 330°C with a deviation around 220°C. There is a plateau between 330 and 380°C followed by linear increase up to 600°C, where the data starts to deviate from linearity. There is no abrupt change in the unit cell parameter. Fossdal et al.[67] mention the

temperature of 250°C for the rhombohedral to cubic transition of the structure for $La_{0.5}Sr_{0.5}FeO_{3-\delta}$ composition. This temperature is close to where there is a little bump in Fig. 4.10; however, the material in this study was found to be hexagonal above this temperature also. At first look, the rhombohedral to cubic transition may be thought to occur around plateau observed around 350°C with continuous second-order phase transition. However, it is not really correct to define an exact temperature for the transition was observed to occur slowly over a wide range of temperature. The differential thermal analysis conducted on the sample supported this observation, no sudden change in the signal was observed. The material could be indexed as hexagonal even after the plateau. The explanation for the plateau region is a subject of discussion, as it is not attributed to a phase change. Blond and Richet[87] conducted a study a on linear expansion of the $La_{0.495}Sr_{0.396}Fe_{0.9}Ti_{0.1}O_{3-\delta}$ material sintered under N_2 atmosphere. When the expansion was measured in air, the material showed considerable reduction in size around 300°C, which was variable depending on the atmosphere of the measurement. This was attributed to the oxygen uptake of the material and the material did not show an opposite effect during cooling as the equilibrium was reached in air at high temperatures. The plateau observed for LSF could be explained with similar oxygen uptake causing material to decrease its size with simultaneous thermal expansion causing it to increase in proportional amounts so that a plateau is observed instead. However, the data points at 300° and 180° measured during cooling of the setup coincide perfectly with the heating values. This suggests that the material follows a similar trend during cooling. This would not be the case if there would be oxygen loss at this temperature, which is not probable under air atmosphere.

An increased expansion rate is observed at temperatures higher than 600°C. This increase is attributed to the oxygen loss in the material that causes chemical expansion in addition to thermal expansion as explained previously in chapter 3. The same kind of behavior was observed by other authors for measurements conducted by XRD or dilatometry.[54, 57, 63, 67]

Another important point is the hysteresis observed during cooling. The unit cell size calculated from the diffractograms measured during cooling of the system are systematically higher in the temperature range T = 550 – 750°C. The diffraction data above this temperature is not available for cooling. The cell sizes measured during heating and cooling coincides well at 500°C and below. This can be attributed to the slow kinetics for oxygen incorporation, which has been observed by others as well. This causes hysteresis in other properties such as electrical conductivity. Necessarily long equilibration times are required to avoid the hysteresis.

The ratio of the hexagonal parameters, c and a, can be used to check the changes in the structure in the hexagonal region (below 400°C). The c/a ratio takes the structural anisotropy into account. Note that half of the hexagonal cell with c/2 is used, which is the

unit cell used to calculate the rhombohedral structure. This ratio is shown in Fig. 4.11 as a function of temperature together with the value of calculated rhombohedral angle, α'. The left hand-side of the graph shows the c/a ratio and the right-hand side shows the α' in degrees. The dashed line shows the linear fit to the α' data.
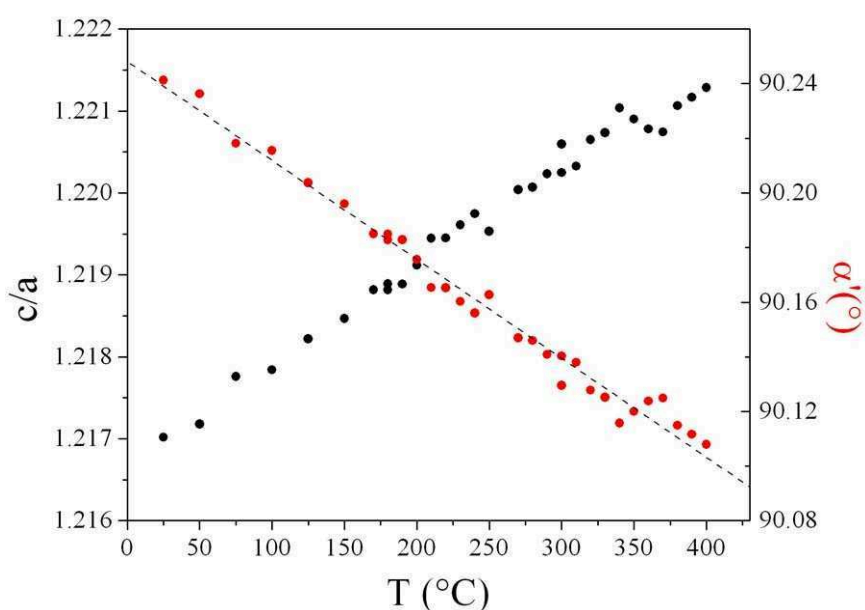
Fig. 4.11. The ratio of the hexagonal parameters, c/a, and rhombohedral angle, α', as a function of temperature.

The ratio c/a increases with increasing temperature. This means that the hexagonal structure is expanding more in the z-direction than the x-direction, which relaxes the rhombohedral angle. The corresponding decrease in the α' can be seen in Fig. 4.11. The interaxial angle decreases from 90.24° at RT to 90.11° at 400°C. The change in the angle is linearly related to the measurement temperature. Normally this angle would be 90° for the cubic structure. Assuming that the linear relation continues further with temperature, extrapolation of the linear fit intersects 90° at the temperature of 610°C. Therefore, above this temperature the structure should be cubic without any distortion. However, it is not possible to take this temperature as a fact because, as already mentioned before, it becomes difficult to fit the peaks according to hexagonal structure well below this temperature and above 400°C.

The expansion of the unit cell is compared to the expansion of the bulk sample measured by dilatometry experiment in Fig. 4.12. The black symbols show the uniaxial expansion of the sintered bar, measured as explained in section 3.3.3 and the red symbols correspond to the expansion of the unit cell measured by X-ray diffraction using synchrotron radiation. Both values are relative expansion shown in percentage where l_0 and a_0 denote the initial length and unit cell parameter at room temperature.
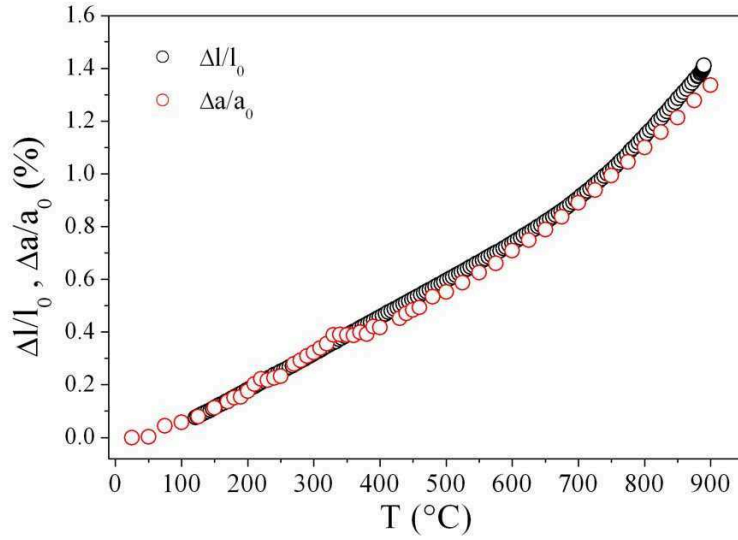
Fig. 4.12. Relative expansion of unit cell parameter, a, and total length, l, of LSF measured by dilatometry and synchrotron radiation, respectively.

The expansions of unit cell and the bulk sample (corresponding to atomic and macroscopic scales, respectively) coincide well according to Fig. 4.12. After the plateau in the unit cell expansion ($\Delta a/a_0$) stays slightly lower than the bulk expansion ($\Delta l/l_0$). The slopes (coefficient of thermal expansion) are very similar to each other. The deviation from linearity at high temperatures seems to start slightly later (around 650°C) in bulk than the unit cell (~600°C). The coefficient of thermal expansion (CTE) is lower in the case of the unit cell, which is 22.4×10^{-6} K^{-1} while it is 26.0×10^{-6} K^{-1} for the bulk material. This difference in the CTE suggests that there is additional expansion in case of polycrystalline material, which may be related to the weakened grain boundaries at high temperatures.

4.4.2. Structure of $La_{0.5}Sr_{0.5}Fe_{1-y}(Ti/Ta)_yO_{3-\delta}$ heat treated in air, Ar and (H$_2$/Ar) atmospheres

In the previous section, the structure of LSF material was refined using synchrotron radiation. The conventional X-ray diffraction was used to refine the structures of LSF, LSFTi2, and LSFTa1 at room temperature. The calcined powders were cooled down to room temperature slowly to assure oxygen equilibrium. Additionally, the same powders were heat treated in Ar at 850°C for 3 days and cooled to room temperature in Ar atmosphere to avoid oxygen uptake. Finally, the samples used for electrical conductivity (results are given in the next chapter) experiments under reducing atmospheres (4% H$_2$ – 96% Ar) for weeks were crushed into fine powders and used to check the phase composition. The conductivity samples were cooled down to room temperature in air atmosphere.

The X-ray diffractograms of LSF heat treated in air (as-produced, cooled down slowly), Ar, and (H$_2$/Ar) are shown in Fig. 4.13 with black, blue, and red lines, respectively.
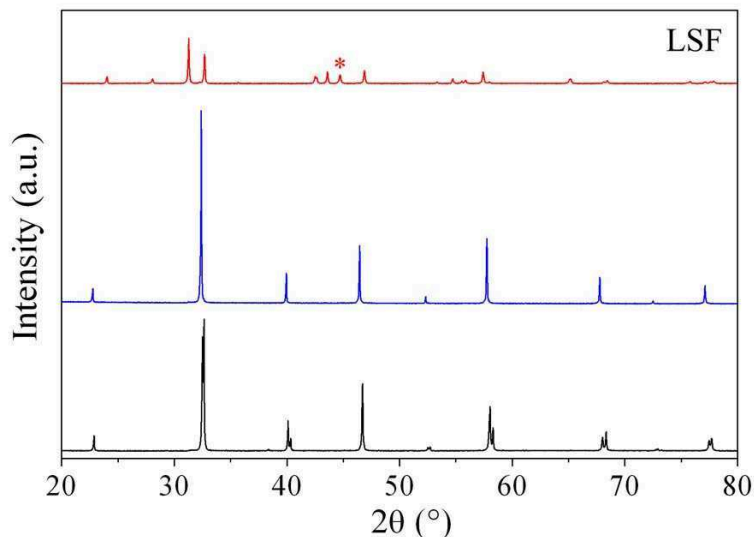
Fig. 4.13. X-ray diffractograms of LSF heat-treated in air (black curve), Ar at 850°C for 3 days (blue curve), and total conductivity sample in 4%H$_2$-Ar over a week (red curve).

Indexing of the diffractogram shown in 4.13 (black curve) reveals that the calcined LSF has a hexagonal structure at room temperature with unit cell parameters of a = 5.51061 Å, c = 13.41531 Å, and the volume of 352.81 Å^3. These dimensions are in very good agreement with the ones obtained by synchrotron measurements, which has a difference of 0.006%. The unit cell parameters of the hexagonal and cubic structures are shown in Table 4.2 together with the parameters of LSFTi2 and LSFTa1.

The material was indexed as cubic with a = 3.9073 Å at room temperature after the heat treatment in Ar atmosphere at 850°C for 3 days. LSF becomes cubic at high temperatures, as we know from high temperature measurements shown before and from literature.[67] Ar atmosphere causes the non-stoichiometry to increase and when the material is cooled in the same atmosphere, i.e. in the absence of oxygen, the non-stoichiometry and therefore, the chemical expansion is maintained in the material. When the calculated rhombohedral parameter, a', is compared to the cubic parameter of Ar treated sample, an obvious (~ 0.5 %) increase is observed, which is the result of the non-stoichiometry kept in the sample.

After the long-term conductivity measurement conducted under 4%H$_2$-Ar atmosphere, the LSF sample was found to have a tetragonal structure (I4/mmm) similar to SrLaFeO$_4$ (JCPDS 01-071-1744), which has half the amount of Fe in the structure compared to perovskite LSF. This is confirmed by the amount of Fe formed in the metal state. The main peak of Fe is indicated with an asterisk (*) in Fig. 4.13. The comparison of the main peaks of

the main tetragonal phase and the Fe metal gives a ratio of 3:1 meaning that around one quarter of the Fe ions in the original perovskite was reduced to the metal state. The resulting Fe deficient structure does not exactly have the formula $SrLaFeO_4$ but has a very similar tetragonal structure.

Table 4.2. Room temperature unit cell parameters of calcined and heat treated (in Ar at 850°C) LSF, LSFTi2, and LSFTa1

Sample	Calcined Samples, air, RT					Heat treated, Ar		
	a (Å)	c (Å)	V (Å^3)	a'(Å)	α' (°)	a (Å)	V (Å3)	Δa (%)
LSF	5.51061(18)	13.41577(65)	352.81	3.88868	90.23	3.9073	59.6527	0.48
LSFTi2	5.53027(18)	13.45271(66)	356.31	3.90150	90.26	3.9114	59.8407	0.25
LSFTa1	5.54756(18)	13.49234(66)	359.60	3.91347	90.27	3.9237	60.407	0.26

The XRD plots of LSFTi2 and LSFTa1 are shown in figures 4.14 and 4.15, respectively. In Fig. 4.14, the diffractograms of heat-treated and Ar-treated LSFTi2 are shown with black and blue lines. The plot for the LSFTa1 sample measured under the 4%H_2-Ar atmosphere is also shown in Fig. 4.15 with red line, in addition to the air and Ar treated samples.
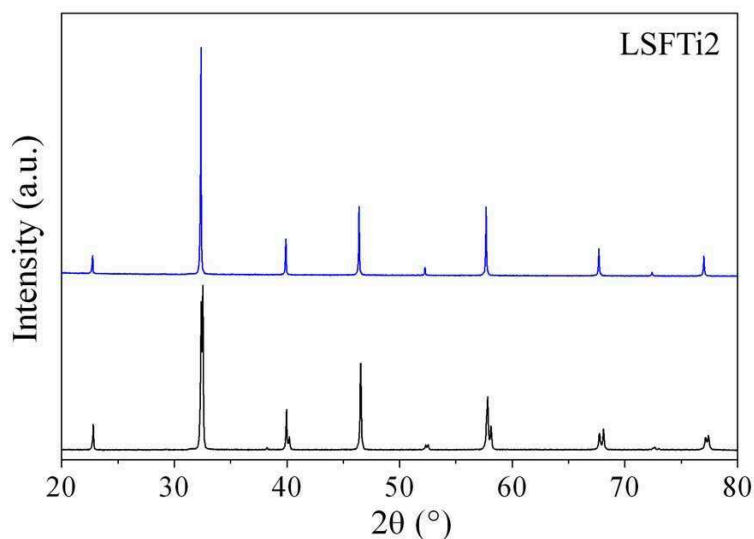
Fig. 4.14. X-ray diffractograms of LSFTi2 heat-treated in air and in Ar at 850°C for 3 days, shown with black and blue, respectively.
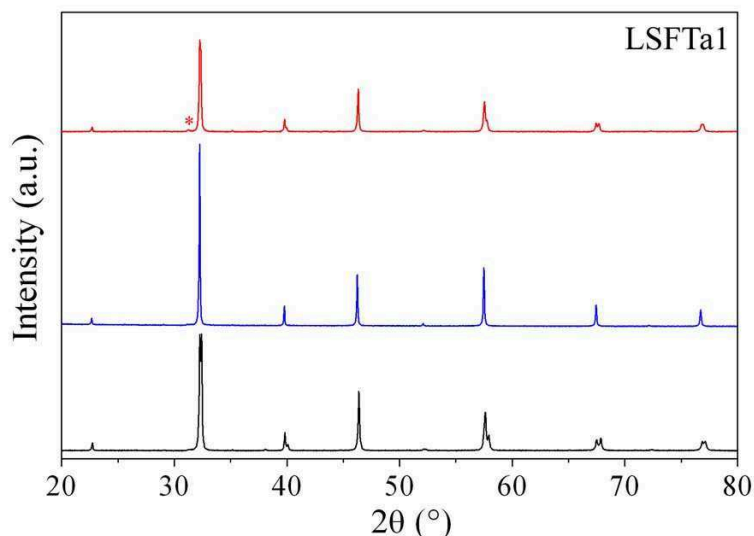
Fig. 4.15. X-ray diffractograms of LSFTa1 heat treated in air, Ar at 850°C for 3 days, and measured as a conductivity sample in 4%H$_2$-Ar over a week, shown with black, blue, and red lines, respectively.

LSFTi2 and LSFTa1 samples were also found to have hexagonal structures with the space group R-3c. The calculated unit cell parameters are shown in Table 4.2 together with LSF. As can be seen from the table, the unit cell is expanding with the addition of Ti and Ta due to larger ionic sizes of Ti^{4+} and Ta^{5+} compared to Fe^{4+} ion. This result is in agreement with the effective ionic radii calculations shown in section 3.2.2.

Both Ar-treated samples were refined as cubic as in the case of LSF. The cubic unit cell parameters are shown in Table 4.2. For comparison reasons, the pseudo-cubic unit cell parameters (a' and α') were calculated for calcined powders for half of the unit cell (i.e. c/2). The change in the unit cell length (in %) is also shown in Table 4.2. The earlier mentioned 0.48% increase in the case of LSF due to the oxygen vacancy formation is reduced for LSFTi2 (0.25 %) and LSFTa1 (0.26 %). This suggests reduced oxygen formation for the substituted materials, in agreement with the dilatometry measurements shown in Chapter 3.

As a result of the long-term conductivity measurement under reducing atmosphere, LSFTa1 material was indexed as hexagonal with a = 5.55203 Å, c = 13.53268 Å, and V = 361.26 Å^3. As the sample was cooled down to room temperature in air atmosphere, it seems that LSFTa1 recovered its hexagonal structure, although the unit cell volume was larger at room temperature compared to the samples only calcined in air. LSFTa1 was found to be much more stable compared to LSF maintaining the perovskite structure with a small amount of second phase formed. The second phase formed is indicated with an asterisk in Fig. 4.15.

4.5. Electronic and structural states by x-ray absorption data

The normalized Fe 2p x-ray absorption spectra of LSF, LSFTi2, and LSFTa1 are shown in Fig. 4.16 in separate plots for each composition. In addition to the usual three compositions, x-ray absorption measurements were conducted also on the sample with 20% Ta-substitution to see the effect of further higher-valence substitution on LSF sample. In each plot, the samples heat treated in air are denoted with red lines, while the samples heat treated in Ar-atmosphere at 850°C are denoted with thinner blue lines.
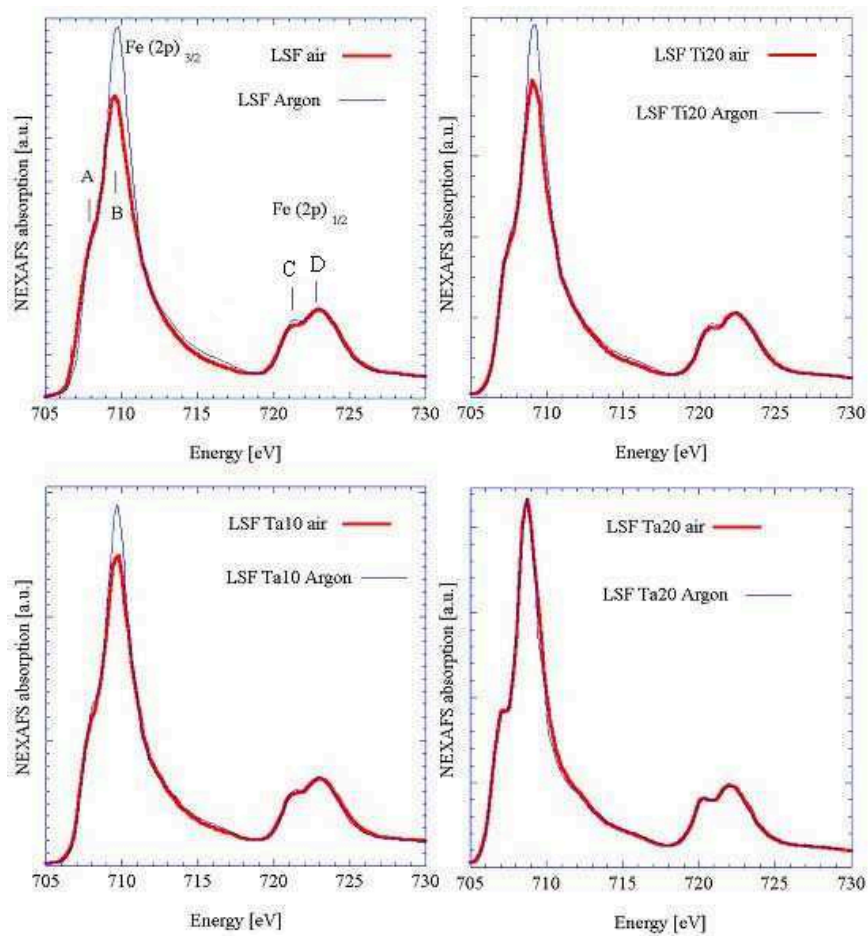
Fig. 4.16. Fe 2p x-ray absorption spectra for heat treated LSF, LSFTi2, LSFTa1, and LSFTa2 in air and Ar.

In Fig. 4.16, the spectra in the range of 705 – 730 eV showing the 2$p_{3/2}$ (L$_3$) (denoted with A and B) and 2$p_{1/2}$ (L$_2$) (denoted with C and D) multiplets are plotted. The details of the edges were given in section 4.2. Basically, the lower and higher energy peaks of the multiplets denote the t$_{2g}$ (A and C) and e$_g$ (B and D) orbitals. The Fe 2p spectra for all samples seem similar to each other and to the published data by Abbate[61]. Therefore, in line

with the literature, Fe ions in measured samples were found to be in the high-spin $3d^5$ (t_{2g}^3 e_g^2) configuration following the splitting behavior shown in Fig.4.2 previously.

The dependence of Fe $3d$ spectra on the composition is seen to be very low in this study (Fig. 4.16), as observed by others as well.[88] The spectra for LSF, LSFTi2, and LSFTa1 are especially similar to each other resembling a spectrum in between the reported spectra of $La_{0.5}Sr_{0.5}FeO_{3-\delta}$ and $La_{0.3}Sr_{0.7}FeO_{3-\delta}$ (shown in Fig. 4.4). The two peaks of $2p_{3/2}$ (L_3) multiplet are not as obviously separated as in the case of $La_{0.5}Sr_{0.5}FeO_{3-\delta}$, but also not as integrated as in the case of $La_{0.3}Sr_{0.7}FeO_{3-\delta}$. On the other hand, LSFTa2 shows spectra more like $La_{0.5}Sr_{0.5}FeO_{3-\delta}$.[61] The independence of Fe $3d$ absorption on amount of Sr-substitution was explained by the doped holes going into the states of primarily O $2p$ character instead of $3d^4$.

The intensity ratios of the two peak doublets (L_2/L_3) are compared to see the relation to the Fe^{4+}/Fe^{3+} ratio. Both ratios are shown in Table 4.3 below. The formal hole concentration (Fe^{4+}/Fe^{3+}) for the air treated samples was calculated assuming a stoichiometric samples at room temperature.

Table 4.3. Formal hole concentration (Fe^{4+}/Fe^{3+}) for air-treated samples, ratio of $2p_{1/2}$ and $2p_{3/2}$ absorption peaks, L_2/L_3, for air- and Ar-treated samples

Sample	Fe^{4+}/Fe^{3+} (air)	L_2/L_3 (air)	L_2/L_3 (Ar)
LSF	1.00	0.29	0.24
LSFTi2	0.60	0.27	0.23
LSFTa1	0.50	0.28	0.24
LSFTa2	0.14	0.22	0.22

It can be seen both from the spectra in Fig.4.16 and Table 4.3 that the intense L_3 peak around 708 eV is stronger (L_2/L_3 is lower) in case of the Ar-treated samples of LSF, LSFTi2, and LSFTa1 while both of the spectra for LSFTa2 sample are more or less identical. This suggests that the samples treated in Ar resemble more Fe^{3+} type iron, which is in agreement with the expectation that the samples are reduced under Ar atmosphere.

The O $1s$ x-ray absorption spectra of LSF, LSFTi2, LSFTa1, and LSFTa2 are shown in Fig. 4.17. As before, red lines indicate the samples heat-treated in air and the blue lines indicate the samples treated in Ar. The insets in the plots show the so-called pre peaks, which are enlarged regions between 526 and 531 eV.
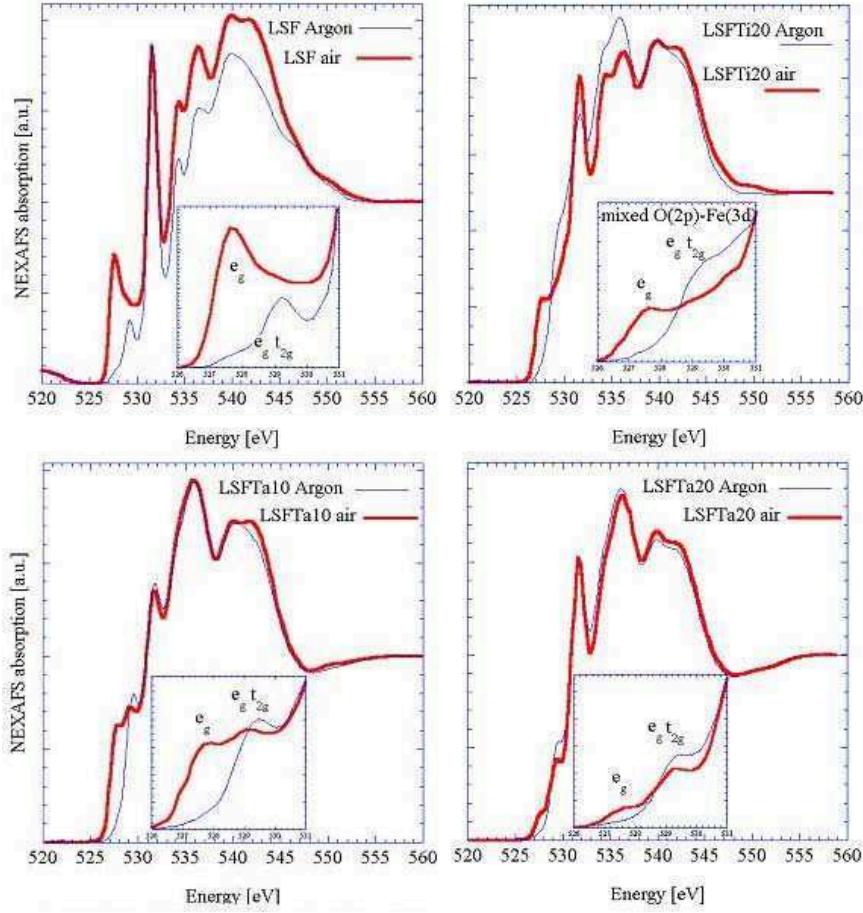
Fig. 4.17. O 1*s* x-ray absorption spectra for heat-treated LSF, LSFTi2, LSFTa1, and LSFTa2 in air and Ar.

The peaks at 527 – 530 eV of the O 1*s* spectra (shown in the insets with higher magnification) belong to the mixed states of O 2*p* and Fe 3*d*. To be more precise, the pre-peak around 528 eV has spin-up e_g character and denoted as $e_g\uparrow$. The peak around 530 eV belongs to spin-down $e_{g\downarrow}$ + $t_{2g\downarrow}$ character. The sharp peaks around 532 eV belong to CO_2 adsorbed on the surface of the samples and have high intensity because of the surface sensitivity of the technique. Furthermore, the peaks at 534.4 and 536 eV belong to O 2*p* covalently mixed with La 5*d* and Sr 4*d*, respectively. Finally the peaks at 540 and 544.8 eV form due to the interactions of oxygen with Fe 4*sp* and La 6*sp*.

The oxygen 1*s* (K-edge) spectra show more details on the structure and are more dependent on the composition as it can be observed in Fig. 4.17.[61, 89, 90] The most interesting feature in Fig. 5.17 is the change of the pre-peak. The $e_g\uparrow$ (~528 eV) peak is not observed in case of $LaFeO_3$ material and is formed by substitution of Sr, therefore indicates the hole formation.[90] The $e_g\uparrow$ peak is considerably larger in case of LSF and becomes smaller for LSFTi2 and LSFTa1. It almost disappears for LSFTa1, which indicates a mostly 3+ state of Fe and very small hole concentration. In case of the samples treated in Ar, the $e_g\uparrow$ peak

basically disappears for all the substituted samples, also remaining very small for LSF. This means that the conductivity in these materials would decrease considerably under argon atmosphere.

By deconvolution of these peaks, the areas of $e_g\uparrow$ and $e_g\downarrow + t_{2g}\downarrow$ can be calculated. It was shown by Braun et al.[91] from the results given in this section that the ratio $e_g\uparrow / (e_g\downarrow + t_{2g}\downarrow)$ could be correlated to the hole concentration calculated using non-stoichiometry measured by TGA and the conductivity of the materials. The total conductivities (at 307 K) of LSF, LSFTi2, LSFTa1, and LSFTa2 were 50, 2.28, 0.82, and 0.06 S/cm, respectively, decreasing exponentially with substitution in the order shown. Although the ratio $e_g\uparrow / (e_g\downarrow + t_{2g}\downarrow)$ could be related to the hole concentration linearly, it did not explain the exponentially decreasing total conductivity. Therefore, it was speculated that the disorder caused by the substitution could be an additional cause for the conductivity decrease.[91]

By means of X-ray absorption spectroscopy, the effect of B-site substitution on the hole concentration of the materials were studied. The data was presented more in a qualitative manner, although it promises a quantitative analysis.

4.6. Comparison of oxygen non-stoichiometry and expansion of $La_{0.5}Sr_{0.5}Fe_{1-y}(Ti/Ta)_yO_{3-\delta}$

Up to this point, the crystal structure, electronic structure, and expansion behavior of the materials were characterized. In Chapter 2, the relation of non-stoichiometry and isothermal expansion was discussed. The linear relation observed for Cr-based materials were mentioned. In this section of the thesis, this aforementioned statement will be checked for $La_{0.5}Sr_{0.5}Fe_{1-y}(Ti/Ta)_yO_{3-\delta}$ materials. The non-stoichiometry of the materials under Ar-atmosphere and its relation to the isothermal expansion reported in Chapter 3 will be discussed.

The reduction in mass with temperature related oxygen loss was measured by thermal gravimetric analysis (TGA). The TGA curves are shown in Fig. 4.18 together with the corresponding thermal expansion curves of LSF, LSFTi2, and LSFTa1 measured in air as a function of temperature. Note that the TGA analyses were conducted on powders while the dilatometry experiments on bars, as explained in section 3.3.3. Average coefficients of thermal expansion (CTE) calculated from these curves are given in Table 4.5. Two values for CTE are given for the lower and higher temperature ranges.
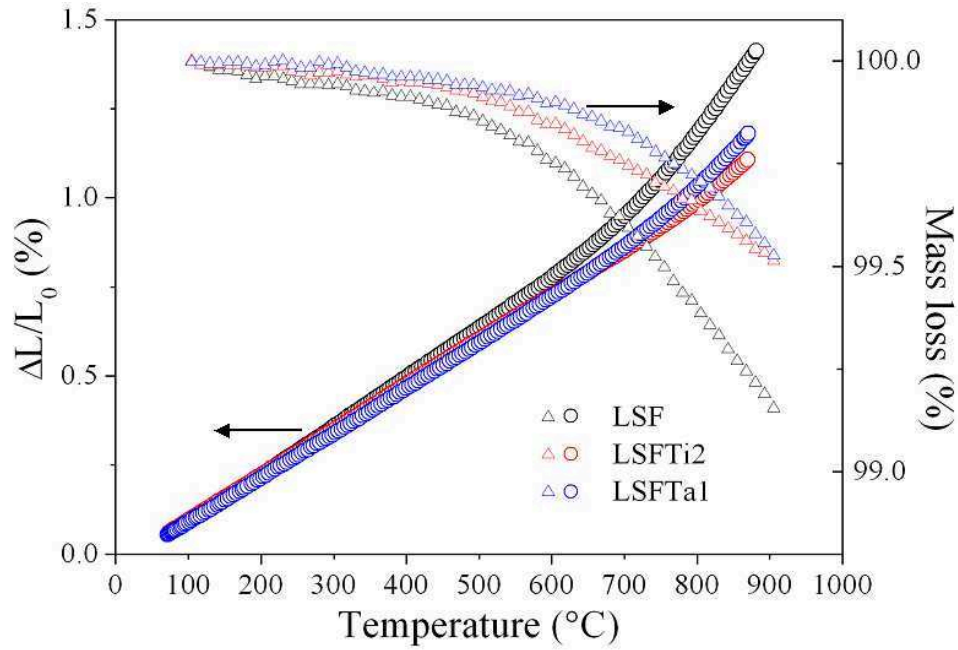
Fig. 4.18. Dilatometry and TGA curves for LSF, LSFTi2, and LSFTa1 measured in air as a function of temperature.

Table 4.5. The coefficient of thermal expansion (CTE) of LSF, LSFTi2, and LSFTa1 in lower and higher temperature regions.

Sample	T-range (°C)	CTE, $\alpha \times 10^{-6}$ (K^{-1})
LSF	120 – 680	14.0 ± 0.0
	700 – 880	26.0 ± 0.5
LSFTi2	100 – 750	12.6 ± 0.1
LSFTa1	100 – 690	12.7 ± 0.0
	710 – 890	18.4 ± 0.2

The dilatometry curves deviate from linearity around 600°C for LSF and at higher temperatures for LSFTa1 and especially for LSFTi2. The higher CTEs after these temperatures are attributed to chemically induced expansion in addition to the thermal expansion as mentioned before, which is a typical feature [52, 57] for LSF type perovskite. The CTEs are lowered with Ti and Ta substitution (Table 4.5) while the linear expansion range is shifted to higher temperatures.

According to thermal gravimetric analysis, the mass loss related to oxygen vacancy formation becomes considerable after 400°C. This temperature is lower than what is observed on dilatometry curves. However, considering the dilatometry samples are in solid form while the TGA is conducted on powders, this difference can be attributed to a slower oxygen exchange rate for the dense samples.

In order to calculate the non-stoichiometry of the materials, two TGA runs were made in air and Ar atmosphere up to 900°C until the equilibrium of the mass was achieved. The difference in the mass loss at 900°C in air and Ar were used to calculate the non-stoichiometry ($\Delta\delta$) of the materials. The non-stoichiometry ($\Delta\delta$) vs. the isothermal expansion of the materials ($\Delta l/l_0$) induced during atmosphere change from air to Ar at 900°C is shown in Fig. 4.19.
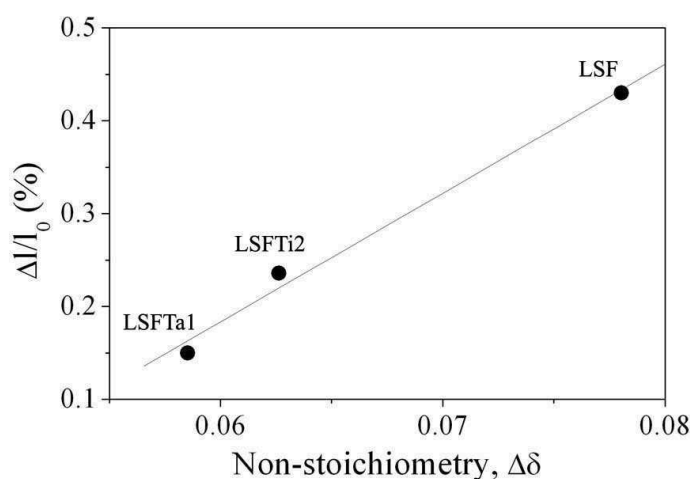
Fig. 4.19. Non-stoichiometry (δ) and isothermal expansion at 900°C from air to Ar.

The dependency shown in 4.19 suggests a linear relation between non-stoichiometry change and isothermal expansion. If each oxygen vacancy formed results in reduction of B-site cation, it will also be accompanied by a certain amount of expansion of the structure, depending on the composition of the material. The linear relation suggests that the expansion of the material per unit amount of oxygen vacancy is the same for all materials. This assumption is valid only in case of non-interacting defects. A similar linear relation was shown for LaCrO$_3$-based materials[50] over a broad range of pO$_2$. In case of LSF materials, the situation is more complex since the structure is not thermodynamically stable at highly reducing atmospheres and tend to decompose, resulting in reduction of the structure. However, according to XRD results shown in previous section, LSF, LSFTi2, and LSFTa1 were shown to be stable in Ar-atmosphere and therefore the relation holds true for the measurement conditions used in this case.

4.7. Summary and conclusions

The crystal structures of LSF, LSFTi2, and LSFTa1 were studied by x-ray diffraction using synchrotron radiation or conventional x-ray source. The structure of LSF was studied by synchrotron radiation up to 900°C with intervals of 10 K up to 450°C and 25 K

afterwards. These measurements provided high-resolution diffraction data that could be used to refine the crystal structure of the host composition. LSF was found to be hexagonal (rhombohedral) at room temperature with a slight tilting of the cubic unit cell, resulting in a rhombohedral structure. The tilting angle decreased gradually over a large temperature range (25 – 400°C); therefore the transition from rhombohedral to cubic structure is believed to take place gradually between these temperatures, may be even higher. However, the structure refinement could be done using hexagonal symmetry up to 400°C and cubic above this temperature. The material showed an increased expansion above 620°C due to oxygen loss accompanied by reduction of Fe^{4+} to Fe^{3+}, which is a larger ion.

In order to compare the crystal structure of LSFTi2 and LSFTa1 to the host material LSF, X-ray diffraction was used. All three materials were indexed as hexagonal. The crystal structure of LSF was in agreement with the results obtained from synchrotron measurements. The rhombohedral (tilting) angle, α', was slightly increased with substitution of Ti and Ta.

Moreover, all samples were heat treated under Ar-atmosphere at 850°C for 3 days and their structures were refined as cubic at room temperature. The differences in the unit cell parameters of calcined and Ar-treated samples at room temperature were related to chemical expansion. This increase in the unit cell size of LSF (from calcined to Ar treated sample) was found to be doubled compared to LSFTi2 and LSFTa1.

The crystal structures, thus stability of the LSF and LSFTa1 samples kept in highly reducing partial pressure of oxygen ($4\%H_2$ – $96\%Ar$) were checked by XRD. The rhombohedral LSF sample was decomposed to a tetragonal structure similar to $LaSrFeO_3$ with tetragonal structure and Fe in elemental form. LSFTa1 was found to have rhombohedral structure with a very small amount of second-phase formation. It was concluded that the substitution of Ta improved the chemical stability of LSF considerably.

X-ray absorption technique was used to study the electronic structure of the samples. LSFTa2 sample was included in this particular measurement to see the effect of further doping on electronic structure. Fe $2p$ and O $1s$ spectra were recorded on calcined samples, which were cooled down to room temperature in a controlled manner, and the heat-treated samples under Ar-atmosphere at 850°C for 3 days. LSF sample was found to have similar electronic structure to previously published data, which was reported to host the doped holes in O $2p$ character rather than $3d^4$. Along substitution with Ti and Ta, Fe $2p$ spectra remain more or less the same although the ratio of L_2/L_3 decreases, suggesting a decrease in the hole concentration, Fe^{4+}/Fe^{3+}. The Ar-treated samples were found to be more in Fe^{3+} state while the sample with 20% Ta basically remained the same. The O $1s$ spectra were more dependent on the composition and heat-treatment. The $e_g\uparrow$ peak, which is induced by doping (indicative of holes), was considerable higher in case of LSF and almost disappeared in case of Ar-treated samples.

Finally, TGA was used to study the non-stoichiometry of the materials in Ar at 900°C compared to room temperature states ($\Delta\delta$). The non-stoichiometry difference was dropped with Ti and Ta substitutions. A linear relation was found between $\Delta\delta$ and the chemical expansion ($\Delta l/l_0$) of the samples both measured at 900°C along the atmosphere change from air to Ar.

In conclusion, LSFTi2 and LSFTa1 showed improved properties considering the chemical stability and expansion behavior of the materials. According to the XAS measurements, the hole concentration decreases with substitution, which will cause a decrease in the electrical conductivity of the materials. Electrical conductivities of the materials will be studied in the next chapter of this thesis.

Chapter 5

Total conductivity of $La_{0.5}Sr_{0.5}Fe_{1-y}(Ti/Ta)_yO_{3-\delta}$

In this chapter of the thesis, total conductivities of LSF, LSFTi2, and LSFTa1 measured by 4-point DC conductivity technique are reported. The conductivities were studied as a function of temperature for all three compositions and as a function of partial pressure of oxygen for LSF and LSFTa1.

5.1. Introduction

It was mentioned before that one of the prerequisites of implementing perovskite dense ceramic membranes for partial oxidation is that the materials should have mixed ionic-electronic conductivity. The mixed conductivity is commonly used to denote the situation where both conductivities have similar values. However, most of the materials, especially among perovskites, found to have substantial ionic conductivities actually are predominantly electronic conductors and called mixed conductors. In this respect, the term mixed conduction is actually used more in relation to the ionic conductivity being high enough to provide necessary oxygen semi-permeability with predominant electronic conduction. However, it is known that the amount of charge carriers decreases with lowered oxygen activity and the above-mentioned situation is changed. Moreover, the electronic conduction is highly dependent on the nature of the B-site cation together with the doping elements.

Therefore in this chapter, the effect of B-site substitution on the conductivity of LSF is studied. Additionally, the conductivity behavior at very low partial pressure of oxygen is studied.

5.2. Theory

Conductivity is the measure of the ease of a material to conduct an electrical current. Basically, the conductivity of a species is the product of the concentration and the mobility of the charge carrier. Frequently, there is more than one charge carrier that contributes to the electronic conduction in a material. In such a case, partial conductivity for each charged particle is defined as:

$$\sigma_i = \mu_i n_i z_i e \tag{5.1}$$

where μ_i is the mobility of the species i, n is the number of charged particles per unit volume, z is the valence, and e is the electronic charge, where the product ($n_i z_i e$) is the charge density . Therefore, when the effects of variables on the conductivity are considered, such as composition, structure and temperature, then the influence on two properties, mobility and concentration, need to be addressed. The total conductivity is the sum of the partial conductivities:[69]

$$\sigma = \sigma_1 + \sigma_2 + \sigma_3 + ... \tag{5.2}$$

An important parameter is the transference number, which is the fraction of the partial conductivity of a charge carrier compared to total conductivity, $t_i = \sigma_i/\sigma$.

In case of LSF-based materials, the total conductivity is the sum of the oxygen ionic (σ_i) and electronic (σ_e) conductivities.

The general properties of materials considering the mobile electronic charge carriers can be described using the electron energy band structure. The electrons occupy atomic orbitals as explained in the previous chapter and form discrete energy levels, which can be considered continuous in case of large number of atoms. There are generally some energy levels containing no orbitals and these result in band gaps. In very simple terms, valence and conduction bands are formed by the occupied and the unoccupied bands, respectively. The size of the band gap becomes the key to tag the material as metal conductor (overlapped valence and conduction bands or semi filled conduction band), semi conductor (small band gap < 3 eV), or insulator (large band gap > 3 eV).[92]

Temperature dependence of conductivity

The Arrhenius equation for conductivity (σ) can be written as follows:

$$\sigma = \frac{A}{T} \exp\left(-\frac{E_a}{kT}\right) \tag{5.3}$$

where A is the pre-exponential constant, T is the temperature (in K), E_a is the activation energy, and k is the Boltzman constant.[93] The activation energy of the samples are calculated from the slope of the $\ln(\sigma.T)$ versus $1/T$ plots.

Conductivity in perovskite materials

The electronic conduction in the region I in Fig. 2.3 occurs by small polaron hopping mechanism with a thermally activated mobility,[94] between Fe^{4+} and Fe^{3+} cations, while it changes to Fe^{3+} and Fe^{2+} at low pO_2 (region III). The electronic conduction in the p-type region can be illustrated as:

$$Fe^{4+}–O^{2}–Fe^{3+} \longrightarrow Fe^{3+}–O^{2-}–Fe^{3+} \longrightarrow Fe^{3+}–O^{2-}–Fe^{4+}$$
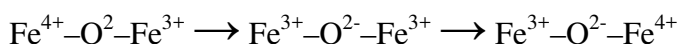
The hopping of mobile charge carriers between neighboring Fe cations occurs via O 2p orbital since the overlap of d orbitals is small and there is a strong overlap of e_g and t_{2g} orbitals with the filled O 2p orbitals. In the region I, the concentrations of $[Fe_{Fe}^{\bullet}]$ (Fe^{4+}) and $[Fe_{Fe}^{x}]$ (Fe^{3+}) can be written as follows,

$$\left[Fe_{Fe}^{\bullet}\right] = x - 2\delta \text{ and } \left[Fe_{Fe}^{X}\right] = 1 - x + 2\delta \tag{5.4}$$

The conductivity in this region is p-type due to Fe^{4+} and therefore depends on the concentration of Fe^{4+}. The concentration of Fe^{4+}, $[Fe_{Fe}^{\bullet}]$, in terms of partial pressure of oxygen can be derived as Eq. 5.5 using equations 2.4 and 2.8.

$$\left[Fe_{Fe}^{\bullet}\right] = \frac{\sqrt{(K_{ox}\delta)}(1 - x + 2\delta)pO_2^{1/4}}{\sqrt{(3 - \delta)}} \tag{5.5}$$

From equation 5.1 we know that the conductivity is proportional to the concentration of the charged particles. Therefore, in the p-type conductivity region, electrical conductivity is proportional to $[Fe_{Fe}^{\bullet}]$ and thus to $pO_2^{1/4}$ through Eq. 5.4. Similar equations can be written for the n-type region (region III), where the main defects are $[V_O^{\bullet\bullet}]$ and $[Fe_{Fe}']$. Then the conductivity is found to be proportional to oxygen partial pressure by $pO_2^{-\frac{1}{4}}$. This relation holds of course as long as the perovskite structure is stable at the considered pO_2 regions.

Similar approaches were found to be useful for modeling of the conductivity data of $(La,Sr)FeO_3$-based perovskite materials using the stoichiometry data (i.e. defect concentrations) in the temperature ranges 750 - 1000°C and pO_2 of 10^{-19} - 0.21 atm.[95, 96] Yaremchenko et al.[96] conducted a modeling study on $La_{0.3}Sr_{0.7}Fe_{0.8}Al_{0.2}O_{3-\delta}$ for total conductivity (σ) using the following equation. The fitting results are shown in Fig. 5.1.

$$\sigma = \sigma_i + \sigma_p^0 \times pO_2^{1/4} + \sigma_n^0 \times pO_2^{-1/4} \tag{5.6}$$
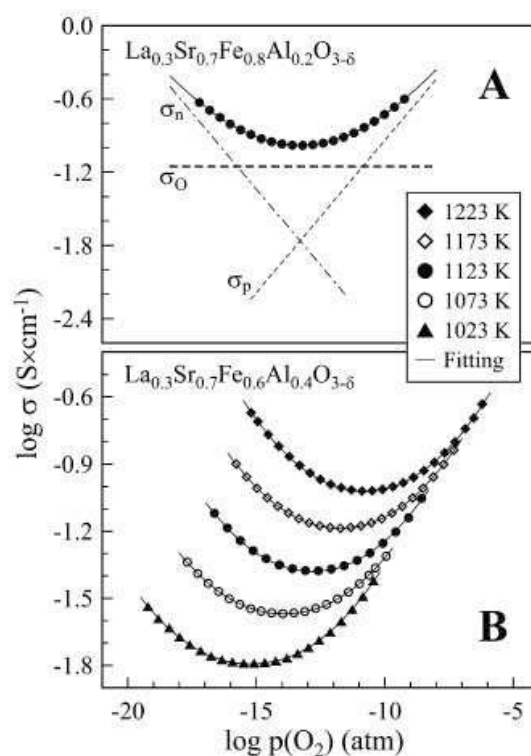
Fig. 5.1. The conductivity of $La_{0.3}Sr_{0.7}Fe_{0.8}Al_{0.2}O_{3-\delta}$ as a function of pO_2 reported by Yaremchemko et al.[96]

In Fig. 5.1 A, the separate contributions of p-type, n-type, and ionic, σ_i, (denoted as σ_0 in the figure) conductivities were plotted. A constant ionic conduction is given in the figure although it varies depending on pO_2 due the change in oxygen vacancy concentration and their association as mentioned by the author as well.[96] The fit using the equation 5.5 was in agreement with the experimental data under reducing conditions. However, under oxidizing conditions where pO_2 is $10^{-5} - 0.5$ atm, the n-type electronic transport is negligible and the power of pO_2 deviates from ¼.[96]

A common problem noted by several authors was the slow equilibration kinetics in the intermediate pressure range.[95-97] The pO_2 range for slow kinetics depends on the measurement temperature, however, generally starts below 10^{-5} atm and goes down to 10^{-12} at 750°C. In the slow equilibration region, meaningful results could be obtained when necessarily long equilibration times were allowed and it was attributed to either short-range order of oxygen vacancies or phase separation between a perovskite phase and a vacancy ordered phase.[98]

The conductivity in the materials under consideration is reckoned to be mainly electronic (p-type) since the ionic conduction is very low.[51] As a result of a study on $(La,Sr)(Co,Fe)O_{3-\delta}$ materials, electronic and ionic conductivities were found to be in the range of 100–1000 S/cm and 0.01-1 S/cm, respectively.[30] These values correspond to the ionic transference numbers around $10^{-4}–10^{-2}$.

In the defect chemical analysis of electronic conductivity of $La_{0.4}Sr_{0.6}FeO_{3-\delta}$ by Bucher and Sitte[99], it was found that the modeling of the oxygen nonstoichiometry dependency of electronic conductivity (σ) failed when σ was related to the site (charge carrier) fractions or when a charge carrier mobility as a function of available sites was introduced. Therefore, it was concluded that the mobility of charge carriers is additionally affected by the fraction of oxygen vacancies.[99]

$La_{0.5}Sr_{0.5}FeO_{3-\delta}$ material was reported to be the optimum composition in $La_{1-x}Sr_xFeO_3$ series considering electronic conductivity since Fe^{4+}/Fe^{3+} ratio is close to 1.[100] A similar result was shown by Patrakeev et al.[59] and further doping (x > 0.5) was reported to deteriorate the conductivity rather because of development of oxygen vacancy ordering. The conductivity was found to decrease further with B-site substitution by Ga[101] and Al[96] but aluminum substitution was noted to be less favorable with respect to gallium in terms of oxygen ionic transport. On the other hand, the electronic conductivity was reported to be enhanced by substitution of B-site cation by less redox stable cations such as Co.[93]

5.3. Experimental

4-probe total conductivity measurements

The total conductivity of the samples was investigated as a function of temperature by 4-point DC technique using a Milli-Ohmmeter RESISTOMAT 2318 (Burster Praezisionsmesstechnik GmbH & Co KG, Germany). The tests were conducted on bars with dimensions of about 3×4×25mm, which were prepared as explained in Section 3.2.1. The bars were painted on both ends with Pt-paste (CL11-5100, W. C. Heraeus GmbH & Co. KG, Germany) and contacted by attaching Pt-wires around the bars, approximately 15mm away from each other. The specimens were heated up to 900°C by 5K/min with dwell times (30 – 180 min) approximately every 100K to obtain the equilibrium conductivity values. In addition to the heating program with ramps every 100 K, first a continuous heating and cooling program was used with a heating and cooling rate of 1 K/min.

Fig. 5.2. 4-probe electrical conductivity setup taken from Ref.[102]

The total conductivity of the samples were calculated from:

$$\sigma = \frac{l}{RA} \tag{5.7}$$

where l is the distance between the voltage leads, R is the measured resistance, which is I/V (I: applied current, V: measured voltage), and A is the cross-section area of the measured sample.

The atmosphere for the conductivity measurements was adjusted using mass-flow controllers (Voegtlin Instruments, Switzerland) and gas mixture of N_2, Ar, O_2, and 4%H_2-96%N_2 mixture. Oxygen partial pressure was measured by a Rapidox 2100 Oxygen Analyzer (Cambridge Sensotec Limited, England).

5.4. Total conductivity of La$_{0.5}$Sr$_{0.5}$Fe$_{1-y}$(Ti/Ta)$_y$O$_{3-\delta}$

Fig. 5.3. shows the total conductivity of LSF as a function of temperature. The conductivity was measured by 4-point DC technique with continuous heating ramp of 1 K/min up to ~900°C and kept at this temperature for two hours before cooling down to room temperature with 1 K/min. Three consecutive runs of this measurement are shown in the figure. The first run is shown with black circles, while the second and third runs are shown with red and blue circles, respectively.
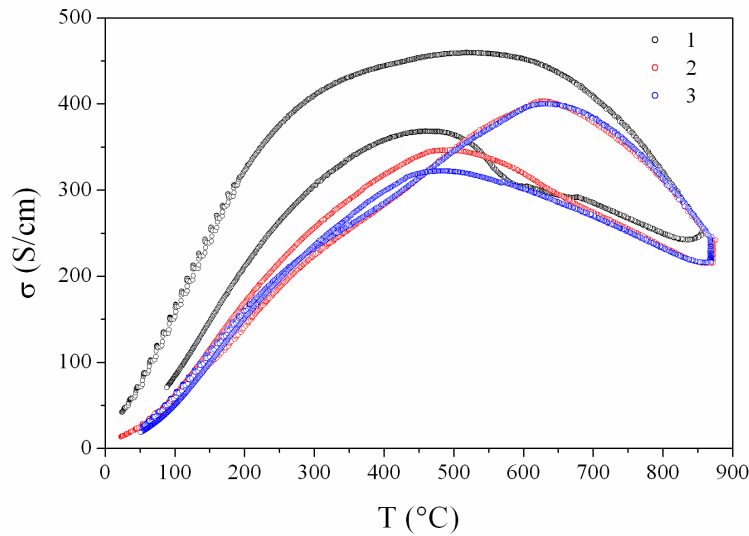
Fig. 5.3. Total DC conductivity of LSF as a function of temperature measured three times consecutively.

The material shows semiconductor behavior up to a certain temperature after which the conductivity starts to decrease as seen in Fig. 5.3. Additionally, a large hysteresis was seen on measurements. The conductivity decreased in the second and third runs. Further measurements conducted with the same temperature program showed similar curves to the third run.

The decrease in the conductivity at elevated temperatures is related to the decrease of carrier concentration as a result of reduction of B-site cation due to oxygen vacancy formation [93]. As a result, the electronic transport, which occurs via Fe^{4+}-O- Fe^{3+} bonds when thermally activated, is partially blocked.

As mentioned above, the conductivity measured during cooling was much lower than the heating values at temperatures higher than 450°C (hysteresis). The rate of oxygen uptake during cooling was slower compared to oxygen loss during heating. In addition, there was additional oxygen vacancies formed during the isotherm at the peak temperature that resulted in the increased amount of hysteresis. Therefore, necessary equilibration time has to be allowed during the measurement (slower than 1 K/min in this case), otherwise the results reflect an undefined state of the material and does not have scientific relevance.

An interesting feature seen in Fig. 5.3 is the change in the slope of the third curve around 220°C. There are clearly two linear regions, one starting at 100°C and continues up to 220°C and the other one up to the temperature where the conductivity starts to decrease. The temperature for the slope change in Fig. 5.3 coincides well with the temperature at which a deviation was seen in the unit cell size of the LSF material, as shown in the previous chapter in Fig. 4.10. There was no clear explanation for the deviation of the unit cell parameter since there was no big change in the crystal structure except the increase in the unit cell size.

Assuming that the conductivity measurements up to 400°C were reproducible and thus belongs to equilibrium state, the slight structural change may have an effect on the electronic conductivity. Further analyses are required to clear this subject.

Following the equation 5.4, the Arrhenius plots of total conductivities of LSF, LSFTi2, and LSFTa1 are shown in Fig. 5.4 as log σT (Scm^{-1}K) vs. 1000/T (1/K) plots. LSF, LSFTi2, and LSFTa1 are denoted by black, red, and blue symbols, respectively.
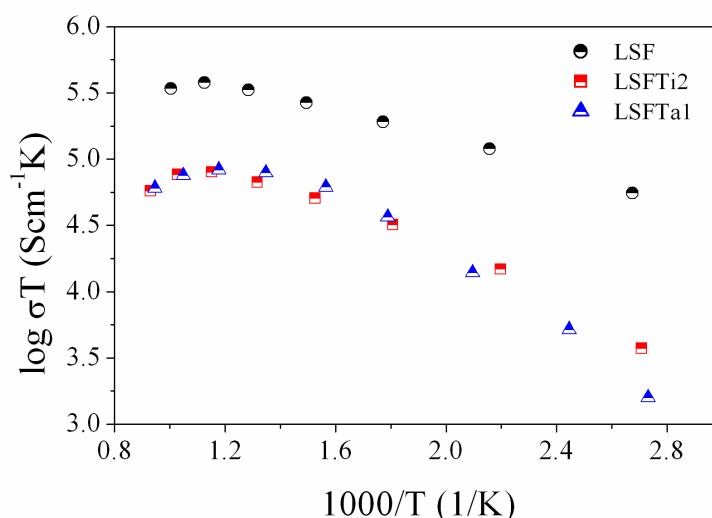
Fig. 5.4. The Arrhenius plots of total conductivities of LSF, LSFTi2, and LSFTa1.

All three samples show a maximum around 600°C followed by a decrease in the conductivity. The log (σT) vs. 1/T relation shown in Fig. 5.4 would be linear following the equation 5.4 if the carrier concentration was constant. As explained previously, the carrier concentration varies with temperature in case of LSF materials and therefore the pre-exponential constant becomes a function of it. Stevenson et al.[93] modified the Arrhenius equation by inserting the non-stoichiometry as a variable into the pre-exponential term and in this way, they could model the conductivity as a function of temperature using the non-stoichiometry data measured by TGA.

Substitution of Ti and Ta lowers the Fe^{4+}/Fe^{3+} ratio (in addition to the lowered Fe concentration) resulting in reduced electronic conductivity. It is observed that the substitution of 20% Ti^{4+} and 10% Ta^{5+} show a similar effect on the conductivity. The activation energy increases with Ti and Ta-substitutions and the total conductivity of LSF decreases to one forth with 20% Ti or 10% Ta on the B-site. The activation energy (E_a) changes as a function of temperature. In the lower temperature range E_a is 0.044, 0.053, and 0.107 eV for LSF, LSFTi2, and LSFTa1, respectively, which are in the same range with similar perovskite (La,Sr)FeO$_3$-based materials [93].

Fig. 5.5 illustrates the total conductivities of LSF and LSFTa1 measured as a function of pO_2 at 900°C. Open circles show the conductivity of $La_{0.5}Sr_{0.5}FeO_{3-\delta}$ reported in literature.[59] As explained previously in the theory part of this chapter (5.2) these materials are expected to be proportional to $pO_2^{1/4}$, followed by a minimum of conductivity. The ¼ line is shown as a guideline with red dashed line. The blue line is shown as the estimation of the continuation of the conductivity of LSFTa1 following the ¼ line and the estimated minima is shown with blue dashed line.
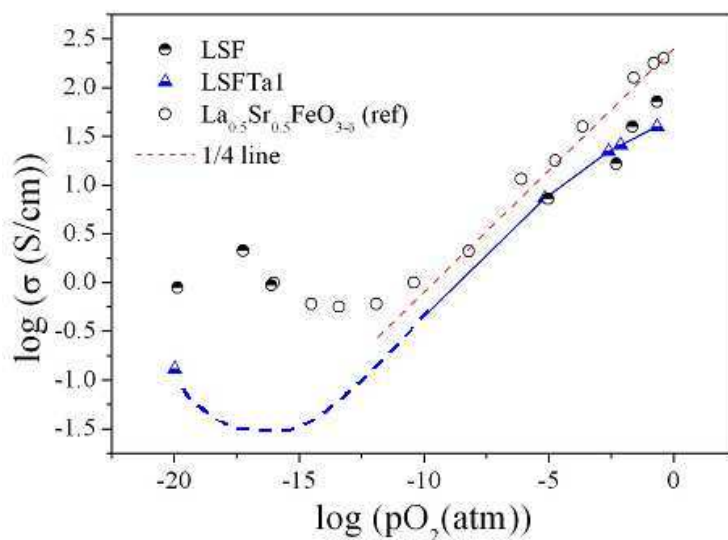
Fig. 5.5. Total conductivity of LSF and LSFTa1 measured at 900°C as a function of pO_2 and conductivity values of $La_{0.5}Sr_{0.5}FeO_{3-\delta}$ taken from Ref.[59]

The conductivities of LSF and LSFTa1 were measured under air/Ar and Ar/H$_2$ mixtures; therefore the data in the intermediate pO_2 was not achievable. The intermediate regions are assumed to be following a similar trend ($pO_2^{1/4}$ dependency followed by a minima) to the reported data. The conductivity of LSF at higher pO_2 is lower than the values reported by Patrakeev et al. [59], which is also shown in Fig. 5.5. It shows linear dependence to $pO_2^{1/4}$ down to pO_2 values where a minima is seen, after which electron-like charge carrier contribution dominates (n-type).[59] At this region, the conductivity is proportional to $pO_2^{-1/4}$. In the work of Patrakeev et al., the conductivity changes around the minima was found to be smoother than expected from a conduction behavior with hole and electron contributions. This was taken as an indication for an additional ionic contribution.[59] The individual contributions of electronic and ionic conductivity were shown in Fig. 5.1, which was taken from the Ref.[96]

The estimated minimum in conductivity of LSF fits in a similar pO_2 value to the reference data shown in Fig. 5.5 and is shifted to lower pO_2 with Ta-addition. The conductivity of LSFTa1 is in a similar range with LSF in the higher pO_2 region although is

lower in air. However, it seems to be considerably lower (more than an order of magnitude) at lower pO_2. Note that, there is actually only one data point at low pO_2 for LSFTa1 but it is reasonable to consider it as a continuation of the increase after the minima due to the fact that the material was found to have a perovskite structure after this measurement as reported in the previous chapter. Therefore, the difference in the conductivity at minima of LSF and LSFTa1 can be attributed to the difference in the ionic conductivity contribution.

The conductivity of LSF shows degradation following the increase in the so-called n-type conductivity region. This is caused by the decomposition of the material under these conditions as proven by XRD results shown in section 4.4. The LSF sample was found to have a tetragonal structure (I4/mmm) similar to $SrLaFeO_4$ (JCPDS 01-071-1744) together with Fe in the metal state (indicated with (*) in Figure 4.13). However, LSFTa1 material was found to be more stable maintaining the perovskite structure with a small amount of second phase formed.

5.5. Summary and conclusions

Electronic conductivity of LSF, LSFTi2, and LSFTa1 were studied by 4-probe dc conductivity measurements as a function of temperature. The measurements conducted on LSF with continuous heating and cooling ramps (1 K/min) showed strong hysteresis at temperatures higher than 450°C in addition to the overall decrease in the conductivity after the second run. All the materials showed a maximum after which the conductivity decreased related to an increase in the oxygen nonstoichiometry introduced to the samples at higher temperatures. Substitution of Ti and Ta resulted in substantial decrease in the total conductivity of LSF due to the decrease in the carrier concentration (Fe^{4+}).

The conductivities of the LSF and LSFTa1 materials were measured as a function of partial pressure of oxygen under O_2/Ar and Ar/4%H_2 mixtures. Assuming that the conductivity was proportional to $pO_2^{1/4}$ and $pO_2^{-1/4}$ in the p-type and n-type regions, it was possible to estimate the minima where ionic conductivity prevails. The minimum was moved to lower pO_2 with substitution of Ta in addition to the decreased conductivity. A decrease in the conductivity of LSF was observed in the electronic charge carrier dominated region due to phase decomposition at pO_2 below 10^{-17} atm. The XRD measurements conducted on the conductivity samples showed that the LSF material was decomposed to a main tetragonal phase similar to $LaSrFeO_4$ and Fe in elemental form. LSFTa1 material, on the other hand, was found to sustain the perovskite structure with a small amount of second-phase formation.

Chapter 6

Mechanical Properties of $La_{0.5}Sr_{0.5}Fe_{1-y}(Ti/Ta)_yO_{3-\delta}$ Materials

In this chapter, the techniques used for measuring the mechanical properties are explained. Young's modulus measured by impulse excitation technique, 4-point bending strength, and fracture toughness measured by single-edge-V-notched beam method are reported. The failure mechanism of the fractured surfaces is discussed by means of fractography using SEM.

6.1. Introduction

In the general introduction and motivation part of this thesis, the reader was introduced to the fact that the membrane material should be able to meet a number of requirements including a certain amount of oxygen flux, both thermodynamic and structural stabilities, and of course the comparable cost to the existing oxygen production technologies. The importance of the stability, considering structure and expansion (thermal and isothermal) behaviors, of the considered $La_{0.5}Sr_{0.5}FeO_{3-\delta}$ membrane materials has already been discussed in previous chapters. It was shown that 10-20 % substitution of Fe with a redox stable cation improves the expansion behavior and chemical stability under reducing conditions. Therefore, it is at this point important to explore the corresponding effects of B-site substitution also on the mechanical properties of these materials.

The sources of stress in an oxygen separation membrane can be summarized as temperature gradients in the material, oxygen activity gradients, differential thermal expansion coefficients (membrane and sealing), and external mechanical loading. The magnitude of the stress depends on the material properties, the operating conditions and the geometry of the design. For such an application as implementation of oxygen separation from air into partial oxidation of hydrocarbons, requiring high-temperature and varying conditions, mechanical properties of the material becomes very important so that the reliability can be estimated. Therefore, it is the aim of this chapter to provide an understanding of mechanical properties, such as Young's modulus, fracture strength, and fracture toughness, and determine the effect of B-site compositional changes on the mentioned mechanical properties.

6.2. Theory

Mechanical properties are not only critical for structural ceramics but also in functional ceramic applications depending on the design and the conditions used. Mechanical properties are often the limiting criteria in several applications due to the fact that the materials do not exhibit plastic deformation. Most ceramics undergo mainly elastic deformation and fail suddenly before the plastic deformation. However in some cases plastic deformation is possible at high temperatures with thermally activated dislocation motion (creep). Elastic properties depend basically on the chemical bonding that determines the stiffness of the atomic bonds. The ionic and/or covalent bonding in ceramics provides high compressive strength. However, they are brittle due to their inability to accommodate strains. The complex structure of ceramic materials compared to metals, in other words, loss of symmetry in crystal structure is mainly responsible for their brittleness.[103] The compressive

strength of ceramics is much higher than their tensile strength while flexural strength is in between and often used for reporting their mechanical properties.

Young's modulus (E) or elastic moduli in other words, is a materials property that corresponds to uniformly increasing the separation between the atoms and therefore, to the forces between atoms and the structure energy. The relation shows similarity with thermal expansion coefficient and lattice energy. Crystals with high elastic modulus often have low thermal expansion coefficients.[69]

Fracture toughness (K_{Ic}) is an indication of the amount of stress required to propagate an already existing crack in the material. K is actually called the stress intensity factor. "Ic" in the subscript denotes the "mode I crack", where "mode I" is the condition that the crack plane is normal to the direction of the tensile stress. If the fracture toughness of a material is known, at a given stress the size of the flaw it can tolerate can be calculated or the critical flaw size can be calculated from the other two values in accordance with the Griffith equation as will be shown later. Strength is a property dependent on the material properties and the flaw size and distribution in the material. However, the fracture toughness is a material property and therefore it is very important for designing an application. If the fracture toughness of a material can be increased with a mechanism (such as crack tip interactions and shielding), it means that the reliability of the brittle material can be increased.

6.2.1. Elastic deformation and Hooke's Law

According to Hooke's law, up to the proportional limit, stress is directly proportional to the strain:

$$\sigma = E\varepsilon \qquad (6.1)$$

where σ is the stress, E is the Young's modulus, which represents a material constant for a uniaxial tensile deformation, and ε is the strain.

The same can be written for shear stress (τ), shear strain (γ), and shear modulus (G). When a material extends, the cross-section decreases. The ratio of decrease in cross-section to the increase in length is called the Poisson's ratio (μ) and relates E and G ($\mu = E/2G-1$ for isotropic materials). Poisson's ratio is found to be between 0.2 and 0.3 for most materials in elastic deformation range.[69] This has been a simplified version of Hooke's law where stress and strain are given as scalars, i.e. zero-order tensors. However in reality, stress and strain are both second-order tensors, defined by 9 components each. This gives:

$$\sigma_{ij} = E_{ijkl}\varepsilon_{kl} \text{ or in a simplified form: } \sigma_i = E_{ij}\varepsilon_j \qquad (6.2)$$

where i and j take values from 1 to 6.

In case of polycrystalline ceramics, the random array of crystals forms an elastically isotropic material; therefore, only two elastic constants (E_{11} and E_{12}) are needed for describing a linear elastic deformation. A ceramic is expected to obey the Hooke's Law over a range, in reality however, there are often deviations. E in polycrystalline ceramic materials is generally in the range of 100-500 GPa, and the fracture stress, σ_f, is in the range 70-1000 MPa.

All materials exhibit lower strengths than theoretical strengths due to the presence of defects, which serve as a concentration point for stress. Ceramics, which have brittle nature, acquire their strength mostly from their atomic bonding whereas in case of metals; there are additional factors such as interactions of dislocations with defects. Adjusting the composition as well as the microstructure can alter the elastic behavior of a material.

The way a material is processed is very important for its mechanical behavior. Microstructural imperfections are the main reason for the failure. Therefore, it is necessary to identify the origin of the failure so that the processing can be improved if necessary.

6.2.2. Effects of porosity and microcracking on elastic constants

Porosity is one of the defects introduced to the material during processing. It decreases the elastic modulus because the load-bearing area is reduced and the stress concentrates near the pores. A relation for porosity was suggested for materials with small amount of pores as shown below: [104]

$$E = E_0 \left(1 - Ap + Bp^2\right) \tag{6.3}$$

where E_0 is the Young's modulus for the dense material, p is the porosity fraction, A and B are constants, 1.9 and 0.9, respectively. Another model suggested by Ramakrishna and Arunachalam[105] is given equations 6.4-6.6 as follows:

$$E = E \frac{(1-p)^2}{(1+b_E p)} \tag{6.4}$$

$$b_E = 2 - 3\nu_0 \tag{6.5}$$

The porosity dependence of materials was found to be well fitted by these equations in most cases.[106]

The shape of the pores is not considered in this case. There are solutions considering the shape, however the difficulty in reality is that the pores do not generally have a specific geometry.

Microcracks form a small amount of porosity and they can lead to substantial reduction in elastic constants. Anisotropy in thermal expansion and phase changes in the material are common reasons for microcracking. When the elastic-constants are extremely low, this may be taken as a sign for microcrack formation in the material.

In the presence of a crack, a failure criterion can be given by the Griffith equation as shown below: [104]

$$\sigma_f = \sqrt{\left(\frac{2E\gamma}{\pi c}\right)} \qquad (6.6)$$

According to this equation, the fracture stress (σ_f) depends on the material parameters, Young's modulus (E), thermodynamic surface energy (γ), and the half of the crack length, c.

6.2.3. Literature review on the mechanical properties of perovskite materials

Most of the literature available on mechanical properties of perovskite materials is reported for room temperature measurements. Alkaline earth substituted La-based perovskites with Co, Mn, Cr, Ga on the B-site are reported to have fracture strengths in the range of 100-160 MPa with the corresponding fracture toughness values in the range of 1.3-2.8.[107-111]

One of the end members of $La_{1-x}Sr_xFeO_{3-\delta}$ perovskites, $LaFeO_3$, is ferroelastic (exhibits spontaneous strain) and it has orthorhombic structure from room temperature to around 1000°C, where it transforms to rhombohedral structure.[112] Compared to some other perovskites, it has a higher room temperature fracture strength, which is around 202 MPa and increases up to 235 MPa at 800°C. The fracture toughness of $LaFeO_3$ was reported to be 2.5 MPa.m$^{1/2}$ at RT, decreasing to 2.1 at 600°C followed by an increase to 3.1 MPa.m$^{1/2}$ at 800°C.[113] This was found to be correlated to the crystallographic strain, as explained by Abrahams[114]. As a general trend found in the literature, orthorhombic perovskites seem to have higher fracture toughness compared to rhombohedral or cubic ones.[108, 113, 115] The fracture strength of rhombohedral and cubic perovskites tend to decrease with increasing temperature while fracture toughness remains constant or decreases with temperature.[108, 111, 115, 116] However, an opposite trend was reported for lanthanum strontium manganite perovskites with rhombohedral structure. The flexural strength measured by 4-point bending tests showed increase with increasing temperature.[117]

Another important material property, Young's modulus of the mentioned materials is reported in the range 120-200 GPa.[109, 117, 118] Chou et al. studied the room temperature mechanical properties of $La_{1-x}Sr_xFe_{0.8}Cr_{0.2}O_3$ where x ranged from 0.2 to 0.8.[118] They reported elastic moduli in the range of 128-192 GPa and the material with the highest Sr-content was found to have the lowest modulus. In addition, the materials with high Sr showed extensive cracking and had lower indentation toughness.

The work of Orlovskaya et al. on Sr-doped $LaCoO_3$ perovskites showed that the fracture strength of a 90% dense sample was increased from 76 MPa to 150 MPa when the density was improved to 99%.[111] The strength of the less dense sample was found relatively independent of temperature, while the strength of the dense sample decreased linearly up to 850°C.

In a work by Montross[108], the Young's modulus was found to correspond to the changes in the Cr_{3+} to O_{2-} average interatomic distance found by Rietveld fitting of the XRD data. Young's modulus increased with increasing Cr-O interatomic distance.

Orlovskaya et al. reported on deformation behavior of $La_{0.6}Sr_{0.4}FeO_3$ which also has rhombohedral structure at room temperature.[119] This material was discovered to show inelastic deformation behavior during compression testing. The material showed hysteresis during cycling of the load. The behavior was found similar to the ferroelastic deformation of lead zirconate titanate or $LaCoO_3$ materials with the difference that $La_{0.6}Sr_{0.4}FeO_3$ material did not show domain/twin structure. Therefore, the reason of inelastic behavior was thought to be either because of possible phase transition during compression test, or because of dislocation motion since a lot of dislocations were observed in the material by TEM investigations.[119]

Lein et al.[120] studied the mechanical properties of $La_{0.5}Sr_{0.5}Fe_{1-x}Co_xO_{3-\delta}$, with x = 0.5, 0.75, and 1. The Young's moduli were found to be 130 – 133 GPa. Non-linear stress-strain behavior observed was attributed to ferroelasticity. The 4-point bending strength and the fracture toughness were 107 – 128 MPa and 1.16 MPa.m$^{1/2}$, respectively. The fracture mode changed from transgranular at low temperature to intergranular at high temperatures.

Up to the author's best knowledge, there is no available literature on mechanical properties of B-site substituted $La_{0.5}Sr_{0.5}FeO_{3-\delta}$. It is believed that the knowledge of mechanical properties of this materials and especially the effect of B-site substitution is essential to help understand and improve the stability of membranes.

6.3. Experimental

6.3.1. Impulse excitation method for determination of elastic moduli at room temperature

The impulse excitation method is a non-destructive testing method based on measuring the natural frequency of vibration of materials. The test piece is tapped slightly causing it to vibrate at its natural frequencies and a microphone or a piezoelectric transducer measures the frequency. The sample can vibrate in different modes (flexural, torsional, and longitudinal) simultaneously, however, it is supported and tapped in such a way that only one mode is measured.

The setup used in this work is shown in Fig. 6.2. The supports are put 0.224×L away from the ends, where L is the total length of the sample. In this setup for measuring the flexural frequency, both the transducer and the point of impact are located at the antinodes of the standing wave; therefore the positions of impact and detector can be changed to the end of the sample. The piezoelectric transducer is connected to an amplifier and a frequency analyzer. Prior to the measurements, the equipment is checked if it works properly by measuring an alumina reference sample. The test piece is required to be parallel-faced. Further details can be found in the CEN standard.[121]
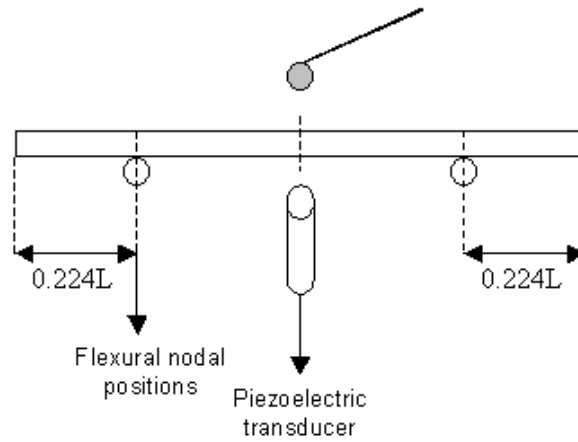

Fig. 6.2. The configuration of impulse excitation technique to measure Young's modulus, Ey.

The Young's modulus of the test piece is calculated from[122]:

$$E = 0.946 \frac{mf^2 l^3}{wt^3}\left(1 + 6.585\frac{t^2}{l^2}\right) \qquad (6.7)$$

where E is dynamic Young's modulus (GPa), m is the mass of the test piece (g), w is the width perpendicular to flexural mode vibration (mm), t is the thickness in the direction of flexural vibration (mm), l is the length of the test piece (mm), and f is the fundamental frequency of flexural vibration (kHz).

The accuracy of the method depends on the precision of the preparation of the test pieces and quality of the test equipment. An accuracy of ± 1% is reported for Young's modulus if the requirements for sample preparation are met.[121]

In this work, Young's modulus, E, for all samples was measured using a Grindo-Sonic Mk5 Industrial (Lemmens, Germany). Five samples from each composition were measured.

6.3.2. 4-point bending for determination of flexural strength and fracture toughness

Bending test is a common method for the determination of strength of a ceramic component. The loading configuration can be three- or four-point bending. Four point bending test is a procedure where the test piece is supported near the ends and loaded equally at two symmetrical points from the center of the rectangular bar.[123] The picture of the bending apparatus used in this work (USM, Zwick Z005, Germany) is shown below in Fig. 6.3. In the apparatus used in this study, the roller bearers were 20 and 36 mm away from each other. Four-point is often preferred since the specimen has a larger surface area under the maximum stress, which is also free of shear stresses. The corners of the test pieces are chamfered to minimize the failure from the defects at the corner.
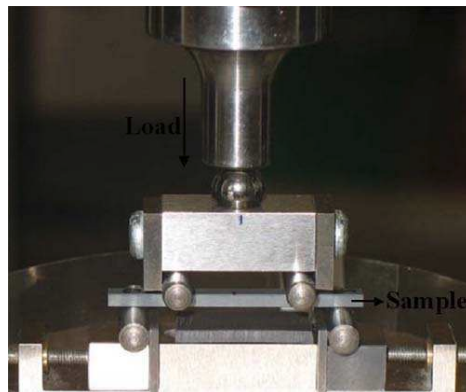

Fig. 6.3. 4-point bending testing apparatus.

The load is applied with a constant rate and the peak load at failure occurs is recorded. The rate of the loading is adjusted so that the fracture occurs within 5 to 15 s so that the possible sub critical crack growth is minimized. A crosshead displacement speed of 0.2

mm/min was used for this study. The maximum nominal stress at which the sample fails is calculated from the maximum load applied, assuming a linear stress-strain behavior (Hookean) applies. The four-point flexural strength (σ_f) is calculated from following equation:

$$\sigma_f = \frac{3F_{max}(d_{or} - d_{ir})}{2wt^2}$$

(6.8)

where:

σ_f : the fracture strength (MPa)

d_{or} : the distance between the outer rollers

d_{ir} : the distance between the inner rollers

F_{max} : the peak force at fracture (N)

w : the width of the test piece in mm (the mean of three measurements)

t : the thickness of the test piece in mm (the mean of three measurements)

The measured bending (or flexural) strength of materials is affected by many factors depending on the microstructure of the test piece. These factors include homogeneity, surface structure, dimensions and tolerances, and humidity. Therefore it is important to follow certain guidelines in preparation of the test pieces.[123] The origin of fracture in a bending test can provide valuable information about the nature and the position of the defects in the materials. Therefore, fractography is used for interpretation of fracture surfaces after bending tests. There are guidelines for carrying out fractographic investigations, e.g. by the European Committee for Standardisation[124] or others[125].

Due to the high deviation in four-point bending strength due to the presence of different defect sizes, it is desirable to use as many samples as possible. 10 samples are desirable for an average strength value for the more reproducible results and 30 samples for Weibull statistics so that the information on defect size distribution can be obtained.

In this study, 4-point bending measurements were conducted on 11 LSF, 10 LSFTi2, and 5 LSFTa1 samples due to availability of the samples.

6.3.3.   Single-edge-V-notched   beam   (SEVNB)   method   for determination of fracture toughness

The fracture toughness of the materials with the single-edge-V-notched beam (SEVNB) method[126] is measured at room temperature in four-point bending apparatus as explained in the previous section. A crosshead displacement speed of 0.3 mm/min was used

for the tests. V-notches were introduced into the test bars in the center of each specimen's surface, which had the smallest width. The V-notches are produced in a specifically constructed notching machine, first by cutting a 0.6mm deep notch with a razor blade and then polishing a V-shaped deeper notch further down with a diamond saw sprinkled with diamond paste. The geometry of the V-notch with approximate dimensions is shown in Fig. 6.4.
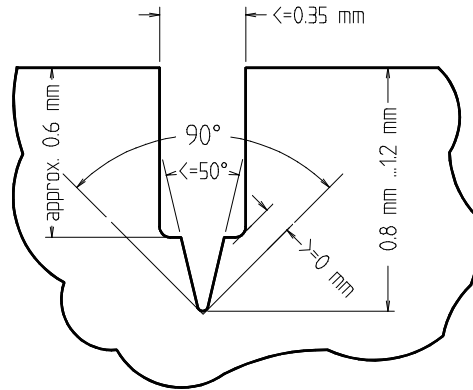

Fig. 6.4. Schematic of V-notch geometry taken from Ref.[126]

The fracture toughness (K_{Ic}) is calculated from the following equations:

$$K_{Ic} = \frac{F_{max}}{w\sqrt{t}} Y \tag{6.9}$$

$$Y = \frac{d_{or} - d_{ir}}{t} \frac{3\sqrt{\varepsilon}}{2(1-\varepsilon)^{3/2}} \left[1.9887 - 1.326\varepsilon - \frac{(3.49 - 0.68\varepsilon + 1.35\varepsilon^2)\varepsilon(1-\varepsilon)}{(1+\varepsilon)^2} \right] \tag{6.10}$$

$$\varepsilon = \frac{a}{t} \tag{6.11}$$

where:

F_{max} : the peak force at fracture expressed in N

w, t : the width and the height of the test piece in mm, respectively

a : notch depth in mm

d_{or}, d_{ir}: outer and inner spans of rollers

The fracture toughness of the material can be influenced by the width of the notch. Work by Kübler[127] and others[128] showed that an acceptable notch tip radius should be equal or less than twice the size of a major micro structural feature such as the grain size.

In this study, fracture toughness measurements were conducted on 3 LSF, 2 LSFTi2, and 4 LSFTa1 samples.

6.3.4. Test pieces

The rectangular bars used for mechanical tests were synthesized, uniaxially pressed, and sintered as explained in chapter 3 of this thesis. A picture of a set of sintered bars prior to surface preparation is shown in Fig. 6.5. Grinding and polishing of the samples according to the standard EN 843-1 were done by PremaTech Chand Advanced (USA). Due to the extreme bending in the sintered pieces, the final dimensions of the bars were slightly lower than the dimensions mentioned in the standards. Therefore, the standard sample holders were modified accordingly.

Fig. 6.5. The picture of sintered LSFTa1 bars prior to machining.

According to the standard EN 843-1, the test piece should be rectangular within conventional engineering practice. Out-of-squareness of sides compared to faces should be less than 5°. The long edges of the test piece should be chamfered at 45° to a distance of 0.12 mm $\pm$ 0.03 mm.

The test pieces were ground using 320-500 mesh grinding wheel to have a surface roughness less than 2 μm, ignoring obvious pores, Afterwards, they were polished using abrasives of less than 30 μm grit size, decreasing the size progressively down to 6 μm, giving surface roughness of 1 μm. Test pieces were washed and dried in an oven at 110°C for 2 hours and kept in desiccator prior to measurements.

Rectangular bars prepared as mentioned in section 3.3 were used first to measure the Young's Modulus (E_y) by Impulse Excitation technique and then for 4-point bending test, either for the determination of the fracture strength (σ_f) or the fracture toughness (K_{Ic}). Fractographic analyses were conducted on selected samples by SEM (Vega Plus 5136 MM, Tescan) after bending tests.

6.4. Mechanical properties of $La_{0.5}Sr_{0.5}Fe_{1-y}(Ti/Ta)_yO_{3-\delta}$

6.4.1. Young's modulus (Ey)

The dimensions of the LSF, LSFTi2, and LSFTa1 bars used for the impulse excitation technique are shown in Table 6.1. These include length, thickness, width, mass, and density. The values correspond to the average dimensions of 5 bars for each composition. The densities shown are geometrical densities calculated from the dimensions and the mass. The Young's modulus, Ey, calculated from measured fundamental frequency of flexural vibration at room temperature and the given dimensions, as explained in Section 6.3.1 are also shown in Table 6.1. The values given in brackets in Table 6.1 show the standard deviation on the last digit.

Table 6.1. The averages of length (l), thickness (t), width (w), mass (m), and density (ρ) of the measured bars, and the Young's modulus of LSF, LSFTi2, and LSFTa1

Composition	l (mm)	t (mm)	w (mm)	m (g)	ρ (g/cm³)	Ey (GPa)
LSF	42.14(2)	2.24(1)	3.352(2)	1.871(9)	5.91(1)	147(1)
LSFTi2	42.16(2)	2.267(5)	3.358(3)	1.843(3)	5.74(2)	141(1)
LSFTa1	42.17(2)	2.24(2)	3.353(8)	1.93(2)	6.09(2)	145(1)

The Young's modulus of LSF was measured as 147 GPa, decreasing to 141 GPa with 20% Ti and to 145 GPa with 10% Ta substitution. It was pointed out before that the Young's modulus, Ey, is a material property and related to the bonding of the material. Therefore, it could be possible to see a difference in this materials property with the change of the composition. In case of LSF materials substituted with Ti or Ta, the changes in the Ey are not very significant. However, both of the dopants cause decrease in Ey. Although the technique is known to be highly accurate, the microstructure of the materials may cause shift in the theoretical values. Density of the samples is an important property to check.

The Young's moduli of the materials are plotted as a function of their relative densities in Fig. 6.6. The relative densities were calculated from geometrical densities given in Table 6.1 and the theoretical densities of these materials found by XRD (section 4.4.1).
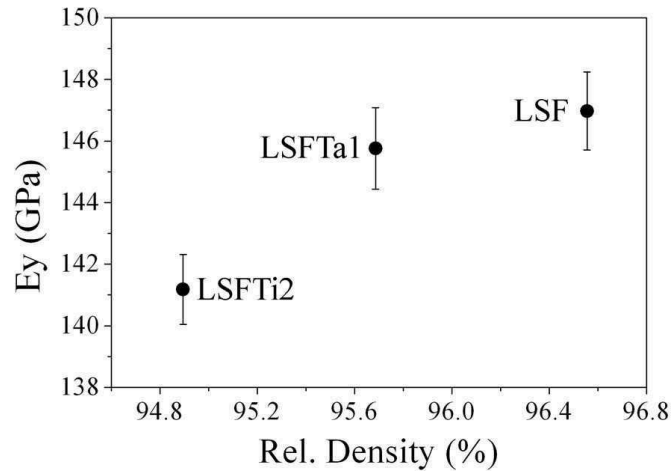
Fig. 6.6. Young's modulus of LSF, LSFTi2, and LSFTa1 as a function of relative density.

According to the trend seen in Fig. 6.6, the Ey increases with higher relative density. This suggests that the three compositions could have even closer Ey values than the measured ones if the materials would be perfectly dense. As a result, Ey seems to be more dependent on the relative density of the samples rather than the B-site substitution.

6.4.2. 4-point bending strength (σ_f)

The fracture strength of the materials was measured at room temperature. It is important to keep in mind that the fracture strength of the materials is not a characteristic material property and depends highly on the structure of the material, especially, the flaw size and their distribution. The fracture strength of LSF, LSFTi2, and LSFTa1 are shown in Fig. 6.7. The mean values correspond to 11 LSF, 10 LSFTi2, and 5 LSFTa1 samples.
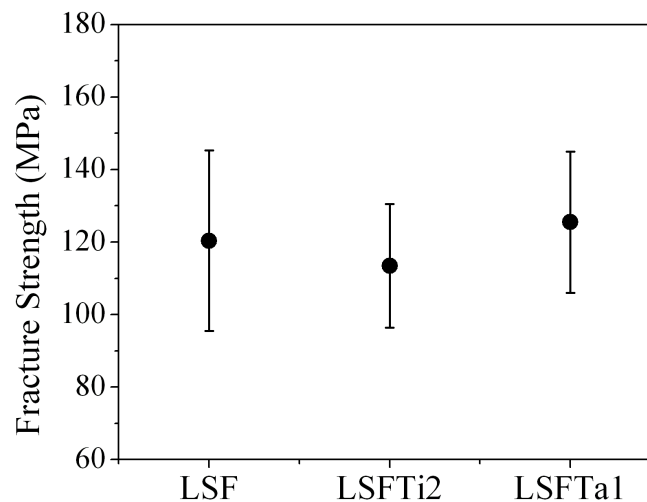

Fig. 6.7. Fracture strength of LSF, LSFTi2, and LSFTa1.

All the compositions show considerable deviations and it is not possible to see any further difference between these three materials. However, the mean values are in similar range to the reported ones for similar materials.[120, 129]

6.4.3. Fracture toughness (K_{Ic})

In order to measure fracture toughness, single-edge-V-notch beam technique was used as explained in Section 6.3.3. An example of a V-notch introduced to an LSFTa1 sample is shown in Fig. 6.8. In this figure, (a) shows the SEM picture of the whole notch, and (b) shows the SEM picture of the tip of the notch. The radius of the notch is indicated with r, which is around 10 µm in this case.
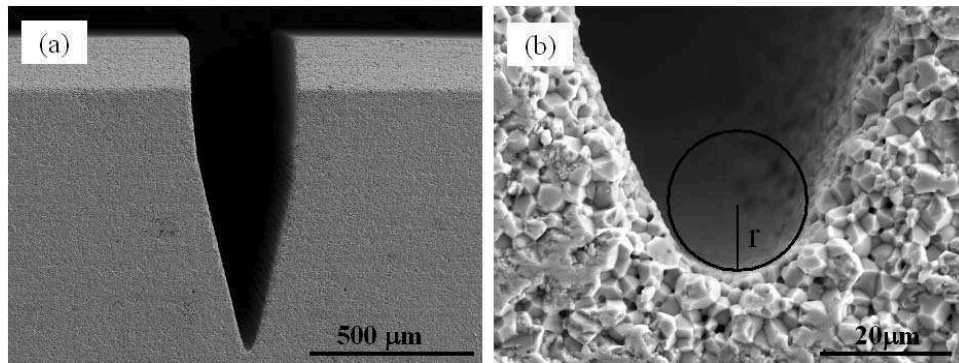

Fig. 6.8. a) A notch introduced to an LSFTa1 sample, b) closer look to the notch showing the notch size.

The shape and the size of the notch are important for the sake of the measurements. In case of LSF(Ti/Ta) materials, the notch shape was always correct and the size was in the range of 9-12 µm. The radii of the tip were slightly higher than the optimum size suggested[127, 128] for the technique. However, it was not possible to obtain sharper tip-size for all three materials due to the brittle nature of these compositions. In spite of this, it is believed that the samples provide a base data set for comparison. The fracture toughness values (K_{Ic}) of LSF, LSFTi2, and LSFTa1 are shown in Fig. 6.10. K_{IC} are given in MPa.m$^{1/2}$.
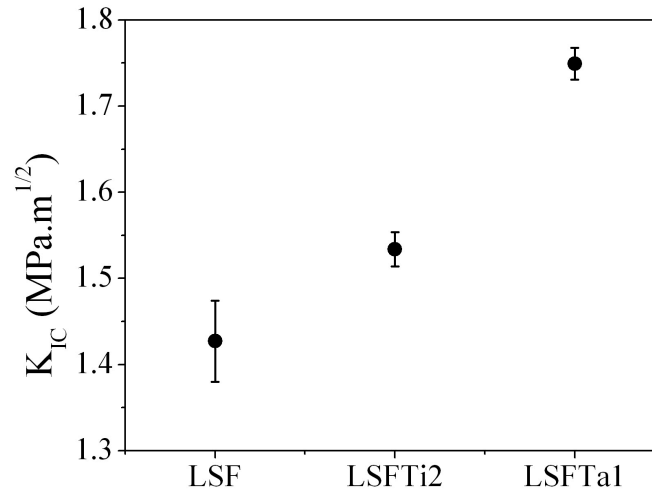
Fig. 6.9. Fracture toughness of LSF, LSFTi2, and LSFTa1.

Fracture toughness of the LSF material increases depending on the B-site substitution with the highest value obtained for 10% Ta substitution. It increases almost 25% from 1.43 to 1.75 MPa.m$^{1/2}$, together with decreased standard deviation. LSFTi2 has a slightly higher fracture toughness (1.53 MPa.m$^{1/2}$) compared to LSF. The basic equation between the fracture strength, σ_f, and the fracture toughness, K_{Ic}, is written as $\sigma_f = K_{Ic}/Y\sqrt{c}$, where Y is constant dependent on the test geometry and the crack dimensions and c is the crack size. According to this equation, for the same size of a flaw for all the compositions, the one with the highest fracture toughness can bear the highest load.

In general, several approaches can be suggested to improve the strength and reliability of a material if we consider this equation. These include decreasing the flaw size and improving the fracture toughness by a toughening mechanism. In this context, LSFTa1 sample would provide better reliability at the same operation conditions according to the results obtained.

6.4.4. Fractography

The fracture surface of brittle materials has very distinctive features, which gives important information about the origin of the fracture. Therefore, fractographic analyses were conducted on the measured samples. In general the region around the fracture origin is relatively smooth (mirror region) and becomes rougher as the crack propagates (mist region), and finally the surface becomes extremely rough with the crack branching (hackle region).[104] Although difficult in polycrystalline materials, the surface in the latter mentioned region, hackle marks point towards the fracture origin of the fracture and therefore are very useful.

Some of the surfaces are shown in Fig. 6.10. Left column of the figure shows the general views of the fractured surfaces while the right column shows the corresponding fracture origins. Fig. 6.10 (a) and (c) show two LSF samples, (e) shows an LSFTa1 sample, and (g) shows an LSFTi2 sample with (b), (d), (f), and (h) showing closer look to the fracture initiation points. The arrows are shown to indicate the direction of the hackle marks, which are pointing outwards from the fracture origin.
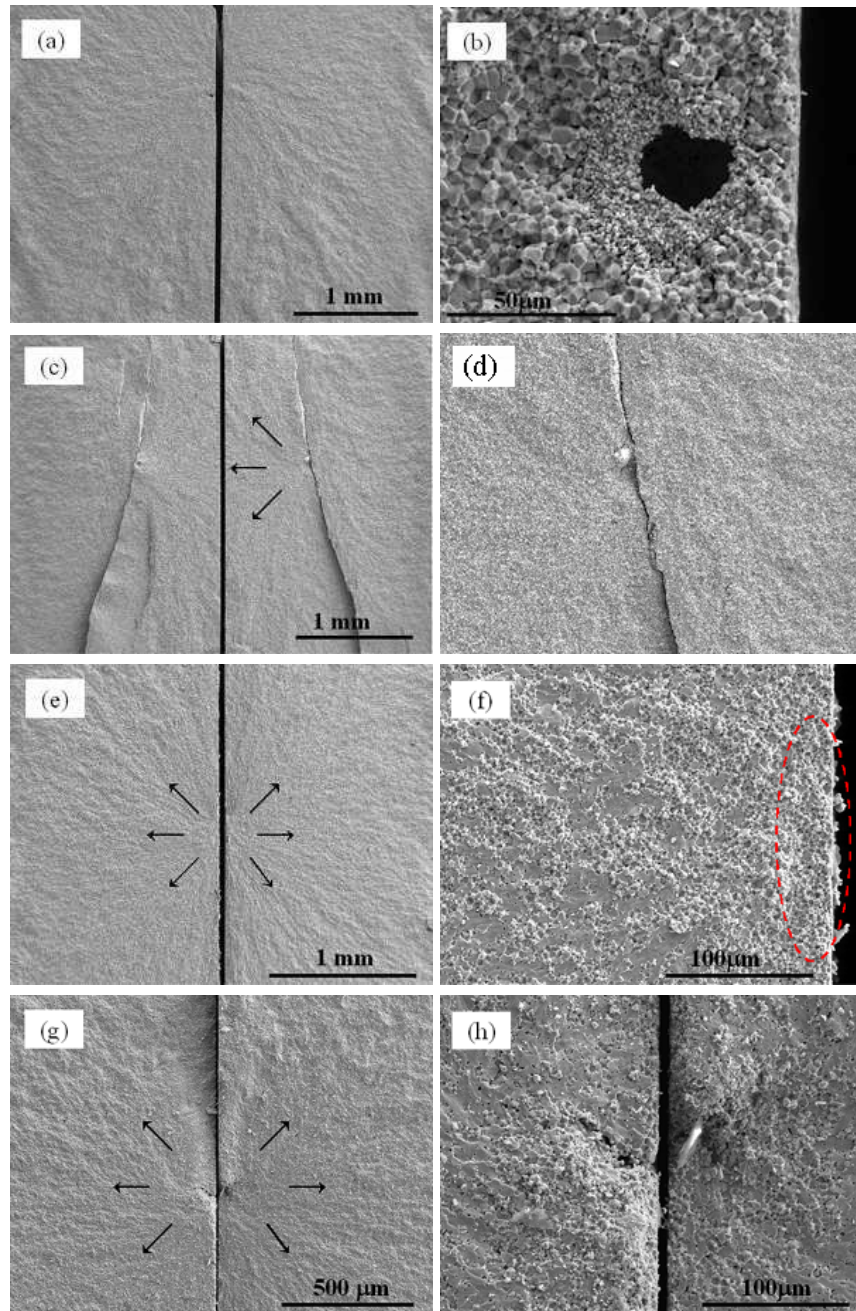

Fig. 6.10. SEM images of 4-point bending fracture surfaces of a) LSF, b) magnified pore shown in (a), c) LSF, d) magnified crack shown in (c), e) LSFTa1, f) magnified porous area shown in (e), g) LSFTi2, and h) magnified void shown in (g).

All three compositions show a mixture of transgranular and intergranular fracture, while intergranular portion is higher for LSF. This is in agreement with previous results shown in chapter 3. The fractography characterizations conducted by SEM on fractured surfaces showed that the fractures originated mostly from inhomogeneous regions, and delaminations, and in some cases from large pore or inclusions. In most cases, it originated on the surface where the tensile forces apply, while in few occasions, the initiation point was rather in the bulk.

Fig. 6.10 (a) shows an LSF sample, at which the fracture initiated at a large pore. The image (b) shows the pore that is around 30 μm in diameter. The hackle marks can be seen in (a), however, the shapes are not simply straight as it may occur in case of a fracture originated around a pore.[124] Fig. 6.10 (c) and (d) show the surface of a different LSF sample for which the crack initiation is in the bulk of the sample. A small inclusion or a hard agglomerate is observed in the origin and an extended crack along the width of the sample, parallel to the tensile surface. Especially in case of LSF, several samples showed this kind of extended cracks along the bulk, which maybe related to residual stresses in the material induced during cooling of the sintered sample. In case of LSFTa1, on the other hand, majority of the sources for fracture were found to be relatively more porous regions on the surface, an example of which is shown in Fig. 6.10 (e) and (f). The hackle marks are more obvious in this case pinpointing the fracture origin. Finally, an example of a fracture surface of LSFTi2 is shown in Fig. 6.10 (g) and (h). In the image (h), an elliptical void with a length of around 40 μm is observed. It is not very easy to decide on the exact size and shape of the void, however, a crystallite (either an impurity or a large grain) is seen on the right surface. A few more cases similar to shown here were observed in case of LSFTi2 samples. This may be the reason that LSFTi2 samples show the lowest 4-point bending strength and Ey compared to LSF and LSFTa2.

A simple calculation for the crack size for failure of LSF can be calculated using Griffith equation shown before ($\sigma_f = K_{Ic}/Y\sqrt{c}$). The calculated crack size can be found to be in the region 20 – 100 μm depending on the crack geometry and it is in good relation to the observed crack sizes (Fig. 6.10).

6.5. Summary and conclusions

The mechanical properties of LSF, LSFTi2, and LSFTa1 were studied at room temperature by means of impulse excitation, 4-point bending, and single-edge-V-notched beam techniques. The change in the Young's modulus (Ey) of LSF was found to be very low, although decreasing with Ti/Ta doping. A relation was observed between Ey and the relative

density of the compositions, with LSFTi2 having the lowest Ey (141 GPa) for the relative density of 94.9% and LSF having the highest Ey (147 GPa) for the density of 96.6%.

Four-point bending fracture strengths of the materials were in the same range, around 120 MPa, all with high standard deviations. The origins of fractures were studied by SEM. The initiation points of fracture were found to be processing flaws such as delamination, inhomogeneous areas like porous regions, or voids. Several LSF samples were found to have delamination, which was thought to cause higher standard deviation for this material. Relatively porous regions and elliptical voids were found to be more common for the LSFTa1, and LSFTi2 materials, respectively.

Finally, the fracture toughness (K_{Ic}) of the samples was measured by 4-point bending after introducing a defined sized notch (around 10 μm) to the tensile surface of the material. In this way the fracture origin was already defined. The biggest effect of B-site doping was seen on the fracture toughness of the materials. The toughness of LSF was increased from 1.43 MPa.m$^{1/2}$ to 1.53 MPa.m$^{1/2}$ for LSFTi2 and to 1.75 MPa.m$^{1/2}$ for LSFTa1. Although this value is still low compared to some other perovskite materials, it is considered an improvement in case of B-site doping of materials.

The mechanical properties measured in this work provide a good basis for comparison of the materials. However, it should be kept in mind that the results are not necessarily transferable to the real components as they are dependent on the microstructure and geometry of the component.

Chapter 7

Transport properties of La$_{0.5}$Sr$_{0.5}$Fe$_{1-y}$(Ti/Ta)$_y$O$_{3-\delta}$

In this chapter of the thesis, transport properties of La$_{0.5}$Sr$_{0.5}$Fe$_{1-y}$(Ti/Ta)$_y$O$_{3-\delta}$ materials are reported. These include the chemical diffusion and the surface exchange coefficients measured by potential-step technique, where the current relaxation of the material is monitored after a sudden change of the oxygen on one side of the measured sample. The effects of Ti/Ta substitutions on these properties are discussed. Transport coefficients of LSF were studied as a function of pO$_2$ at 1000°C. The electrochemical cells were investigated by scanning electron microscopy after finalizing the measurements.

7.1. Introduction

In the previous chapters of this thesis, the structural, chemical, physical, and mechanical properties of the considered $La_{0.5}Sr_{0.5}FeO_{3-\delta}$-based materials were examined. All of these properties are interrelated and important; however, considering the application aimed for these materials, which are oxygen separation membranes, the transport properties can be considered as one of the most important in the material selection process. The transport properties actually are related to solid-state electrochemistry, which deals with all phenomena where a chemical change occurs as a result of electric forces or vice versa. In the oxygen separation membrane application of these materials, the performance is mainly determined by the kinetics of the oxygen exchange kinetics, which involves the diffusion of oxygen in the solid and the associated surface exchange kinetics. Therefore, their understanding is crucial to identify a suitable material and the conditions for the application.

This chapter aims to investigate the effect of the substitution on the mentioned transport coefficients of LSF, LSFTi2, and LSFTa1. An overview of the oxygen transport in perovskite materials was explained in the theoretical background, section 2.3 in an attempt to make the coefficient calculations clearer. In the next section, information on techniques used for determining the transport coefficients and literature survey on the transport coefficients are reported.

7.2. Theory

7.2.1. Techniques used for the determination of the transport coefficients

Diffusion processes in materials can be studied by several techniques.[130, 131] There are nuclear methods, which include tracer diffusion and quasielastic neutron scattering (QENS), and the non-nuclear methods such as DC or AC conductivity and relaxation techniques. Each technique has distinct advantages and disadvantages.

QENS is the only technique that gives information on diffusion on an atomic level. Atomic diffusion parameters like hopping rates of atoms or ions and the barrier heights for the jump processes can be obtained by this method.[132]

Another method is Secondary Ion Mass Spectroscopy (SIMS), which is a direct method relying on the measurement of the concentration of an ion, ^{18}O isotope, on the sample itself as a function of depth or position.[133-135] This technique is used to measure the tracer diffusion coefficient (D^*).

The most commonly used techniques to determine the transport coefficients, i.e. the chemical diffusion ($\tilde{D}$) and surface exchange coefficients (k_S), are relaxation techniques. In relaxation experiments, the response of the sample to a change in the surrounding oxygen activity is measured as a function of time, until the equilibrium is reached giving a certain relaxation time, τ. The measured response can be weight[136], conductivity[137-140], or the flux of the diffusing species[141-143,]. Coefficients are calculated by fitting the relaxation data to the Fick's second law, expressed in different ways depending on the measured response.

Electrochemical relaxation techniques can be preferable among the other techniques considering that it provides coulometric titration data by monitoring the cell current as a result of incorporation or removal of oxygen as a function of time.[143] Therefore, the change in the nonstoichiometry of a sample can be measured. The kind of cell design used by Belzner[143] et al. and modified by Diethelm et al.[37] provides the advantage of monitoring the oxygen activity at the specimen surface with respect to a reference electrode.

Diethelm et al. studied electrochemical impedance spectroscopy as a means to determine the chemical diffusion and surface exchange coefficients.[37, 42, 144-146] It was shown that when this technique is applied to the cell geometry with a gas space between the sample and the YSZ pump, a complex impedance model could be derived and an equivalent circuit could be used to analyze the impedance data distinguishing the different contributions (oxygen pump, diffusion, and surface exchange) to the overall response. The technique was found to have restrictions giving large error bars at low temperature and pO_2 and requiring long times at low frequency measurements.[37]

There seems to be many inconsistencies in the reported values for diffusion coefficients (especially for D*) determined by different methods (chemical, tracer, and conductivity measurements).[130] The reported studies show that the possible reasons are the differences in diffusion paths or sample chemistry, which may depend on the density or the microstructure of the sample.

7.2.2. Potential step technique and data analysis

The approach followed in this work for the analysis of the potential-step relaxation data differs from that described in previous publications;[42, 147] a single expression, based on asymptotic expressions, but valid over the full time scale, is used to fit the complete data range in order to extract the oxygen transport parameters.[148]

The principle of the measurement is to apply a voltage step across the YSZ slab, which corresponds to a change in the oxygen partial pressure (pO_2) at the surface of the sample. The potential step applied to the sample with reference to the electrode defines the oxygen partial pressure change on the electrolyte surface, which will cause the material to

adjust itself to the new equilibrium activity by loosing or incorporating oxygen with simultaneous ionic conductivity. This equilibration results in an electrical current through the oxygen pump, which is monitored as current relaxation.

Fick's second law can be used to express the transient diffusion of oxygen as in Eq. 7.1 with the following assumptions in effect. The material is supposed to be a good conductor so that the potential difference across the sample is negligible. Therefore, one dimensional diffusion process in the sample can be expressed as,

$$\frac{\partial c}{\partial t} = \frac{\partial}{\partial x}\left(\frac{\tilde{D}\partial c}{\partial x}\right)$$
(7.1)

The general solution of the equation 7.1 for the current relaxation following a potential-step in its infinite series form can be written as,[149]

$$I(t) = Q\sum_{n=1}^{\infty}\frac{2\Lambda^2\tilde{D}\exp(-\lambda_n^2\tilde{D}t/L^2)}{L^2(\lambda_n^2 + \Lambda^2 + \Lambda)}$$
(7.2)

where $\tilde{D}$ is the chemical diffusion coefficient, L is the thickness of the sample, Q is the total charge passed during the potential step, $\Lambda = k_T L/\tilde{D}$, with k_T, the surface exchange coefficient associated to the total electrochemical cell resistance (R_T), and λ_n are the roots of the transcendental equation

$$\lambda\tan(\lambda) = \Lambda$$
(7.3)

Eq. 7.2, in its infinite series form, and Eq. 7.3 are not practical for data analysis, it is therefore useful to use approximations for both short and long time.[147] At short-time ($t < t_c \equiv 0.154\ L^2/\tilde{D}$), the relaxation current can be described by[146]

$$I(t) = \frac{Qk_T}{L}\left[\frac{R_S}{R_T - R_S}\exp\left(-\frac{t}{\tau_g}\right) + \exp\left(\frac{t}{\tau_d}\right)\mathrm{erfc}\left(\sqrt{\frac{t}{\tau_d}}\right)\right]$$
(7.4)

where $\tau_d = \tilde{D}/k_T^2$ is the time constant associated with the diffusion process, τ_g is the time constant of the oxygen pump response and R_S is the resistance associated with the surface exchange reaction. The first exponential term of Eq. 7.4 corresponds to the rapid response of the oxygen pump and gas space to a potential step, whereas the second term describes the diffusion process.[146] The latter is analogous to the expression used for analysing depth

profiles in isotopic exchange experiments, which describes diffusion in a semi-infinite media with linear surface exchange boundary conditions.[150]

At large time ($t > t_c$), the relaxation current can be described by an appropriate number of terms of Eq. 7.2. It can be shown that the two first terms are sufficient to obtain a consequent overlap between the long- and short-time expressions (Eqs. 7.2 and 7.4) around $t = t_c$. The use of Eq. 7.2 requires the simultaneous determination of the roots of Eq. 7.3. Although a numerical routine has been proposed[151] for this calculation, it is still useful to work with an explicit expression of those roots. An approximation for λ_1 was first given in:[146]

$$\lambda_1 = \sqrt{\frac{\Lambda}{1 + \Lambda/3}}$$
(7.5)

For the other roots, Eq. 7.5 was linearized to obtain

$$\lambda_n = (n-1)\pi\left(1 + \frac{\Lambda}{\Lambda + (n-1)^2\pi^2}\right) \quad \text{for n} > 1$$
(7.6)

These approximations are accurate within less than 1% for $\Lambda \leq 1$. As we will see below, this condition is practically always fulfilled for the data obtained in this study.

Prior to the total fitting of the relaxation data, initial estimations of the parameters were obtained by partial fittings of the data in three steps. An exponential fit to the first seconds of the I vs. t plot, which belongs to the response of the oxygen pump, provides values for V/R_T, $R_S/(R_T-R_S)$, and τ_g following the first part of Eq. 7.4 that becomes,

$$I(t) = \frac{V}{R_T} + \frac{R_T}{V}\frac{R_S}{(R_T - R_S)}\exp\left(-\frac{t}{\tau_g}\right)$$
(7.7)

where V is the applied potential step.

A long-term fit to the $\ln(I)$ vs t plot gives estimates for the first term of Eq. 7.2 (V/R_T', and τ_d') from the following equation, which is valid when t << L/k,

$$I(t) = \frac{V}{R_T'}\exp\left(-\frac{t}{\tau_d'}\right)\mathrm{erfc}\left(-\frac{t}{\tau_d'}\right)$$
(7.8)

Finally, a linear fit to the I vs $\sqrt{t}$ plot at the time the response of the oxygen pump vanishes provides estimates for Eq. 7.8 (V/R_T and τ_d) following the equation,

$$I(t) = \frac{V}{RT}\left(1 - 2\sqrt{\left(\frac{t}{\tau_d \pi}\right)}\right) \qquad (7.9)$$

which is a short time solution to Fick's second law, an approximation of Eq. 7.8 valid at short time (a simplified form of Eq 7.8 by series expansion of the complementary error function). Where R_T' is the modified total cell resistance and $\tau_d' = R_T' C_S$, C_S being the capacitance of the sample. This equation is valid when $t << \tilde{D}/k^2$. A more detailed explanation of the fitting model is explained in the Ref.[146]

Finally, the current relaxation data could be fitted over the complete time domain (4 decades) to a hybrid solution matching Eqs. 7.2 and 7.3 at $t = t_c$. The fits were performed using the NLLS fitting algorithm of ORIGIN (OriginLab Corporation, Northampton, USA).

7.2.3. Related literature data on transport coefficients

There has been research on the transport properties of mixed ionic-electronic conducting materials, similar to LSF composition. Sitte et al.[152] reported the transport coefficients of $La_{0.6}Sr_{0.4}FeO_{3-\delta}$ studied by conductivity relaxation technique. They reported surface exchange coefficients in the range $1\times10^{-5} - 9\times10^{-5}$ cm/s and chemical diffusion coefficients in the range $5\times10^{-7} - 1.8\times10^{-5}$ cm^2/s at 700°C.

Atkinson et al.[153] found that the tracer diffusion coefficient (D*) and surface exchange coefficient (k) increase with increasing temperature and decreasing oxygen activity. On the other hand, $La_{0.4}Sr_{0.6}FeO_{3-\delta}$ material was reported by Preis et al. [154] to show a decrease of $\tilde{D}$ and k_S with decreasing pO_2 at 700 and 900°C measured at partial pressures of $7\times10^{-4} - 2.6\times10^{-4}$. The same material was reported to have a chemical diffusion coefficient around 3.4×10^{-6} cm^2/s and a surface exchange coefficient of 2.6×10^{-5} cm/s at 700°C. For $La_{1-x}Sr_xCoO_{3-\delta}$ (x =0.2, 0.5, and 0.7) at T = 750 – 850°C, chemical diffusion coefficients in the range of $1\times10^{-7} - 5\times10^{-6}$ and $8\times10^{-7} - 1.3\times10^{-5}$ were reported at $pO_2 = 10^{-4}$ bar and ~0.4 bar.[155] Corresponding surface exchange coefficients in the same conditions were found to be around $6\times10^{-6} - 6\times10^{-5}$ and $6\times10^{-4} - 2\times10^{-3}$ in the low and high pO_2 values mentioned before. The transport coefficients were found to be fairly constant at higher pO_2 values but significantly lower at reduced pO_2. In addition, it was shown that the activation energy for chemical diffusion increased with decreasing pO_2 and this was attributed to an increased energy of formation of mobile oxygen vacancies as a result of ordered structure.

A work on $La_{0.4}Ba_{0.6}Fe_{0.8}Co_{0.2}O_{3-\delta}$ materials conducted by potential-step and impedance spectroscopy to determine transport properties on the same cell showed that the

diffusion coefficients from both techniques were similar while the surface exchange coefficients differed by a factor of 2-3, which was attributed to the effects of the oxygen pump and high-frequency errors in impedance spectroscopy.[42]

In general, the tracer diffusion coefficient (D^*) is more than two orders of magnitude lower than the chemical diffusion coefficient ($\tilde{D}$) for the same material with a relation $\tilde{D} \approx \gamma \times D^*$, which is a simplified version of Eq. 2.22 where γ is called the thermodynamic factor and is equal to $-1/2\ \partial\ln p O_2/\ \partial\ln\delta$ and can be found from the $p O_2$ dependence of the non-stoichiometry of the material. The $\tilde{D}$ coefficients calculated this way for $La_2Cu_{0.5}Ni_{0.5}O_4$ materials from D^* (measured by isotopic exchange) were in good agreement with the measured $\tilde{D}$ by electrical conductivity relaxation technique and the thermodynamic factor, γ, was in the range 292-385 in the temperature range of 500-900°C.[156]

There is no data available on chemical diffusion and surface exchange coefficients of $La_{0.5}Sr_{0.5}FeO_{3-\delta}$ and Ti- and Ta- substituted LSF, except for the reported data given below.[148]

7.3. Experimental

Potential-step measurements

The pellets used for the potential-step measurements were prepared as explained in section 3.3.1. The disc-shaped pellets were uniaxially pressed using dies with 10 mm diameters. The sintering was carried out as explained previously in section 3.3.1. The active surfaces of the pellets were polished by SiC paper down to 2500 grit. The thickness of the LSF, LSFTi2, and LSFTa1 samples used for potential step measurements were 0.76, 1.24, and 0.96 mm, respectively.

The potential step measurements for the characterisation of oxygen transport in mixed conducting oxides were conducted using a cell design developed by Diethelm et al.[37, 147] The schematic of this set-up is shown in Fig. 7.1.
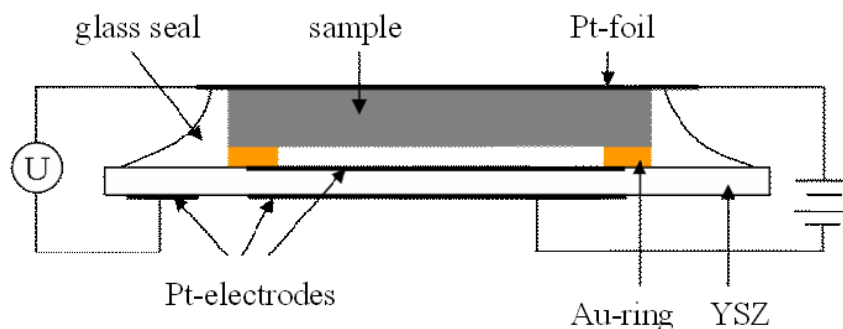
Fig. 7.1. Schematic of the electrochemical cell set-up used for the potential step relaxation measurements, redrawn after the Ref.[37]

An oxygen pump consisting of an YSZ slab with Pt electrodes on both sides is placed on one side of the pellet as shown in the schematic. The upper electrode is electrically contacted through a gold ring that also acts as a spacer between the sample and the oxygen pump. The top and lateral surfaces of the sample are coated with gold paste and are sealed with glass. The gold coating prevents any reaction between the glass and the sample. After assembling the sample with the oxygen pump, the cell was first heated up rapidly to burn the organics and densify the gold coating. The glass sealing was then added and the cell was heated to 950°C for measurement.

The measurement sequence followed in this work was to apply first a -20 mV vs. air potential step, followed by -20 → 0 mV potential step, therefore measuring the equilibration kinetic for both reduction and oxidation. The cell was then cooled down to the next temperature and the same sequence was applied. At each step, the decay of the relaxation current to 0 (i.e. a few µA) was taken as an indication of equilibrium. At a given temperature, the applied potential was also decreased step-wise down to -100 mV vs. air in order to observe the evolution of the oxygen transport parameters with varying pO_2.

7.4. Transport coefficients of $La_{0.5}Sr_{0.5}Fe_{1-y}(Ti/Ta)_yO_{3-\delta}$ measured by potential-step relaxation technique

7.4.1. Non-linear fitting of relaxation and time constants

A typical current relaxation curve obtained as a result of potential-step experiment is shown in Fig. 7.3 (a). The relaxation curve below belongs to the response of LSF material to a potential step from –20 to 0 mV, therefore an oxidation step, at 900°C. The fitting steps to obtain initial estimates for the total fit explained previously in section 7.3.2 are also shown in the same figure. The partial fits corresponding to equations 7.7, 7.9, and 7.8 are shown in Fig. 7.3 (b), (c), and (d), respectively. In all figures, the current (I) is shown in mA and the time on x-scale is shown in seconds. The results of the fitting are shown with red lines in the plots b-d. Note that the potential step of 20 mV corresponds to a oxygen partial pressure difference of 0.16 bar at 900°C.
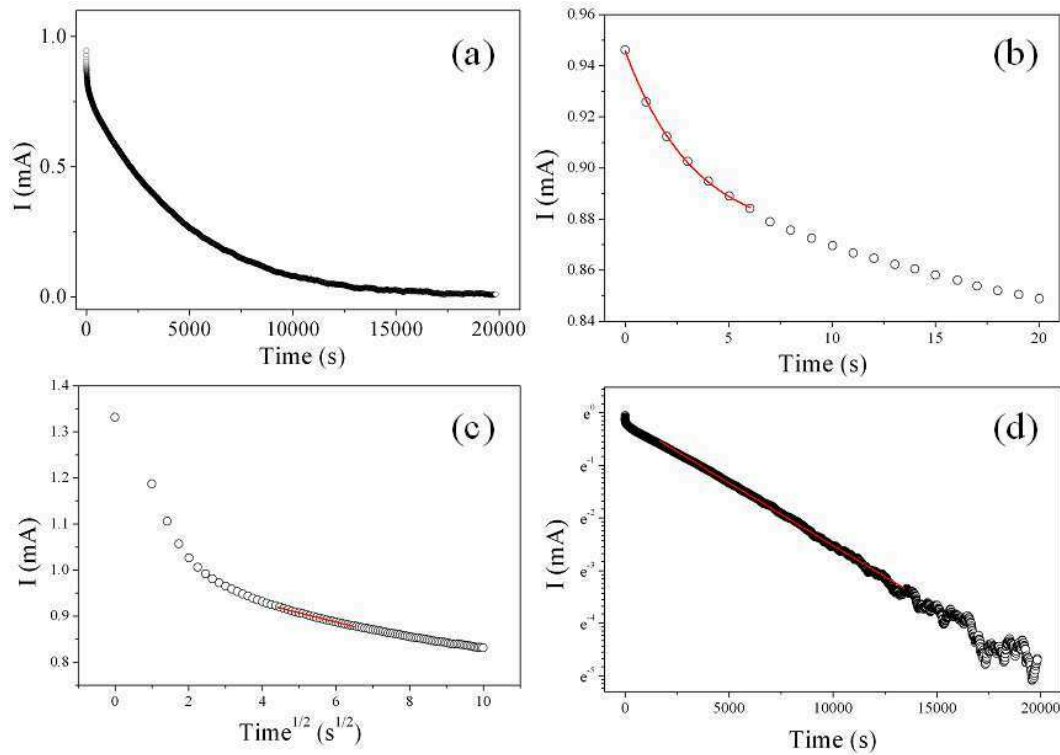

Fig. 7.3. (a) An example current relaxation data, the response of LSF to a potential step from –20 to 0 mV at 900°C, (b) the first 20 seconds of the data in (a) with red line showing the fit to the Eq. 7.7, (c) the first 100 seconds of the data in (a) plotted as a function of square root of time with red line showing the fit to the Eq. 7.9, (d) the data in (a) plotted in logarithmic scale on the y-axis with red line showing the fit to the Eq. 7.8.

According to Fig. 7.3 (a), the equilibration of LSF at 900°C takes about 20,000 seconds (~5.5 hours) when the oxygen activity is changed by a potential step of 20 mV. When the relaxation is plotted with a logarithmic current scale, the current response shows a typical exponential decay after a few hundreds of seconds as seen in Fig. 7.3 (d). The response of the oxygen pump vanishes after some seconds (Fig. 7.3 (b)), giving way to the response of the sample. The linear dependence of I to the square root of time (short-time response), shown in Fig. 7.3 (c) is not very obviously linear, however, a linear section of the plot just after the response of the oxygen pump vanishes, is taken as the fitting range.

The relaxation currents of the LSF sample as a result of a –20 mV potential vs. air step are shown in Fig. 7.4 as a function of temperature (750 – 1000°C), along with the best fits to the hybrid solution. The data has been plotted with a logarithmic time scale to show the quality of the fit over the complete time domain (over four decades).
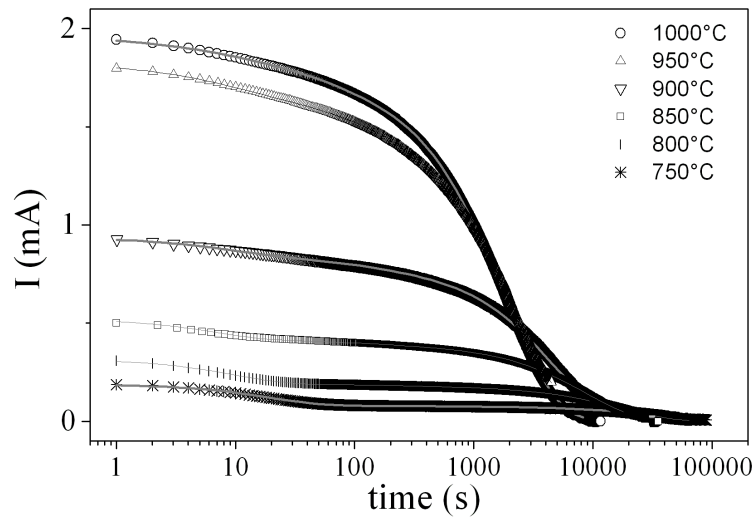

Fig. 7.4. 27. Relaxation curves of LSF for a –20 mV potential step as a function of T (750 – 1000°C).

The equilibration time becomes longer with lowered temperature, exceeding 20 hours for the same material at 750°C while it is around 3 hours at 1000°C, resulting in extremely long measurement times at low temperatures.

The respective time constants of the gas composition change, τ_g, and diffusion process, τ_d, of LSF material are given in Table 7.1 for different temperatures, along with the switch time (t_c) between the short- and long-time behaviour.

Table 7.1. Temperature dependence of time constants related to the gas composition change (τ_g) and the diffusion process (τ_d), and of the time boundary between short-time and long-time expressions for LSF material measured during a reduction step

T (°C)	t_c (s)	τ_g (s)	τ_d (s)	Λ	L_c (mm)
1000	150	3.1	1700	0.76	0.06
950	145	2.7	1789	0.73	0.07
900	296	3.0	4528	0.65	0.29
850	632	4.9	9087	0.67	0.49
800	1432	9.1	17383	0.73	0.62
750	1984	19.7	50847	0.50	1.08

It can be seen that τ_g increases with decreasing temperature. This is due to the combined increase of the gas space capacity and interfacial resistance.[146] It is important that $\tau_g \ll t_c$ for purpose of analysing, otherwise the response of the oxygen pump could hinder the evaluation of the transport parameters. This problem is similar to that of the reactor time-lag in conductivity relaxation measurements as discussed by den Otter et al.[157]

In the same table, the values of the constant Λ (= $k_T L/\tilde{D}$) and the critical thickness ($L_c = \tilde{D}/k_S$) are also reported for all temperatures for the same sample. The constant Λ remains smaller than 1 over the complete experimental range, therefore satisfying the validity criteria for the approximations shown in equations 7.5 and 7.6.

L_c is the so-called critical thickness of the sample below which the transport of oxygen becomes limited by the surface exchange kinetics. It can be seen in Table 7.1 that L_c increases as the temperature decreases, indicating that the oxygen transport in the sample becomes surface limited at lower temperatures. The comparison of critical thickness among the compositions will be discussed the next section.

7.4.2. The chemical diffusion ($\tilde{D}$) and the surface exchange (k_S) coefficients of $La_{0.5}Sr_{0.5}Fe_{1-y}(Ti/Ta)_yO_{3-\delta}$

The relaxation experiments were conducted during a reduction step ($0 \rightarrow$ -20mV) followed by an oxidation step (-20 $\rightarrow$ 0mV). The two relaxation curves are shown in Fig. 7.5 for comparison. The data shown belongs to LSF material measured at 800°C.
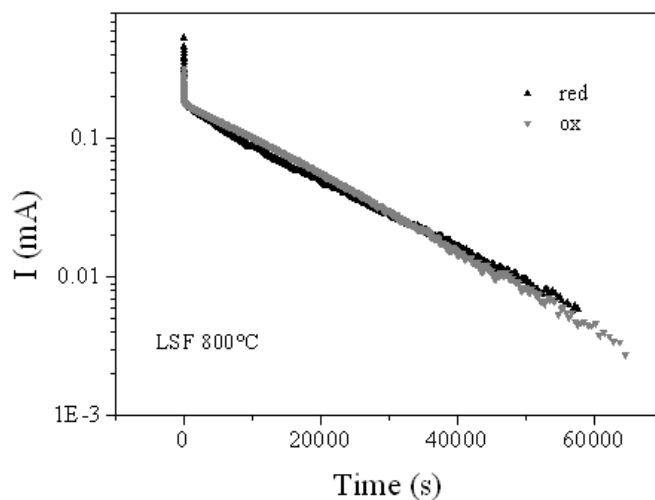
Fig. 7.5. Relaxation curves of LSF at 800°C measured during reduction and oxidation steps.

It is visible in Fig. 7.5 that the response of the sample to a reduction step differs from that of an oxidation step. The same situation was observed for all samples and temperatures. Therefore, the resulting transport coefficients are different from each other depending on the measurement condition (reduction or oxidation). The discrepancy between oxidation and reduction experiments was reported for $La_{0.4}Sr_{0.6}FeO_{3-\delta}$ measured by conductivity relaxation.[154] Oxidation experiments were remarkably faster compared to the corresponding reduction experiments, resulting in orders of magnitude higher diffusion coefficients compared to reduction experiments. In some cases it was not even possible to determine the diffusion coefficient from oxidation experiments.[154]

The chemical diffusion ($\tilde{D}$) and surface exchange (k_S) coefficients, obtained from the fits for all the compositions, are displayed as Arrhenius plots in Figs. 7.6 and 7.7 respectively. In both figures, the data for reduction and oxidation runs are shown by filled and open symbols, respectively. The corresponding activation energies (E_A) are reported in Table 7.2 together with transport coefficients at 900°C.

Table 7.2. Oxygen transport data for LSF, LSFTi2, and LSFTa1 obtained from fitting. The number between brackets indicates the uncertainty on the last digit

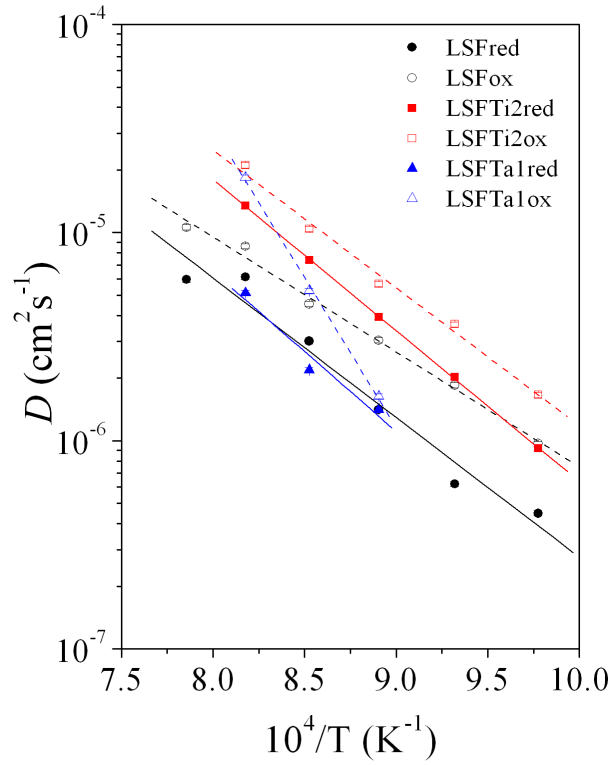| Composition	Voltage step (mV)	$D_{900°C}$ (cm^2/s)	$E_{a,D}$ (kJ/mol)	$k_{S,900°C}$ (cm/s)	$E_{a,k}$ (kJ/mol)
LSF	$0 \rightarrow -20$	$3.01(8)\ 10^{-6}$	$128(2)$	$1.02(6)\ 10^{-4}$	$240(5)$
	$-20 \rightarrow 0$	$4.5(1)\ 10^{-6}$	$106(2)$	$2.6(2)\ 10^{-4}$	$288(4)$
LSFTi2	$0 \rightarrow -20$	$7.4(2)\ 10^{-6}$	$139(2)$	$5.0(4)\ 10^{-4}$	$249(5)$
	$-20 \rightarrow 0$	$1.04(3)\ 10^{-5}$	$126(2)$	$4.1(2)\ 10^{-4}$	$251(5)$
LSFTa1	$0 \rightarrow -20$	$2.19(6)\ 10^{-6}$	$147(4)$	$1.47(1)\ 10^{-4}$	$169(10)$
	$-20 \rightarrow 0$	$5.3(1)\ 10^{-6}$	$276(2)$	$1.44(1)\ 10^{-4}$	$324(5)$

Fig. 7.6. Arrhenius plots of chemical diffusion coefficients, $\tilde{D}$, for LSF, LSFTi2, and LSFTa1.
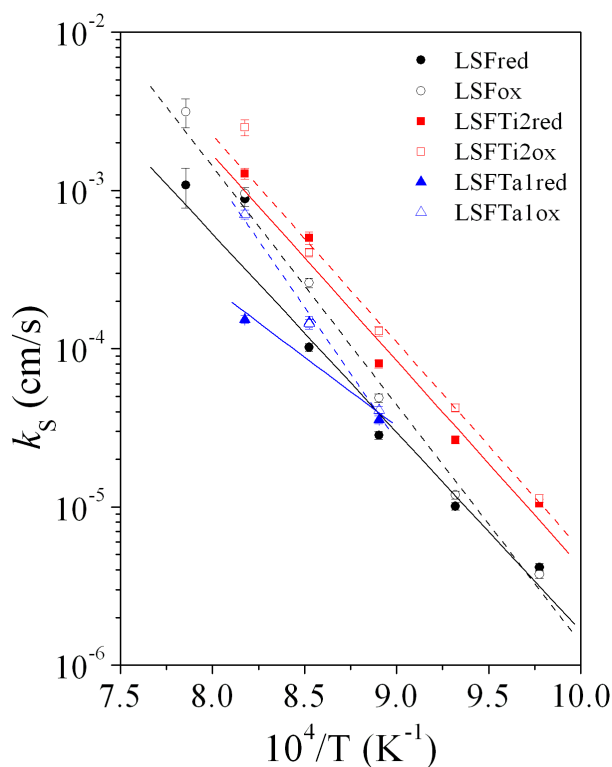
Fig. 7.7. Arrhenius plots of surface exchange coefficients, k_S, for LSF, LSFTi2, and LSFTa1.

Figures 7.6 and 7.7 show that the oxidation values are systematically higher than the reduction values. Moreover, the oxygen transport parameters are slightly higher for LSFTi2 than LSF and LSFTa1. This difference is attributed to the difference in concentration of the mobile species between the two compositions. For small defect concentrations (as in air), the chemical diffusion coefficient is inversely proportional to the mole fraction of defects (assuming there is local equilibrium);[158] it will therefore be higher in LSFTi2 than in LSF.

Transport coefficients of LSF at 1000°C as a function of pO$_2$

In order to see the effect of partial pressure of oxygen on the transport coefficients, potential step measurements were conducted further with increased potential applied to the LSF cell at 1000°C. The relaxation data obtained at this temperature with increasing applied potential across an LSF sample (from 0 to –100 mV vs. air) are shown in Fig. 7.8.
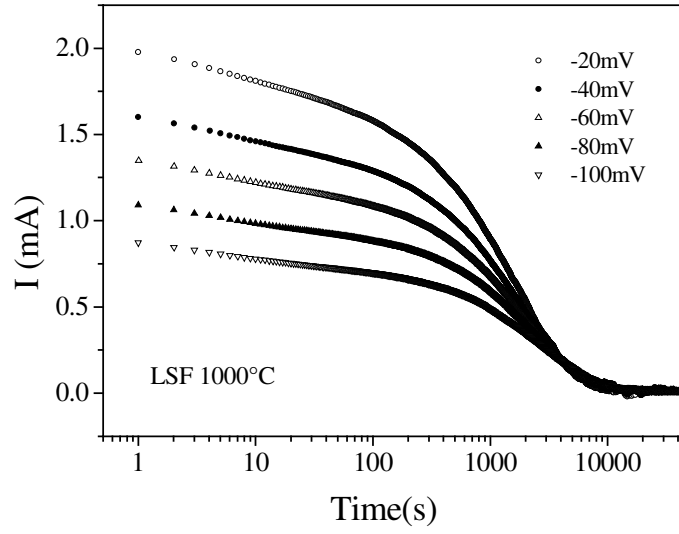
Fig. 7.8. Relaxation data of LSF measured at 1000°C with different potential reduction steps (-20 – -100 mV).

Since the equilibrium is reached between each step with the current decaying to 0, the corresponding oxygen partial pressure can be evaluated using the Nernst law in the following form,

$$\Delta E = -\frac{RT}{nF} \ln\left(\frac{c_{O_2}}{c_{O_2}^{eq}}\right) = -\frac{RT}{nF} \ln\left(\frac{pO_2}{pO_2^{eq}}\right) \tag{7.10}$$

where R is the ideal gas constant, T temperature in K, F the Faraday constant, n the number of electrons transferred in the cell reaction (-4 in this case), $c_{O_2}^{eq}$ the concentration of oxygen in air, and c_{O_2} the resulting concentration after the application of the potential to the cell (ΔE). The concentration terms are replaced by partial pressure considering $c_{O_2} = pO_2/p_{total}$ in an ideal gas mixture.

The resulting oxygen transport coefficients, $\tilde{D}$ and k_S, calculated by fitting the relaxation curves in Fig. 7.8 are given in Fig. 7.9, showing their pO_2 dependence. The coefficients obtained from oxidation relaxation curves are also displayed in the same figure. The coefficient obtained from any potential step is plotted so that the corresponding voltage and the pO_2 are the average of the initial and the final values of this step.
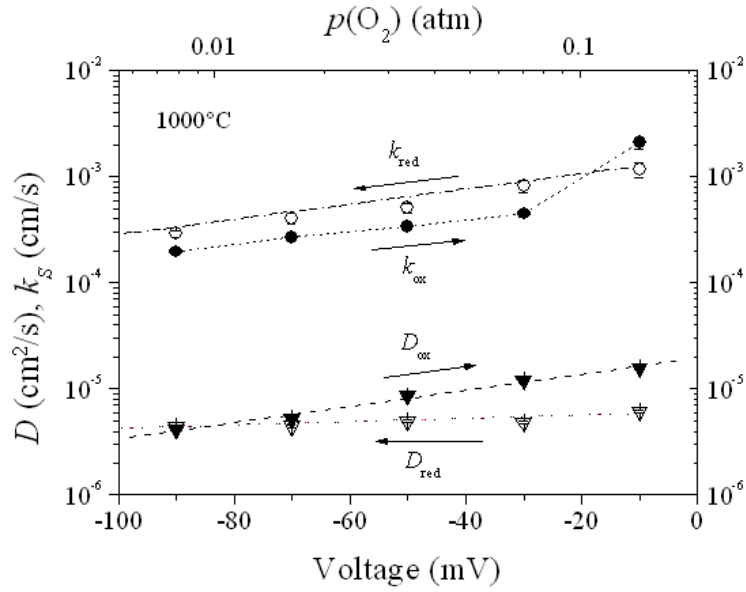
Fig. 7.9. $\tilde{D}$ and k_S coefficients of LSF measured at 1000°C as a function of voltage and the corresponding pO$_2$.

Close to 0 bias, i.e. in air, both $\tilde{D}$ and k_S obtained from oxidation runs are higher than for the reduction runs, which is consistent with the data in Figs. 7.6 and 7.7. But as the voltage is increased negatively, i.e. as the pO_2 is lowered, the tendency is reversed for k_S. Both k_S and $\tilde{D}$ tend to decrease with decreasing pO_2, following approximately a $(pO_2)^{1/2}$ trend.

Critical thickness of LSF, LSFTi2, and LSFTa1 calculated from transport coefficients

For comparison, the critical thickness values of LSF, LSFTi2, and LSFTa1 are plotted in Fig. 7.10 as a function of temperature, measured both for reduction and oxidation steps, shown with solid and open symbols, respectively.
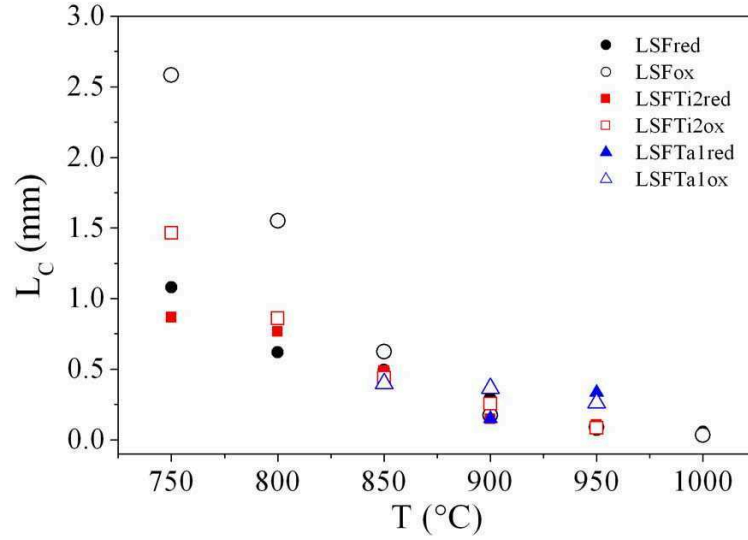
Fig. 7.10. The critical thickness, L_c (mm), of LSF (black circles), LSFTi2 (red squares), and LSFTa1 (blue triangles) as a function of T (°C).

The critical thickness, which is the ratio $\tilde{D}/k_S$, increases with decreasing temperature in case of all samples reaching the thickness of 2.6 mm for LSF at 750°C, measured during an oxidation step. The values obtained during oxidation and reduction steps of LSF results in a considerable difference at low temperatures. The oxidation L_c values show an exponential dependence to the temperature. According to Fig. 7.10, all the samples have higher thickness than the critical value down to 800°C, except that LSF has a considerably high L_c calculated from the oxidation data. However, it can be concluded that at 750°C the oxygen diffusion process is controlled by surface kinetics in all three samples.

It is known that L_c is not an intrinsic material property but may depend on the value of surface exchange coefficient, therefore the surface condition of the sample, i.e. surface roughness or porosity of the surface. It was shown in literature that the overall oxygen flux of the material could be improved by surface modifications, that is, by improving surface exchange coefficient.[159] In addition to the chemistry of the coating layer, the porosity of the layer was found to be very important.[160]

7.4.3. Post-mortem analysis of electrochemical cells

The electrochemical cells used for potential step measurements were investigated using SEM after long-term tests over several weeks. An SEM image of the cross-section of the measured LSFTi2 sample is shown in Fig. 7.11. The sample, YSZ slab, gold-ring spacer, and the formed gas-pocket are indicated in the figure.
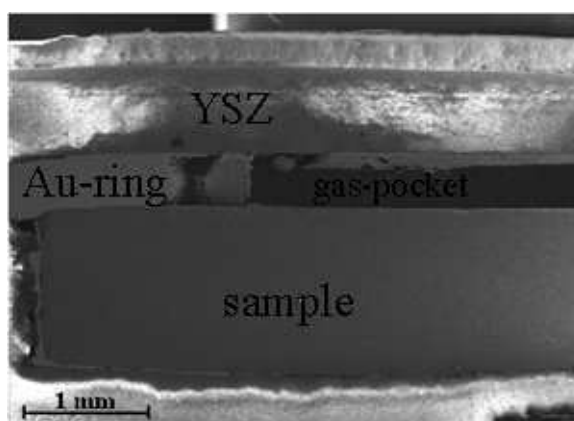

Fig. 7.11. The SEM image of the cross-section of the measured LSFTi2 electrochemical cell.

A similar electrochemical cell without the gold spacer was suggested and used by Belzner et al.[161], however, this cell design was found problematic in case of cobaltates due to interfacial reaction between the YSZ pump and the sample.[37] Therefore, such reaction with the YSZ is not expected in the presented case here. However, the surface of the pellet where oxygen exchange occurs was checked by SEM in addition to the cross-section of the cell. The images of the cross-section of the LSF cell are shown in Fig. 7.12. In the figure, the side of the pellet in contact with gold sealing is shown in (a) and (b). Fig. 7.12 (c) and (d) show the region close to the air pocket and in contact with gold sealing in SE and BSE mode, respectively.
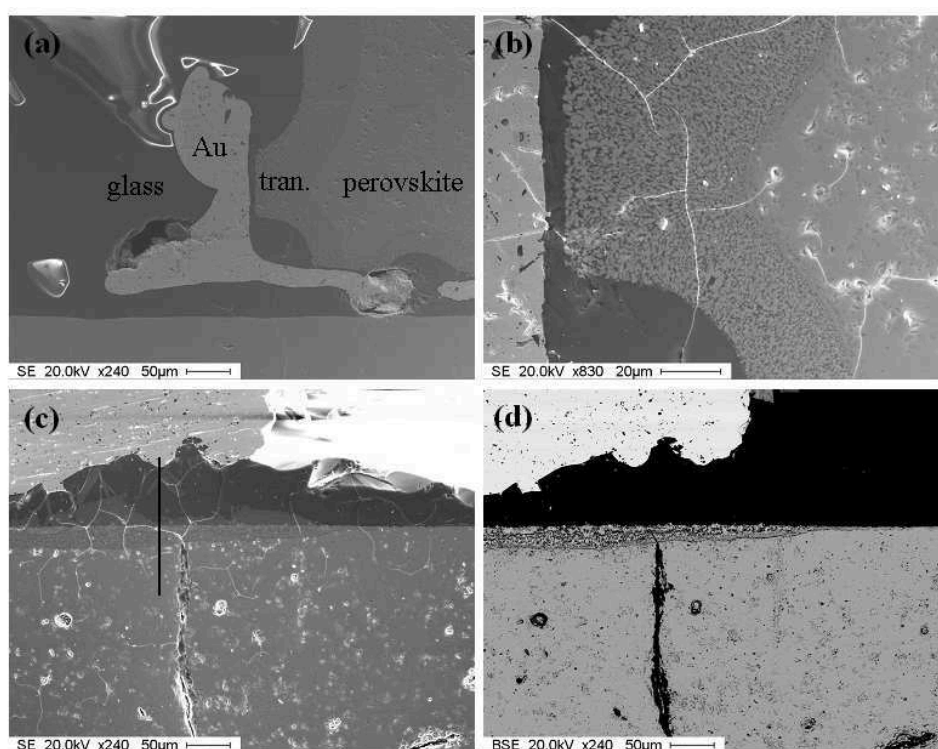
Fig. 7.12. SEM micrographs of the measured LSF cell (a) the corner of the sample, which is in contact with gold sealing, (b) the magnified transition region shown in (a), (c) the region close to the gas-pocket where the sample is in contact with the gold-spacer (d) the same image as in (c) in BSE mode.

There was slight diffusion (~50 μm) of Ca, Na, and mostly Si into the perovskite structure from the sides of the sample, where the sample was covered first by gold and then sealed by glass as seen in Fig. 7.12 a and b. However, the glass was found to come into contact with the sample and it diffused towards the surface of the sample along the Au-contacting areas. Fig. 7.12 shows the distinct regions of glass, gold, the transition region of the sample where the elements in glass diffused, and the perovskite phase. (b) shows the so-called transition region with higher magnification. It is possible to differentiate the two phases in this region. In order to make sure that the diffusion of the glass was restricted to this area, elemental analysis by SEM-EDX was conducted on the contact surface close to the gas-pocket in the same sample. The line of the scan is shown in Fig. 7.12 (c). It was confirmed by the line scan that the diffusion distance was restricted to the region clearly seen in the SEM image.

There were no elements from glass found on the surface of the sample facing the gas-pocket. As a result, the amount of diffusion from the glass sealing was not considered effective on the results given in previous sections.

7.5. Summary and conclusions

In this chapter, electrochemical characterization of LSF, LSFTi2, and LSFTa1 was performed using the potential step technique. The current relaxation of the materials as a result of an applied voltage was monitored as a function of temperature and pO_2. A cell design where the sample was blocked ionically on one surface and electronically on the other was used. The chemical diffusion ($\tilde{D}$) and the surface exchange (k_S) coefficients were calculated from the relaxation data by fitting asymptotic equations using Fick's second law. The transport coefficients calculated from oxidation steps were found to be higher than the values for reduction step. LSFTi2 material was found to have slightly higher coefficients compared to LSF and LSFTa1. Both chemical diffusion and surface exchange coefficients decreased with reduced partial pressure of oxygen. The critical thickness (L_c) of the samples was calculated using the chemical diffusion and surface exchange coefficients. The L_c increased with decreased temperature exceeding 1 mm in all samples at 750°C, suggesting that the flux was controlled by surface exchange rate at this temperature.

Scanning electron microscopy was used to investigate the microstructures of the samples after the long-term measurements. Special attention was given to the surface of the pellets at which the oxygen exchange occurred. Slight diffusion of glass sealing into the sample (max 50 μm) was observed, however, the surface active for oxygen exchange was found free of the elements from the glass, such as Si, Na, and Ca.

Chapter 8

Oxygen permeation under air/argon gradient and ionic conductivity of $La_{0.5}Sr_{0.5}Fe_{1-y}(Ti/Ta)_yO_{3-\delta}$

In this chapter of the thesis, the oxygen permeation flux of $La_{0.5}Sr_{0.5}Fe_{1-y}(Ti/Ta)_yO_{3-\delta}$ materials are reported, the effect of Ti/Ta substitutions is discussed. The permeation measurements were conducted on planar disc-shaped membranes under air/Ar gradient. Ionic conductivities of the samples were calculated using these results and the electrochemical data reported in the previous chapter. In addition, the chemical diffusion and surface exchange coefficients were used to calculate the oxygen permeation for comparison with the results obtained from permeation measurements.

8.1. Introduction

In the previous chapter, the oxygen transport properties including the chemical diffusion and surface exchange coefficients were examined. These coefficients provide information on the diffusion of oxygen in the bulk and the surface exchange kinetics and they can be used to calculate an overall behavior of the materials, in reality, the oxygen flux obtained from the material may differ. Some of the reasons for this can be due to the surface condition, the geometric shape of the sample, simplifying assumptions for the oxygen diffusion in the sample or different measurement conditions. It should be noted that the $\tilde{D}$ and k_S measured in the previous chapter basically corresponds to the air atmosphere and their relation to oxygen permeation requires certain assumptions such as extrapolation to real pO_2 difference. Even though these parameters are important to understand the oxygen permeation through the oxide, it is difficult to predict precisely the permeation rate out of these values and therefore the permeation rate is better determined experimentally.

One of the most useful characterization methods to determine the overall performance of the material is to measure the oxygen permeation, also known as the oxygen transport rate. The oxygen permeation flux is a measure of the amount of oxygen passing through the membrane per unit area and time and is mostly reported in $\mu mol.cm^{-2}.s^{-1}$ or $ml.cm^{-2}.min^{-1}$. It is measured by imposing an oxygen partial pressure gradient across the membrane either by flowing oxygen-rich and lean gases on two sides of the membrane or by vacuuming on one side of the membrane, depending on the use of the oxygen separation membrane. In this case, the method using two gasses with different oxygen activity is considered because the particular interest is the partial oxidation use in this study.

The aim of this chapter is to study the oxygen permeation of LSF, LSFTi2, and LSFTa1 planar membranes under air/argon gradient as a function of temperature and under air/(argon + air mixture) gradient as a function of pO_2 for LSF sample.

8.2. Theory

The theory of the oxygen transport in mixed conducting oxides was explained in the previous chapter (section 2.3) and Wagner's equation for bulk transport was introduced. In this section, the equations that will be used later in the chapter will be given.

8.2.1. Calculation of oxygen permeation flux from transport coefficients

The chemical diffusion ($\tilde{D}$) and surface exchange (k_S) coefficients can be used to calculate the oxygen permeation flux (J_{O_2}) using the equation[37],

$$j_{O_2} = -\frac{j_v}{2} = -\frac{\Delta\delta}{2V_m\left(\dfrac{1}{k_0} + \dfrac{1}{k_L} + \dfrac{L}{\tilde{D}}\right)} \tag{8.1}$$

where j_v is the oxygen vacancy flux, $\Delta\delta$ is the difference in oxygen nonstoichiometry across the membrane, V_m is the molar volume, k_0 and k_L are the surface exchange coefficients on both sides of the membrane. For direct comparison, the permeation values were calculated by using the following formula, to which a term for the partial pressure of oxygen is incorporated,

$$j_{O_2} = -\frac{\Delta Q}{\Delta E \times V_{cell} \times \left(\dfrac{1}{k_S} + \dfrac{L}{\tilde{D}}\right)} \frac{RT}{16F^2 \ln \Delta pO_2} \tag{8.2}$$

Where ΔQ is the total charge extracted from the sample during the potential step, ΔE is the potential step applied, V_{cell} is the volume of the sample, R and F are gas and Faraday's constants, and ΔpO_2 is the oxygen partial pressure difference across the membrane.

8.2.2. Literature on permeation of MIEC perovskites

As explained before, the oxygen permeation through a membrane is basically controlled by these two parameters, the diffusion in the bulk and the surface oxygen exchange on the air and the lean side of the membrane. The surface exchange kinetics are shown to play a role (partial or totally) in determining the rate of oxygen transport in real life, therefore has an effect on the overall rate up to an extent as it was shown in Fig. 2.4.[162] However, as long as the bulk diffusion prevails the sample thickness has an influence on the oxygen permeation flux, which increases with decreasing thickness. In addition, the permeation flux is known to be affected by microstructural features such as grain size[43], porosity, surface roughness. These dependencies might lead to scatter in the published data. Additionally, it is important to pay attention to the conditions of the measurements.

The general trends of the permeation flux as a function of composition were explained in Chapter 2. In this section, the permeation values measured in conditions similar to this study will be given (when available) for comparison. The effect of redox stability of the B-site cation on the oxygen flux is known. The more stable the cation is, the lower the oxygen flux gets. In the pioneering work by Teraoka et al.[22] it was shown that the oxygen flux of a 1.5 mm thick $La_{0.6}Sr_{0.4}CoO_{3-\delta}$ membrane measured in helium was decreased from 0.7 to 0.45 $\mu mol.cm^{-2}.s^{-1}$ by substitution of 20% Fe on the B-site at 865°C. Whereas it was increased to 1.32 $\mu mol.cm^{-2}.s^{-1}$ by substitution of 20% Cu when measured under the same conditions.

The oxygen permeation flux of $La_{0.5}Sr_{0.5}FeO_{3-\delta}$ was found to increase with decreasing pO_2 on the lean side down to 0.021 atm at 950°C and to 0.008 atm at 800°C. The flux was independent of the membrane thickness at 800°C suggesting that the surface exchange was dominating; however, thinner membrane showed higher flux at 950°C showing an thickness influence[52]. In the same work, it was shown that the oxygen flux was decreased by substitution of 10% Ti on the Fe side and the thickness dependency was increased at both measurement temperatures.

Lein et al.[163] measured the $La_{0.5}Sr_{0.5}FeO_{3-\delta}$ material under air/helium gradient at temperatures above 1000°C. At this temperature the oxygen flux was around 0.18 $ml.cm^{-2}.min^{-1}$ and the flux measured at around 1070°C was found to decrease slightly over time from 0.5 to 0.4 $ml.cm^{-2}.min^{-1}$ after 10 days and remain stable after 20 more days. The decrease of the flux at 1148°C with decreasing pO_2 was related to the surface exchange becoming dominant. After the long-term measurements, $SrFe_{12}O_{19}$ was observed on the air side of the membrane.

There is no published data on the oxygen permeation of LSFTa1 material in any condition and of LSFTi2 measured under air/argon gradient.

8.3. Experimental set-up for permeation measurements

The pellets used for the permeation measurements were prepared as explained in section 3.3.1. The disc-shaped pellets were uniaxially pressed using dies with 30 mm diameter. Both surfaces of the pellets were polished by SiC paper down to 2500 grit.

The oxygen permeation measurements were conducted under air/argon gradient. The pellets with a diameter of 25 mm were clamped between two alumina tubes with two gold-rings as sealings between the sample and the alumina tubes.[164] The schematic of the permeation measurements is shown in Fig. 8.1. The membrane was initially heated in an air/argon gradient up to 1050°C in order to soften the gold and tighten the sealing. The temperature was then decreased to the measurement temperature. Air (50 ml/min) was flown on one side of the sample and argon (100 ml/min) on the other.
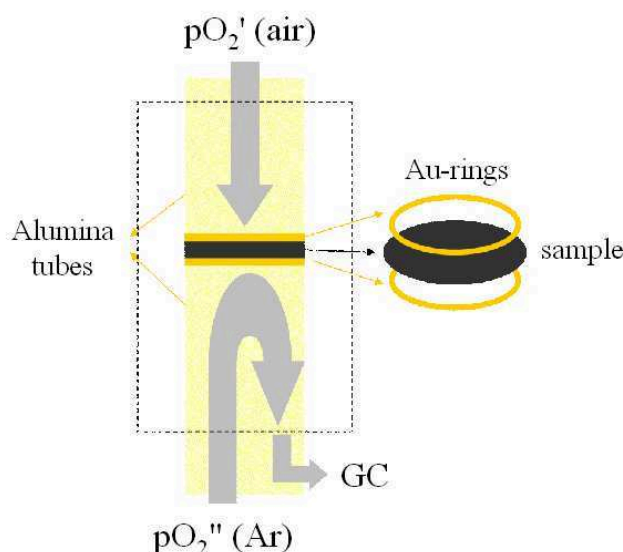
Fig. 8.1. The schematic of the setup for permeation measurements for planar membranes.

The composition of the outlet gas from the argon side was analyzed using a gas chromatograph (Varian) equipped with a molecular sieve 5 Å capillary column.[42, 164] The permeation measurements were conducted during cooling from 1000°C to 750°C at 25 or 50 K intervals. The final permeation values at each temperature were recorded after a certain dwell time for equilibration.

The thickness of the LSF, LSFTi2, and LSFTa1 membranes were 1.27, 1.1, and 0.92 mm, respectively. All the permeation values were normalized to 1 mm to allow the comparison among the compositions, which had slightly differing membrane thickness. The normalization was done assuming the permeation increases linearly with decreasing thickness. Therefore, the values were multiplied by the thickness of the sample and divided by 1 mm to conserve the same unit.

Bouwmeester et al.[7] stated that the sealing of the pellets decreases the active surface for oxygen flux where the bulk remains the same and this causes deviation from one-dimensional oxygen transport. Therefore, neglecting the edge effects may affect the results. They introduced a geometrical factor (G) for the correction of the flux that depends on a/b and b/L, where a is the radius of the active surface of the pellet, b the radius of the whole pellet and L the thickness of the sample. The geometric factor, G, increases with decreasing a/b ratio (the fraction of the sealed area increases) and with decreasing b/L. With the sample size and geometry used in this study, both a/b (~0.9) and b/L are large, therefore the geometrical factor is negligible.

8.4. Oxygen permeation of $La_{0.5}Sr_{0.5}Fe_{1-y}(Ti/Ta)_yO_{3-\delta}$

8.4.1. Permeation under air/Ar gradient

The initial temperature program for the permeation measurements was to cool down the sample by 5 K/min and allow 1 hour for equilibration. The permeation of LSFTi2 membrane measured during cooling from 1000°C to 750°C and heating back to the same temperature with this program is shown in Fig. 8.2 (in logarithmic scale) as a function of the inverse of the temperature. The membrane was kept at 750°C over two days prior to the heating.
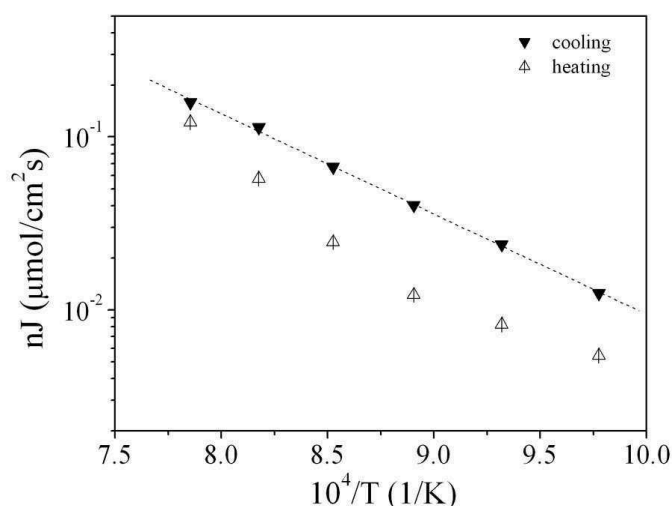
Fig. 8.2. The permeation of LSFTi2 measured during cooling and heating after 1 hour of equilibration time at each temperature, solid and open symbols show the cooling and heating curves, respectively.

The values measured during cooling showed a logarithmic dependence to the inverse of the temperature, decreasing more than an order of magnitude from 0.14 at 1000°C to 0.01 $\mu molcm^{-2}s^{-1}$ at 750°C. The permeation dropped considerably at 750°C over the time it was kept at this temperature. The sample recovered the permeation values only after reaching 1000°C. Therefore, the samples were kept at the same temperature until the equilibrium values were attained, which took a varying amount of time from a few hours at high temperature (> 900°C) to a few days at lower temperature (< 850°C). In addition, the equilibration time was observed to be systematically longer for a heating step than for a cooling step. The slow equilibration of the permeation flux through a LSF membrane following a heating step from 925 to 950°C is shown in Fig. 8.3. It is observed in this figure that it takes around 200 hours to reach the equilibrium permeation value.
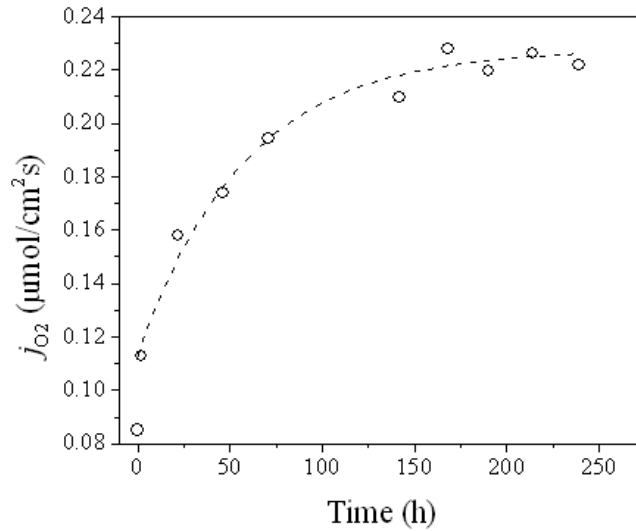
Fig. 8.3. Slow equilibration of the permeation of the LSF membrane during heating from 925 to 950°C.

The difference in equilibrium rates during cooling or heating is consistent with the kinetical difference between oxidation and reduction steps of the potential step measurement discussed in the previous chapter (7.4.2). During cooling, the membrane incorporates oxygen to maintain its equilibrium oxygen concentration, which corresponds to an oxidation process. On the other hand, during heating, the membrane releases oxygen, which corresponds to a reduction process. As a result of the potential-step measurements, the chemical diffusion and surface exchange coefficients measured during oxidation step were higher than the reduction values. Therefore, both techniques provide the similar result that the incorporation of oxygen into the structure occurs faster than the release of it.

The equilibrated oxygen permeation data for LSF, LSFTi2, and LSFTa1 are shown in Fig. 8.4 as Arrhenius plots. In order to allow direct comparison, the values were normalized as mentioned before by multiplying the fluxes by the membrane thickness assuming that the oxygen transport through the membrane is governed by bulk diffusion. The corresponding activation energies are shown in the same figure in kJ/mol.
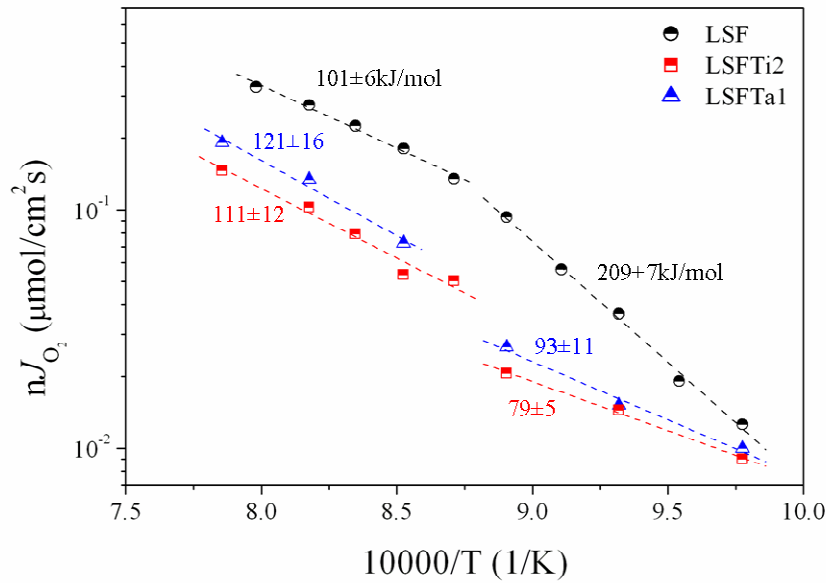
Fig. 8.4. Arrhenius plots of equilibrated permeation for LSF, LSFTi2, and LSFTa1 with the corresponding activation energies.

LSF has higher permeation than LSFTi2 and LSFTa1. The partial substitution of Fe with Ti or Ta decreases the concentration of oxygen vacancies that are the mobiles species, and thus reduce both the oxygen permeation flux and the ionic conductivity. This result is consistent with the data reported in literature for similar compositions substituted with Ti and Ga.[52, 53] The activation energies in the higher temperature zone (100-120 kJ/mol) are similar to the reported values for similar materials such as $La_{0.4}Sr_{0.6}Fe_{0.8}Co_{0.2}O_{3-\delta}$[14] with E_a = 105.6 kJ/mol (air/helium gradient) and $La_{0.5}Sr_{0.5}FeO_{3-\delta}$[163] with E_a = 105 kJ/mol (during cooling under air/helium gradient).

Another important feature seen in Fig. 8.4 is that all the plots show a discontinuity around 875°C, which corresponds to the temperature below which the equilibration of the flux becomes very slow. In the higher temperature region, all three samples have similar activation energies within the error limits. However, in the lower temperature region they are very different.

In case of LSFTi2 and LSFTa1, there is a drop in the permeation around 875°C. The activation energies below this temperature are lower (79 and 83 for LSFTa1 and LSFTi2, respectively) than the higher temperature activation energies (111 and 123 kJ/mol). This behavior suggests a change in the structure of the material. Structure related changes in the permeation were reported by Deng et al.[165] for $SrCoO_{3-\delta}$ and $Sr_{0.9}Ca_{0.1}Co_{0.89}Fe_{0.11}O_{3-\delta}$. In their case, both materials showed sharp decrease, which was related to the phase transformation from hexagonal to cubic for $SrCoO_{3-\delta}$ and from brownmillerite to cubic for the latter material. The phase changes were shown by high-temperature XRD measurements and could be observed by differential thermal analysis. However, for these materials, the change in the

permeation was substantial dropping from values above 1 $\mu molcm^{-2}s^{-1}$ to values around 10^{-6} $\mu molcm^{-2}s^{-1}$. Kruidhof et al. reported a similar behavior for $SrCo_{0.8}Fe_{0.2}O_{3-\delta}$ to the one observed in this study. The behavior was attributed to an order-disorder transformation, from the high temperature perovskite phase, where the oxygen vacancies are distributed randomly, to the lower temperature two-phase low-temperature form. The two-phase structure involves brownmillerite phase in addition to perovskite, where the vacancies are ordered and thus less mobile.[166] The possibility of oxygen vacancy ordering will be discussed further later.

The discontinuity observed for LSF has a different characteristic compared to LSFTi2 and LSFTa1. LSF basically shows two regions with different activation energies. The activation energy doubles to 209 kJ/mol at temperatures lower than 875°C. The critical thickness of the LSF sample at 875°C can be deduced from the Fig. 7.10 reported in the previous chapter. According to the figure, L_c is 0.6-1 mm from the reduction and oxidation potential step measurements. However, L_c was reported to increase with decreasing pO_2. Considering that the thickness of the LSF permeation membrane was 1.27 mm, it is possible that the oxygen transport in the LSF membrane under air/argon gradient was governed by surface exchange kinetics above 875°C. This two-region behavior with different activation energies for $La_{0.5}Sr_{0.5}FeO_{3-\delta}$ materials has not been observed in studies reported by other authors; however, the measurement conditions were either not the same (low pO_2)[52] or the conditions of the measurements were not clear.[163] On the other hand, in a study on the same composition a similar behavior was observed.[43] The material was found to be independent of thickness at higher temperature region suggesting that the surface exchange was the rate limiting.

On the other side, slow equilibration in LSF-based materials has already been reported by other groups[52, 59, 95] at intermediate pO_2 ranges (10^{-7}-10^{-14} atm) but no clear explanation was given. This behavior could be related to a gradual ordering of oxygen vacancies as discussed by Grenier *et al.* for $La_{1-x}Sr_xFeO_3$ and other related compounds such as $La_{1-x}Ca_xFeO_3$ and $CaTi_{1-2y}Fe_{2y}O_{3-y}$.[24] Mössbauer spectroscopy showed that even at low levels of vacancies, the defects tend to associate, transforming the octahedral site of the metal M into a tetrahedral site, this despite the maintenance of the pseudo-cubic symmetry observed by XRD. The presence of Fe seems to favor this transformation because it can equally occupy each type of site.[167] Association of vacancies is expected to reduce their mobility or, in other words, to reduce the concentration of mobile species. This might have an important influence on the ionic conductivity, which is proportional to the concentration of mobile species.

In order to evaluate the temperature and pO_2 conditions in which such an order-disorder transition would occur, an approximate phase diagram was established on the basis of the observations reported by Grenier et al.[24] The critical oxygen non-stoichiometry (y_c), beyond which ordering occurs, was determined from the structural evolution of various compositions of LSF annealed at different temperatures (T_r). The temperature dependence of

y_c is shown in Fig. 8.5 along with the diagram. For each value of y_c, the corresponding pO_2 was determined for LSF using the data from the work of Mizusaki et al.[33].
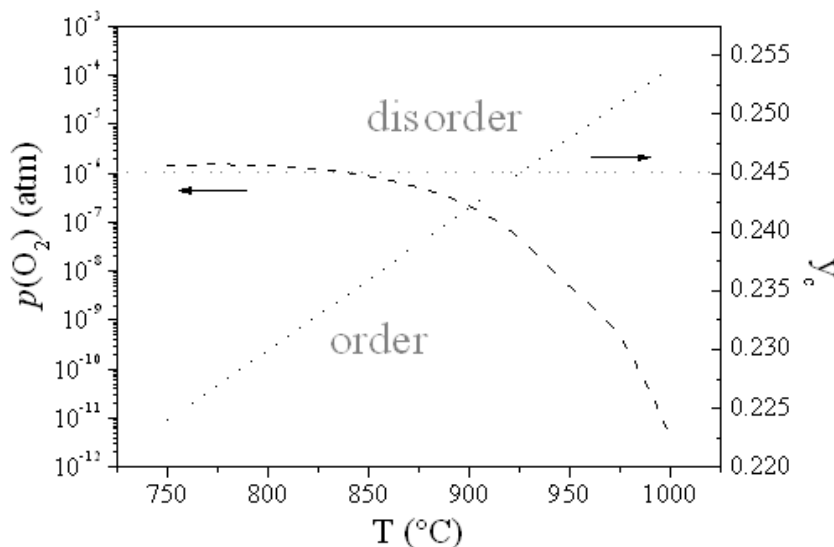

Fig. 8.5. Phase diagram for the order–disorder transition in LSF with the values of the critical oxygen nonstoichiometry redrawn from the data in Ref.[24], taken from Ref.[148]

According to this approximate diagram, the order-disorder transition occurs at more reducing pO_2 as the temperature is increased. Below 850°C, the critical pO_2 is around 10^{-6} atm., which is close to the value obtainable in an air/argon gradient. It is therefore possible that such an order-disorder transition may occur during permeation experiment in an air/argon gradient. The TGA results reported in section 4.6 show that LSF material has nonstoichiometry change ($\Delta\delta$) of around 0.08 at 900°C under argon atmosphere. Lein et al.[63] measured the room temperature stoichiometry (3-δ) as 2.965, at 900°C in air as 2.875, and at 900°C in N_2 atmosphere as 2.785, therefore the total non-stoichiometry at 900°C in N_2 is 0.215. The nonstoichiometry change at 900°C from air to N_2 is calculated as 0.09, which is in good agreement with the value measured in this study. As a result, although the nonstoichiometry of the LSF material is close to what is shown in Fig. 8.5, the ordering of the vacancies remain speculative, especially for LSFTi2 and LSFTa1, which are expected to lower total nonstoichiometry at the same conditions.

The permeation values of LSF, LSFTi2, and LSFTa1 will be discussed further in the next chapter considering their behavior when measured as partial oxidation membranes.

The dependence of oxygen permeation flux of LSFTi2 membrane to the partial pressure of oxygen measured at 850, 900, 950, and 1000°C is shown in Fig. 8.6. The data is plotted as a function of logarithm of pO_2 of the lean side.
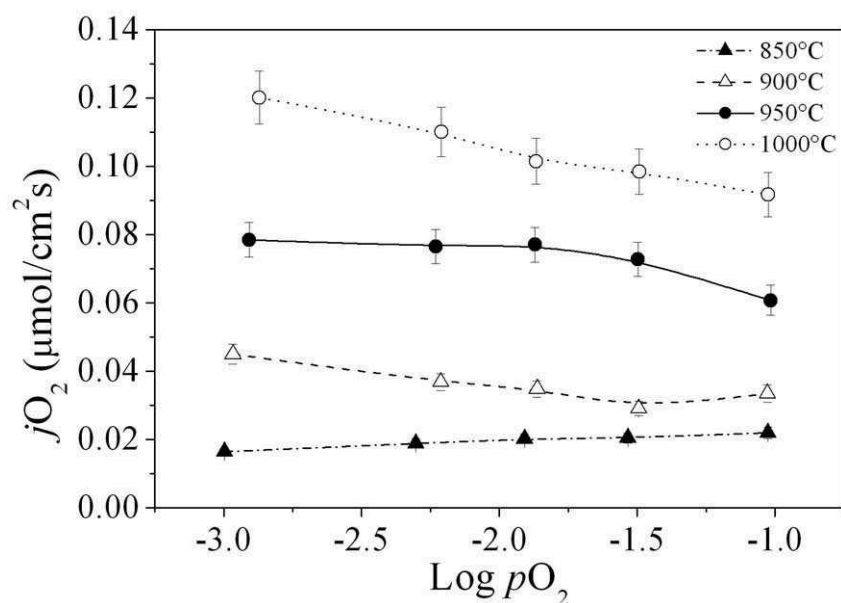
Fig. 8.6. Permeation of LSFTi2 as a function of pO_2 measured at temperatures 850°C-1000°C.

The permeation of LSFTi2 increases with decreasing pO_2 except for at the lowest temperature, 850°C. The permeation is expected to increase with lowered partial pressure of oxygen as this increases gradient and thus the driving force across the membrane. This of course is the case as long as the bulk diffusion of oxygen is the rate-determining step. Therefore, these results indicate that at 850°C, either the surface exchange rate becomes a rate-limiting factor or the oxygen vacancy ordering affects the permeation rate. A similar result was observed by Lein et al.[163] for $La_{0.5}Sr_{0.5}FeO_{3-\delta}$ material, decreasing pO_2 caused first leveling and then dropping of the flux at 1045°C and the authors attributed this result to change of rate limiting step from diffusion to surface exchange.

As a final remark, all three samples were investigated by scanning electron microscopy on their surfaces and along the cross-sections. No phase change or second-phase formation was observed in any case.

8.4.2. Oxygen permeation flux calculated from electrochemical data

In order to compare and see the relation of electrochemical coefficients and the oxygen permeation flux, the calculated permeation values of LSF, LSFTi2, and LSFTa1 are shown in Fig. 8.7 along with the measured values. The calculated values correspond to the averages of the two permeation values calculated from oxidation and reduction steps assuming an air/argon gradient. The measured permeation values are the ones previously shown in Fig. 8.4. In the calculation of the permeation Eq. 8.2 was used unless otherwise mentioned in the legend.
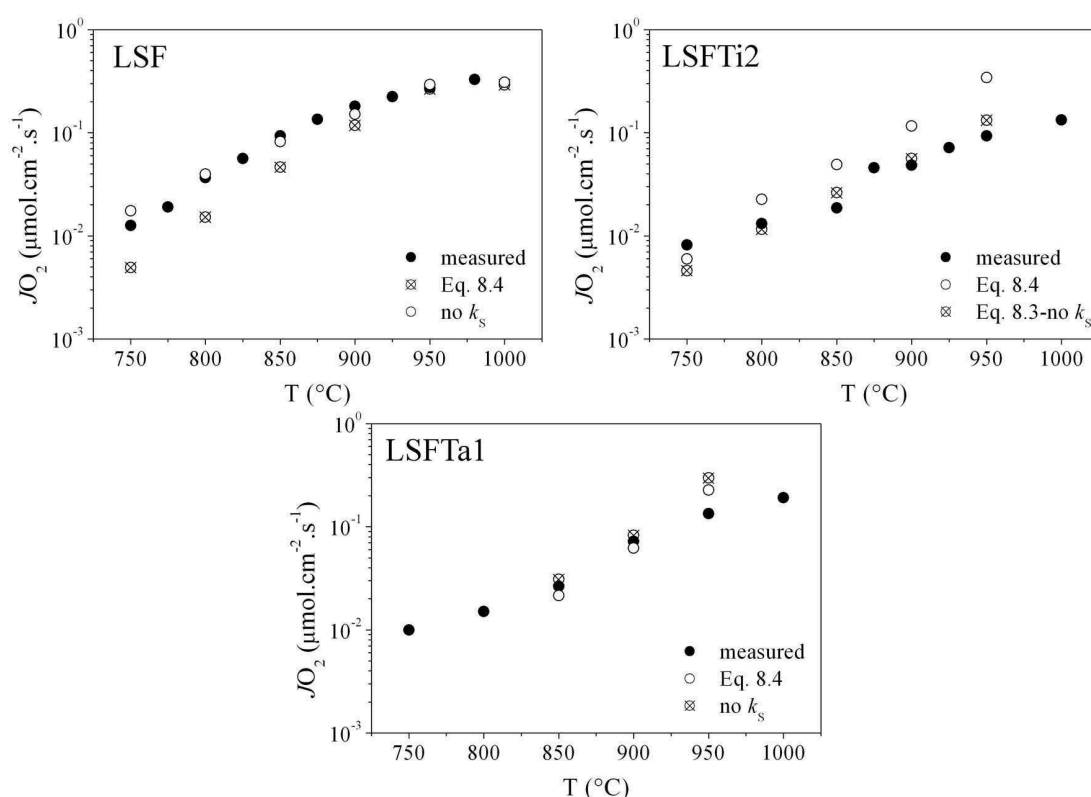
Fig. 8.7. Permeation values of LSF, LSFTi2, and LSFTa1 directly measured and calculated from transport coefficients measured by potential step (Chapter 7).

Two calculated permeation values are given in Fig. 8.7, one of which was calculated using Eq. 8.1 and the other one was calculated using the same equation by with the surface exchange coefficient (k_S) omitted. At temperatures above 900°C, both values are in good agreement with the measured values. However, the calculations made by omitting the k_S seem to fit much better at lower temperature. In case of LSFTa1, the calculations (with or without k_S) provide similar values except at 950°C. The calculated permeation value is higher than the measured one. This result is understandable if the high activation energy, $\tilde{D}$ and k_S are values measured during oxidation step of LSFTa1 material are considered. Finally, for

LSFTi2 sample, the calculated permeation fluxes from Eq. 8.2 resulted in considerably higher permeation either with or without the surface exchange coefficient. For this sample, another permeation calculation was made using equation 8.1 (without k_S). The non-stoichiometry difference across the membrane ($\Delta\delta$) was estimated using the value measured by TGA at 900°C changing the atmosphere from air to argon (shown previously in Fig. 4.19) together with the nonstoichiometry values obtained from potential-step measurements. The permeation calculated in this way was in better agreement.

8.4.3. Ionic conductivities calculated from electrochemical and permeation data

As previously explained in section 2.3.3, the ionic conductivity of the samples can be calculated by implementing the results of the potential step and permeation measurements into the equations 2.17 and 2.18, respectively. The resulting ionic conductivities (σ_i) of LSF, LSFTi2, and LSFTa3 are shown in Fig. 8.8. The conductivities calculated from transport coefficients (the average of oxidation and reduction steps) are shown in the left plot as an Arrhenius plot. These values are compared with the conductivities calculated from the oxygen flux in separate plots as given on the right side of the figure and designated as LSF, LSFTi2, and LSFTa1. It is important to point out that the relaxation data were measured in air whereas the permeation data correspond to the averaged values over an air/argon gradient.
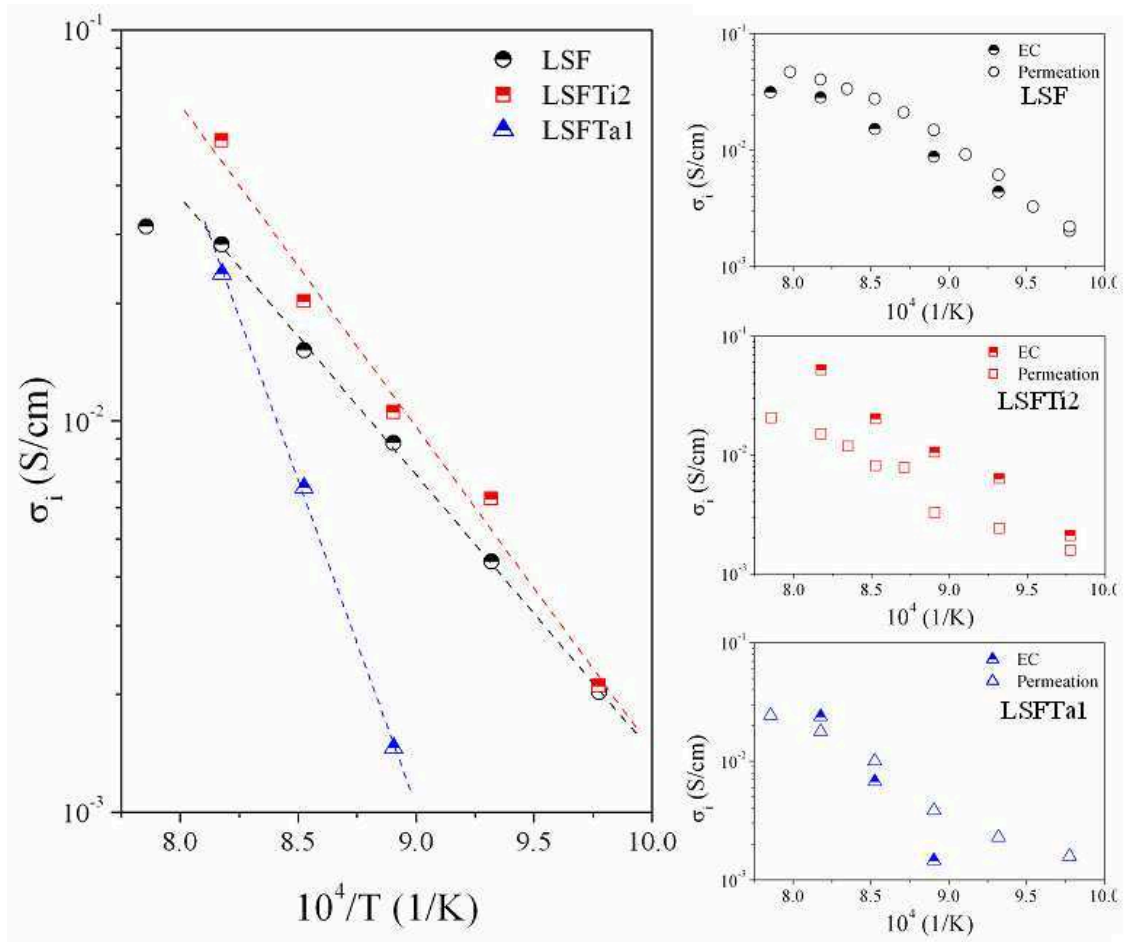
Fig. 8.8. Ionic conductivity values calculated from permeation and electrochemical data.

The ionic conductivities of LSF, LSFTi2, and LSFTa1 calculated from transport coefficients (air) are in the range of 0.0068 – 0.02 S/cm at 900°C and the highest value belongs to LSFTi2. The corresponding oxygen ion transference numbers are $1 \times 10^{-4} – 4 \times 10^{-4}$.

In case of LSF, the ionic conductivities calculated from both data are consistent considering the abovementioned condition. On the contrary, the LSFTi2 values differ more. This indicates that oxygen transport in LSFTi2 is strongly lowered in more reducing conditions. The activation energies (E_a) calculated from the Arrhenius plots ($\ln(\sigma_i.T)$ vs. $1/T$) of the data given in Fig. 8.8 are shown in Table 8.1 below. The activation energies calculated for potential step and permeation measurements are denoted by $E_{a,PS}$ and $E_{a,permeation}$, respectively. The ionic conductivities at 900°C determined from PS data are listed together with the total conductivities reported previously in Chapter 5. The oxygen ion transference numbers shown are the fraction of ionic conductivity compared to the total conductivities. These values indicate clearly that the ionic conductivity is negligible compared to the total conductivity.

Table 8.1. Activation energies of ionic conductivities of LSF, LSFTi2, and LSFTa1 calculated from potential step and permeation measurements, the oxygen ion transference number t_O at 900°C calculated from PS data

Composition	$E_{a,PS}$ (kJ/mol)	$E_{a,permeation}$ (kJ/mol)	$\sigma_{i, PS, 900°C}$ (S/cm)	$\sigma_{total, 900°C}$ (S/cm)	t_0
LSF	116	81	0.0152	156	1×10^{-4}
		175			
LSFTi2	175	108	0.0162	37*	4×10^{-4}
LSFTa1	308	116	0.0068	42	2×10^{-4}

* The value was determined by extrapolating the conductivity data to 900°C

The ionic conductivity of LSF and LSFTi2 are in the same range while it is decreased to less than half by Ta substitution. The activation energies calculated from both methods show large differences, especially in case of LSFTa1 owing to the high E_a of the transport coefficients during oxidation. However, in general the values are in similar range with the published data.[93, 96] Fagg et al.[51] reported that $La_{0.4}Sr_{0.6}Ti_{0.4}Fe_{0.6}O_{3-\delta}$ material has an ionic conductivity around 0.01 S/cm at 900°C, an activation energy of 133 ± 17, and ionic transference number of 6.3×10^{-4} at 915°C. On the other hand, considerably higher ionic conductivity (~0.4 S/cm) for $La_{0.5}Sr_{0.5}FeO_{3-\delta}$ material is reported at 900°C.[59]

8.5. Summary and conclusions

The oxygen permeation fluxes of disc-shaped planar membranes of LSF, LSFTi2, and LSFTa1 materials were measured under air/argon gradient. The permeation was measured as a function of temperature. The permeation of LSF material was reduced from 0.18 µmol.cm^{-2}.s^{-1} to 0.05 and 0.07 µmol.cm^{-2}.s^{-1} by the substitution of Ti and Ta, respectively at 900°C.

All three samples showed a change in the permeation behavior around 875°C. The activation energy for the oxygen permeation of LSF was doubled at lower temperatures (750 – 875°C) compared to the higher temperature region (875 – 1000°C). The change in the activation energy was attributed to a change in the rate-determining step, which is chemical diffusion at low temperatures to surface exchange at higher temperatures. On the other hand, LSFTi2 and LSFTa1 showed a decrease of the permeation around 875°C. The activation energies at lower temperature region were lower for both materials than the high-temperature region. Oxygen vacancy ordering was considered to explain this behavior. The oxygen permeation of LSFTi2 was measured as a function of pO_2 in the temperature range of 850 – 1000°C. As a result, the permeation was found to increase with lowered pO_2 except for the measurements conducted at 850°C, which decreased instead. These results indicated that the oxygen transport was surface exchange limited at 850°.

The ionic conductivities of LSF, LSFTi2, and LSFTa1 were calculated using the permeation data measured under air/argon gradient and the transport coefficients (chemical diffusion and surface exchange) measured by potential step technique discussed in the previous chapter. At 900°C, the materials had ionic conductivities in the range of 0.0068 – 0.02 S/cm, highest value belonging to the LSFTi2 sample. The corresponding oxygen ion transference numbers were 1×10^{-4} – 4×10^{-4} at 900°C in air, which shows that the materials are predominantly electronic conductors.

Chapter 9

Partial Oxidation Reactor Testing of La$_{0.5}$Sr$_{0.5}$Fe$_{1-y}$(Ti/Ta)$_y$O$_{3-\delta}$

The permeation of the LSF, LSFTi2, and LSFTa1 samples was measured using air and argon/methane mixture as a function of temperature. LSF and LSFTi2 were measured in tubular form, while a planar membrane was used for LSFTa1 sample. The measurements were initiated under air/argon gradient and methane was introduced slowly to the lean side as far as the membrane remained intact. The microstructure of the POX membranes was investigated by scanning electron microscopy after the tests were terminated.

9.1. Introduction

The main process of partial oxidation was explained in Chapter 1 of this thesis together with the necessary properties a membrane material should possess. In the previous chapter, the oxygen permeation flux of the LSF, LSFTi2, and LSFTa1 membranes was investigated using air on the oxygen rich side and Ar on the lean side. These measurements provided important information on the effect of B-site substitution and determination of the rate limiting step, either surface exchange or bulk oxygen transport. However, it is known that the oxygen partial pressure gradient imposed on the material by air and argon is not nearly close to the real operating conditions of these materials as partial oxidation reactors, where methane is used on the lean-side. Therefore, the technically relevant conditions imposed on the materials are expected to cause additional problems, such as increased chemical strain, cation segregation and phase decomposition. A material can be tested using small gradients in order to see if it is feasible to consider or for a comparison, however, it is vital to test the material under realistic conditions to see the real performance of it. In addition, it is necessary to evaluate important parameters such as methane conversion and carbon monoxide selectivity. It is often possible to find permeation studies on a material conducted most probably under an air/inert gas gradient; however, it is much less common practice to do measurements using reducing gases and also the long-term stability tests.

As the concluding chapter of this thesis, the LSF, LSFTi2, and LSFTa1 materials were investigated as partial oxidation reactors. Due to geometrical considerations tubular membranes were decided for partial oxidation tests and thermoplastic extrusion was preferred to produce tubular membranes as it provides a flexible dimension range and high green density. It was possible to produce LSF and LSFTi2 tubes using thermoplastic extrusion. Due to time restrictions, the LSFTa1 POX membrane was produced as a planar pellet.

9.2. Theory

Thermoplastic extrusion is found useful for producing tubular membranes for oxygen separation applications.[168] Tubes rather than plates may be preferable for oxygen separation membranes considering the mechanical stability, effectiveness, and the ease of application, e.g. for sealing purposes. Thermoplastic extrusion has been used by several groups to produce perovskite tubes of different compositions.[70, 164, 168, 169] Very good mechanical stability of the green body is a big advantage considering the handling of the samples and this provides the possibility to produce tubes with thin walls (<200μm).

Evaluation of POX reactor data

When the membrane was operated as a POX reactor using methane (CH_4), the oxygen fluxes of the membranes could not be measured directly from the outlet gas as the oxygen permeating through readily reacts with CH_4. Instead, they were calculated (together with the POX reactor performances) from the gas composition of the outlet gas and using conservation equations as explained by Diethelm et al.[164] The compounds defined from the gas chromatography measurements are N_2, H_2, H_2O, CO, CO_2, and CH_4. The conversion of CH_4 (X_{CH_4}) and the selectivity of CO (S_{CO}) are calculated using the fractions of above mentioned compounds (x_{CH_4}, x_{CO}, and x_{CO_2}) by following equations,

$$X_{CH_4} = 1 - \left(\frac{x_{CH_4}}{x_{CH_4} + x_{CO} + x_{CO_2}} \right) \tag{9.1}$$

$$S_{CO} = \frac{x_{CO}}{x_{CO} + x_{CO_2}} \tag{9.2}$$

The oxygen fluxes of the membranes were calculated using the conservation equations for C, H, and O as shown below in equations 9.3, 9.4, and 9.5, respectively.

$$x_{CH_4,in} = x_{CH_4,out} + x_{CO,out} + x_{CO_2,out} \tag{9.3}$$

$$4x_{CH_4,in} + 2x_{H_2O,in} = 4x_{CH_4,out} + 2x_{H_2O,out} + x_{H_2,out} \tag{9.4}$$

$$2x_{O_2,perm} + x_{H_2O,in} + 2x_{O_2,leak} = 2x_{O_2,out} + x_{H_2O,out} + x_{CO,out} + 2x_{CO_2,out} \tag{9.5}$$

The subscripts "in", "out", "perm", and "leak" are used to indicate the fraction belonging to the inlet gas, outlet gas, the oxygen permeating through the membrane, and oxygen leaking to the system, which is corrected from the amount of N_2, respectively.

9.3. Experimental

Two types of geometries were used for the performance test of the membranes. LSF and LSFTi2 membranes were produced in tubular shape by thermoplastic extrusion.[170] The details of the production of the tubular membranes are explained in Appendix A. The planar

LSFTa1 permeation membrane was prepared by uniaxial pressing and sintering as explained in section 8.3.

The schematic of the set-up for partial oxidation measurements of tubular membranes is given in Fig. 9.1.
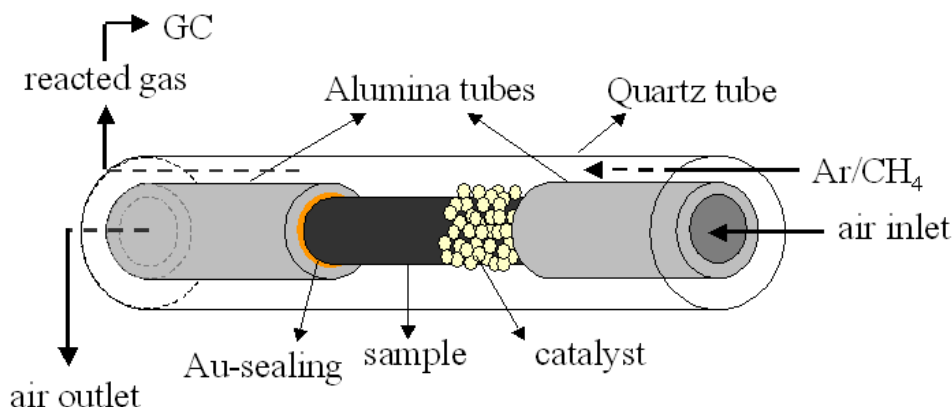

Fig. 9.1. Schematic of the setup for permeation measurements for tubular membranes.

The tube was fixed at the ends to alumina tubes using gold-paste for sealing. Then they were introduced in a quartz-tube (with 10mm internal diameter). The space between the measured mixed-conducting tube and the quartz tube was filled with MgO granulates (~1mm in diameter) coated with a POX catalyst. The planar membrane was measured as explained in section 8.2.

The membrane was initially heated in an air/argon gradient up to 1050°C in order to soften the gold and tighten the sealing. The temperature was then decreased to the measurement temperature. Ar or methane-Ar mixture was fed to this catalytic side and air to the inner side. In order to prevent an abrupt change in the material, CH_4 was introduced to the catalytic side gradually starting from 5%. Gas flow rates of 100ml/min were used for both sides. The composition of the outlet gas from the catalytic side was analyzed using a gas chromatograph (GC) (Varian) equipped with a molecular sieve 5 Å capillary column.[42, 164] The permeation measurements were conducted during cooling from 1000°C to 750°C at each 50 K after a certain dwell time for equilibration.

9.4. Microstructure and density of $La_{0.5}Sr_{0.5}FeO_{3-\delta}$ and $La_{0.5}Sr_{0.5}Fe_{0.8}Ti_{0.2}O_{3-\delta}$

The densities of the sintered bodies were reported in section 3.3.1. The densities (and the relative densities) of LSF, LSFTi2, and LSFTa1 were 5.98 (97.7%), 5.82 (96%), and 6.235 g/cm^3 (97.8%), respectively. The relative densities of the sintered tubes are shown in Table 9.1 together with the dimensions of the tubes used for permeation measurements.

Table 9.1. Physical properties of the LSF and LSFTi2 tubes and LSFTa1 pellet measured for oxygen permeation flux.

Sample	Relative density (%)	Outer diameter (mm)	Wall thickness (mm)
LSF	95.8 ± 0.7	5.00 ± 0.02	0.47 ± 0.01
LSFTi2	95.1 ± 0.2	4.80 ± 0.03	0.36 ± 0.0
LSFTa1*	97.8		1.32**

* planar membrane, ** pellet thickness

The densities of LSF and LSFTi2 tubes are slightly lower than the pressed pellets as they had relative densities exceeding 97%. As all samples (either extruded or uniaxially pressed) were sintered at the same max temperature and duration, the difference in the density is most probably due to the different green densities, thus the production technique. The green densities obtained for the tubes after removal of the organics is most probably less than the uniaxially pressed pellets.

An image of the extruded tubes is shown in Fig. 9.2 (a). The tubes shown have different thickness; ~0.5 and ~0.2 mm. Typical microstructures of fractured surfaces of sintered tubes are shown in Fig. 9.2 (b) and (c) for LSF and LSFTi2, respectively.
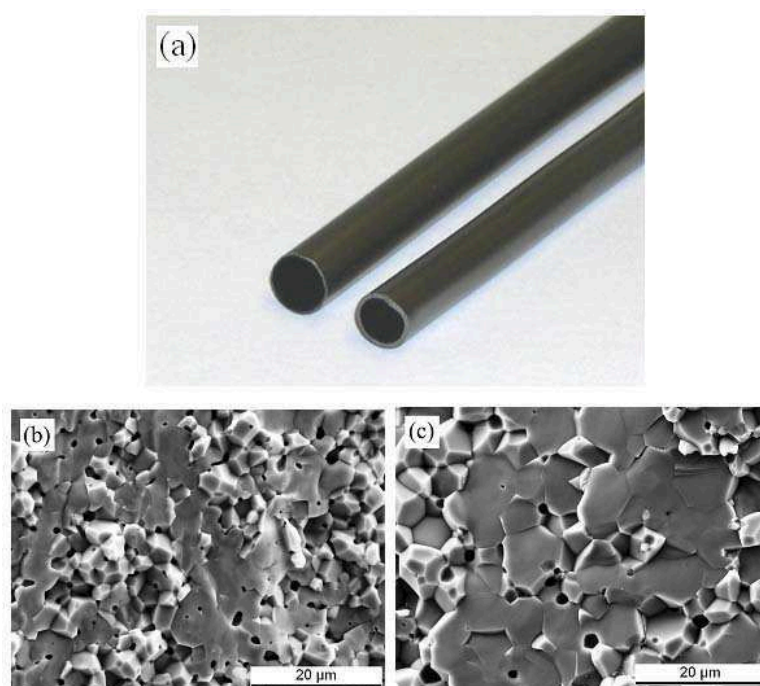
Fig. 9.2. a) Sintered LSF tubes, fracture surfaces of b) LSF, and c) LSFTi2 tubes.

It was possible to obtain tubes with wall thickness slightly more than 100 μm, which kept the spherical shape and remained intact through sintering. The samples show a similar fracture behavior to the pellets, reported in Chapter 3, with a mixture of inter- and intra-granular fracture.

9.5. Partial oxidation performance of membranes

Note that, from this point of the thesis, the tubular LSF and LSFTi2 and planar LSFTa1 samples, which are discussed in this section will be referred as POX membranes although in some cases it was not possible to conduct the measurement with methane. The samples discussed in Chapter 8 will be referred as planar membranes.

Arrhenius plots of normalized oxygen permeation flux (nJ_{O2}) of LSF, LSFTi2, and LSFTa1 POX and planar membranes measured under air/Ar gradient are shown as separate plots in Fig. 9.3 (a), (b), and (c), respectively. The permeation of planar membranes measured under air/Ar, previously shown in Chapter 8 as Fig. 8.4 are added to Fig. 9.3 to make the comparison easier. The permeation data was normalized to 1 mm for direct comparison of the materials. The thicknesses of all the membranes are indicated in the legend of each plot. The dashed lines are the linear fits to the plots used for calculation of activation energies. The as measured permeation (without normalization, J_{O2}) of the materials are shown in the same figure as (d), (e), and (f). The actual oxygen permeation fluxes at 900°C together with the

activation energies are shown in Table 9.2. The values in parentheses show the deviation on the last digit.
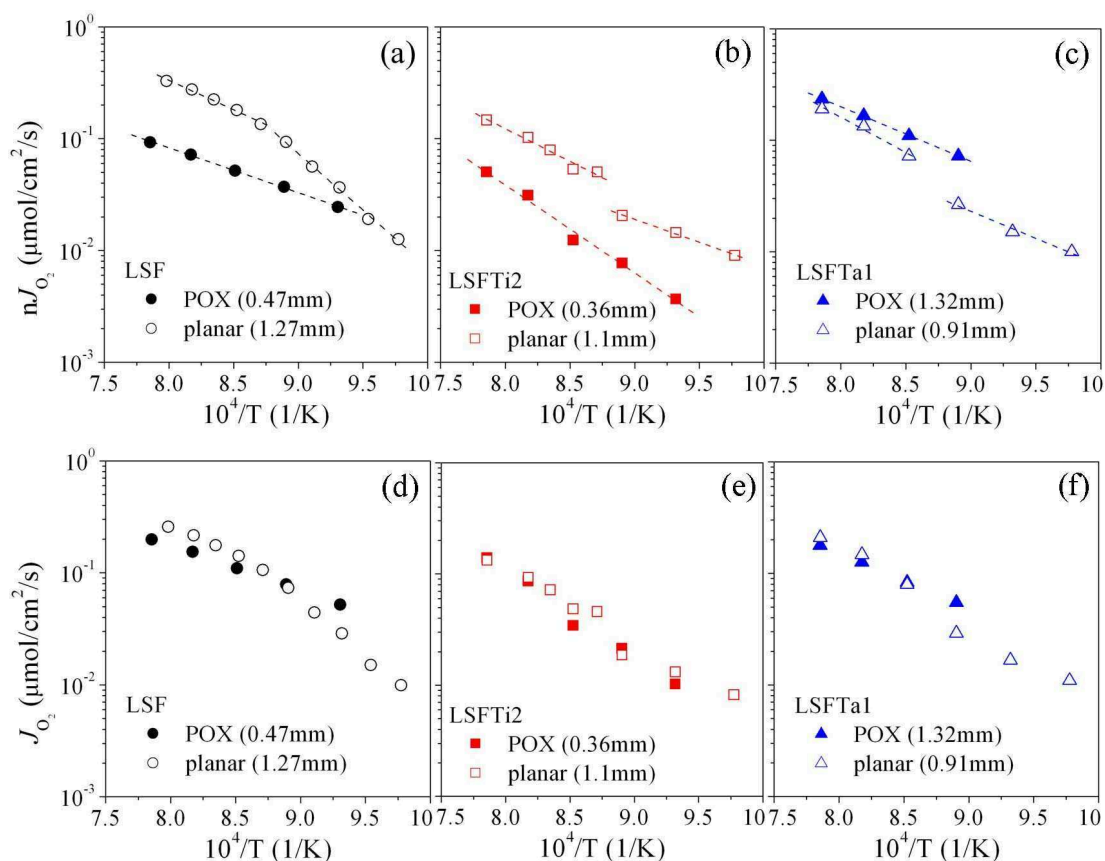

Fig. 9.3. Normalized and as measured oxygen permeation fluxes of (a) & (d) LSF, (b) & (e) LSFTi2, and (c) & (f) LSFTa1 POX membranes measured under air/Ar gradient together with the Arrhenius plots of permeation of planar membranes under air/Ar.

Table 9.2. The oxygen permeation fluxes of LSF, LSFTi2, and LSFTa1 at 900°C and the corresponding activation energies.

Sample	Condition	$J_{O_2, 900°C}$ ($\mu mol.cm^{-2}.s^{-1}$)	E_a (kJ/mol)
LSF	Air/Ar	0.11	76(2)
LSFTi2	Air/Ar	0.034	150(9)
	Air/(5%CH$_4$–95% Ar)	0.49	81(2)
LSFTa1	Air/Ar	0.083	94(2)
	Air/CH$_4$	0.71	83(3)

The comparison of the normalized fluxes of POX membranes measured with Ar at the lean-side (Fig. 9.3 (a) and (b)) shows that the LSFTi2 tube exhibited lower permeation and

higher activation energy compared to the LSF tube. This is in agreement with the previous permeation measurements shown in Chapter 8 and the literature.[52, 171] The POX membranes show a different behavior compared to the planar membranes. The permeation measurements on planar membranes of the LSF, LSFTi2, and LSFTa1 compositions revealed that there were discontinuities in the Arrhenius plots for all cases, section 8.4.[148] Below the discontinuity temperature the equilibration of the flux was found to be very slow and this was attributed to possible ordering of oxygen vacancies or surface exchange kinetics. The discontinuous behavior is not observed in case of POX membranes, at least in case of LSF and LSFTa1. It was found useful in this case to plot the data also as they were measured without the correction for their thickness as shown in Fig. 9.3 (d)-(f) to see the effect of thickness.

For LSF samples, it is observed that the normalized permeation values are considerably different from each other at higher temperatures while the values become closer at lower temperatures although the activation energy is vastly different. On the other hand, the results shown in Fig. 9.3 (d) indicate an opposite behavior. According to this figure, the thickness of the material has a very small effect on the permeation flux and the activation energies are in the same range. In the previous chapter, diffusion controlled permeation flux was suggested for LSF planar material, where the activation energy coupled with bulk diffusion was double of the higher temperature surface controlled region. In case of LSF as a POX membrane, the thickness is 0.47 mm, less than half of the thickness of the planar membrane (1.27 mm). The decreased thickness of the LSF POX membrane obviously results in surface exchange controlled oxygen permeation over the measurement temperature range and an enhanced permeation at lower temperatures. A similar result was observed by Diethelm et al.[43] for $La_{0.5}Sr_{0.5}FeO_{3-\delta}$ membranes that had different grain sizes and thicknesses. The bulk limited fluxes were found to be affected by grain size. The oxygen permeation at temperatures higher than 900°C was found to be independent of sample thickness among the finer grained samples.

The normalized fluxes of 0.34 mm thick LSFTi2 POX membrane and 1.1 mm thick LSFTa1 planar membranes show a big difference in values (Fig. 9.3 (b)). However, the as measured permeation values, shown in (e), coincide reasonably well; although the drop in permeation causing two temperature regions is not very obvious in case of LSFTi2 sample. The fact that the permeation of the POX membrane three times thinner provides similar amount of oxygen permeation flux indicates that both samples are governed by surface exchange kinetics over the whole temperature range. However, the decrease in the permeation remains speculative although it is possible that there may be an additional effect of ordering at temperatures lower than 900°C.

Finally in case of LSFTa1 membranes, both samples show similar permeation values in the higher temperature range with similar activation energies, which is also in similar

range with the activation energies of other materials when the surface exchange is rate determining. The POX sample does not show the discontinuity previously observed for the planar membrane, however the measurement range is not as wide as in case of planar membrane. Therefore, it is possible that the discontinuity temperature shifted slightly to lower temperatures improving the surface exchange at lower temperatures.

The LSF POX membrane fractured after the introduction of 5% CH_4. Therefore, no measurement points are available for LSF tubular membrane with methane in the catalytic gas stream. The LSFTi2 POX membrane could be measured with 5%CH_4 + 95%Ar mixture. However, this membrane also failed shortly after increasing CH_4 amount to 10%. In case of LSFTa1 planar POX membrane, 100% CH_4 could be reached. The Arrhenius plots of oxygen permeation fluxes of LSFTi2 measured with 5% CH_4 + 95% Ar mixture and LSFTa1 with 100% CH_4 are shown Fig. 9.4. Due to the fact that surface exchange kinetics was found to be rate determining previously in this chapter, the data were not normalized for the thickness. The dashed lines are the linear fits to the data, which were used to calculate the activation energies shown in Table 9.1.
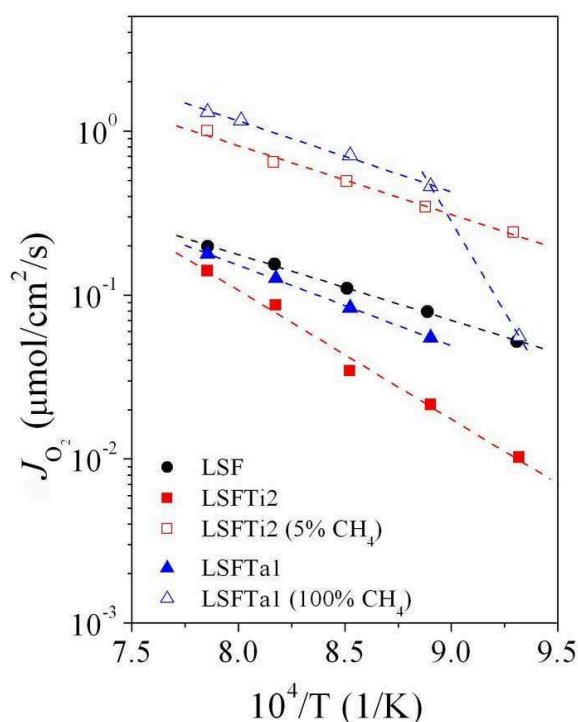

Fig. 9.4. Oxygen permeation fluxes of LSF, LSFTi, and LSFTa1 membranes measured under air/Ar, LSFTi2 membrane measured with 5% CH_4, and LSFTa1 membrane measured with pure CH_4.

The oxygen permeation of LSFTi2 was enhanced noticeably by the introduction of 5% methane to the gas stream. The oxygen permeation at 900°C was increased to 0.49 µmol

cm^{-2}s^{-1}, a factor of 14 compared to argon atmosphere. However, a leakage was observed when increasing the amount of methane to 10% at 1000°C. This indicates that the stability limit of the membrane material was exceeded. The activation energy decreases to the levels (81 kJ/mol) similar to that of LSF for example, for which the rate of the transport was surface exchange reaction. In case of LSFTi2 also, it is believed that the oxygen diffusion is not the rate-limiting step at these conditions. The failure of the LSFTi2 membrane brought the question if it could be avoided by a more controlled gas atmosphere change at lower temperatures. It is possible that the increased amount of chemical expansion at higher temperatures creates more stress on the membrane compared to lower temperatures. Pei et al.[45] identified two kinds of fracture for tubular SrCo0.8Fe0.2O3-δ membranes; the first kind that appeared shortly after the reaction started at 800°C and was attributed to chemical strain caused by large pO_2-gradient while the second kind was observed after long-term tests and was attributed to structure change.

In case of LSFTa1 membrane, the permeation was measured as a function of temperature only after the lean gas was pure methane and the amount of methane was increased gradually at 900°C. The oxygen flux was increased almost an order of magnitude with 100% methane on the catalytic side. Moreover, the membrane was operated 1000 hours at 1000°C without a problem. The experiment was stopped afterwards. The performance of the oxygen permeation flux as a function time is shown in Fig. 9.5 in normalized values.
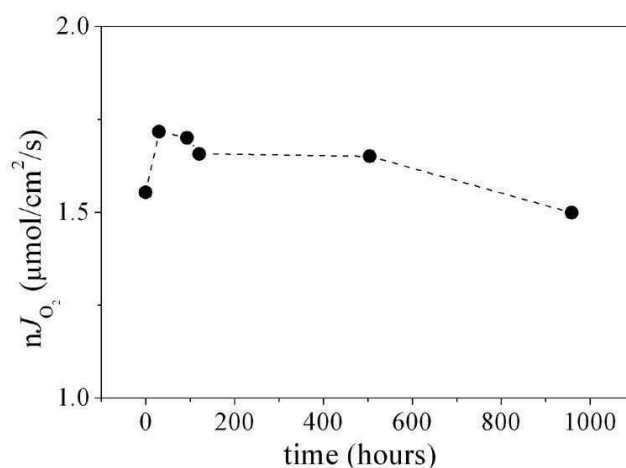

Fig. 9.5. Oxygen permeation flux of the LSFTa1 membrane at 1000°C measured under air/CH$_4$ gradient as a function of time.

The initial permeation of LSFTa1 increases from 1.55 μmol cm^{-2}s^{-1} and reaches up to 1.7 μmol cm^{-2}s^{-1} in 30 hours and then starts decrease again. The overall decrease from the beginning until the measurement was terminated is 3.7% per 1000 hours.

The selectivity of CO (S_{CO}) during the measurement remained at 100%, while the methane conversion (X_{CH4}) decreased from 76% to 66%. It should be noted that the flowing

conditions were not optimized and the performance information is given as complementary to the measurements. The methane conversion and CO selectivity of the LSFTi2 membrane measured with 5% methane as a function of temperature is shown below in Fig. 9.6.
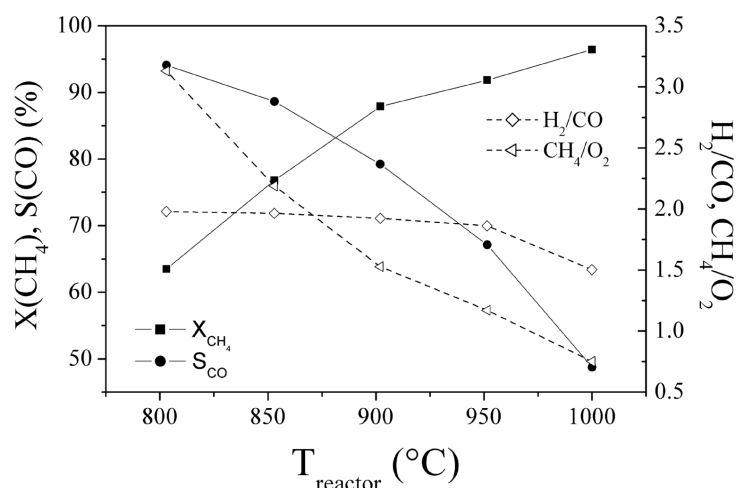

Fig. 9.6. Methane conversion (X_{CH4}) and CO selectivity (S_{CO}) of LSFTi2 (air/Ar – 5% CH_4) as a function of temperature.

The methane conversion reaches a value of 87% at 900°C and 96.4% at 1000°C while CO selectivity is 79% at 900°C and lowered to 49% at 1000°C. As it can be seen in Fig. 9.4, the methane inlet was not adjusted to the oxygen permeation flux; therefore the CH_4/O_2 varies from 0.75 to 3, which explains the changes in CO selectivity and methane conversion. In a study by Kharton et al.[172], the selectivity of partial oxidation of methane was found to be determined by the oxygen nonstoichiometry level. In order to identify the effect of B-site substitution on the catalytic performance of LSF-based materials, further investigations are needed.

9.6. Post-mortem analysis of membranes measured as POX-reactor

After their failure, the LSF and LSFTi2 tubes were investigated using scanning electron microscopy and energy dispersive X-ray analysis (EDX). Fig. 9.5 shows the SEM micrographs of the LSF and the LSFTi2 tubes after the permeation tests. The LSF membrane operated with 5% methane for a short time and LSFTi2 was operated with 5% methane and failed shortly after the amount was increased to 10%. In the Fig. 9.5 (a) and (b) show the fracture and inner (air) surfaces of LSF while (c) and (d) are the fracture and inner (air) surfaces of LSFT2.
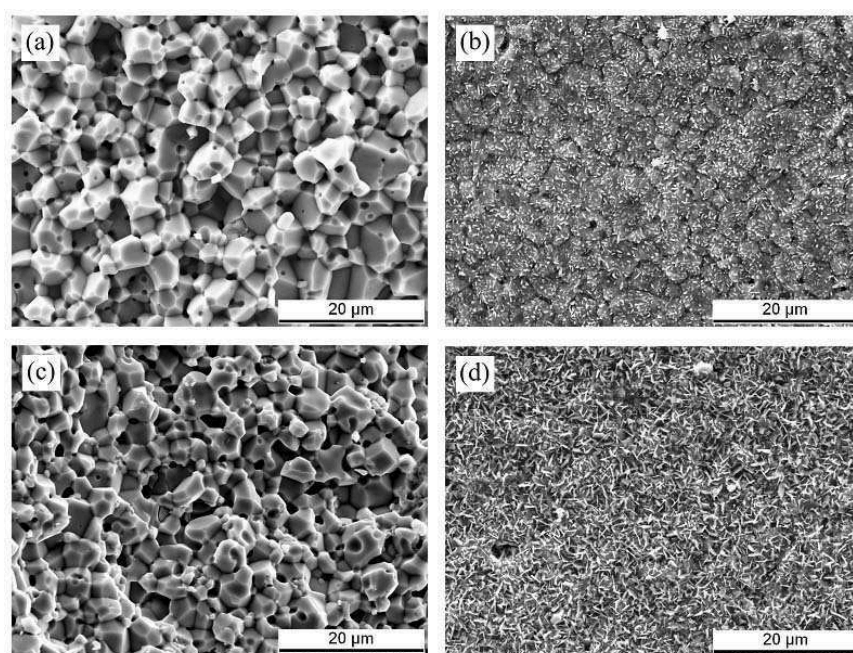
Fig. 9.5. Fracture surface and inner surface (air side) of LSF (a,c) and LSFTi2 (b,d).

According to back-scattered (BSE) image there was no obvious change in the composition through out the thickness of the membrane for both LSF and LSFTi2. However, fine structures were formed on the air-exposed surface of the tubes, which were not easy to differentiate in the back-scattered image. The amount of the second phase formed is more pronounced in the case of LSFTi2 covering the whole surface (Fig. 9.5 (d)). These structures may be result of contamination from outside or beginning of phase decomposition. XRD analysis was applied to the air-exposed surface of the same membrane. A second phase was confirmed in addition to the perovskite, however, due to the curved nature of the sample, exact diffraction peak positions were not available. In addition, SEM-EDX analysis on both surface of the LSFTi2 tube prevailed no inclusion on the surface, which supported the possibility of kinetic decomposition of the structure on the surface. The SEM pictures and the corresponding EDX analyses of lean- and air-side of the measured LSFTi2 sample is shown in Fig. 9.6 (a) and (b), respectively.
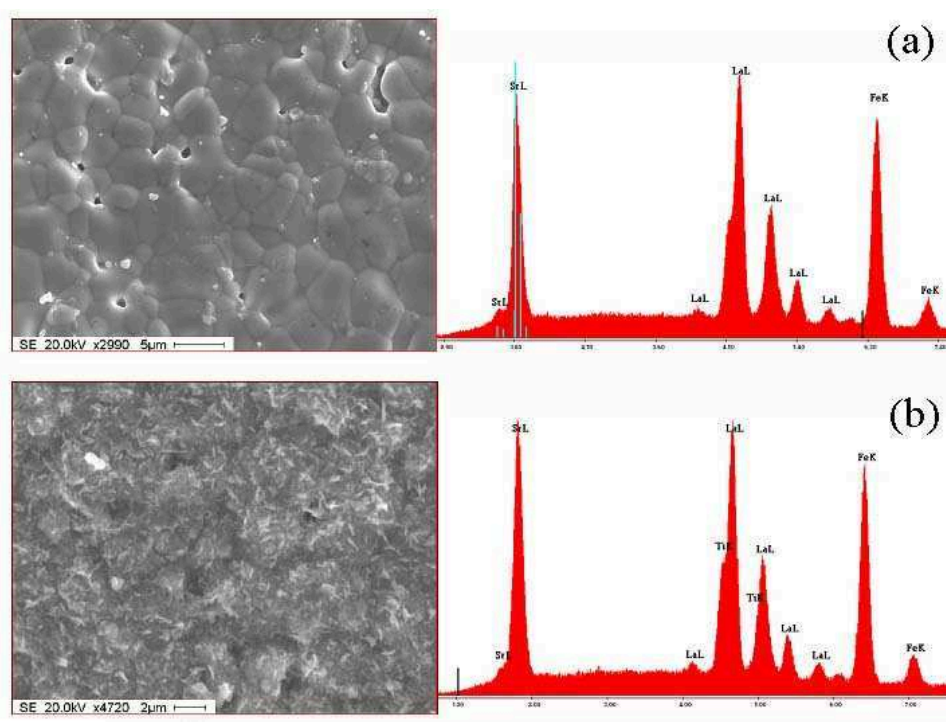
Fig 9.6. The catalytic- (a) and the air-side (b) of the LSFTi2 membrane after the measurement with corresponding EDX elemental analyses.

The EDX analyses of the surfaces show similar patterns. The only difference observed is that the Sr-count on the air-side of the material is increased compared to the La-count accompanied by slight increase of Fe-count. Therefore, it is concluded that a second-phase rich in Sr and Fe is formed on the air-side. Kaus et al. found similar phase formation as a dense layer on the air side of the $La_{0.6}Sr_{0.4}Fe_{0.8}Cr_{0.2}O_{3-\delta}$ membrane, which has similar needle-like structure.[173] This structure was found to be $SrFeO_{19}$ platelets, however, the same was not observed for 40% Ti-substituted sample. Kinetic decomposition at the air-side of the $La_{0.5}Sr_{0.5}FeO_{3-\delta}$ membrane was reported also by Lein et al.[163] The structure of the second phase was reported to be $SrFeO_{19}$ in this case also. Cation segregation in the opposite direction of accompanying oxygen flow has been observed for other materials also, causing second phase formation on the air-side of the membranes. In case of $La_{1-x}Ba_xFe_{0.8}Co_{0.2}O_{3-\delta}$ material, $BaCoO_3$ was formed on the air-side.[14] The migration of Co on this site was accompanied by its deficiency on the catalytic side. Another material, $La_{0.6}Sr_{0.4}Fe_{0.8}Co_{0.2}O_{3-\delta}$ was also reported to have cation segregation on the air-side forming SrO and $CoFeO_4$ confirmed by XRD and Raman measurements.[174] As in the other cases reported, this side exposed to air was found to be La deficient, in agreement also with the findings in this study. In the later presented studies, it was concluded that the oxygen flux was not affected by the formation of this phase on the surface and that this layer was porous enough for air to reach the sample surface that remained as perovskite. In this study, it is not possible to argue if the

second-phase formation on the surface had any effect on the failure of the membranes. However, at least in case of LSF material, it can be deduced that the effect should be minimal as the phase formation had barely started and not formed a layer yet.

For LSFTa1 material, investigation of the structure of the measured membrane is still needed. However, the degradation of the oxygen flux as a function of time with CH_4 on the lean-side suggests a change in the structure occurring over time and this may as well be related to a similar decomposition of the material.

The fracture of the ceramics was mostly intergranular after operation while it was a mixture of inter- and intragranular in the case of as-sintered tubes (Fig. 9.2 (b) and (c)). This suggests a structural change in the grain boundaries ending up in weaker bonds, in good agreement with the observation that the materials were considerably more brittle after the permeation measurements. A possible explanation for this behavior may be related to the high thermal and isothermal expansion coefficients of the LSF materials.[52, 57] As it is been discussed extensively previously in this thesis that the isothermal expansion is a result of the gradual reduction of the B-site cation resulting in a larger cation radius,[50] the difference in the local pO$_2$ through the membrane may therefore cause internal stresses resulting in micro cracks and lower mechanical stability. Furthermore, the difference in the expansion behavior of the grains and grain boundaries may become more pronounced with increased chemical expansion of the material. These can explain the difficulties faced in permeation measurements under methane atmosphere as well.

Considering the findings that the surface exchange reactions control the oxygen transport rate, improving surface reactions can play an important role in obtaining necessary flux rates. There have been several studies focusing mainly on surface modifications resulting with success. One approach is to coat the surface of the membrane with a porous layer. For example, the oxygen permeation of $BaCe_xFe_{1-x}O_{3-\delta}$ (x = 0.15-0.85) was improved up to twice when the membranes surface was coated with a porous layer of $Ba_{0.5}Sr_{0.5}Co_{0.8}Fe_{0.2}O_{3-\delta}$ (~10 µm).[175] Another approach used by Murphy et al.[176] was to increase the oxygen uptake on the oxygen supply side by depositing catalytic metal particles on this site, which facilitates the dissociation of molecular oxygen. The process doubled the oxygen permeation of non-perovskite $SrFeCo_{0.5}O_x$ membranes. Deposition of platinum also on the permeate side of the membrane was reported to enhance the permeation of $La_{1-y}Sr_yFeO_{3-\delta}$ as reported by van Hassel et al.[177] Therefore, there are indications that surface exchange reactions for both oxygen dissociation at the air-side or forming at the reaction side can be limiting for oxygen transport.

The LSFTa1 membrane reaches a flux of 0.71 µmol cm^{-2}s^{-1} at 900°C, which is more than 1 ml.cm^{-2}.min^{-1}. This is lower than the targeted flux of 10 ml.cm^{-2}.min^{-1} (as explained in Chapter 1), an estimated value to obtain necessary amount of syngas conversion so that the technique can offer advantages over the existing processes. Following similar approaches as

explained above, it is believed that the permeation rate of LSFTa1 membrane may be improved considerably. An improved permeation together with the enhanced stability of this material compared to its base composition can be a good candidate for application as an oxygen separation membrane for partial oxidation of hydrocarbons.

9.7. Summary and Conclusions

Tubular LSF and LSFTi2 (produced as explained in Appendix A) and the planar LSFTa1 membranes (so-called POX membranes) were investigated as partial oxidation reactors using air on one side and a argon-methane mixture on the other side. The Arrhenius plots of permeation fluxes measured under air/Ar gradient were compared to the previous measurements conducted on planar membranes (Chapter 8). The different thicknesses of the POX and planar membranes gave insight to the rate-determining step for the oxygen transport. Oxygen permeation in all membranes was found to be limited by surface exchange reactions, which resulted in similar activation energies around 80-100 kJ/mol in most cases. Considering the measurements conducted in the same conditions (air/Ar), the activation energies were found to increase in the order LSF<LSFTa1<LSFTi2.

Methane was introduced to the lean-side of the POX membranes gradually. LSF POX membrane failed after introduction of 5% CH_4 to the system, which is thought to be a result of chemical expansion. Similarly, LSFTi2 membrane failed shortly after CH_4 amount was increased to 10%. However, the permeation of LSFTi2 was increased considerably, by a factor of 14 to 0.49 μmol cm^{-2}s^{-1} at 900°C. LSFTa1 membrane, on the other hand, was stable even with pure CH_4 on the lean side. In this case, the permeation was increased by a factor of 9 to 0.71 μmol cm^{-2}s^{-1} at 900°C. Long-term permeation test was conducted with pure methane almost 2000 hour, 1000 of which was at 1000°C. At this temperature, the permeation decreased by 3.7% per 1000 hours. In the conditions the measurements were conducted (not optimized), the CO selectivity was 100% through out the long-term test at 1000°C and the methane conversion was between 66-76%.

The SEM and EDX analysis on the measured membranes revealed that a structure was formed at the air exposed surfaces of the LSF and LSFTi2 membranes. The amount of second-phase was low in case of LSF while the surface of the LSFTi2 membrane was totally covered by this phase. The SEM EDX analysis showed that the air exposed surface was deficient in La and enriched mostly in Sr and Fe. Therefore, it was concluded that a second-phase rich in Sr and Fe was formed on this side as a result of cation migration to this surface, which is in the opposite direction of oxygen migration.

Chapter 10

Summary and General Conclusions

10.1. Summary

The use of dense mixed ionic electronic conducting (MIEC) ceramic materials for oxygen separation membranes has become a subject of interest due to advantages over the present oxygen production techniques such as cryogenic distillation or pressure swing adsorption. The main advantage is the decreased cost of production in addition to the 100% O_2 selectivity obtained by the oxygen separation membranes. An important application foreseen for these membranes is the partial oxidation of methane (CH_4, the major component of abundant natural gas) to synthetic gas (syngas), which is the most important intermediate in upgrading process of methane into liquid products.

The major disadvantage of MIEC membranes is the low chemical and dimensional stability of those materials, which have high oxygen permeation rates. The reason for this tendency lies in the fact that both properties, oxygen transport and dimensional stability, are directly related to the oxygen vacancy concentration. High concentration of oxygen vacancies, which are available for oxygen transport, is one of the prerequisites for high oxygen permeation flux; on the other hand, the material expands as a consequence of reduction of B-site transition metal ion, which accompanies the oxygen vacancy formation. B-site substitution of transition metal ion with a more redox stable cation has been used to improve the stability of the membrane materials in reducing low pO$_2$ atmospheres.

In this thesis, the use of mixed ionic-electronic conducting (MIEC) membranes, especially for partial oxidation of methane is addressed considering the effect of B-site substitution on the stability and performance of the membranes. $La_{0.5}Sr_{0.5}FeO_{3-\delta}$ (LSF) was chosen as the host material because of its reported stability compared to cobalt containing perovskites and oxygen permeation rate. B-site substitution was selected to improve the stability for application in partial oxidation membranes. However, instead of using a random substituting element, a B-site substitution screening was carried out by substitution of 10 or 20% of the elements Mg, Al, Ga, In, Sn, Zr, Cr, Ti, Ta, and V, in order to identify the most promising element for the chosen host material considering the isothermal expansion. Although in similar amounts, the effect of different substitutions on isothermal expansion was varying depending on the element. The elements with high-valence (Ta^{5+}, 10%) were observed to be more effective in lower amounts compared to lower valence elements with higher amounts (Ti^{4+}, 20%). The compositions $La_{0.5}Sr_{0.5}Fe_{0.8}Ti_{0.2}O_{3-\delta}$ (LSFTi2) and $La_{0.5}Sr_{0.5}Fe_{0.9}Ta_{0.1}O_{3-\delta}$ (LSFTa1) were chosen as the most promising candidates characterized more in detail.

The crystal structure of LSF, LSFTi2, and LSFTa1 was studied by x-ray diffraction using synchrotron or conventional x-ray radiations. The room temperature structures in air were all found to be rhombohedral, changing to cubic at high temperatures (450°C for LSF).

Under slightly reduced oxygen partial pressure (i.e. after Ar-treatment) the rhombohedral symmetry changed to cubic and the unit cell showed an increase. This difference in the unit cell size depending on the thermal treatment in different oxygen partial pressures was related to the isothermal expansion of the samples and was doubled for LSF compared to LSFTi2 and LSFTa1.

Similar trend was observed by TGA studies, which showed that the non-stoichiometry difference, $\Delta\delta$, was dropped to half with Ti and Ta substitutions. A linear relation was found between $\Delta\delta$ and the chemical expansion ($\Delta l/l_0$) of the samples both measured at 900°C along the atmosphere change from air to Ar. All materials showed an increased expansion above a certain temperature due to oxygen loss accompanied by reduction of Fe^{4+} to Fe^{3+}, which is a larger ion. The coefficient of thermal expansion at higher temperatures was decreased by B-site substitution from 26.0×10^{-6} K^{-1} for LSF to 18.4×10^{-6} K^{-1} for LSFTa1.

XAS measurements showed that the hole concentration decreased with substitution of Ti and Ta, which would cause a decrease in the electrical conductivity of the materials. In line with this observation the substitution of Ti and Ta resulted in substantial decrease in the total conductivity compared to LSF. The conductivity measurements carried out as a function of pO$_2$ showed that the minimum in the conductivity, which occurs where basically all Fe ions become 3+, was moved to lower pO$_2$ with substitution of Ta in addition to the decreased conductivity. A further decrease in the conductivity of LSF was observed in the electronic charge carrier dominated region due to phase decomposition. XRD studies revealed that the LSF material was decomposed to a main tetragonal phase similar to LaSrFeO$_4$ and Fe in elemental form. LSFTa1 material, on the other hand, was found to sustain the perovskite structure with only a small amount of second-phase formation. It was concluded that the substitution of Ta improved the chemical stability of LSF considerably under reduced pO$_2$.

In addition to the electrical properties, the mechanical properties of the materials were investigated in terms of Young's modulus, bending strength, and fracture toughness. Although the Young's modulus (Ey) and four-point bending fracture strengths of the materials were found in the same range, the fracture toughness (K$_{Ic}$) of the samples of LSF was improved by B-site substitution.

Up to this point in the thesis, the effect of B-site substitution was investigated on properties such as structural, chemical, and mechanical. The trends observed so far proved the underlying aim of the B-site substitution to be right. Basically, most of the investigated properties gave evidence for the improved stability of the host material, especially by 10% Ta substitution. By substitution, the non-stoichiometry change of the material in two different atmospheres was reduced accompanied by reduced isothermal expansion of the unit cell and the bulk material. Additionally, phase stability of the material at reduced pO$_2$ was improved. However, this was one side of the story considering mostly the stability issues. As mentioned before, the oxygen permeation rate was expected to have opposite tendency. The second part

of the thesis addresses the transport properties of the selected materials to identify the impact of the improved stability.

The transport properties were studied using the potential step technique. The transport coefficients calculated from oxidation steps were found to be generally higher than the values for reduction steps. Both coefficients decreased with reduced partial pressure of oxygen. The critical thickness (L_c) of the samples was calculated using the chemical diffusion and surface exchange coefficients. The L_c increased with decreasing temperature exceeding 1 mm in all samples at 750°C, suggesting that the diffusion rate was controlled by surface exchange rate at this temperature and above.

The oxygen permeation fluxes of disc-shaped planar membranes were measured under an air/argon gradient. The permeation rate of LSF material was reduced from 0.18 $\mu mol.cm^{-2}.s^{-1}$ to 0.05 and 0.07 $\mu mol.cm^{-2}.s^{-1}$ by the substitution of Ti and Ta, respectively at 900°C. All three samples showed a change in the permeation behavior around 875°C. The change in the activation energy of LSF was attributed to a change in the rate-determining step, which was most likely chemical diffusion at low temperatures and the surface exchange at higher temperatures. On the other hand, LSFTi2 and LSFTa1 showed a decrease in the permeation around 875°C. Oxygen vacancy ordering was considered to cause this behavior.

Based on the potential step and permeation measurements, the ionic conductivities were calculated. The ionic conductivities calculated by permeation measurements should be considered with caution because the surface exchange kinetics may contribute to the permeation rate as discussed previously. At 900°C, the ionic conductivities calculated from potential step measurements (close to air atmosphere) were in the range of 0.0068 – 0.0152 S/cm, the highest value belonging to the non-substituted LSF sample in agreement with the permeation measurements. The corresponding oxygen ion transference numbers were 1×10^{-4} – 4×10^{-4} at 900°C in air. The ionic conductivity is negligible compared to the total conductivity and thus the material is a dominant electronic conductor; however, the ionic conductivities are in similar range as similar perovskite materials.

In order to characterize the LSF, LSFTi2 and LSFTa1 as partial oxidation reactors using air on one side and an argon-methane mixture on the other side, tubular LSF and LSFTi2 membranes produced by thermoplastic extrusion and the planar LSFTa1 membrane were investigated. Oxygen permeation in all membranes was found to be limited by surface exchange reactions. Considering the measurements conducted in the same conditions (air/Ar), the activation energies were found to increase in the order LSF<LSFTa1<LSFTi2. LSF failed in the POX application after introduction of 5% CH_4 to the system, which was thought to be a result of chemical expansion causing cracks. The permeation of LSFTi2 was increased considerably, by a factor of 14 to 0.49 $\mu mol\ cm^{-2}s^{-1}$ at 900°C. However, the membrane could be measured for a short time and failed shortly after CH_4 amount was increased to 10%. The LSFTa1 membrane, on the other hand, was stable even with pure CH_4 on the lean side. In this

case, the permeation was increased by a factor of 9 to 0.71 μmol cm^{-2}s^{-1} at 900°C. A long-term permeation test was conducted with pure methane for almost 2000 hours, 1000 of which was at 1000°C. At this temperature, the permeation decreased by 3.7% per 1000 hours.

The SEM and EDX analysis on the measured membranes revealed that a structure indicating a second phase was formed at the air exposed surfaces of the LSF and LSFTi2 membranes. The amount of the second-phase was low in case of LSF while the surface of the LSFTi2 membrane was totally covered. The SEM EDX analysis showed that the air exposed surface was deficient in La and enriched mostly in Sr and Fe. Therefore, it was concluded that a second-phase rich in Sr and Fe was formed on this side as a result of cation migration to the air-exposed surface, which is in the opposite direction of oxygen transport.

10.2. General conclusions

In literature, when B-site substitution is used to improve the stability of the material, generally similar elements are used and no systematic screening is applied. In this study, several substituting elements were considered. The thermal and isothermal expansion was highly dependent on the substituting element, decreasing with increasing amount and valence state.

The current literature contains studies on La$_{0.5}$Sr$_{0.5}$FeO$_{3-\delta}$ and Ti-substituted versions, however, up to our best knowledge, no information is available on Ta-substituted composition, which is found advantageous in this study, for the application in POX membranes.

The stability of the La$_{0.5}$Sr$_{0.5}$FeO$_{3-\delta}$ material was improved by partial substitution of Ti and Ta on the B-site. The isothermal expansion was reduced, which was related to oxygen non-stoichiometry. A linear relation between non-stoichiometry difference and isothermal expansion similar to LaCrO$_3$-based materials was shown in the measurement range (air-Ar). However, the linear relation may not be feasible with further oxygen vacancy formation as LSF was shown to decompose at reducing atmospheres or a possible vacancy ordering was speculated in case of LSFTi2 sample as a result of permeation measurements.

The mechanical properties of the MIEC materials considered for oxygen separation application are not studied commonly, but maybe important to evaluate the applicability of the materials. In this study, the fracture toughness (although measured at room temperature) was observed to be good indicator for the overall stability of the material. The improvement in the fracture toughness of the material by B-site substitution was found to be in agreement with the improved stability of the material including the isothermal expansion and the stability as a POX reactor. These results suggest an improvement in the bonding of the material. However, no difference was observed in the material property, Young's modulus,

except for the relative density dependence. The possible explanation for the decreased toughness of the host material is the built-up stress in the bulk sample after cooling to room temperature. Slow equilibrium of the materials at intermediate temperatures was observed in electrical conductivity and potential step relaxation measurements. Considering the size of the measured bars, it is feasible that the oxygen stoichiometry was not at equilibrium in the inner parts of the samples creating internal stress. Similar situation was observed for LSF permeation tube, which showed extreme brittleness after cooled down to room temperature, which was related to microcracks formed. Therefore, it may be massively important to allow necessary times for any heat treatment of the samples to ensure that the samples are stress free.

Another important point is that although much research work considers MIEC perovskite materials for partial oxidation applications, the measurements conducted under the operating conditions are very rare. One of the aims of this thesis was to conduct a through characterization of the considered materials including the long-term stability. It was observed that the behavior under different conditions (e.g. inert gas) did not necessarily provide the information if the materials could be used as POX reactors. Therefore, it is important to conduct a (preferably long-term) partial oxidation test to investigate the materials for this application.

The permeation under air/Ar was found to decrease with substitution; however, it was considerably increased by introduction of methane to the system, which was not achieved in case of LSF as the membrane failed shortly after the introduction of methane. Better stability of substituted membranes was observed during the permeation measurements, especially in case of LSFTa1 considering the long-term stability of the LSFTa1 membrane at 1000°C. The obtained flux values for LSFTa1 with pure methane was considerably lower (6-7 times) than the general target for the application, however, was promising for further optimization. One important result obtained was the low degradation rate of the oxygen flux compared to other published work, which sometimes reported more than 50% degradation in shorter times. Although the mechanism of the degradation needs to be addressed further, it is believed to be due to cation migration, which can be reduced at lower temperatures. In conclusion, the stability of the membrane materials could be improved and the accompanying oxygen flux was not dramatically decreased. The positive effect of Ta substitution on the stability of LSF provides a good indication for the application of this material as a POX membrane, although a number of issues still remain to be addressed.

10.3. Outlook

At this point, after obtaining a material that stably operates at the high end of the considered temperature ranges (1000°C) with low degradation, the important problem

remaining is how to obtain necessary oxygen permeation flux to commercialize the technique. Considering that the oxygen permeation rate was limited by surface exchange kinetics, the improvement of the surface can play an important role in the improvement of the permeation rate. As explained in Chapter 9, there are positive indications found by other authors about the effect of surface modifications.

It is important to identify the role of surface exchange kinetics at both oxygen-rich and oxygen-lean sides so that it is known if the rate is determined by oxygen incorporation into or release from the structure. It has been shown that the oxygen permeation could be improved by modifications on both surfaces. Moreover, with increased surface exchange reactions, the thickness of the membrane can be decreased, which may further enhance the oxygen permeation rate. There has been increasing amount of work on asymmetric membranes[178], which has a thin membrane deposited on a porous support made from either the same or a different material such as MgO. Similar approaches can be the next step to optimize the performance of the membranes identified in this work.

Appendix A

Production of Tubular Membranes

Thermoplastic paste extrusion was used to produce membranes in tubular shapes. Paste is simply a mixture of solid and liquid; mixed in such amounts that the resulting material can be shaped easily and the resulting product should retain its shape sufficiently for further processing. In membrane processing, one of the aims is to obtain thin wall thickness; therefore, thermoplastic paste systems were preferred in this work over water-based ones to obtain high green strength.

A.1. Thermoplastic extrusion of LSF and LSFTi2

LSF and LSFTi2 powders were prepared in large amounts in the same way as explained before, however, dried by spray-drying process. The particle size distribution of the powders was measured with a laser diffraction analyzer (LS230, Beckman-Coulter, USA). The specific surface area (SSA) of the powders was determined from a five point N_2 adsorption isotherm obtained from BET (Brunauer-Emmett-Teller) measurements using a Beckman-Coulter SA3100 (Beckman-Coulter, USA).

Tubes of compositions LSF, and LSFT2 with outer diameter of 4.8-6 mm and wall thickness of 0.25-1.1mm after sintering were produced by thermoplastic extrusion. Thermoplastic feedstocks were prepared with filling levels between 44 and 54.5 vol%. Licamont wax (EK 583, Clariant GmbH, Germany) and a polyethylene (PE) binder (1700MN 18C Lacqtene PEBD, elf atochem S.A., Switzerland) were mixed with ceramic powder in a high-shear mixer (Rheomix 3000 Torque Rheometer, Thermo Electron Corporation, Germany) in the temperature range of 110-170°C. A kneader with a volume of 69 cm^3 was used for the preparation of different ceramic contents, while a bigger kneader with a volume of 310 cm^3 was used for the feedstock, which was used for the extrusion of tubes. In order to reach maximum efficiency, the kneading volume was filled to 70%.
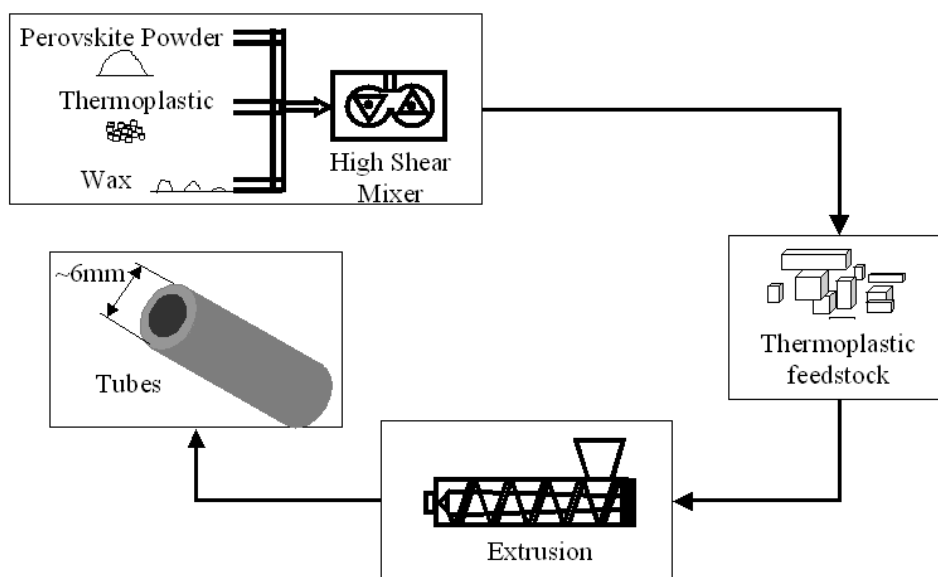
Fig.A.1. Schematic of thermoplastic extrusion.

The rheological behavior of the feedstocks was analyzed by a twin-bore capillary rheometer (RH7-2, Rosand Precision Limited, Germany). A single screw extruder (Rheomix 202, Thermo Electron Corporation, Germany) was used for extrusion of the tubes. The tubes were sintered at 1430°C and 1530°C for 4 hours for LSF and LSFT2 respectively. A slow heating curve was applied before sintering for binder removal. The microstructures of the sintered samples were investigated by SEM (Vega © Tescan).

A.2. Properties of LSF and LSFTi2 powders used for tube production

The average particle size distribution by laser diffraction analyzer showed a Gaussian distribution. The average particle size (d_{50}) and the specific surface areas (SSA) measured by BET are shown in Table A.1. The SEM micrograph of spray-dried LSF particle is shown in Fig. A.2. The spray-drying results in spherical particles as big as 50 μm composed of loosely bound crystallites. This provides easier flow of particles, which is advantageous for processing. It can be seen in the micrograph of the spray-dried powder that in average the particle size of crystallites is less than 1μm, although there are some bigger ones. This suggests that the presence of aggregates results in a higher value of average particle size in laser diffraction analysis. This is supported by the average particle sizes calculated from SSA (Table A.1). Although the trend is the same among the powders, the values are less than half of the sizes measured by laser diffraction. Note that, it is assumed that the particles are spherical and uniform in d_{50}(SSA) calculations.

Table A.1. Mean particle sizes (measured by laser diffraction and calculated from SSA), and SSAs of LSF and LSFTi2.

Sample	d_{50} (µm)	SSA (m²/g)	d_{50}(SSA) (µm)
LSF	1.3	1.89	0.51
LSFTi2	2.1	1.32	0.75
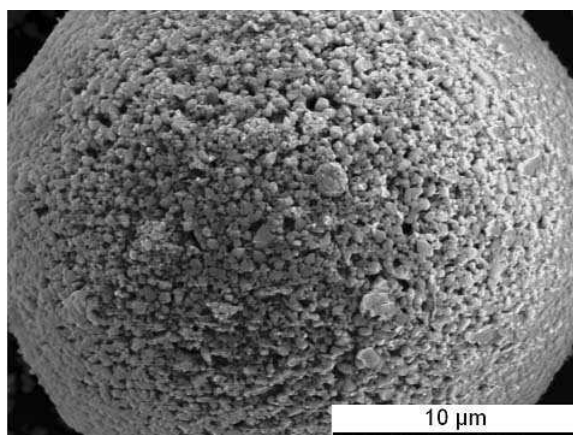
Fig. A.2. SEM-micrograph of spray-dried LSF powder.

A.3. Rheological properties of LSF and LSFTi2

In the preparation of feedstock for extrusion of tubes, it is important to use the right amount of ceramic powder. It has to be high enough to conserve the shape of the extruded tube as well as to obtain a good density after sintering. However, the ceramic powder content should be low enough to prevent abrasion during high-shear mixing and forming process by extrusion. The ratio of PE/Licomont used as the binder system was chosen as 0.5 for the thermoplastic extrusion of LSF and LSFTi2 materials as a result of a study conducted on $La_{0.6}Ca_{0.4}Fe_{0.75}Co_{0.25}O_{3-\delta}$ and $La_{0.5}Sr_{0.5}Fe_{1-y}Ti_yO_{3-\delta}$ (y=0, 0.2).[170] The equilibrium torque was low in this case (12 Nm and 14 Nm for LSF and LSFTi2 respectively) compared to $La_{0.6}Ca_{0.4}Fe_{0.75}Co_{0.25}O_{3-\delta}$ for which the PE/Licomont ratio was lower. This showed that increasing the amount of PE decreases the torque and therefore the abrasion during processing. This can be explained by lower interaction between the particles because of the higher molecular weight of the PE compared to the wax. In addition, no strong fluctuation in the torque was observed for these feedstocks indicating that for LSF and LSFT2 the PE/Licamont ratio used was suitable for an efficient high shear mixing.

Extrusion of straight tubes was found to be strongly dependent on the environment conditions since bending was observed in different directions. Straight tubes could be obtained by preventing any kind of airflow until the tubes cooled down to room temperature.

In recent investigations in our lab, this sort of bending by inhomogeneous cooling was attributed to the partial crystallization of PE during cooling.

Bibliography

1   R. M. Thorogood, Gas Separation and Purification **5**, 83 (1991).

2   P. N. Dyer, R. E. Richards, S. L. Russek, and D. M. Taylor, Solid State Ionics **134**, 21 (2000).

3   A. G. Dixon, W. R. Moser, and Y. H. Ma, Industrial & Engineering Chemistry Research **33**, 3015 (1994).

4   R. M. Thorogood, T. F. Y. Srinivasan, and M. P. Drake, US Patent 5,240,480 (1993).

5   M. Liu, A. G. Joshi, and Y. Shen, US Patent 5,273,628 (1993).

6   M. F. Carolan, P. N. Dyer, J. M. LaBar, and R. M. Thorogood, US Patent 5,261,932 (1993).

7   H. J. M. Bouwmeester and A. J. Burggraaf, in *The CRC Handbook of Solid State Electrochemistry*, edited by P. J. Gellings and H. J. M. Bouwmeester (CRC Press, London, 1997), p. 481.

8   M. A. Pena, J. P. Gomez, and J. L. G. Fierro, Applied Catalysis A: General **144**, 7 (1996).

9   J.-P. Lange and P. J. A. Tijm, Chemical Engineering Science **51**, 2379 (1996).

10   D. J. Wilhelm, D. R. Simbeck, A. D. Karp, and R. L. Dickenson, Fuel Processing Technology **71**, 139 (2001).

11   J. R. Rostrup-Nielsen, in *Studies in Surface Science Catalysis*, edited by D. M. Biddy, C. D. Chang, R. F. Howe and S. Yurchak (Elsevier, Amsterdam, 1988), Vol. 36, p. 73.

12   J. M. Fox, Catalysis Reviews - Science and Engineering **35**, 169 (1993).

13   P. N. Dyer, M. F. Carolan, D. Butt, R. H. E. Van Doorn, and R. A. Cutler, edited by U. S. Patent, 2002).

14   C.-Y. Tsai, A. G. Dixon, W. R. Moser, and B. Ma, AlChe Journal **43**, 2741 (1997).

15   F. A. Kröger and H. J. Vink, Solid State Physics **3**, 307 (1956).

16   P. V. Hendriksen, P. H. Larsen, M. Mogensen, F. W. Poulsen, and K. Wiik, Catalysis Today **56**, 283 (2000).

17   H. J. M. Bouwmeester, Catalysis Today **82**, 141 (2003).

18   U. Balachandran and B. H. Ma, Journal of Solid State Electrochemistry **10**, 617 (2006).

19   B. C. H. Steele, Current Opinion in Solid State & Materials Science **1**, 684 (1996).

20   http://super.gsnu.ac.kr/lecture/inorganic/perovskite.html.

21   V. M. Goldschmidt, Akad. Oslo I. Mat.-Natur **2**, 7 (1926).

22   Y. Teraoka, T. Nobunaga, and N. Yamazoe, Chemistry Letters, 503 (1988).

23   V. V. Kharton, E. N. Naumovich, A. V. Kovalevsky, A. P. Viskup, F. M. Figueiredo, I. A. Bashmakov, and F. M. B. Marques, Solid State Ionics **138**, 135 (2000).

24   J. C. Grenier, M. Pouchard, P. Hagenmuller, and S. Komomicki, in *International Conference on Ferrites*, Japan, 1980), p. 410.

25   J.-C. Grenier, N. Ea, M. Pouchard, and P. Hagenmuller, Journal of Solid State Chemistry **58**, 243 (1985).

26   Y. Teraoka, T. Nobunaga, K. Okamoto, N. Miura, and N. Yamazoe, Solid State Ionics **48**, 207 (1991).

27   Y. Teraoka, H. M. Zhang, S. Furukawa, and N. Yamazoe, Chemistry Letters, 1743 (1985).

28   A. Hammou and J. Guindet, in *The CRC Handbook of Solid State Electrochemistry*, edited by P. J. Gellings and H. J. M. Bouwmeester (CRC Press, London, 1997), p. 415.

29   J. Sfeir, EPFL, 2001.

30   Y. Teraoka, H. M. Zhang, K. Okamoto, and N. Yamazoe, Materials Research Bulletin **23**, 51 (1988).

31   Z. Shao, W. Yang, Y. Cong, H. Dong, J. Tong, and G. Xiong, Journal of Membrane Science **172**, 177 (2000).

32   P. Zeng, Z. Chen, W. Zhou, H. Gu, Z. Shao, and S. Liu, Journal of Membrane Science **291**, 148 (2007).

33   J. Mizusaki, M. Yoshihiro, S. Yamauchi, and K. Fueki, Journal of Solid State Chemistry **58**, 257 (1985).

34   J. Mizusaki, M. Yoshihiro, S. Yamauchi, and K. Fueki, Journal of Solid State Chemistry **67**, 1 (1987).

35   J. Mizusaki, Solid State Ionics **52**, 79 (1992).

36   C. Wagner, Progress in Solid-State Chemistry **10**, 3 (1975).

37   S. Diethelm, Ècole Polytechnique Fédérale de Lausanne, 2001.

38   H. Schmalzried, *Solid State Reactions* (Verlag Chemie, Weinheim, 1981).

39   H. Rickert, *Electrochemistry of Solids: An Introduction* (Springer-Verlag, Berlin, 1982).

40   C. Wagner and W. Schottky, Z. Phys. Chem. **B11**, 25 (1930).

41   I. Riess, in *The CRC Handbook of Solid State Electrochemistry*, edited by P. J. Gellings and H. J. M. Bouwmeester (CRC Press, London, 1997), p. 224.

42   S. Diethelm and J. Van herle, Solid State Ionics **174**, 127 (2004).

43   S. Diethelm, J. van Herle, J. Sfeir, and P. Buffat, British Ceramic Transactions **103**, 147 (2004).

44   M. van der Haar, University of Twente, 2001.

45   S. Pei, et al., Catalysis Letters **30**, 201 (1995).

46   H. Yokokawa, N. Sakai, T. Kawada, and M. Dokiya, Solid State Ionics **52**, 43 (1992).

47   T. Nakamura, G. Petzow, and L. J. Gauckler, Materials Research Bulletin **14**, 649 (1979).

48   L. G. Tejuca, J. L. G. Fierro, and J. M. D. Tascon, Advances in Catalysis **36**, 237 (1989).

49   H. Ullmann, N. Trofimenko, F. Tietz, D. Stover, and A. Ahmad-Khanlou, Solid State Ionics **138**, 79 (2000).

50   A. Atkinson and T. Ramos, Solid State Ionics **129**, 259 (2000).

51   D. P. Fagg, V. V. Kharton, J. R. Frade, and A. A. L. Ferreira, Solid State Ionics **156**, 45 (2003).

52   E. V. Tsipis, M. V. Patrakeev, V. Kharton, A. A. Yaremchenko, G. C. Mather, A. L. Shaula, I. A. Leonidov, V. L. Kozhevnikov, and J. R. Frade, Solid State Sciences **7**, 355 (2005).

53   V. V. Kharton, A. L. Shaulo, A. P. Viskup, M. Avdeev, A. A. Yaremchenko, M. V. Patrakeev, A. I. Kurbakov, E. N. Naumovich, and F. M. B. Marques, Solid State Ionics **150**, 229 (2002).

54   R. E. Williford, T. R. Armstrong, and J. D. Gale, Journal of Solid State Chemistry **149**, 320 (2000).

55   K. Hilpert, R. W. Steinbrech, F. Boroomand, E. Wessel, F. Meschke, A. Zuev, O. Teller, H. Nickel, and L. Singheiser, Journal of the European Ceramic Society **23**, 3009 (2003).

56   A. Zuev, L. Singheiser, and K. Hilpert, Solid State Ionics **147**, 1 (2002).

57   V. V. Kharton, A. A. Yaremchenko, M. V. Patrakeev, E. N. Naumovich, and F. M. B. Marques, Journal of the European Ceramic Society **23**, 1417 (2003).

58   V. V. Kharton, et al., Journal of Membrane Science **252**, 215 (2005).

59   M. V. Patrakeev, J. A. Bahteeva, E. B. Mitberg, I. A. Leonidov, V. L. Kozhevnikov, and K. R. Poeppelmeier, Journal of Solid State Chemistry **172**, 219 (2003).

60   R. D. Shannon, Acta Crystallographica Section A **32**, 751 (1976).

61   M. Abbate, et al., Physical Review B **46**, 4511 (1992).

62   U. Russo, L. Nodari, M. Faticanti, V. Kuncser, and G. Filoti, Solid State Ionics **176**, 97 (2005).

63   H. L. Lein, K. Wiik, and T. Grande, Solid State Ionics **177**, 1795 (2006).

64   O. Fukunaga and T. Fujita, Journal of Solid State Chemistry **8**, 331 (1973).

65   J. A. Kilner and R. J. Brook, Solid State Ionics **6**, 237 (1982).

66   S. E. Dann, D. B. Currie, M. T. Weller, M. F. Thomas, and A. D. Al-Rawwas, Journal of Solid State Chemistry **109**, 134 (1994).

67   A. Fossdal, M. Menon, I. Waernhus, K. Wiik, M. A. Einarsrud, and T. Grande, Journal of the American Ceramic Society **87**, 1952 (2004).

68   M. Suzuki, M. Muraoka, Y. Sawada, and J. Matsushita, Materials Science and Engineering B **54**, 46 (1998).

69   W. D. Kingery, H. K. Bowen, and D. R. Uhlmann, *Introduction to ceramics* (John Wiley & Sons, New York, 1975).

70   M. Trunec, J. Cihlar, S. Diethelm, and J. Van Herle, Journal of the American Ceramic Society **89**, 949 (2006).

71   J. L. Routbort, K. C. Goretta, R. E. Cook, and J. Wolfenstine, Solid State Ionics **129**, 53 (2000).

72   http://nobelprize.org/nobel_prizes/physics/laureates/1901/rontgen-bio.html.

73   F. R. Elder, A. M. Gurewitsch, R. V. Langmuir, and H. C. Pollock, Physical Review **71**, 829 (1947).

74   S. F. A. Kettle, *Physical Inorganic Chemistry. A Coordination Chemistry Approach* (Oxford University Press, Oxford, England, 1996).

75   W. Gawelda, École Polytechnique Fédérale de Lausanne, 2006.

76   D. C. Koningsberger and R. Prins, *X-ray absorption principles, applications, techniques of EXAFS, SEXAFS and XANES* (Wiley, New York, 1998).

77   A. Mineshige, J. Abe, M. Kobune, Y. Uchimoto, and T. Yazawa, Solid State Ionics **177**, 1803 (2006).

78   http://hasylab.desy.de/index_eng.html.

79   http://hasylab.desy.de/facilities/doris_iii/beamlines/b2/index_eng.html.

80   M. Knapp, C. Baehtz, H. Ehrenberg, and H. Fuess, Journal of Synchrotron Radiation **11**, 328 (2004).

81   B. H. Toby, Journal of Applied Crystallography **38**, 1040 (2005).

82   T. J. B. Holland and S. A. T. Redfern, Mineralogical Magazine **61**, 65 (1997).

83   http://www.netzsch-thermal-analysis.com/.

84   http://www.srs.ac.uk/srs/.

85   http://www.srs.ac.uk/srs/stations/station1.1.htm.

86   T. Hahn ed., *International tables for crystallography* (Kluwer Academic Publishers, Dordrecht/Boston/London, 1996).

87   E. Blond and N. Richet, Journal of the European Ceramic Society **28**, 793 (2008).

88   H. Wadati, et al., Physical Review B - Condensed Matter and Materials Physics **71**, 1 (2005).

89   Z. Y. Wu, S. Gota, F. Jollet, M. Pollak, M. Gautier-Soyer, and C. R. Natoli, Physical Review B **55**, 2570 (1997).

90   H. Wadati, et al., Journal of the Physical Society of Japan **75**, 054704 (2006).

91   A. Braun, D. Bayraktar, A. S. Harvey, D. Beckel, J. A. Purton, P. Holtappels, L. J. Gauckler, and T. Graule, **Submitted** (2008).

92   C. Kittel, *Introduction to Solid State Physics* (Wiley, New York, 1996).

93   J. W. Stevenson, T. R. Armstrong, R. D. Carneim, L. R. Pederson, and W. J. Weber, Journal of the Electrochemical Society **143**, 2722 (1996).

94   H. U. Anderson, Solid State Ionics **52**, 33 (1992).

95   C. Y. Park and A. J. Jacobson, Journal of the Electrochemical Society **152**, J65 (2005).

96   A. A. Yaremchenko, M. V. Patrakeev, V. V. Kharton, F. M. B. Marques, I. A. Leonidov, and V. L. Kozhevnikov, Solid State Sciences **6**, 357 (2004).

97   I. A. Leonidov, V. L. Kozhevnikov, E. B. Mitberg, M. V. Patrakeev, V. V. Kharton, and F. M. B. Marques, Journal of Materials Chemistry **11**, 1201 (2001).

98   J. Yoo, C. Y. Park, and A. J. Jacobson, Solid State Ionics **175**, 55 (2004).

99   E. Bucher and W. Sitte, Solid State Ionics **173**, 23 (2004).

100   E. V. Bongio, H. Black, F. C. Raszewski, D. Edwards, C. J. McConville, and V. R. W. Amarakoon, Journal of Electroceramics **14**, 193 (2005).

101   M. V. Patrakeev, E. B. Mitberg, A. A. Lakhtin, I. A. Leonidov, V. L. Kozhevnikov, V. V. Kharton, M. Avdeev, and F. M. B. Marques, Journal of Solid State Chemistry **167**, 203 (2002).

102   J. Richter, ETH Zuerich, 2008.

103   W. Soboyejo, *Mechanical properties of engineered materials* (Marcel Dekker, Inc., New York, 2003).

104   D. J. Green, *An introduction to the mechanical properties of ceramics* (Cambridge University Press, Cambridge, 1998).

105   N. Ramakrishnan and V. S. Arunachalam, Journal of Materials Science **25**, 3939 (1990).

106   A. Atkinson and A. Selcuk, Solid State Ionics **134**, 59 (2000).

107   S. W. Paulik, S. Baskaran, and T. R. Armstrong, Journal of Materials Science **33**, 2397 (1998).

108   C. S. Montross, Journal of the European Ceramic Society **18**, 353 (1998).

109   S. Baskaran, C. A. Lewinsohn, Y. S. Chou, M. Qian, J. W. Stevenson, and T. R. Armstrong, Journal of Materials Science **34**, 3913 (1999).

110   J. Drennan, V. Zelizko, D. Hay, F. T. Ciacchi, S. Rajendran, and S. P. S. Badwal, Journal of Materials Chemistry **7**, 79 (1997).

111   N. Orlovskaya, K. Kleveland, T. Grande, and M. A. Einarsrud, Journal of the European Ceramic Society **20**, 51 (2000).

112   S. Geller and P. M. Raccah, Physical Review B **2**, 1167 (1970).

113   A. Fossdal, M. A. Einarsrud, and T. Grande, Journal of the European Ceramic Society **25**, 927 (2005).

114   S. C. Abrahams, R. L. Barns, and J. L. Bernstein, Solid State Communications **10**, 379 (1972).

[115] K. Kleveland, N. Orlovskaya, T. Grande, A. M. M. Moe, M.-A. Einarsrud, K. Breder, and G. Gogotsi, Journal of the American Ceramic Society **84**, 2029 (2001).

[116] N. M. Sammes and R. Ratnaraj, Journal of Materials Science **30**, 4523 (1995).

[117] D. L. Meixner and R. A. Cutler, Solid State Ionics **146**, 273 (2002).

[118] Y. S. Chou, K. Kerstetter, L. R. Pederson, and R. E. Williford, Journal of Materials Research **16**, 3545 (2001).

[119] N. Orlovskaya, H. Anderson, M. Brodnikovskyy, M. Lugovy, and M. J. Reece, Journal of Applied Physics **100**, 026102 (2006).

[120] H. Lein, Ø. Andersen, P. Vullum, E. Lara-Curzio, R. Holmestad, M.-A. Einarsrud, and T. Grande, Journal of Solid State Electrochemistry **10**, 635 (2006).

[121] E. Standard, European Comittee for Standardization CEN, EN 843 (1995).

[122] European Comittee for Standardization CEN, EN 843 (1995).

[123] E. 843-1, European Committee for Standardization (1995).

[124] E. 843-6, European Committee for Standardisation (2001).

[125] MIL-HDBK-790, Department of Defense (1992).

[126] J. J. Kübler, in *ASTM STP 1409*, edited by J. A. Salem, G. D. Quinn and M. G. Jenkins (American Society for Testing and Materials, West Conshohocken, PA, 2002).

[127] J. Kübler, Ceramic Engineering and Science Proceedings **18**, 155 (1997).

[128] T. Fett, International Journal of Fracture **72**, R27 (1995).

[129] N. Orlovskaya, et al., Journal of Power Sources, doi:10.1016/j.hpowsour.2008.03.072 (2008).

[130] R. Doshi, J. L. Routbort, and C. B. Alcock, in *Defects and Diffusion*, 1995), Vol. 127-128, p. 39.

[131] W. Weppner, in *The CRC Handbook of Solid State Electrochemistry*, edited by P. J. Gellings and H. J. M. Bouwmeester, London, 1997), p. 296.

[132] E. Mashkina, Friedrich-Alexander-Universität Erlangen-Nürnber, 2005.

[133] R. J. Chater, S. Carter, J. A. Kilner, and B. C. H. Steele, Solid State Ionics **53-56**, 859 (1992).

[134] E. Boehm, J. M. Bassat, M. C. Steil, P. Dordor, F. Mauvy, and J. C. Grenier, Solid State Sciences **5**, 973 (2003).

[135] R. A. De Souza and J. A. Kilner, Solid State Ionics **106**, 175 (1998).

[136] B. Ma and U. Balachandran, Solid State Ionics **100**, 53 (1997).

[137] B. Ma, U. Balachandran, J.-H. Park, and C. U. Segre, Solid State Ionics **83**, 65 (1996).

[138] J. E. ten Elshof, M. H. R. Lankhorst, and H. J. M. Bouwmeester, Journal of the Electrochemical Society **144**, 1060 (1997).

[139] J. E. Ten Elshof, M. H. R. Lankhorst, and H. J. M. Bouwmeester, Solid State Ionics **99**, 15 (1997).

140   I. Yasuda and T. Hikita, Journal of the Electrochemical Society **141**, 1268 (1994).

141   M. H. R. Lankhorst and H. J. M. Bouwmeester, Journal of the Electrochemical Society **144**, 1261 (1997).

142   S. Sunde, K. Nisancioglu, and T. M. Gur, Journal of the Electrochemical Society **143**, 3497 (1996).

143   A. Belzner, T. M. Gur, and R. A. Huggins, Solid State Ionics **40-41**, 535 (1990).

144   S. Diethelm, A. Closset, J. Van Herle, A. J. McEvoy, and K. Nisancioglu, Solid State Ionics **135**, 613 (2000).

145   S. Diethelm and J. Van herle, Journal of the European Ceramic Society **24**, 1319 (2004).

146   S. Diethelm, A. Closset, J. Van herle, and K. Nisancioglu, Journal of the Electrochemical Society **149**, E424 (2002).

147   S. Diethelm, A. Closset, K. Nisancioglu, J. Van herle, A. J. McEvoy, and T. M. Gur, Journal of the Electrochemical Society **146**, 2606 (1999).

148   D. Bayraktar, S. Diethelm, P. Holtappels, T. Graule, and J. Van herle, Journal of Solid State Electrochemistry **10**, 589 (2006).

149   J. Crank, *The mathematics of diffusion* (Clarendon, Oxford, 1975).

150   H. S. Carslaw and J. C. Jaeger, *Conduction of heat in solids* (Oxford University Press, London, 1959).

151   M. W. den Otter, L. M. van der Haar, and H. J. M. Bouwmeester, Solid State Ionics **134**, 259 (2000).

152   W. Sitte, E. Bucher, P. Ried, A. Mai, and F. Tietz, Proceedings of the 7th European SOFC Forum, B065 (2006).

153   A. Atkinson, R. J. Chater, and R. Rudkin, Solid State Ionics **139**, 233 (2001).

154   W. Preis, E. Bucher, and W. Sitte, Solid State Ionics **175**, 393 (2004).

155   L. M. van der Haar, M. W. den Otter, M. Morskate, H. J. M. Bouwmeester, and H. Verweij, Journal of the Electrochemical Society **149**, J41 (2002).

156   F. Mauvy, J. M. Bassat, E. Boehm, P. Dordor, J. C. Grenier, and J. P. Loup, Journal of the European Ceramic Society **24**, 1265 (2004).

157   M. W. den Otter, H. J. M. Bouwmeester, B. A. Bouwkamp, and H. Verweij, Journal of the Electrochemical Society **148**, J1 (2001).

158   J. Maier, Journal of the American Ceramic Society **76**, 1212 (1993).

159   G. Etchegoyen, T. Chartier, and P. Del-Gallo, Journal of Solid State Electrochemistry **10**, 597 (2006).

160   K. S. Lee, S. Lee, J. W. Kim, and S. K. Woo, Desalination **147**, 439 (2002).

161   A. Belzner, T. M. Gur, and R. A. Huggins, Solid State Ionics **57**, 327 (1992).

162   H. J. M. Bouwmeester, H. Kruidhof, and A. J. Burggraaf, Solid State Ionics **72**, 185 (1994).

[163] H. L. Lein, K. Wiik, and T. Grande, Solid State Ionics **177**, 1587 (2006).

[164] S. Diethelm, J. Sfeir, F. Clemens, J. Van Herle, and D. Favrat, Journal of Solid State Electrochemistry **8**, 611 (2004).

[165] Z. Q. Deng, W. S. Yang, W. Liu, and C. S. Chen, Journal of Solid State Chemistry **179**, 362 (2006).

[166] H. Kruidhof, H. J. M. Bouwmeester, R. H. E. v. Doorn, and A. J. Burggraaf, Solid State Ionics **63-65**, 816 (1993).

[167] J.-C. Grenier, F. Menil, M. Pouchard, and P. Hagenmuller, Materials Research Bulletin **13**, 329 (1978).

[168] H. Wang, Y. Cong, and W. Yang, Journal of Membrane Science **210**, 259 (2002).

[169] M. Trunec, J. Cihlar, S. Diethelm, and J. Van Herle, Journal of the American Ceramic Society **89**, 955 (2006).

[170] D. Bayraktar, F. Clemens, S. Diethelm, T. Graule, J. Van herle, and P. Holtappels, Journal of the European Ceramic Society **27**, 2455 (2007).

[171] S. Diethelm, J. Van herle, P. H. Middleton, and D. Favrat, Journal of Power Sources **118**, 270 (2003).

[172] V. V. Kharton, et al., Solid State Sciences **7**, 1344 (2005).

[173] I. Kaus, K. Wiik, K. Kleveland, B. Krogh, and S. Aasland, Solid State Ionics **178**, 817 (2007).

[174] F. Iguchi, N. Sata, H. Yugami, and H. Takamura, Solid State Ionics **177**, 2281 (2006).

[175] X. Zhu, Y. Cong, and W. Yang, Journal of Membrane Science **283**, 38 (2006).

[176] S. M. Murphy, D. A. Slade, K. J. Nordheden, and S. M. Stagg-Williams, Journal of Membrane Science **277**, 94 (2006).

[177] B. A. van Hassel, J. E. ten Elshof, and H. J. M. Bouwmeester, Applied Catalysis A: General **119**, 279 (1994).

[178] E. V. Tsipis, J. C. Waerenborgh, V. V. Kharton, E. N. Naumovich, and J. R. Frade, Journal of Physics and Chemistry of Solids **67**, 1882 (2006).

Acknowledgements

Curriculum Vitae

Name: Defne Bayraktar Testa
Date of Birth: 16.03.1978
Nationality: Turkish
Languages: Turkish (native), English (fluent), Italian and German (beginner)

EDUCATION:

2003-2007   Ph.D., Ecole Polytechnique Fédérale de Lausanne (EPFL)**,** Ceramics Laboratory, Materials Science and Engineering
and Swiss Federal Laboratories for Materials Testing and Research (EMPA), Laboratory for High Performance Ceramics

2000-2003   M.Sc., New York State College of Ceramics at Alfred University, Ceramic Engineering, "Harmonic analysis of electrochemical response of uncoated and sol-gel coated PMN-based ferroelectrics"

1999-2000   M.Sc. (Incomplete), Middle East Technical University (METU), Metallurgical and Materials Engineering

1995-1999   B.Sc., Middle East Technical University (METU), Metallurgical and Materials Engineering

PUBLICATIONS:

1. D. Bayraktar, S. Diethelm, T. Graule, J. Van herle, P. Holtappels, "Properties of B-site substituted $La_{0.5}Sr_{0.5}FeO_{3-\delta}$ perovskites for application in oxygen separation membranes", J. Electroceramics, published online, 1573-8663.
2. A. Braun, D. Bayraktar, A. S. Harvey, D. Beckel, J. A. Purton, P. Holtappels, L. J. Gauckler, T. Graule, "A spectral indicator for electron hole depletion and transport blocking upon cation doping in lanthanum strontium ferrous oxide", submitted.
3. D. Bayraktar, F. Clemens, S. Diethelm, T. Graule, J. Van herle, P. Holtappels, "Production and properties of substituted $LaFeO_3$-perovskite tubular membranes for partial oxidation of methane to syngas" *J. Eur. Ceram. Soc.*, **27**, 2455 (2007).

4. D. Bayraktar, S. Diethelm, P. Holtappels, T. Graule, J. Van herle, "Oxygen transport in $La_{0.5}Sr_{0.5}Fe_{1-x}Ti_xO_{3-\delta}$ (x = 0.0, 0.2) membranes", *J. Solid State Electr.*, **10**, 589 (2006).

5. D. Bayraktar and A. C. Tas, "Formation of Hydroxyapatite Precursors at 37□C in Urea- and Enzyme Urease-contatining Body Fluids," *J. of Mater. Sci. Lett.*, **20** (5), 401-403 (2001).

6. D. Bayraktar and A. C. Tas, "Preparation of Biomimetic HA Precursors at 37□C in Urea- and Enzyme Urease-containing Synthetic Body Fluids," "Bioceramics: Materials and Applications III," *Ceramic Transactions*, Vol. 110, pp. 39-52, (Eds.) L. George, R. P. Rusin, G. Fischman, and V. Janas, 2000, The American Ceramic Society, USA, ISBN 1-57498-102-1.

7. D. Bayraktar and A. C. Tas, "Chemical Preparation of Carbonated Calcium Hydroxyapatite Powders at 37°C in Urea-containing Synthetic Body Fluid," *J. Eur. Ceram. Soc.*, **19**, 2573-2579 (1999).